

NORTHWESTERN UNIVERSITY

Metal–Organic Frameworks as Catalysts and Catalysts Supports  
for the Detoxification of Chemical Warfare Agent Simulants

A DISSERTATION

SUBMITTED TO THE GRADUATE SCHOOL  
IN PARTIAL FULFILLMENT OF THE REQUIREMENTS

for the degree

DOCTOR OF PHILOSOPHY

Field of Chemistry

By

Cassandra Terez Buru

EVANSTON, ILLINOIS

March 2020

© Copyright by Cassandra T. Buru 2019

All Rights Reserved

## Abstract

### Metal–Organic Frameworks as Catalysts and Catalysts Supports for the Detoxification of Chemical Warfare Agent Simulants

Cassandra Terez Buru

The continued existence and use of chemical warfare agents (CWAs) have necessitated the development of materials which can safely and efficiently decontaminate these toxic chemicals in an environmentally benign fashion. Among the most prevalent CWAs, nerve agents (sarin, VX) and blistering agents (sulfur mustard [HD]) are considered the most toxic and most effective, respectively. Metal oxide materials have been identified as promising materials for the hydrolysis of organophosphorus nerve agents, a pathway not easily accessible for HD due to limited water solubility. Rather, the selective oxidation of HD to the sulfoxide is a more practical route. An ideal catalyst would be able to perform both reactions. To this end, we have identified multifunctional metal–organic frameworks (MOFs), composed of metal oxide-like nodes connected via organic linkers, as a promising platform for the simultaneous decontamination of nerve and blistering agents.

This thesis interrogates two different approaches for installing functionality in MOFs to perform sulfide oxidation while maintaining the metal oxide-like nodes for hydrolysis. In the first approach, the linkers of the MOFs were used as photosensitizers for the generation of singlet oxygen and subsequent oxidation of HD and its simulant. By using linkers with higher quantum yield, the reactivity of the system was improved. In the second approach, encapsulated species were installed to make use of the MOF porosity. Specifically, guest polyoxometalate (POM) molecules are immobilized within the channel-type pores. POMs are discrete anionic metal oxide clusters which can undergo reversible multi-electron redox reactions for catalysis, but suffer

from low-surface area and instability under catalytic conditions when used homogeneously. The hierarchical channel-type MOF allowed for POM absorption without compromising the stability or porosity of the composite, unlike previous POM@MOF examples. Dependent on the activation conditions, the POM guest was found in one of two locations within the MOF; the mechanism of this movement will be discussed. The composite POM@MOF material exhibited enhanced reactivity in the oxidation of a mustard gas simulant using hydrogen peroxide. Finally, this technique was used to immobilize an aerobically active POM in a MOF to achieve efficient aerobic sulfide oxidation.

## Acknowledgements

Thank you to everyone who has helped me get to this point. Given the limited space and time, I unfortunately cannot list all of the people, but even if you are not mentioned in here, I greatly appreciate all what you have done for me.

I am so lucky to have been advised by Professors Omar Farha and Joe Hupp. I will never know how Omar was able to keep track of not only my project and goals when I was having a rough time, but also everyone else in the group. He was always there to support my personal and professional goals, and he has overall been an amazing advisor. Joe has always offered an alternative perspective, and even though I did not want to pursue many of his suggestions, I am grateful for those insights. I would also like to acknowledge their program assistants over the years, Ben Nelson, Amanda Mahoney, Abby Rosensweig, and Nick Huryk, who have made working here smooth, always being there to answer all my questions (or find the person who can) and get me put into my advisors schedules whenever I wanted.

Thank you to all the group members who have been my mentors, specifically Yangyang Liu, Suyoung Moon, Peng Li, Nic Vermuelen, Zhanyong Li, Chung-wei Kung, Kenichi O'take, Satoshi Kato, Martino Rimoldi, Subhadip Goswami, and Timur Islamoglu. I would like to specifically acknowledge Ashlee Howarth and Aaron Peters for always being there to talk through my chemistry and answer my naïve questions. I would also like to mention my undergraduate students that I mentored, Sean, Rob, and Kevin, who have helped me become a better scientist through teaching and also did my work when I told them to.

Thank you to the rest of the Farha and Hupp group members who have made coming into work enjoyable. I will have fond memories of hanging out with the Dream Team: Amanda Mahoney (again), Paula García-Holley, Ashlee Howarth (again), Marek Majewski, Aaron Peters

(again), Cornelius Audu, and Matt Destefano. I was fortunate to have great officemates, Rebecca Palmer, Jian Liu, Rui Wang, and Paula García-Holley (again). I would also like to thank Yijing Chen, Xinyi Gong, and Hyunho Noh for keeping things interesting.

I would also like to give a shout out to my friends (the survivors of freshman organic), group members (Greg Karahalís, Marika Wieliczko, Jack, Trieu, and Thomas Pickel), and advisors (Jose Soria and Chris Scarborough) from undergrad who inspired me (and warned me not) to pursue graduate school.

Thank you Bryan Rossman for keeping me sane the last few months of grad school; I cannot wait to see what the future has for us and Legs and Pebbles.

I definitely would not be here without the continuous support from my family. Thank you to my brother and sisters, Christopher, Christina, and Clarissa, for always being there to talk and make fun of each other. And finally to my parents, Mommy and Daddy, even though I purposely missed some weekly Skype calls, I am forever grateful to all you have done for me.

## **Dedication**

*To the memory of my grandparents Rose and Leslie Jankovich,  
who have been an unending source of love, support, and inspiration in my pursuit of knowledge,  
and a testament to having endless possibilities and happiness when rooted in faith and family.*

## Table of Contents

<b>Abstract.....</b>	<b>3</b>
<b>Acknowledgements .....</b>	<b>5</b>
<b>Dedication .....</b>	<b>7</b>
<b>Table of Contents .....</b>	<b>8</b>
<b>List of Figures.....</b>	<b>12</b>
<b>List of Tables .....</b>	<b>19</b>
<b>Chapter 1 . Introduction .....</b>	<b>20</b>
<b>1.1 Motivation: Chemical Warfare Agent Detoxification.....</b>	<b>21</b>
<b>1.2 Metal-Organic Frameworks as Catalysts .....</b>	<b>21</b>
1.1.1 Nerve Agent Detoxification.....	22
1.1.2 Sulfur Mustard Detoxification .....	22
<b>1.3 Approach 1: Photosensitizers in Metal–Organic Frameworks.....</b>	<b>23</b>
<b>1.4 Approach 2: Polyoxometalates and their Metal–Organic Framework Composites... </b>	<b>24</b>
<b>1.5 Outline .....</b>	<b>29</b>
<b>Chapter 2 . Efficient and selective oxidation of sulfur mustard using singlet oxygen generated by a pyrene-based metal–organic framework .....</b>	<b>32</b>
<b>2.1 Introduction .....</b>	<b>33</b>
<b>2.2 Experimental Methods.....</b>	<b>36</b>
2.2.1 Material Syntheses .....	36

	9
2.2.2 Physical Methods .....	36
2.2.3 Catalytic Measurements .....	37
<b>2.3 Results and Discussion .....</b>	<b>39</b>
<b>2.4 Conclusions .....</b>	<b>45</b>
<b>Chapter 3 . Improving the efficiency of mustard gas simulant detoxification by tuning the singlet oxygen quantum yield in metal–organic frameworks and their corresponding thin films .....</b>	<b>47</b>
<b>3.1 Introduction .....</b>	<b>48</b>
<b>3.2 Experimental Methods.....</b>	<b>51</b>
3.2.1 Material Syntheses .....	52
3.2.2 Physical Methods .....	53
3.2.3 Material Characterization.....	54
3.2.4 Catalytic Measurements.....	55
<b>3.3 Results and Discussion .....</b>	<b>56</b>
<b>3.4 Conclusions .....</b>	<b>60</b>
<b>Chapter 4 . Adsorption of a catalytically accessible polyoxometalate in a mesoporous channel-type metal–organic framework .....</b>	<b>62</b>
<b>4.1 Introduction .....</b>	<b>63</b>
<b>4.2 Experimental Methods.....</b>	<b>66</b>
4.2.1 Material Syntheses .....	66

4.2.2 Physical Methods .....	10
4.2.3 Catalytic Measurements .....	67
4.2.3 Catalytic Measurements .....	70
<b>4.3 Results and Discussion .....</b>	<b>71</b>
4.3.1 Material Characterization .....	71
4.3.2 Catalytic Measurements .....	84
<b>4.4 Conclusions .....</b>	<b>90</b>
<b>Chapter 5 . Thermally induced migration of a polyoxometalate within a metal–organic framework and its catalytic effects.....</b>	<b>91</b>
<b>5.1 Introduction .....</b>	<b>92</b>
<b>5.2 Experimental Methods.....</b>	<b>94</b>
5.2.1 Material Syntheses .....	94
5.2.2 Physical Methods .....	95
5.2.3 Catalytic Measurements .....	98
<b>5.3 Results and Discussion .....</b>	<b>98</b>
<b>5.4 Conclusions .....</b>	<b>113</b>
<b>Chapter 6 . Restricting polyoxometalate movement within metal–organic frameworks to assess the role of residual water in catalytic thioether oxidation using these dynamic composites.....</b>	<b>115</b>
<b>6.1 Introduction .....</b>	<b>116</b>
<b>6.2 Experimental Methods.....</b>	<b>119</b>

	11
6.2.1 Materials Syntheses .....	119
6.2.2 Physical Methods .....	120
6.2.3 Catalytic Measurements.....	122
<b>6.3 Results and Discussion .....</b>	<b>122</b>
<b>6.4 Conclusions .....</b>	<b>132</b>
<b>Chapter 7 . Aerobic oxidation of a mustard gas simulant using the <math>H_5PV_2Mo_{10}O_{40}</math></b>	
<b>polyoxometalate encapsulated in NU-1000 metal–organic framework .....</b>	<b>133</b>
<b>7.1 Introduction .....</b>	<b>134</b>
<b>7.2 Experimental Methods.....</b>	<b>137</b>
7.2.1 Materials Syntheses .....	137
7.2.2 Physical Methods .....	138
7.2.3 Catalytic Measurements.....	139
<b>7.3 Results and Discussion .....</b>	<b>140</b>
<b>7.4 Conclusions .....</b>	<b>150</b>
<b>References .....</b>	<b>152</b>

## List of Figures

<b>Figure 1-1</b> General scheme for nerve agent hydrolysis .....	22
<b>Figure 1-2</b> Possible detoxification routes for sulfur mustard.....	23
<b>Figure 1-3</b> Routes of forming POM@MOF or POMOF materials starting from the precursors of POMs and MOFs. ....	26
<b>Figure 1-4</b> General approach for creating MOF materials capable of sulfur oxidation and nerve agent hydrolysis .....	30
<b>Figure 2-1</b> a) Pathways of HD detoxification: hydrolysis, dehydrohalogenation and oxidation (toxic/irritating chemicals in red, nontoxic chemicals in green). In the oxidation pathway, toxic bis(2-chloroethyl)sulfone (in red) can be produced as a result of complete oxidation. b) Selective photooxidation of HD simulant, CEES, using singlet oxygen generated by a MOF under LED irradiation, which only produces the nontoxic sulfoxide.....	34
<b>Figure 2-2</b> a) 3D structure of NU-1000, viewed along the c axis. b) NU-1000 viewed along the a axis and concept of generating singlet oxygen by the pyrene moieties in NU-1000 under UV LED.....	35
<b>Figure 2-3</b> Output wavelength of the UV LED (peak ~396 nm). Power density: 450mW/cm <sup>2</sup> .	37
<b>Figure 2-4</b> Gas chromatography (GC) signals indicating the progress of the oxidation of CEES (4.45 min) to CEESO (7.14 min) in the presence of NU-1000 (2.2 mg). For comparison, chromatograms of pure CEESO (7.14 min) and pure CEESO <sub>2</sub> (7.38 min) were also recorded, confirming that CEESO was the only product.....	40
<b>Figure 2-5</b> <sup>13</sup> C NMR spectra of a) Pure 1-chloro-2-(ethylsulfonyl)ethane (CEESO <sub>2</sub> ) in CDCl <sub>3</sub> , b) Pure 2-chloroethyl ethyl sulfoxide (CEESO) in CD <sub>3</sub> OD, c) pure 2-chloroethyl ethylsulfide (CEES) in CDCl <sub>3</sub> , d) oxidation of CEES in the presence of 2.2 mg NU-1000. The reaction is performed in CD <sub>3</sub> OD. NMR sample was taken at 15 min of the oxidation reaction, dissolved in CDCl <sub>3</sub> , indicating the oxidation is completed and only one product, 1-chloro-2-(ethylsulfinyl)ethane (CEESO), was obtained. e) NMR sample was taken at 0 min of the oxidation reaction, dissolved in CDCl <sub>3</sub> .....	40
<b>Figure 2-6</b> a) Conversion of 0.2 mmol of CEES under UV LED irradiation with 1 mol% of pyrene in NU-1000 compared to the MOF linker alone b) Oxidation profile of CEES in the presence of NU-1000 (2.2 mg) while being irradiated with a UV LED with two consecutive injections of CEES (0.2 mmol). c) Proposed mechanism for the oxidation of CEES by singlet oxygen ( <sup>1</sup> O <sub>2</sub> ).....	42
<b>Figure 2-7</b> PXRD of NU-1000, simulated (in black), pre-catalysis (in blue) and post-catalysis (in red).....	44

**Figure 2-8** a) Photo-oxidation of HD under UV LED irradiation and O<sub>2</sub> atmosphere catalyzed by NU-1000. b) Degradation profile of HD (0.4 mmol) in the presence of NU-1000 (5.2 mg) while being irradiated with a UV LED..... 45

**Figure 3-1** a) Reaction pathway for the oxidation of bis(2-chloroethyl)ethyl sulfide (HD) to HDO and HDO<sub>2</sub>. b) Reaction pathway for the oxidation of the HD simulant, 2-chloroethyl ethyl sulfide (CEES), using dioxygen and a photosensitizer..... 49

**Figure 3-2** The structure of NU-1000, PCN-222/MOF-545, and UMCM-313 and their corresponding linkers and common Zr<sub>6</sub>-node..... 50

**Figure 3-3** TBAPy<sup>4-</sup> UV-vis absorption spectrum at 16 μM in 0.1 M NaOH (red) and calibration curve (black) extracted from peak absorbance at 388 nm. .... 55

**Figure 3-4** TBAPery<sup>4-</sup> UV-vis absorption spectrum at 16 μM in 0.1 M NaOH (red) and calibration curve (black) extracted from peak absorbance at 433 nm. .... 55

**Figure 3-5** Reaction profiles of the three MOF powders. PCN-222 and UMCM-313 were irradiated with blue LEDs and NU-1000 was irradiated with UV LEDs of equivalent power density..... 57

**Figure 3-6** Singlet oxygen emission observed on linker excitation in methanol corrected for optical density (0.3). Extracted data shown in **Table 3-1**. H<sub>4</sub>TBAPery required the addition of KOH to solubilize. .... 58

**Figure 3-7** a) Side views of the thin films and b) their reaction profiles for the oxidation of CEES. UMCM-313 thin film was irradiated with blue LEDs and NU-1000 was irradiated with UV LEDs of equivalent power density..... 59

**Figure 4-1** The crystal structure of NU-1000, showing the 31 and 12 Å channels. Each layer is separated by 10 Å windows. The structure for the nodes and linkers are given. The structure and size of the POM, [PW<sub>12</sub>O<sub>40</sub>]<sup>3-</sup>, are shown. .... 65

**Figure 4-2** General catalytic conditions and reaction pathways for 2-chloroethyl ethyl sulfide oxidation with hydrogen peroxide ..... 66

**Figure 4-3** SEM images of NU-1000 before (above) and after (below) [PW<sub>12</sub>O<sub>40</sub>]<sup>3-</sup> incorporation. EDS line scan of NU-1000 after [PW<sub>12</sub>O<sub>40</sub>]<sup>3-</sup> incorporation. EDS legend: Light Blue=W, Green=Zr, Purple=Zn (baseline) ..... 73

**Figure 4-4** Powder patterns for H<sub>3</sub>PW<sub>12</sub>O<sub>40</sub>, NU-1000, and PW<sub>12</sub>@NU-1000 compared to the simulated NU-1000..... 74

**Figure 4-5** Visual representations (top and side view) of the proposed structures for PW<sub>12</sub>@NU-1000, where the POM is located inside the windows between the channels(a), in the hexagonal channels (b), or in the small triangular channels (c). DED mapping of PW<sub>12</sub>@NU-1000 has led to the conclusion that (c) is most representative of the material..... 74

**Figure 4-6** PXRD patterns for the as synthesized  $\text{PW}_{12}@NU-1000$  compared to simulated patterns where the POM is in the mesopores or between the nodes (representations in Figures S2 and 4, respectively) ..... 75

**Figure 4-7** STEM Z-contrast images of  $\text{PW}_{12}@NU-1000$  showing (a) a clear hexagonal arrangement of nodes for the c-axis projection and (b) a cubic arrangement of nodes in the a/b projection. These images are consistent with the structures observed in undoped NU-1000 and imply that the POM exists in regular locations relative to the nodes. .... 76

**Figure 4-8** Experimental ex-situ XRD data collected at 17-BM beamline, APS Room temperature, air atmosphere. Pink spheres represent electron density. .... 77

**Figure 4-9** Volumetric  $\text{N}_2$  isotherm (above) and pore size distribution (below) of NU-1000 and  $\text{PW}_{12}@NU-1000$  ..... 78

**Figure 4-10** TGA (above) showing weight loss of NU-1000,  $\text{H}_3\text{PW}_{12}\text{O}_{40}$  and  $\text{PW}_{12}@NU-1000$  from 25 °C to 700 °C and first derivative curve (below) for NU-1000 and  $\text{PW}_{12}@NU-1000$  over the same range..... 80

**Figure 4-11** Cyclic voltammogram of  $\text{H}_3\text{PW}_{12}\text{O}_{40}$  under  $\text{N}_2$  in pH 2.5  $\text{H}_2\text{SO}_4/ \text{Na}_2\text{SO}_4$  0.5 M buffer solution at 0.025  $\text{Vs}^{-1}$  scan rate. Reductive events labeled.  $\text{W}^{\text{V/VI}}$  reduction events labeled. Formal reduction potentials are -335, -555 and -735 mV vs SCE. The fourth redox event was obscured by hydrogen evolution. .... 81

**Figure 4-12** Cyclic voltammogram of  $\text{PW}_{12}@NU-1000$  under  $\text{N}_2$  immobilized at a glassy carbon electrode in pH 2.5  $\text{H}_2\text{SO}_4/ \text{Na}_2\text{SO}_4$  0.5 M buffer solution at 0.025  $\text{Vs}^{-1}$  scan rate. W-reduction events labeled. Formal reduction potentials are -300, -560, -715, and -890 mV vs SCE. Bare NU-1000 shows no reductive activity in this window. .... 82

**Figure 4-13**  $^{31}\text{P}$  MAS NMR spectra of  $\text{H}_3\text{PW}_{12}\text{O}_{40}$  and  $\text{PW}_{12}@NU-1000$ . External reference: 0.8ppm  $\text{NH}_4\text{H}_2\text{PO}_4$ ..... 82

**Figure 4-14** DRIFTS spectra of the  $\text{H}_3\text{PW}_{12}\text{O}_{40}$ , NU-1000, and the  $\text{PW}_{12}@NU-1000$ . The non-hydrogen bonded O-H stretches, carboxylate stretches, and P-O/W-O stretches are highlighted. .... 83

**Figure 4-15** Reaction profile of CEES oxidation for the  $\text{H}_3\text{PW}_{12}\text{O}_{40}$ , NU-1000, and  $\text{PW}_{12}@NU-1000$  with standard deviation over three trials ..... 85

**Figure 4-16** Selected regions of the  $^1\text{H}$  NMR spectra of CEES, CEESO,  $\text{CEESO}_2$ , and a reaction mixture with all three compounds in  $\text{CD}_3\text{CN}$ . The peaks used for calculation are labeled with chemical shift ..... 85

**Figure 4-17** Reaction profiles for  $\text{PW}_{12}@NU-1000$  for the first run and recycle. Open symbols indicate the reaction was filtered at 2 minutes..... 87

**Figure 4-18** Conversion and selectivity of  $\text{PW}_{12}@NU-1000$  at 60 min over the first run and 2 recycles. Error bars are standard deviation over at least 2 trials. Selectivity was determined by sulfoxide amount / total product. .... 88

**Figure 4-19** DRIFTS of  $\text{PW}_{12}@NU-1000$  before and after catalysis ..... 88

**Figure 4-20** PXRD patterns of  $\text{PW}_{12}@NU-1000$  before and after catalysis..... 89

**Figure 4-21**  $^{31}\text{P}$  MAS NMR spectra of solid  $\text{PW}_{12}@NU-1000$  before and after catalysis ..... 89

**Figure 5-1** Structural representations (left) of the  $\text{PW}_{12}@NU-1000$  previously published, also referred to as  $\text{PW}_{12}@NU-1000-120^\circ\text{C}$ . Structures of the corresponding POM [ $(\text{PW}_{12}\text{O}_{40})^{3-}$ ], MOF node [ $(\text{Zr}_6(\mu_3\text{-O})_4(\mu_3\text{-OH})_4(\text{H}_2\text{O})_4(\text{OH})_4)^{8+}$ ], and MOF linker [1,3,6,8-tetrakis(p-benzoate)pyrene, (TBAPy) $^{4-}$ ] given (right). Light blue prisms= $\text{WO}_5$ , pink prisms= $\text{PO}_4$ , green= $\text{Zr}$ , red= $\text{O}$ , gray= $\text{C}$ , hydrogen atoms omitted for clarity. .... 94

**Figure 5-2** SEM-EDS image and W, Zr, Zn line scans of  $\text{PW}_{12}@NU-1000\text{-scCO}_2$ . Elemental distributions are identical to those found in  $\text{PW}_{12}@NU-1000-120^\circ\text{C}$ .<sup>122</sup> Zn is shown as a baseline. .... 99

**Figure 5-3** PXRD patterns for NU-1000 and  $\text{PW}_{12}@NU-1000$  as-synthesized without solvent removal, activated by supercritical  $\text{CO}_2$ , and activated at  $120^\circ\text{C}$ . .... 100

**Figure 5-4** Variable-temperature powder X-ray diffraction patterns for  $\text{PW}_{12}@NU-1000\text{-scCO}_2$  showing dynamic changes in peak intensities as the material is held at  $120^\circ\text{C}$  ..... 100

**Figure 5-5** Structural representation of one possible POM conformation in  $\text{PW}_{12}@NU-1000\text{-scCO}_2$  inferred by DED analysis. Light blue prism= $\text{WO}_5$ , pink prism= $\text{PO}_4$ , green= $\text{Zr}$ , red= $\text{O}$ , gray= $\text{C}$ , hydrogen atoms omitted for clarity. .... 102

**Figure 5-6** Difference envelope density maps of  $\text{PW}_{12}@NU-1000\text{-scCO}_2$  derived from experimental ex-situ XRD data collected at 17-BM beamline, APS Room temperature, air atmosphere. Two views are shown: down the c-axis (left) and an orthogonal view (right). Green spheres represent electron density for [ $\text{PW}_{12}\text{O}_{40}$ ] $^{3-}$ . Teal= $\text{Zr}$ , red= $\text{O}$ , light gray= $\text{C}$ , white= $\text{H}$ , hydrogens on the nodes are not shown. .... 103

**Figure 5-7** a) Volumetric  $\text{N}_2$  isotherms collected at 77 K, b) DFT-calculated pore size distribution. c) Diffuse reflectance UV-vis spectra, and d) emission spectra at 380 nm excitation of NU-1000,  $\text{PW}_{12}@NU-1000\text{-scCO}_2$ , and  $\text{PW}_{12}@NU-1000-120^\circ\text{C}$ . .... 105

**Figure 5-8** a) Thermogravimetric analysis curve ( $20^\circ\text{C}/\text{min}$ ) showing weight loss of NU-1000,  $\text{H}_3\text{PW}_{12}\text{O}_{40}$  and  $\text{PW}_{12}@NU-1000$  from  $25^\circ\text{C}$  to  $250^\circ\text{C}$  where water loss occurs and b) differential scanning calorimetry curves which were taken simultaneously. Difference in rate around  $175^\circ\text{C}$  attributed to the movement of the POM from mesopores to micropores. The discrepancy in this transition temperature and the temperature in the in situ PXRD is attributed to the ramp temperature ( $120$  to  $175^\circ\text{C}$  takes less than 3 min). .... 106

- Figure 5-9**  $^{31}\text{P}$  MAS NMR spectra of  $\text{H}_3\text{PW}_{12}\text{O}_{40}$  and  $\text{PW}_{12}@ \text{NU-1000-x}$ . External reference: 0.8ppm  $\text{NH}_4\text{H}_2\text{PO}_4$ ..... 108
- Figure 5-10** Cyclic voltammogram of  $\text{PW}_{12}@ \text{NU-1000-scCO}_2$  under  $\text{N}_2$  in pH 2.5  $\text{H}_2\text{SO}_4/\text{Na}_2\text{SO}_4$  0.5 M buffer solution at  $0.025 \text{ V s}^{-1}$  scan rate. Reductive events labeled.  $\text{W}^{\text{V/VI}}$  reduction events labeled..... 109
- Figure 5-11** a) Scheme of the reaction pathway for the oxidation of CEES to CEESO and CEESO<sub>2</sub> under the conditions presented in this work. b) Reaction profiles for the reaction in a) using the catalysts: NU-1000,  $\text{H}_3\text{PW}_{12}\text{O}_{40}$ ,  $\text{PW}_{12}@ \text{NU-1000-120}^\circ\text{C}$ , and  $\text{PW}_{12}@ \text{NU-1000-scCO}_2$ . ..... 110
- Figure 5-12** Selectivities for CEESO of the catalysts for the reaction in **Figure 5-11a** measured at completion. \*When NU-1000 is exposed to enough (5 equivalents)  $\text{H}_2\text{O}_2$ , the reaction is 100% selective for CEESO<sub>2</sub>. ..... 111
- Figure 5-13** Reaction profiles for the reaction in **Figure 5-11a** using only 1 mol% of active clusters with the catalysts  $\text{PW}_{12}@ \text{NU-1000-120}^\circ\text{C}$  and  $\text{PW}_{12}@ \text{NU-1000-scCO}_2$ . Open symbols indicate the reaction was filtered at approximately 30 s. .... 112
- Figure 5-14** PXRD patterns of  $\text{PW}_{12}@ \text{NU-1000-scCO}_2$  before and after catalysis. .... 113
- Figure 6-1** Generic **csq** structure (top) viewed down the *c*-axis and an orthogonal view. Structures for zirconium node and size comparison to  $\text{PW}_{12}$  cluster (top left). Crystal structures and structural linkers of NU-1000 (lower left), NU-1000-NDC (lower center), and NU-1008 (lower right) viewed from the *ab* direction. The *c*- and *c'*- pores are highlighted in purple and pink, respectively. For clarity, hydrogens are omitted, and one possible conformation of NDC has been extracted. Green polyhedron =  $\text{Zr}_6$  node, blue polyhedron =  $\text{WO}_5$ , pink polyhedron =  $\text{PO}_4$ , green sphere = Zr, red = O, gray = C, brown = Br. .... 118
- Figure 6-2** Oxidation of CEES to CEESO and CEESO<sub>2</sub> under the conditions reported in Buru et al. 2018..... 119
- Figure 6-3** SEM-EDX images of NU-1000-NDC before (left) and after (right) PTA loading. 123
- Figure 6-4** SEM-EDX images of NU-1008 before (left) and after (right) PTA loading. .... 124
- Figure 6-5** TGA traces of  $\text{PW}_{12}@ \text{NU-1000-NDC}$  and  $\text{PW}_{12}@ \text{NU-1008}$  under  $\text{N}_2$ . .... 125
- Figure 6-6**  $\text{N}_2$  sorption isotherms of (A) NU-1000-NDC with and without POM and (B) NU-1008 with and without POM. Corresponding DFT-calculated PSD of (C) NU-1000-NDC and its composites and (D) NU-1008 and its composites..... 126
- Figure 6-7** PXRD patterns of the MOFs before and after POM encapsulation. .... 128
- Figure 6-8.** *Ex situ* PXRD patterns of  $\text{PW}_{12}@ \text{NU-1000-NDC}$  (left) and NU-1008 (right). Gray boxes the (2-10) reflection. .... 128

**Figure 6-9** Proposed structures and transitions for  $PW_{12}@NU-1000-NDC$  (top) and  $PW_{12}@NU-1008$  (bottom) under heating conditions. The c- and c'- pores are highlighted in purple and pink, respectively. For clarity, hydrogens are omitted. Green polyhedron =  $Zr_6$  node, blue polyhedron =  $WO_5$ , pink polyhedron =  $PO_4$ , green sphere = Zr, red = O, gray = C, brown = Br. .... 129

**Figure 6-10** *In-situ* PXRD pattern for  $PW_{12}@NU-1000-NDC$  taken with  $MoK\alpha$  radiation source. N=0 is the  $scCO_2$ -dried sample which was heated to 120 °C and held for 12 h..... 130

**Figure 6-11** CEES conversion over time with (left) NU-1000-NDC and its POM composites and (right) NU-1008 and its POM composites. Error bars represent standard deviation of at least 2 trials..... 131

**Figure 7-1** Visual representations of  $[PV_2Mo_{10}O_{40}]$  clusters in NU-1000. Blue shaded area (left) depicts one possible configuration of  $PV_2Mo_{10}@NU-1000-scCO_2$ . Red shaded area (right) depicts one possible structure of  $PV_2Mo_{10}@NU-1000-80^\circ C$ . Unshaded area (middle) is unmodified NU-1000 crystal structure. Arrangements of the two vanadium atoms were random selected. Teal polyhedra= $MoO_5$ , Orange polyhedra= $VO_5$ , Pink polyhedra= $PO_4$ , Red=O, Green=Zr, Gray=C. Hydrogens omitted for clarity. .... 136

**Figure 7-2** SEM images of NU-1000 before (left) and after (right)  $[PV_2Mo_{10}O_{40}]^{5-}$  incorporation. EDS line scans of Mo and Zr compared to baseline Zn. .... 141

**Figure 7-3** The (A)  $N_2$  adsorption-desorption isotherms and (B) PXRD patterns of NU-1000,  $PV_2Mo_{10}@NU-1000-scCO_2$ , and  $PV_2Mo_{10}@NU-1000-80^\circ C$ . Closed symbols in the isotherm represent points collected during adsorption, and open symbols represent points collected during desorption..... 142

**Figure 7-4** *In situ* variable temperature PXRD patterns for  $PV_2Mo_{10}@NU-1000-scCO_2$ . N (y-axis) indicates the number of scans taken at 80 °C. Each scan is 1 min apart. The horizontal dotted white line highlights where the structural change occurs. .... 143

**Figure 7-5**  $^{31}P$  CPMAS NMR spectra of  $H_5PV_2Mo_{10}O_{40}$  and  $PV_2Mo_{10}@NU-1000$ . .... 144

**Figure 7-6** The (A) reaction of CEES under the condition reported here. (B) The kinetic traces of each material used for reaction (A). Catalyst is normalized to the number of POM clusters, the reductant is isobutyraldehyde, 1 mL cyclohexane was used as solvent. Traces are averages of at least 3 trials. .... 146

**Figure 7-7** Gravimetric  $N_2$  adsorption (filled) and desorption (unfilled) isotherms for  $PMo_{12}@NU-1000$  after  $scCO_2$  activation (BET: 1450  $m^2/g$ ). .... 147

**Figure 7-8** PXRD patterns for  $PMo_{12}@NU-1000$  after  $scCO_2$  activation showing POMs primarily located in micropores. .... 147

**Figure 7-9** PXRD patterns of  $PV_2Mo_{10}@NU-1000$  collected *in situ* in (A) air and (B) cyclohexane. Black traces were collected at 30 °C and red traces were collected after ramping ..... 150



## List of Tables

<b>Table 3-1</b> Singlet oxygen quantum yields of the MOF linkers in methanol .....	58
<b>Table 4-1</b> Amount of leached POM in aqueous solutions at different pHs. Amount determined by ICP-OES, ppm was converted to percent of total POM .....	83
<b>Table 4-2</b> Summary of catalytic data. ....	86
<b>Table 5-1</b> Formal reduction potentials expressed in mV. The fourth redox event of the POM was obscured by hydrogen evolution. ....	109
<b>Table 7-1</b> Reaction conditions tuning amount of reductant, temperature, atmosphere, and solvent collected at 45 min. ....	149

## Chapter 1 . Introduction

Portions of this chapter appear in the following manuscripts:

Wasson, M. C.; Buru, C. T.; Chen, Z.; Islamoglu, T.; Farha, O. K. Metal–Organic frameworks: a tunable platform to access single-site heterogeneous catalysts. *Appl. Cat. A* **2019**, *586*, 117214.

Buru, C.T.; Farha, O. K. Strategies for incorporating catalytically active polyoxometalates in metal–organic frameworks for organic transformations. *ACS Appl. Mater. Interfaces* **2020**, *12*, 5345-5360.

Islamoglu, T.; Chen, Z.; Buru, C.T.; Wasson, M.C. Toxic and corrosive gas capture in metal–organic frameworks. *submitted*.

## 1.1 Motivation: Chemical Warfare Agent Detoxification

First used during World War I, CWAs have been responsible for millions of casualties.<sup>1</sup> Among these toxic chemicals, nerve agents and vesicants are considered the most dangerous<sup>2</sup> and most effective.<sup>3</sup> Unfortunately, these highly toxic chemicals are still in use, particularly in the Middle East against civilian and military populations. Beyond the risk of exposure, hundreds of tons of these CWAs exist in stockpiles in the US and abroad.<sup>4</sup> Currently, metal-impregnated activated carbons are used for adsorption of a wide spectrum of toxic chemicals, but their amorphous nature leads to non-uniform pore sizes/geometries, less tunability, slow diffusion, and low capacities when used as filtration cartridges in gas masks. Stockpile materials are typically decontaminated through incineration or through energy-intensive routes such as supercritical water hydrolysis or hydrolysis in caustic chemicals. So, the development of materials to efficiently absorb and detoxify HD for the purpose of clothing protection, military equipment decontamination, and bulk stockpile removal is still necessary.<sup>5,6</sup> Due to safety and security concerns, few studies report on using chemical warfare agents (CWA) because they can only be used in approved government labs. Instead, researchers use simulants or chemically similar compounds with significantly lower toxicity to test materials and to inform upon principles to design materials with improved performances.

## 1.2 Metal-Organic Frameworks as Catalysts

The use of catalysts would allow for the conversion of these toxic chemicals to benign products in a less energy intensive route than currently employed methods. Metal-organic frameworks (MOFs), a rapidly growing class of materials comprised of organic linkers and metal

ions or metal cluster nodes, offer intriguing properties such as tunability, permanent porosity, and stability which make them of interest for use as catalysts for CWA detoxification.<sup>7-10</sup> MOFs can contain catalysts as structural elements, adhered species, or encapsulated species within the MOF pores, trapped by noncovalent interactions.<sup>11-13</sup>

### 1.1.1 Nerve Agent Detoxification

Nerve agents, such as sarin (GB) and VX, are a class of organophosphates that interrupt nervous system signal transmissions, quickly leading to death by asphyxiation.<sup>2,14</sup> These chemicals have a reactive P-X bond which binds to acetylcholine esterase enzymes, rendering them inactive. The Hupp/Farha group has shown that the Lewis acidic metal cluster nodes of Zr(IV)-based MOFs promote the rapid hydrolysis of organophosphate nerve agents such as VX to non-toxic products under basic aqueous conditions (**Figure 1-1**).<sup>15,16</sup> As such, Zr-based MOFs will serve as a starting point on to which functionality capable of other CWA detoxification can be installed.

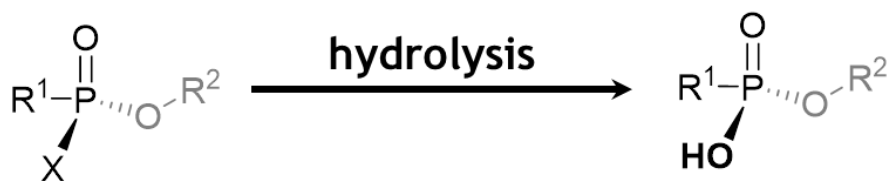


**Figure 1-1** General scheme for nerve agent hydrolysis

### 1.1.2 Sulfur Mustard Detoxification

Sulfur mustard or mustard gas (HD) is a vesicant and alkylating agent which causes blisters on exposed skin and tissues, leading to severe irritation, cancer, and sometimes death.<sup>17,18</sup> Several possible detoxification routes exist (**Figure 1-2**). The slow hydrolysis of HD, however, is

due to the poor water solubility of the agent.<sup>19</sup> Dehalogenation of HD also proves to be a slow degradation pathway that is not practical for wide-spread application.<sup>5</sup> A more promising method for the rapid and safe detoxification of HD involves its selective oxidation to the sulfoxide derivative, since the over-oxidized sulfone has similar toxicity to the parent HD.<sup>20</sup> To accomplish oxidation, two approaches will be taken: using photosensitizers as linkers and using encapsulated species to perform oxidation. 2-chloroethyl ethyl sulfide (CEES) will be used as a simulant for sulfur mustard as its toxicity is 100x less than sulfur mustard.

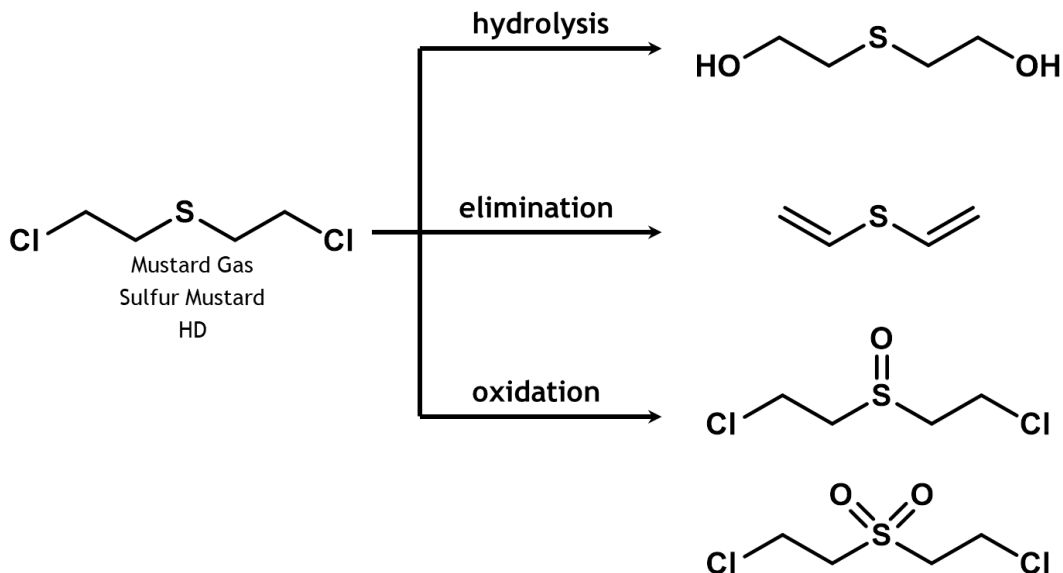


**Figure 1-2** Possible detoxification routes for sulfur mustard

### 1.3 Approach 1: Photosensitizers in Metal–Organic Frameworks

Molecular singlet oxygen ( $^1\text{O}_2$ ) is a great choice of an oxidant since it is environmentally-benign, and typical oxidizing agents like hydrogen peroxide often lead to the over-oxidized product.<sup>21–23</sup> Ground state  $^3\text{O}_2$  is generally unreactive, so a type 2 photosensitizer is employed to generate  $^1\text{O}_2$ . The Hupp and Farha groups previously have demonstrated that PCN-222/MOF-

545, a porphyrin-based MOF acts as a photosensitizer to generate  $^1\text{O}_2$  under LED irradiation which can be used to oxidize CEES to 2-chloroethyl ethyl sulfoxide (CEESO) with a half-life ( $t_{1/2}$ , the time at which 50% conversion is achieved) of 13 min.<sup>24</sup> Follow-up work showed that PCN-222/MOF-545 performs simultaneous oxidation of CEES and hydrolysis of the nerve agent simulant, dimethyl 4-nitrophenol phosphate (DMNP), in methanol and pH 10 buffer mixture under blue LED irradiation with half-lives of 12 and 8 min for CEES and DMNP, respectively.<sup>25</sup> It is still necessary to improve upon our MOF-based catalysts to provide near-instantaneous protection against CWAs if they are to be used to prevent agent exposure. Incorporation of different photosensitizers in MOFs will be described in this document.

#### 1.4 Approach 2: Polyoxometalates and their Metal–Organic Framework Composites

Immobilization of typically homogenous catalysts on a stabilizing solid heterogeneous support, such as a MOF, can protect complexes from surrounding solvent or poisons and prevent species aggregation, the mechanism by which many catalysts become deactivated.<sup>26</sup> These composite materials are typically denoted [catalyst]@[support], when the catalyst is encapsulated within the support. Here, polyoxometalates (POMs) as typically homogeneous catalysts are installed in the pores of MOFs to alter stability and/or reactivity during organic transformation reactions.<sup>27</sup> POMs, typically, are discrete anionic metal oxide clusters composed of group V or VI transition metals in their highest oxidation state.<sup>28–33</sup> Common structures include the Keggin ( $[\text{XM}_{12}\text{O}_{40}]^{n-}$ ), Wells-Dawson ( $[\text{X}_2\text{M}_{18}\text{O}_{62}]^{n-}$ ), and sandwich-type ( $[\text{A}(\text{XM}_9\text{O}_{34})_2]^{n-}$ ), where X is typically Si or P, M is typically Mo or W, and A is another transition or rare earth metal. The versatility of POMs allows for substitution of metals within these structures with virtually any element on the periodic table.<sup>34</sup> Applications of these materials<sup>35,36</sup> include corrosion resistant

coatings,<sup>37</sup> ion battery components,<sup>38,39</sup> polymer dopants,<sup>40,41</sup> water oxidation catalysts,<sup>42–45</sup> and Brønsted acid catalysts.<sup>46,47</sup> Due to their high solubility, low surface area, and instability under reaction conditions, the processability of POMs alone is often poor.<sup>48</sup> To overcome these undesirable properties, significant efforts have been made to heterogenize POMs on a variety of supports, including mesoporous silica,<sup>21,49</sup> high surface area carbon,<sup>50,51</sup> zeolites,<sup>52</sup> polymers,<sup>53</sup> metal-organic macrocycles,<sup>54</sup> covalent–organic frameworks,<sup>55</sup> and metal–organic frameworks (MOFs), among others.<sup>56</sup>

Unlike conventional supports, MOFs offer a highly tunable, crystalline scaffold for anchoring small to large molecules.<sup>57–61</sup> The use of polyoxometalates within MOF structures dates back to reports by Hagrman *et al* in the late 1990's.<sup>62,63</sup> Reports of catalytic applications with these hybrid materials did not appear in the literature until about a decade later. When a POM is immobilized on a MOF, the composite is a POM/MOF; when a POM is immobilized in a MOF, the composite is a POM@MOF. Due to the well-ordered nature of the MOF support, POM@MOF materials are typically crystalline allows for uniform binding/active sites for structure-property relationships and potential investigation via diffraction methods for structure elucidation. Further, the microenvironment around the immobilized POM, which can be finely tuned by altering the MOF support, could yield unique reactivity and selectivity. POM@MOF materials have been reported for several applications including gas storage/separation,<sup>64–67</sup> heavy metal or small/large molecule absorption/sensing,<sup>68–72</sup> proton conduction,<sup>73,74</sup> supercapacitors,<sup>75,76</sup> magnets,<sup>77</sup> optical contrast materials,<sup>78</sup> templates,<sup>79</sup> drug carriers,<sup>80</sup> solid electrolytes,<sup>81</sup> and catalysis. POM@MOFs can act as single site heterogeneous catalysts<sup>82</sup> or in conjunction with the MOF support.

Based on the desired POM@MOF and catalytic application, several synthetic procedures could be employed, which will be discussed in this review. These strategies (**Figure 1-3**) are labeled: Encapsulation (also known as bottle-around-ship or templated synthesis), Coprecipitation, and Postsynthetic Impregnation. Polyoxometalate open frameworks (POMOFs) contain the POM as a structural unit and will not be explored since the  $Zr_6$  node functionality will be lost. Further POMOFs have their active sites blocked by linkers, which would lead to decreased catalytic activity.

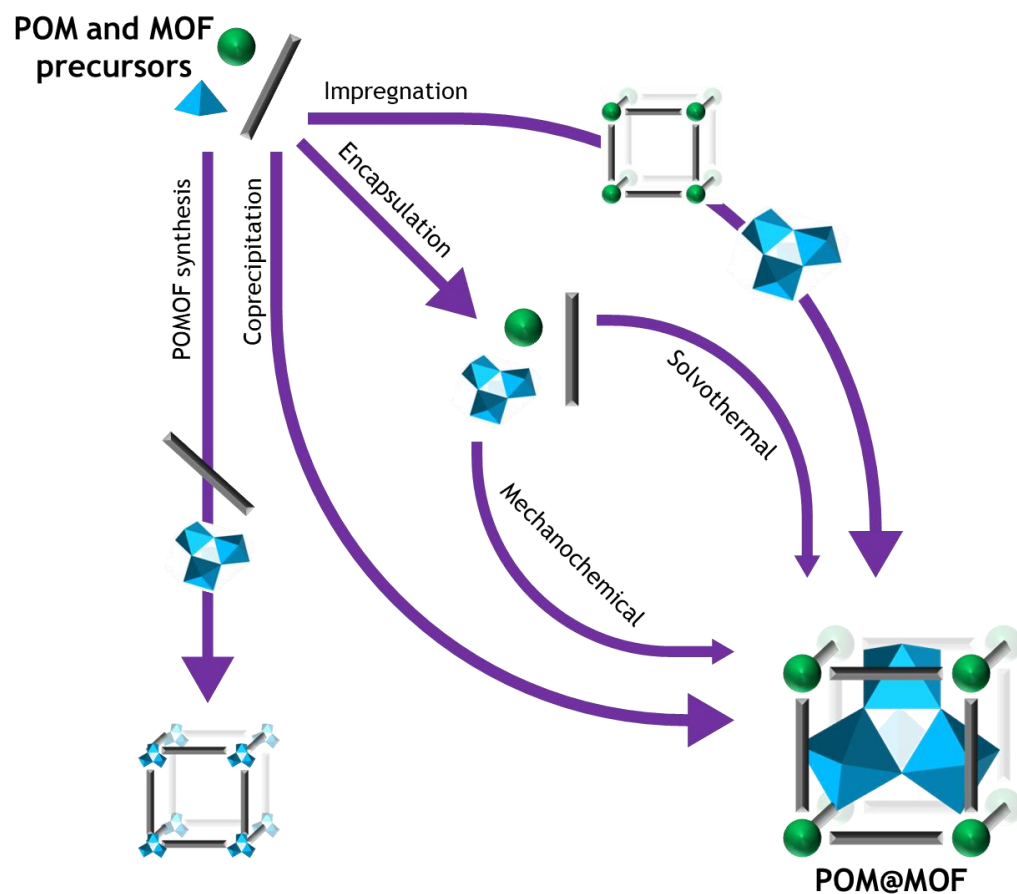


**Figure 1-3** Routes of forming POM@MOF or POMOF materials starting from the precursors of POMs and MOFs.

The majority of POM@MOF synthesis for catalytic applications involves forming a MOF around a pre-formed POM in a process known as templated synthesis, or encapsulation. In

this bottle-around-ship method, the POM is added to a mixture of MOF precursors prior to solvothermal or mechanochemical synthesis. To be successful, the POM must be stable under the MOF synthesis conditions, and the linkers must preferentially bind to the nodes rather than the POMs, thus forming POMOFs. The self-assembly of the MOF surrounding the POM can be directed by interactions of the POM with the linkers or encouraged by high POM concentration. While encapsulation route is straightforward and has been applied to many different MOF systems, many systems suffer from POMs blocking the channels and limiting access to all active sites. This means that higher POM loading equates to lower catalytic activity, an undesirable relationship. Further, the syntheses are complicated by POM serving as potential “nodes”, potentially exchanging metals with the desired metal node and also substituting metals in the POM.<sup>83</sup> Solvothermal encapsulation also relies upon the POM being stable to the synthetic conditions, as too acidic or basic could lead to degradation.

Since MOFs are generally synthesized solvothermally, a major cost of their synthesis is the solvent and solvent disposal. The advent of mechanochemical synthesis of MOFs has generated recent attention since this technique does not require (or requires very little amount of) solvent.<sup>84-90</sup> Naturally, composite MOF-based materials synthesized mechanochemically have been reported.<sup>69,91-95</sup> To date, only a few MOFs have been synthesized mechanochemically, so there is still much to be explored with this technique.

Simultaneous POM synthesis with formation of the surrounding MOF would yield a coprecipitated composite material. Due to the complicated synthetic conditions yielding multiple difficult-to-separate phases, this coprecipitation route has not been investigated for many POM@MOF constructs.<sup>96</sup> While coprecipitation is an attractive method to synthesize POM@MOF composites since only the basic building units are necessary, the multiple possible

combinations of these building blocks hinder the isolation of one phase selectively, and this method is unlikely to become widely applicable.

In MOF systems where apertures are large enough to accommodate POM diffusion, a postsynthetic route to incorporate POMs within MOFs using pre-formed MOF particles in a solution of pre-formed POM is possible; this strategy is referred to as the impregnation method. Most studies relying on post-synthetic impregnation of POM use the MIL-101 framework, which consists of trinuclear chromium nodes (could also be Al- or Fe-based) linked via terephthalate linkers and crystallizes in mtn net with 2.9 and 3.4 nm cages connected via 1.2 and 1.6 nm apertures.<sup>97</sup> Kholdeeva and coworkers first reported catalysis using POM@MIL-101, specifically using mono-substituted heteropolytungstates for alkene oxidations.<sup>98</sup> Since then, many Keggin, substituted Keggin, Lacunary, and Wells-Dawson POMs supported on MIL-101(Cr) have been reported to catalyze various oxidation and acid-catalyzed reactions, including alkene oxidation,<sup>99–103</sup> alcohol oxidation,<sup>104</sup> sulfide oxidation,<sup>105–108</sup> Biginelli reaction,<sup>109</sup> Friedel-Crafts acylation,<sup>110</sup> Pechmann condensation,<sup>110</sup> and Baeyer condensation.<sup>111,112</sup> While MIL-101 is mesoporous and has the potential to incorporate several POMs per cage, only 1 POM per cage (10 wt%) is irreversibly adsorbed. The impregnation method of POM@MOF synthesis is limited to systems where MOFs have an intrinsic propensity for anion interactions, i.e. specific functional groups, positive zeta potential, or positive charge. Without these favorable interactions, POM loading into the MOF is unlikely and the resulting composite material would likely be unstable in liquid environments. This synthetic route is also limited to MOFs with large enough apertures, without which the POMs would adhere to the surface of the MOF and not benefit from the high surface area, crystalline support. In addition to particle size, comparing

synthetic routes is complicated by the influence of specific protocols on other factors like defect density, POM location, and acidity.<sup>113–116</sup>

To combat some of the drawbacks inherited in these systems, hierarchical porous zirconium-based MOFs are an attractive support for POMs, owing to their high thermal and chemical stability and propensity for large molecule and oxyanion adsorption.<sup>117,118</sup> The hierarchical structure would allow for high POM loadings without sacrificing activity, as the secondary channels can function for substrate diffusion. Further, Zr-based MOFs are known to adsorb oxyanions and would have an intrinsic interaction with POMs. As a proof of concept, NU-1000 was chosen. NU-1000, a pyrene-based MOF with oxozirconium nodes, crystallizes into a hierarchical channel-type structure with 3.1 nm hexagonal channels and 1.2 nm triangular channels interconnected with orthogonal 1 x 0.8 nm apertures.<sup>119–121</sup> Due to the size of the channels, a Keggin-type  $[PW_{12}O_{40}]^{3-}$  anion has several locations within the MOF that POM can adopt in  $PW_{12}@NU-1000$ .<sup>122</sup> Details will be discussed in later chapters.

## 1.5 Outline

The work described in this document involves the design, synthesis, characterization, and catalysis of MOFs functionalized for sulfur mustard detoxification, specifically oxidation. Towards this goal, two approaches were chosen for the oxidation of sulfur mustard using a framework capable of nerve agent hydrolysis was tested with the HD agent, also generating **(Figure 1-4)**. In the first approach, photosensitizers will be used as linkers in Zr-based MOFs. In the second approach, catalytically active POMs will be installed in the pores of Zr-based MOFs.

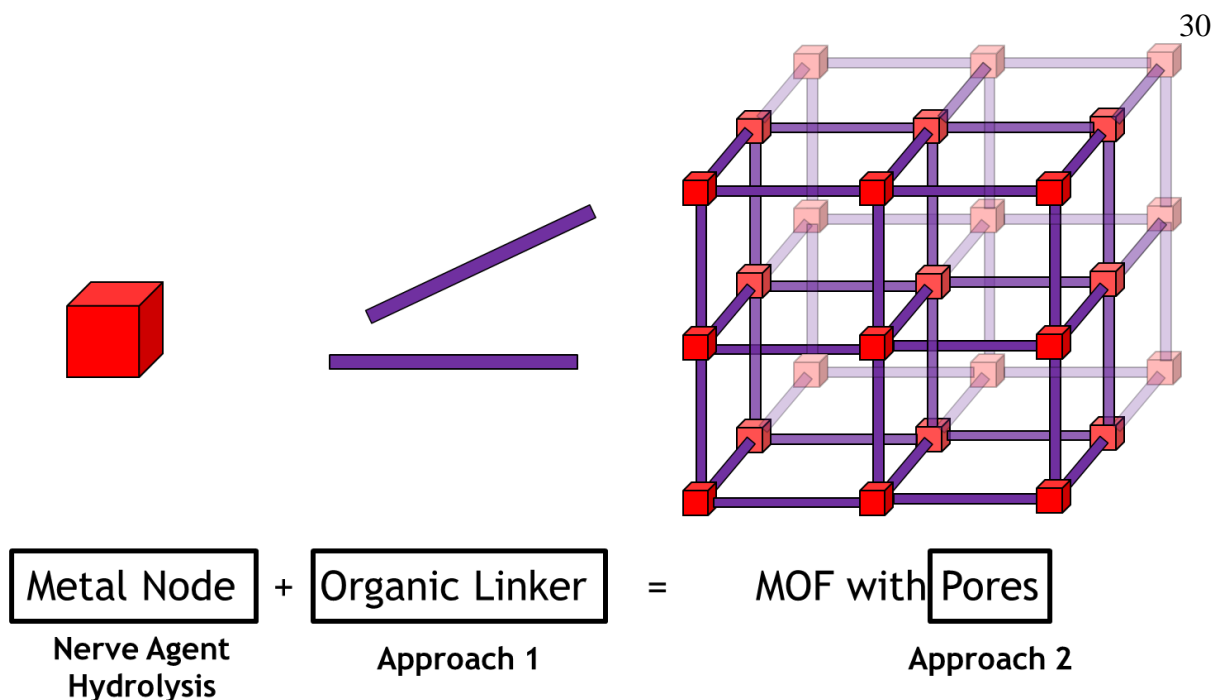


**Figure 1-4** General approach for creating MOF materials capable of sulfur oxidation and nerve agent hydrolysis

Chapter 2 improves upon previous MOF photocatalysts by using NU-1000 as a photocatalyst. Here, the pyrene-based linkers were used as UV light absorbers to generate singlet oxygen. The singlet oxygen then oxidized CEES, a mustard gas simulant. The oxidation was found to selectively give the desired sulfoxide in methanol. Further, this MOF was also used to test against the detoxification of the real HD agent, also selectively.

In Chapter 3, the photocatalysis work is further improved by using UMCM-313 as a photocatalyst. By increasing the conjugation in the linker, the singlet oxygen quantum yield was found to be higher in the perylene-based MOF than the previous pyrene- or porphyrin-based MOFs. The oxidation of CEES was also found to be selective when UMCM-313 was illuminated with blue LED. Further, the NU-1000 and UMCM-313 MOFs were grown as solvothermal thin films to realize low catalyst loadings. As a result the turnover frequencies increase 100-fold.

Chapter 4 describes a proof of concept work with the Keggin-type POM,  $\text{H}_3\text{PW}_{12}\text{O}_{40}$ , immobilized in NU-1000. Taking advantage of the MOF crystallinity, the POMs were found to be located within the micropore of NU-1000 after thermal activation. The composite was found to be stable to leaching and exhibited enhanced reactivity in the oxidation of CEES using hydrogen peroxide.

Chapter 5 again takes advantage of the MOF crystallinity and readdresses some peculiarities of the  $\text{PW}_{12}@$ NU-1000 system. Namely, the structure of the as-synthesized material did not match the structure of the material activated at elevated temperatures. The as-synthesized material structure was preserved by using a supercritical  $\text{CO}_2$  method of activation. Depending on whether heat was used or not, the POM was found in the micropore or mesopore of NU-1000, respectively. This led to different accessibility of the POM to substrate, where the structure with more accessible POMs performed superior to the structure with the POMs hindered by the MOF structure.

Chapter 6 attempts to determine the mechanism by which the POM moves in NU-1000 by installing the POM in different MOFs with topological differences. From analysis of the different structures and how the POMs moved, it was determined that the transformation occurred within the MOF rather than having the POMs leach out and diffuse back in.

Chapter 7 describes the use of an aerobically active POM in NU-1000 to perform the oxidation of CEES. By using air instead of  $\text{H}_2\text{O}_2$ , the practicality of the catalyst could be better realized for real-world applications. The slightly smaller diameter of the aerobically active POM compared to the previously used POMs led to interesting observations, namely lower temperatures could be used to facilitate the POM migration and the presence of solvent could hinder this migration.

**Chapter 2 . Efficient and selective oxidation of sulfur mustard using singlet oxygen generated by a pyrene-based metal–organic framework**

Portions of this chapter appear in the following manuscript:

Liu, Y.\*; Buru, C. T.\*; Howarth, A.J.; Mahle, J.J.; Buchanan, J.H.; DeCoste, J.B.; Hupp, J.T.; Farha, O.K. Efficient and Selective Oxidation of Sulfur Mustard using Singlet Oxygen Generated by a Pyrene-based Metal–Organic Framework. *J. Mat. Chem. A* **2016**, *4*, 13809-13813.

## 2.1 Introduction

First used during World War I, chemical warfare agents (CWAs) have been responsible for mass casualties around the world.<sup>1,24,123</sup> Among the most effective and widely used of these chemicals, bis(2-chloroethyl) sulfide (mustard gas or HD) is a blistering agent and vesicant that can be readily and cheaply produced.<sup>4,123</sup> Despite an international ban, HD continues to threaten civilian and military populations due to continued production, distribution, and stockpiling.<sup>4,123</sup> Very recently, HD was found in the Syrian stockpiles. Current detoxification methods include incineration and hydrolysis, but these methods not only are ineffective, but also pose great risks to humans if the agents are not completely degraded. As a result, there is a continuing need to develop new materials or methods for the safe and efficient detoxification of stockpiles of these toxic chemicals.<sup>5</sup>

Zr<sup>IV</sup>-based metal-organic frameworks (MOFs) have been shown to be excellent candidates for the sorption and degradation of CWAs due to their exceptional chemical stability and high porosity.<sup>15,16,132,124–131</sup> MOFs are generally comprised of metal ions or metal clusters connected with polytopic organic linkers in a crystalline array.<sup>133–137</sup> MOFs are known for their high surface area, permanent porosity, tunability, and thermal stability, allowing for applications in gas storage, sensing, separations, and heterogeneous catalysis.<sup>138–141</sup> The rapid hydrolysis of organophosphate CWAs catalyzed by MOFs has been a particular interest to the US/world military. However, hydrolysis of HD is much slower due to its water immiscibility and this reaction yields by-products such as HCl, 1,4-thioxane, and thiodiglycol which are also toxic and irritating to tissues. Similar problems exist with degradation of HD via the dehydrohalogenation pathway (**Figure 2-1**).<sup>4,142,143</sup> On the other hand, oxidation has been proven to be a viable HD degradation pathway that does not require reaction in water. Oxidative degradation products of

HD can include sulfoxide and sulfone derivatives (**Figure 2-1**).<sup>21,22,144–148</sup> While the partially oxidized sulfoxide is considered nontoxic, the sulfone has vesicant properties similar to the parent HD.<sup>20,146</sup> Therefore, selective partial oxidation is critical for the safe degradation of HD. When using strong oxidizing agents, such as hydrogen peroxide and tert-butyl hydroperoxide, both partially and fully oxidized products are often observed.<sup>21–23,149</sup>

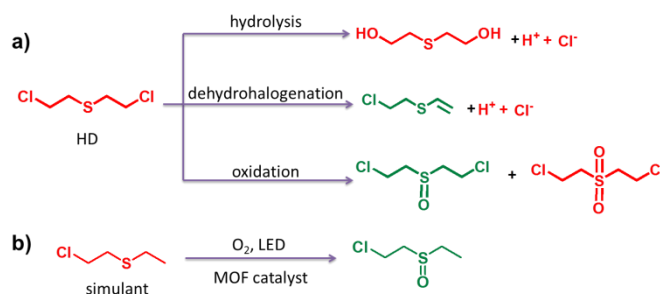


**Figure 2-1** a) Pathways of HD detoxification: hydrolysis, dehydrohalogenation and oxidation (toxic/irritating chemicals in red, nontoxic chemicals in green). In the oxidation pathway, toxic bis(2-chloroethyl)sulfone (in red) can be produced as a result of complete oxidation. b) Selective photooxidation of HD simulant, CEES, using singlet oxygen generated by a MOF under LED irradiation, which only produces the nontoxic sulfoxide.

We recently demonstrated the first use of a porphyrinic MOF to efficiently and selectively oxidize an HD simulant via singlet oxygen (<sup>1</sup>O<sub>2</sub>) generation without producing the toxic sulfone (**Figure 2-1**).<sup>24</sup> While the triplet ground state of dioxygen, <sup>3</sup>Σ<sub>g</sub><sup>-</sup>, is kinetically inert, the <sup>1</sup>Δ<sub>g</sub> singlet excited state of dioxygen shows significantly different chemical reactivity.<sup>150,151</sup> In general, photosensitizers absorb light of a given wavelength to generate an excited singlet state of the photosensitizer. With efficient singlet to triplet intersystem crossing, the triplet excited state of the photosensitizer will form and can transfer energy to ground state triplet oxygen, thereby yielding singlet oxygen.<sup>150,151</sup> In our previous study, we heterogenized a porphyrinic photosensitizer by incorporating it into the organic linkers of a MOF, PCN-222/MOF-545.<sup>24,132</sup> This approach isolates the porphyrin moieties due to the spacing between linkers in the three-dimensional (3-D) structure of MOFs and thus eliminates the problem of

aggregation which often occurs with free porphyrins and diminishes their singlet oxygen production.<sup>16,152,153</sup> Additionally, due to the highly modular nature of MOFs, the porphyrinic struts can be replaced easily with different photosensitizers, with properties that can give rise to frameworks with higher stability, better reactivity, and easier scalability.

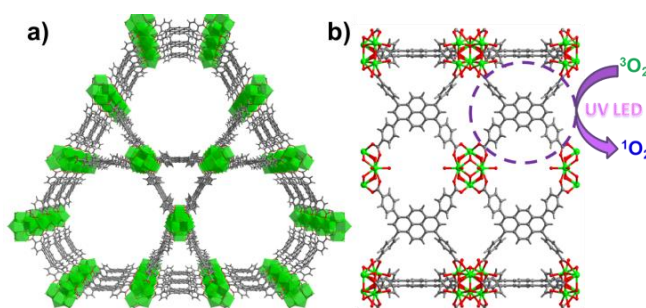


**Figure 2-2** a) 3D structure of NU-1000, viewed along the c axis. b) NU-1000 viewed along the a axis and concept of generating singlet oxygen by the pyrene moieties in NU-1000 under UV LED.

Pyrene is a widely used organic chromophore and the photophysical properties of pyrene have been extensively studied and are well understood.<sup>154</sup> Due to the presence of a low energy triplet state combined with efficient intersystem crossing from the singlet to triplet state, pyrene and its derivatives have been previously studied for singlet oxygen generation.<sup>155</sup> NU-1000<sup>119</sup> (**Figure 2-2**), is a 3-D Zr-based MOF constructed using the tetratopic pyrene-containing linker, 4,4',4'',4'''-(pyrene-1,3,6,8-tetrayl)tetrabenzic acid (H<sub>4</sub>TBAPy).<sup>156</sup> NU-1000 not only inherits some of the photophysical properties of pyrene, but also has permanent porosity, high surface area, and exceptional stability and can be prepared on a large scale<sup>120</sup> (**Figure 2-2**). As shown in **Figure 2-2**, pyrene-containing linkers and Zr<sub>6</sub> nodes self-assemble to form the 3-D hierarchical channel structure of NU-1000 with channel diameters of 31 Å and 12 Å. This open channel structure facilitates the diffusion of substrates and products throughout the MOF. In addition, the 3-D structure of NU-1000 heterogenizes and isolates the pyrene moieties in an ordered array,

which should help to enhance the efficiency of singlet oxygen generation by preventing aggregation and photodegradation.<sup>157</sup>

In this chapter, we demonstrate the use of NU-1000 in the selective photocatalytic degradation of a mustard gas simulant CEES and, for the first time, HD itself.

## 2.2 Experimental Methods

### 2.2.1 Material Syntheses

NU-1000 was synthesized via published procedure.<sup>120</sup> CASARM (Chemical Agent Standard Analytical Reference Material) quality sulfur mustard (HD, >98%, Lot # HD-U-5038-CTF-N) was synthesized in house for research purposes only. **Danger!!! Sulfur mustard and other chemical warfare agents should only be handled in a lab and by personnel that are certified to do so. Even small doses of CWAs are known to be highly dangerous and potentially lethal.** All other reagents were purchased from commercial sources and used without further purification.

### 2.2.2 Physical Methods

NMR spectra were collected on a 500 MHz Bruker Avance III system equipped with DCH CryoProbe at IMSERC (Integrated Molecular Structure Education and Research Center) at Northwestern University. Powder X-ray diffraction (PXRD) patterns were collected on a Rigaku Smartlab instrument. Samples were scanned at 45 kV and 160 mA, a step size of  $2\theta = 0.02^\circ$  (1.28 s per step) over a  $2\theta$  range of 2 to  $30^\circ$ . Inductively coupled plasma-optical emission spectroscopy (ICP-OES) measurements were performed on a Thermo iCap7600 ICP-OES Spectrometer. Standard solutions with Zr concentrations of 2, 8, 20 and 40 ppm were used for the calibration curve. The ICP sample was prepared by diluting 0.20 mL of the filtrate from the

oxidation reaction (2.2 mg NU-1000 as catalyst) to 25 mL with millipore water. Nitrogen adsorption isotherm measurements were carried out on a Micromeritics Tristar II 3020 at 77 K. Samples were heated at 120 °C under vacuum for 12 h prior to measuring the isotherms. GC-MS analysis was performed on a time-of-flight GC mass spectrometer from Waters Micromass GCT Premier. GC-FID analysis were carried out on an Agilent Technologies 7820A GC system equipped with an Agilent J&W GC HP-5 capillary column (30 m × 320 μm × 0.25 μm film thickness). LED irradiation was performed using solderless LEDs purchased from RapidLED which were then mounted on aluminum to give a homemade irradiation setup. The LEDs were hooked up in series to a Mean Well LPC-35-700 constant current driver also purchased from RapidLED. The irradiation setup contains two UV LEDs ( $\lambda_{\text{max}} = 390\text{-}400$  nm, **Figure 2-3**) that are mounted facing each other ~1.5 cm apart.

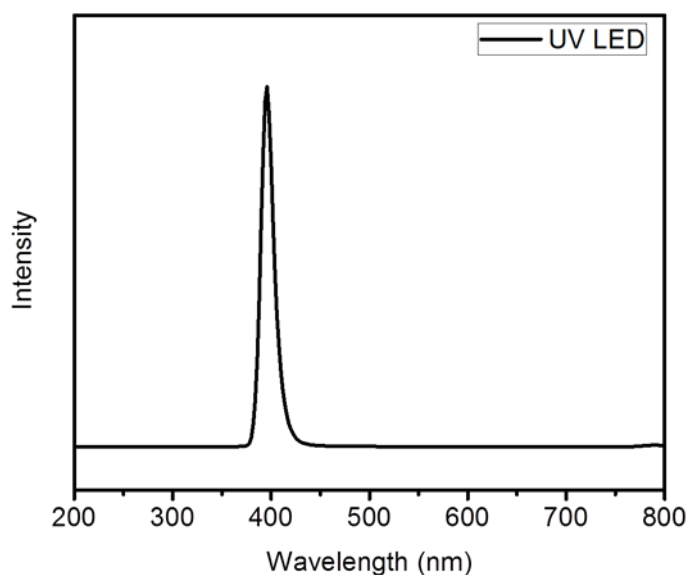


**Figure 2-3** Output wavelength of the UV LED (peak ~396 nm). Power density: 450mW/cm<sup>2</sup>

### 2.2.3 Catalytic Measurements

**CEES Oxidation and Catalyst Recyclability.** For catalytic tests, 1 mol% of NU-1000 (2.16mg, 2 μmol by pyrene unit) was dispersed in 1 mL anhydrous methanol and sealed in a

glass microwave vial. After purging with O<sub>2</sub> for 20 min, 23 μL (0.2 mmol) 2-chloroethyl ethylsulfide (CEES) and 10 μL (0.08 mmol) internal standard (1-bromo-3,5-difluorobenzene) were added to the microwave vial with a microsyringe. The microwave vial was then exposed to UV LED irradiation. Aliquots were withdrawn from the reaction with a syringe every 3 min, filtered and diluted with anhydrous methanol. Samples were then subjected to GC-FID to monitor the reaction and GC-MS to analyze the final products. NMR spectroscopy was also used to confirm the oxidation products. CD<sub>3</sub>OD instead of MeOH was used in the reaction for NMR studies. To compare the pyrene-based linker to the MOF itself, 1.35 mg (2 μmol, 1 mol%) 4,4',4'',4'''-(pyrene-1,3,6,8-tetrayl)tetrabenzoic acid (H<sub>4</sub>TBAPy) was used in place of NU-1000.

Under optimized conditions, which is 1 mol% catalyst loading (catalyst loading is calculated based on moles of pyrenes in NU-1000) and UV LED irradiation, 0.2 mmol 2-chloroethyl ethylsulfide (CEES) can be completely oxidized to 1-chloro-2-(ethylsulfinyl)ethane (CEESO) within 15 min. GC results suggested there was no sulfone product formed in this process, even after an additional 24 hours of irradiation. Under the same condition but with different catalyst loading (0.5 mol % or 2 mol %), the oxidation takes longer than 15 min.

The reusability of the catalyst NU-1000 was studied by making multiple injections of CEES (0.2 mmol) into the same reaction. Before each injection, the solution was purged with O<sub>2</sub> for 20 min. GC-FID was used to monitor the reaction progress and calculate the conversion of the reaction after each injection.

**HD Oxidation.** NU-1000 (5.2 mg) was dispersed in 1 mL of methanol in a sealed quartz vial. After purging with O<sub>2</sub> for 20 min and irradiating with a UV LED for 20 min, 50 μL (0.4 mmol) of HD was added to the vial with a syringe, and continue irradiating with UV LED. 25 μL

aliquots were taken at various time points, filtered, and removed from the light, before being analyzed by GC-FID, with the final time point analyzed by GC-MS.

CASARM (Chemical Agent Standard Analytical Reference Material) quality sulfur mustard (HD, >98%, Lot # HD-U-5038-CTF-N) was synthesized in house for research purposes only. Danger!!! Sulfur mustard and other chemical warfare agents should only be handled in a lab and by personnel that are certified to do so. Even small doses of CWAs are known to be highly dangerous and potentially lethal.

## 2.3 Results and Discussion

The absorption bands of NU-1000 are centered at 300 nm and 390 nm consistent with pyrene-based absorptions.<sup>158</sup> As a result, a UV LED ( $\lambda_{\text{max}} = 390\text{-}400$  nm) was chosen for the generation of singlet oxygen from pyrene. CEES was selectively oxidized to the nontoxic product CEESO and no 2-chloroethyl ethyl sulfone (CEESO<sub>2</sub>) was observed in the gas chromatography spectrum (GC) (**Figure 2-4**). The selectivity of the photooxidation reaction was corroborated by NMR experiments (**Figure 2-5**). <sup>13</sup>C NMR peaks of the reaction mixture after 15 min match that of CEESO indicating that the reaction is complete after 15 min and only nontoxic sulfoxide product is formed.

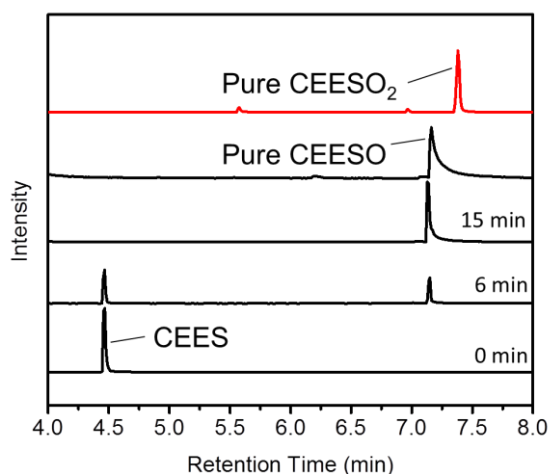


**Figure 2-4** Gas chromatography (GC) signals indicating the progress of the oxidation of CEES (4.45 min) to CEESO (7.14 min) in the presence of NU-1000 (2.2 mg). For comparison, chromatograms of pure CEESO (7.14 min) and pure CEESO<sub>2</sub> (7.38 min) were also recorded, confirming that CEESO was the only product.

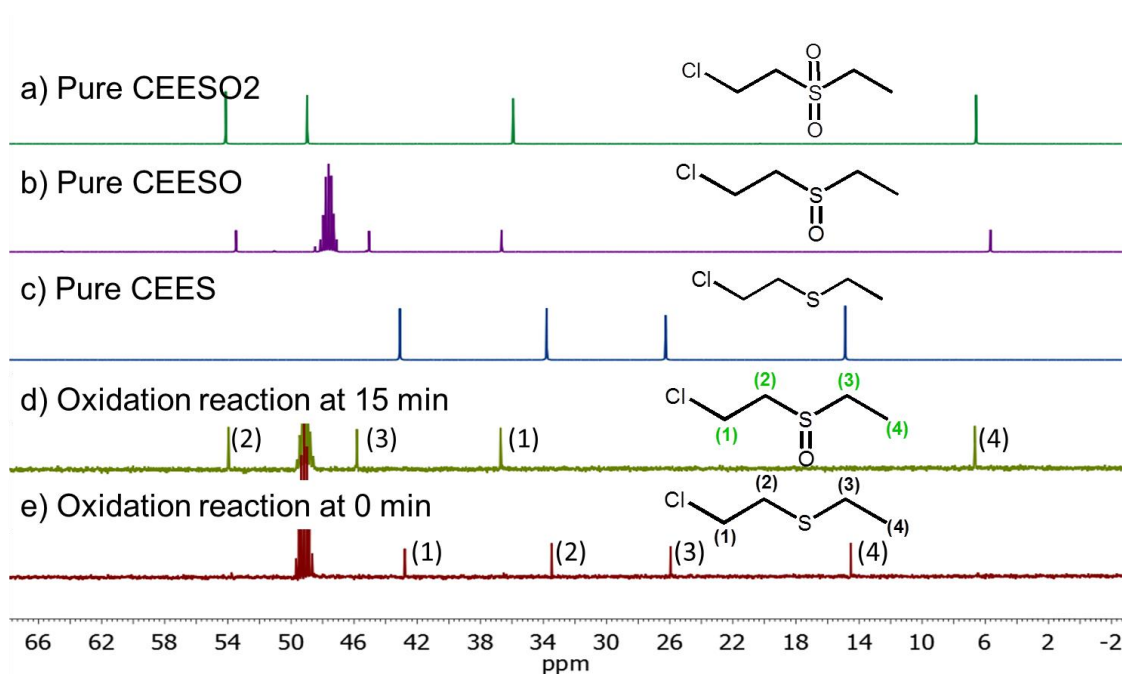


**Figure 2-5** <sup>13</sup>C NMR spectra of a) Pure 1-chloro-2-(ethylsulfonyl)ethane (CEESO<sub>2</sub>) in CDCl<sub>3</sub>, b) Pure 2-chloroethyl ethyl sulfoxide (CEESO) in CD<sub>3</sub>OD, c) pure 2-chloroethyl ethylsulfide (CEES) in CDCl<sub>3</sub>, d) oxidation of CEES in the presence of 2.2 mg NU-1000. The reaction is performed in CD<sub>3</sub>OD. NMR sample was taken at 15 min of the oxidation reaction, dissolved in CDCl<sub>3</sub>, indicating the oxidation is completed and only one product, 1-chloro-2-(ethylsulfinyl)ethane (CEESO), was obtained. e) NMR sample was taken at 0 min of the oxidation reaction, dissolved in CDCl<sub>3</sub>.

Under optimized conditions, which is 1 mol% catalyst loading (catalyst loading is calculated based on moles of pyrenes in NU-1000) and UV LED irradiation, 0.2 mmol 2-chloroethyl ethylsulfide (CEES) can be completely oxidized to 1-chloro-2-(ethylsulfinyl)ethane (CEESO) within 15 min (**Figure 2-6**). GC results suggested there was no sulfone product formed in this process, even after an additional 24 hours of irradiation. Under the same condition but with different catalyst loading (0.5 mol % or 2 mol %), the oxidation takes longer than 15 min. When the linker, H<sub>4</sub>TBAPy, was used for catalysis under the same conditions, complete conversion of CEES occurs after 30 min, as shown in **Figure 2-6**. The half-life of the MOF is 6.2 min and the half-life of the MOF linker is 10.5 min. By incorporating the photosensitizer into the struts of the MOF in NU-1000, we are able to improve the rate of the reaction. This phenomenon is attributed to the heterogeneous nature of the MOF, which separates the pyrenes in a rigid framework, preventing deactivation by aggregation.

**Figure 2-6** presents the kinetics of the photooxidation reaction using 2.2 mg (1 mol %) NU-1000 as the catalyst. Two consecutive injections of CEES (0.2 mmol) were added to the reaction and they were both selectively oxidized to CEESO with half-lives of about 6 and 3 min, respectively. This indicates that the catalyst NU-1000 is reusable and that the reaction is very fast and efficient.

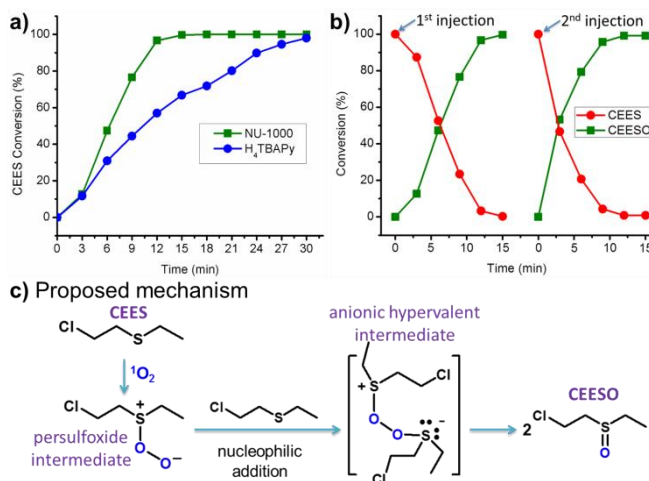


**Figure 2-6** a) Conversion of 0.2 mmol of CEES under UV LED irradiation with 1 mol% of pyrene in NU-1000 compared to the MOF linker alone b) Oxidation profile of CEES in the presence of NU-1000 (2.2 mg) while being irradiated with a UV LED with two consecutive injections of CEES (0.2 mmol). c) Proposed mechanism for the oxidation of CEES by singlet oxygen (<sup>1</sup>O<sub>2</sub>).

It should be noted that in the catalytic photooxidation reaction, there is an induction period after the initial injection of CEES resulting in the half-life of the first cycle being longer than that of the second (**Figure 2-6**). The same phenomenon was also observed in the case of PCN-222/MOF-545. Based on previous studies<sup>159,160</sup> on the oxidation of sulfur-containing compounds by singlet oxygen, a reaction mechanism was proposed for the selective photooxidation of CEES, as shown in **Figure 2-6**. At the initial stage of the reaction, CEES and <sup>1</sup>O<sub>2</sub> form a persulfoxide intermediate, which has a sufficient lifetime to undergo an intramolecular reaction with a second CEES molecule through nucleophilic addition.<sup>160</sup> This gives rise to an unstable anionic hypervalent intermediate and then breaks down into two sulfoxide products (CEESO). This mechanism would not only explain the selectivity of the photooxidation, but would also account for the induction period in the first cycle as it may correspond to the time it takes for the persulfoxide intermediate to accumulate before it reacts with another CEES molecule, which slows down the initial reaction rate. As for the second cycle,

if residual persulfoxide intermediate from the first cycle is present (within the MOF) when fresh CEES is added, no induction behavior would be expected. In any case, compared to the first cycle, the second cycle is characterized by a shorter reaction half-life and a simpler conversion-versus-time plot.

To ascertain whether the catalysis is heterogeneous, the catalyst NU-1000 was removed by filtration after the reaction was complete and the Zr concentration in the filtrate was tested by inductively coupled plasma optical emission spectroscopy (ICP-OES, detection limit ca. 5 ppb). No Zr was detected in the filtered solution by ICP-OES. In addition, no pyrene molecules were observed by  $^1\text{H}$  NMR or  $^{13}\text{C}$  NMR spectroscopy of the filtrate. Both ICP and NMR experiments therefore indicate the catalysis is indeed heterogeneous and catalyzed by the generation of singlet oxygen from solid NU-1000. Furthermore, no degradation of the catalyst was observed, as the structure of NU-1000 remains intact after the catalysis, which was confirmed by powder X-ray diffraction (PXRD) experiments (**Figure 2-7**).

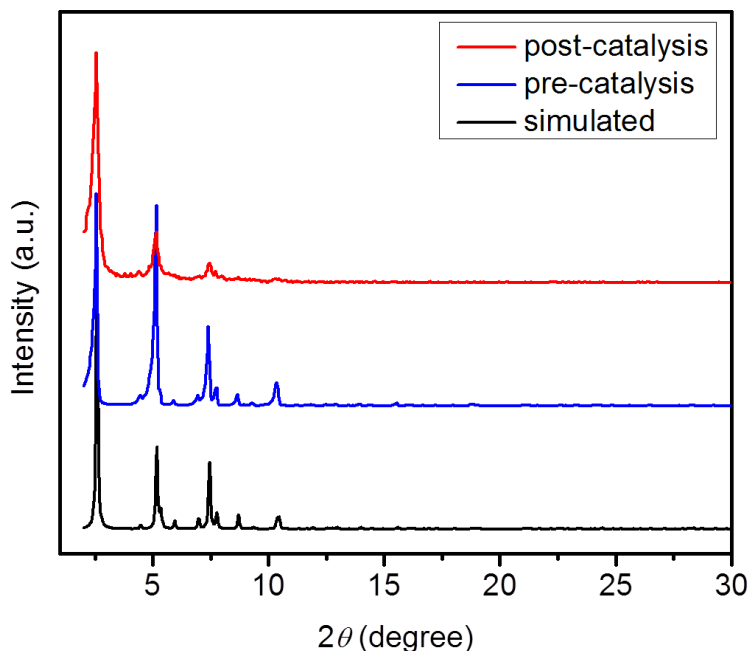


**Figure 2-7** PXR D of NU-1000, simulated (in black), pre-catalysis (in blue) and post-catalysis (in red).

Given the extraordinary selectivity and activity of this photooxidation method, we chose to test the detoxification of CWA HD. The experimental setup and conditions are similar to those of CEES oxidation. Monitored by GC-MS, we observed HD was selectively oxidized to nontoxic products bis(2-chloroethyl)sulfoxide, which partially undergoes an elimination reaction, affording (2-chloroethylsulfinyl)ethane (**Figure 2-8**). These two products are the only two products observed by GC-MS, with no evidence of toxic sulfones. This indicates that the photocatalytic method with NU-1000 as a photosensitizer and a UV LED as the light source is very selective for HD oxidation, where only the partially oxidized sulfoxide product was obtained. This is indeed a very effective and safe method for HD detoxification as it only produces nontoxic degradation products.

The kinetics of HD oxidation were studied by GC-FID with aliquots withdrawn from the reaction every 10 min. As shown in **Figure 2-8**, the half-life for HD oxidation was found to be 33 min when using 1.2 mol% catalyst loading (calculated based on pyrene molecule). — We measured the reaction temperature under the UV LED irradiation, which heats up to approximately 50°C. We did a control experiment identical to the base experiment without UV LED irradiation, instead we heated it in a water bath to 50°C, and no reaction was observed over 120 min. — The shorter half-life observed for CEES oxidation is attributed to greater solubility in MeOH for the simulant compared to HD. An induction period was also observed in the oxidation of HD by  $^1\text{O}_2$ ; is presumably it is attributable to the formation of persulfoxide intermediate as discussed above for the catalytic oxidation of CEES.

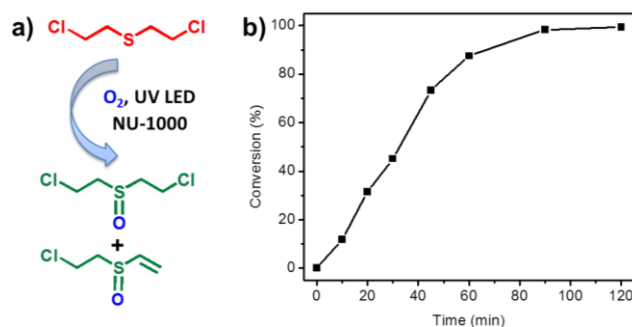


**Figure 2-8** a) Photo-oxidation of HD under UV LED irradiation and  $\text{O}_2$  atmosphere catalyzed by NU-1000. b) Degradation profile of HD (0.4 mmol) in the presence of NU-1000 (5.2 mg) while being irradiated with a UV LED.

## 2.4 Conclusions

In conclusion, singlet oxygen, generated by a pyrene-based MOF NU-1000 under UV LED irradiation, selectively oxidizes an HD simulant CEES to the nontoxic sulfoxide product. The large apertures and 3-D structure of NU-1000 not only further improves the singlet oxygen generation by heterogenizing and isolating the pyrene moieties in an ordered array, but also

facilitate the diffusion of substrates and products. In addition, the proposed mechanism of CEES oxidation by singlet oxygen gives insight into the reaction selectivity and the first-cycle induction behavior for the progress of the reaction. Finally, this method was applied for the detoxification of the warfare agent HD and was found to be effective in selectively oxidizing HD to a nontoxic product.

**Chapter 3 . Improving the efficiency of mustard gas simulant detoxification  
by tuning the singlet oxygen quantum yield in metal–organic frameworks and  
their corresponding thin films**

Portions of this chapter appear in the following manuscript:

Buru, C. T.; Majewski, M.B.; Howarth, A.J.; Lavroff, R.H.; Kung, C.-W.; Peters, A.W.;  
Goswami, S.; Farha, O.K. Improving the Efficiency of Mustard Gas Simulant Detoxification by  
Tuning the Singlet Oxygen Quantum Yield in Metal–Organic Frameworks and Their  
Corresponding Thin Films. *ACS Appl. Mat. Inter.* **2018**, *10*, 23802-23806.

### 3.1 Introduction

Global concerns over the use and stockpiling of chemical warfare agents (CWAs) has necessitated the development of efficient materials to safely handle and detoxify these dangerous weapons.<sup>1,123</sup> CWAs still exist in stockpile locations consisting of thousands of metric tons and are also being used against military personnel and civilians, in spite of international bans and treaties which have called for their elimination.<sup>6</sup> One common CWA, bis(2-chloroethyl)sulfide (mustard gas, sulfur mustard, or HD, **Figure 3-1**), is a notorious vesicant which alkylates DNA, causing irreversible damage to exposed skin and tissues.<sup>4,17,161</sup> Finding and developing environmentally-friendly technologies that will effectively and safely neutralize HD, without the concurrent accumulation of harmful byproducts, remains an ongoing challenge.

The partial oxidation of HD (bis(2-chloroethyl)sulfide) to HDO (bis(2-chloroethyl)sulfoxide, **Figure 3-1**) is a promising detoxification pathway.<sup>5</sup> However, the completely oxidized sulfone, HDO<sub>2</sub>, has similar vesicant properties as the parent HD,<sup>20,146</sup> necessitating the implementation of a material that is selective for the partial oxidation to mitigate formation of toxic by-products. A readily available oxygen source to achieve this reaction is atmospheric O<sub>2</sub>. Triplet O<sub>2</sub> (<sup>3</sup>Σ<sub>g</sub><sup>-</sup>), as found in the air, lies in the ground state and is kinetically inert. In order for oxygen to become reactive, a photosensitizer can be used to promote ground state triplet O<sub>2</sub> to a singlet excited state (<sup>1</sup>Δ<sub>g</sub>).<sup>151</sup>

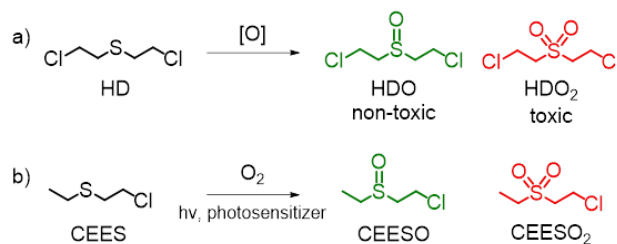


**Figure 3-1** a) Reaction pathway for the oxidation of bis(2-chloroethyl)ethyl sulfide (HD) to HDO and HDO<sub>2</sub>. b) Reaction pathway for the oxidation of the HD simulant, 2-chloroethyl ethyl sulfide (CEES), using dioxygen and a photosensitizer.

Previously, our team, among others, has demonstrated the selective aerobic oxidation of mustard gas and its simulant, 2-chloroethyl ethyl sulfide (CEES, **Figure 3-1**), to nontoxic products by LED (light emitting diode) irradiation of photosensitizers immobilized (as structural linkers or postsynthetically-tethered ligands) in metal–organic frameworks (MOFs).<sup>24,162–166</sup> CEES was initially used for these studies because its toxicity is 100 times less than that of HD<sup>167</sup> while retaining the thioether moiety. MOFs are a growing class of highly tunable materials composed of inorganic nodes and multitopic organic linkers.<sup>7–10,140</sup> The versatility of MOFs allows for the design of crystalline, porous, and functional materials for applications including gas storage/separation,<sup>168</sup> toxic waste remediation,<sup>118,169</sup> and catalysis.<sup>170</sup> Using a MOF scaffold to heterogenize soluble organic photosensitizers imparts the advantages of a solid-state catalyst, namely, ease of recovery and possible reuse of the catalytic material, larger solvent scope, greater stability, and, perhaps most importantly, separation of chromophores to prevent aggregation and nonproductive excited state decay processes.<sup>171–173</sup> Zr<sub>6</sub>-based MOFs, in particular, are especially attractive supports to generate singlet oxygen due to their high thermal and chemical stability.<sup>174,175</sup> Recently, a series of robust Zr-based MOFs containing different photosensitizers as linkers while possessing an identical **csq** topology were studied for singlet oxygen generation and subsequent CEES oxidation.<sup>24,162</sup> The porphyrin-based PCN-222/MOF-

545 and pyrene-based NU-1000 (**Figure 3-2**) MOFs, demonstrated half-lives (time at 50% CEES conversion) for the reaction in Scheme 1b of 13 and 6 min, respectively, when illuminated with commercially available LEDs.

The efficiency of a photosensitizer for singlet oxygen generation may be correlated to the singlet oxygen generation quantum yield ( $\Phi_{\Delta}$ ). For the PCN-222/MOF-545 linker, 5,10,15,20-tetrakis(4-carboxyphenyl)porphyrin ( $H_4TCPP$ ), in methanol, the reported  $\Phi_{\Delta}$  is 0.55.<sup>176</sup> The quantum yield for the linker of NU-1000, 1,3,6,8-tetrakis(p-benzoate)pyrene ( $H_4TBAPy$ ), has not been reported, but is expected to be similar to pyrene ( $\Phi_{\Delta} = 0.6 - 0.76$ ).<sup>177</sup> As anticipated with these two examples, the higher  $\Phi_{\Delta}$  for pyrene decreases the half-life of the CEES oxidation reaction in NU-1000 compared to PCN-222/MOF-545. By increasing conjugation in the linker to 2,5,8,11-tetrakis(4-carboxyphenyl)perylene ( $H_4TBAPery$ ), we expect to observe a higher singlet oxygen quantum yield<sup>177</sup> and therefore a shorter half-life for the partial oxidation of CEES using the Zr-based MOF, UMCM-313 (**Figure 3-2**).

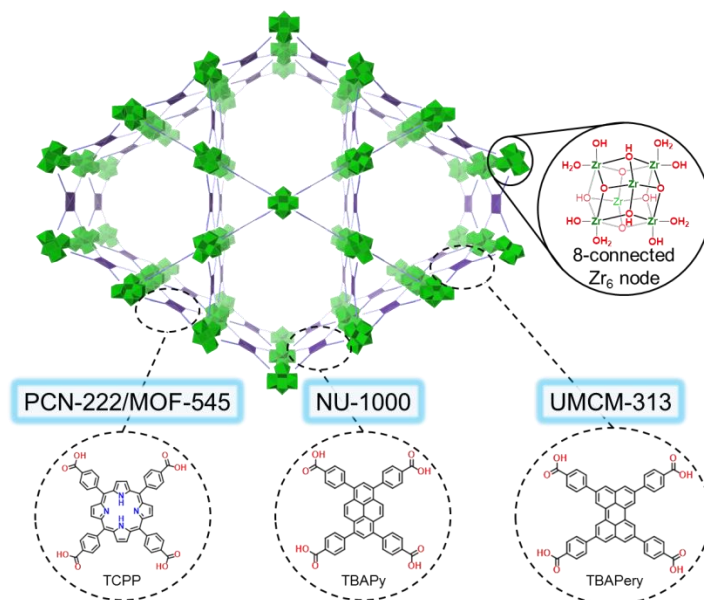


**Figure 3-2** The structure of NU-1000, PCN-222/MOF-545, and UMCM-313 and their corresponding linkers and common Zr<sub>6</sub>-node.

In addition to leveraging MOFs with a higher quantum yield of singlet oxygen formation, the synthesis of MOF thin films in an attempt to further improve the reaction rate of CEES oxidation and to demonstrate the potential practicality of these MOF-based systems. MOF thin films are commonly explored as sensor materials<sup>178,179</sup> and for electrocatalysis.<sup>180</sup> By using a thin film in a photocatalytic reaction, we anticipate that light scattering by the individual crystallites will be reduced allowing photons to address more than the outermost surface layer of chromophores. Together with the nanoparticulate nature of solvothermally grown thin films, the light absorption cross-section of the material should increase. Further, a thin film will afford some insight into how MOFs can function as catalytic surface coatings for detoxification applications. MOF thin films can be deposited post-synthetically or grown directly on a substrate material,<sup>181</sup> with the latter being more mechanically stable. We have previously reported the solvothermal growth of NU-901 on a fluorine-doped tin oxide (FTO) glass substrate and, more recently, have expanded the study to the growth of NU-1000 films with loadings on the order of  $10^{-8} \text{ mol}\cdot\text{cm}^{-2}$ .<sup>182,183</sup>

In this chapter, this series of photosensitizer-based Zr-MOFs with **csq** topology is expanded to include the perylene-based MOF, UMCM-313, where perylene is known to have a higher singlet oxygen quantum yield in solution under certain conditions compared to pyrene or porphine.<sup>177</sup> In addition, we demonstrate that using thin films of NU-1000 and UMCM-313, to achieve low catalyst loadings, waste less catalyst, and minimize light scattering, significantly enhances the turnover frequencies for the CEES oxidation reaction compared to using bulk powders of each MOF.

### 3.2 Experimental Methods

### 3.2.1 Material Syntheses

**General** Bulk PCN-222/MOF-545, bulk NU-1000, thin films of NU-1000, and linkers for NU-1000 and UMCM-313 were synthesized according to literature procedure.<sup>120,183–185</sup> All other chemicals, except those listed below, were used as received from Fisher Scientific or Sigma Aldrich. All gasses for activation and quantification were Ultra High Purity Grade 5.

**Synthesis of bulk UMCM-313** The procedure employed in this work is analogous to that used to prepare 10  $\mu\text{m}$  crystals of NU-1000.<sup>186</sup>  $\text{ZrOCl}_2 \cdot 8\text{H}_2\text{O}$  (50 mg, 0.28 mmol), benzoic acid (625 mg, 5.1 mmol), and 12.5 mL of dimethylformamide (DMF) were well sonicated in an 8-dram vial. The solution was heated for 1 h at 80  $^\circ\text{C}$  and allowed to cool to room temperature. Then, 2,5,8,11-tetrakis(4-carboxyphenyl)perylene ( $\text{H}_4\text{TBApery}$ , 16.5 mg, 0.225 mmol) dissolved in 12.5 mL of DMF was added. Trifluoroacetic acid (TFA, 250  $\mu\text{L}$ , 7.4 mmol) was added, and the solution was sonicated for 10 min. The vial was heated at 120  $^\circ\text{C}$  for 3 days.

**Synthesis of UMCM-313 thin films** Fluorine doped tin oxide (FTO) glass was cut into 1.25  $\times$  3 cm rectangles. The glass was cleaned by sonication in sequential baths of soapy water, ethanol, and acetone for at least 15 min each. Then, the FTO was dried in a 120  $^\circ\text{C}$  oven for 2 h. While the substrate dried, 0.5 mM solution of linker in 20 mL DMF was made in a 20 mL scintillation vial. The dried glass was placed in the solution with the FTO side face down. The glass was allowed to sit in the linker solution for 24 h. The FTO was then rinsed gently with DMF twice and dried at 120  $^\circ\text{C}$  for 2 h. In a separate vial, benzoic acid (625 mg, 5.1 mmol) and  $\text{ZrOCl}_2 \cdot 8\text{H}_2\text{O}$  (50 mg, 0.28 mmol) were added together in 12.5 mL of DMF. The solution was sonicated until everything was dissolved and placed in an 80  $^\circ\text{C}$  for 1 h. Once out of the oven, the solution was cooled to room temperature before  $\text{H}_4\text{TBApery}$  (24.8 mg) was added, followed by 250  $\mu\text{L}$  of TFA. The vial was sonicated for 10 min while the FTO was cooled to room

temperature. Then the substrate was placed in the vial with the FTO side face down. The vial was placed at the bottom of a gravity convection oven (VWR® symphony™) with the temperature set at 90 °C for at least 18 h.

**General MOF Activation Procedure** All MOFs were synthesized in DMF. The solid was washed three times with 30 mL of DMF. The solvent was then exchanged with 30 mL of acetone once. The MOFs were allowed to soak in acetone overnight before washing three more times with 30 mL of acetone. After the final wash, the MOFs were thermally activated at 120 °C for 12 h under vacuum before sorption and subsequent experiments.

**General Thin Film Activation Procedure** The films were carefully washed with DMF three times. Then the films were immersed in a vial containing pure acetone for 24 h, exchanging the acetone three times. When the solvent was fully exchanged, the films were dried in a vacuum oven at 80 °C for 12 h before subsequent experiments.

### 3.2.2 Physical Methods

X-ray diffraction (XRD) patterns of bulk MOFs were collected on a STOE STADI MP instrument using  $K\alpha_1$  Cu radiation in transmission geometry. XRDs patterns of the thin films were measured on a Rigaku ATX-G workstation. Solution  $^1\text{H}$  NMR spectra were collected on a 500 MHz Bruker Avance III system equipped with DCH CryoProbe at IMSERC (Integrated Molecular Structure Education and Research Center) at Northwestern University. Scanning electron microscopy (SEM) images were collected using a Hitachi S4800-II cFEG SEM microscope at Northwestern University's EPIC/NUANCE facility. All samples were coated with ~14 nm of  $\text{OsO}_4$  immediately prior to imaging. GC-FID measurements were carried out on an Agilent Technologies 7820A GC system equipped with an Agilent J&W GC HP-5 capillary column (30 m  $\times$  320  $\mu\text{m}$   $\times$  0.25  $\mu\text{m}$  film thickness). All samples were filtered and diluted with

dichloromethane prior to injection. Starting temperature: 70 °C, Hold: 0.5 min, Ramp: 30 °C/min, Time: 1 min, Ramp: 75 °C/min, End temperature: 250 °C. The disappearance of the reactant was calculated relative to a 0-minute time point. All MOF samples were activated by heating 20 to 100 mg of material at 120 °C for 12 h under high vacuum on a Micromeritics Smart VacPrep instrument. N<sub>2</sub> adsorption and desorption isotherm measurements were performed on a Micromeritics Tristar II at 77 K. LED irradiation was performed using solderless LEDs purchased from RapidLED which were then mounted on aluminum to give a homemade irradiation setup. The LEDs were connected in series to a RapidLED 0-10V Dimmable LED driver. The irradiation setup contains two or four UV LEDs ( $\lambda_{\text{max}} = 395 \text{ nm}$ , FWHM = 12 nm) or blue LEDs ( $\lambda_{\text{max}} = 450 \text{ nm}$ , FWHM = 18 nm) that are mounted facing each other ~5 cm apart. UV-Vis spectra were collected on a Cary 5000 spectrophotometer in single beam mode. MOF thin films were digested in 0.5 M NaOH prior to measurement. Loadings were determined by calibration curve. Steady-state singlet oxygen emission was measured on a HORIBA Nanolog fluorimeter equipped with a InP/InGaAs NIR detector (0.2s-1s integration times and 14 nm excitation and emission slit widths were needed). Emission spectra were corrected for monochromator wavelength dependence. Samples were prepared at concentrations where the optical density was 0.3 and were excited at wavelengths corresponding to optical absorbance maxima (390 nm for the pyrene-based linker, 414 nm for the porphyrin linker, and 450 nm for the perylene-based linker). Quantum yields were determined relative to a Rose Bengal standard which has a quantum yield of singlet oxygen production in methanol of 0.76.<sup>150</sup>

### ***3.2.3 Material Characterization***

All bulk MOFs were characterized by powder X-ray diffraction (PXRD), scanning electron microscopy (SEM), and N<sub>2</sub> sorption. All thin films were characterized by XRD and

SEM. The amount of MOF in each film was quantified using a calibration curve obtained from UV-visible absorption spectra of the linkers in conjunction with the absorption of a base-digested film (**Figure 3-3** and **Figure 3-4**).

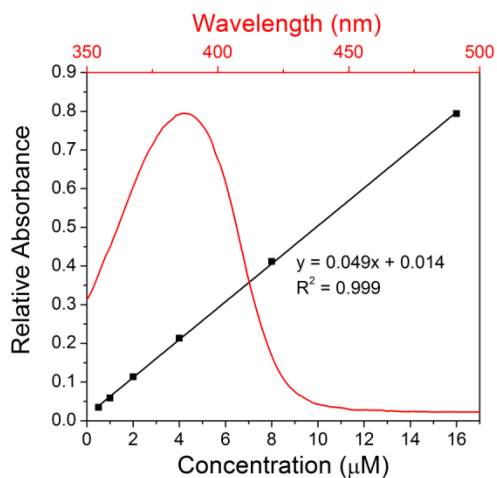


**Figure 3-3** TBAPy<sup>4-</sup> UV-vis absorption spectrum at 16 μM in 0.1 M NaOH (red) and calibration curve (black) extracted from peak absorbance at 388 nm.

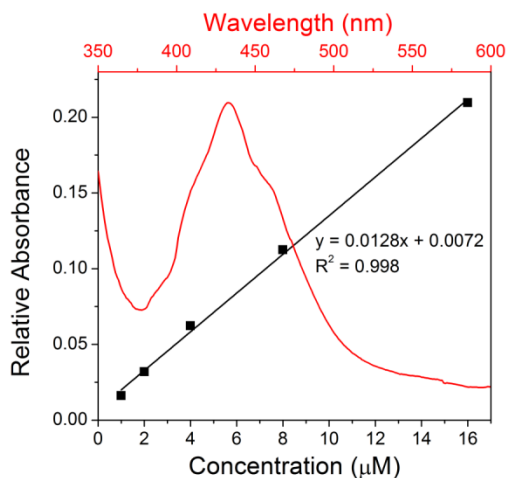


**Figure 3-4** TBAPery<sup>4-</sup> UV-vis absorption spectrum at 16 μM in 0.1 M NaOH (red) and calibration curve (black) extracted from peak absorbance at 433 nm.

### 3.2.4 Catalytic Measurements

***CEES Oxidation with Bulk MOF.*** The LEDs were fixed to an aluminum sheet housing containing 4 LEDs facing inward, ~5 cm apart. The power density of the UV LEDs was lowered to  $2.2 \text{ W/cm}^2$  to match the power density of the blue LEDs. For the photocatalytic experiments, the MOFs (0.001 mmol, 1 mol% by chromophore) were suspended in 1 mL methanol in a  $17 \times 83$  mm microwave vial. The mixture was sonicated to ensure homogeneous dispersion of MOF particles. The vial was sealed and purged with  $\text{O}_2$  for 20 min, then the simulant (CEES, 23  $\mu\text{L}$ , 0.2 mmol) and internal standard (1-bromo-3,5-difluorobenzene, 10  $\mu\text{L}$ ) were added. The vial was placed in the center of the LED microreactor. CEES conversion data points were collected at regular intervals of irradiation. Conversion of CEES was calculated relative to the internal standard by gas chromatography (GC-FID) and the selectivity was verified by  $^1\text{H}$  NMR spectroscopy.

***CEES Oxidation with Thin Film MOFs.*** Thin film samples were prepared by cutting the FTO substrate into four pieces (ca.  $0.4 \times 1.5$  cm) at the conclusion of MOF growth. One piece was used for characterization and the other three were used for catalysis studies. To test CEES oxidation, the sample thin film was placed in a microwave vial containing 1 mL of methanol. The vial was sealed and purged with  $\text{O}_2$  for 20 min, followed by addition of the internal standard and CEES amounting to a MOF loading of 0.0032 mol%. Of note, some pieces of FTO were too large to be completely submerged by 1 mL of solvent, so only the submerged area was considered catalytically active and only two LEDs, ~5 cm apart and set to  $1.1 \text{ W/cm}^2$ , were used to irradiate the thin films.

### **3.3 Results and Discussion**

In this study, PCN-222/MOF-545, NU-1000, and UMCM-313 were considered because they are Zr-based MOFs with **csq** topology, minimizing any topology or node dependent contribution to catalytic activity. Given the Soret band of H<sub>4</sub>TCPy lies around 420 nm, a blue LED ( $\lambda_{\text{max}} = 450$  nm, FWHM = 18 nm) was chosen for irradiation of this MOF due to the red-shift observed when these chromophores are immobilized in a MOF.<sup>187,188</sup> For H<sub>4</sub>TBAPy, the maximum absorption band lies around 390 nm, so a UV LED ( $\lambda_{\text{max}} = 395$  nm, FWHM = 12 nm) was used. The UMCM-313 linker has an absorption band around 430 nm, so the blue LED was chosen for irradiation.

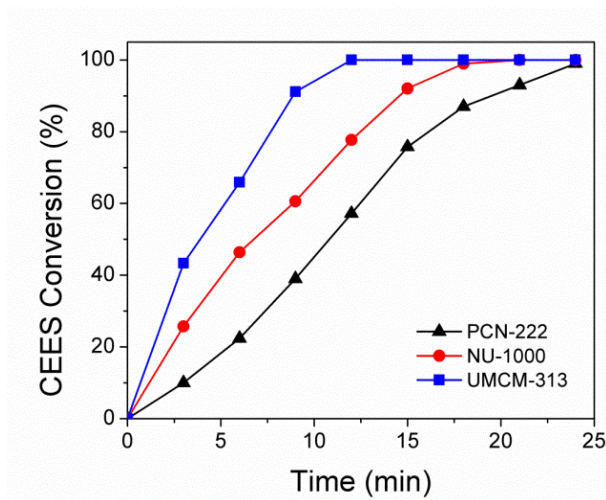


**Figure 3-5** Reaction profiles of the three MOF powders. PCN-222 and UMCM-313 were irradiated with blue LEDs and NU-1000 was irradiated with UV LEDs of equivalent power density.

From a plot of CEES conversion vs. time (**Figure 3-5**), PCN-222, NU-1000, and UMCM-313 yield half-lives of 11, 6, and 4 min, respectively. An increase in irradiation intensity accounts for the half-life improvement of PCN-222/MOF-545 versus previously reported results.<sup>24</sup> Initial turnover frequencies (TOF) for these reactions are 8–14 mol<sub>CEES</sub>•mol<sub>chromophore</sub><sup>-1</sup>•min<sup>-1</sup> under these conditions. The reactivity trend for the bulk MOFs is consistent with the measured singlet oxygen quantum yield of the corresponding linkers measured by singlet oxygen

emission relative to a standard (**Figure 3-6** and Table 3-1), namely porphyrin<pyrene<perylene.

Quantum yields were calculated using  $\Phi = \Phi_{ref} \frac{I}{I_{ref}} \frac{OD_{ref}}{OD} \frac{n^2}{n_{ref}^2}$  (**Equation 3-1**):

$$\Phi = \Phi_{ref} \frac{I}{I_{ref}} \frac{OD_{ref}}{OD} \frac{n^2}{n_{ref}^2} \quad \text{(Equation 3-1)}$$

where  $\Phi_{ref}$  is the  $^1\text{O}_2$  quantum yield of the reference, rose bengal, I is intensity, OD is optical density, and n is the refractive index.<sup>189</sup>

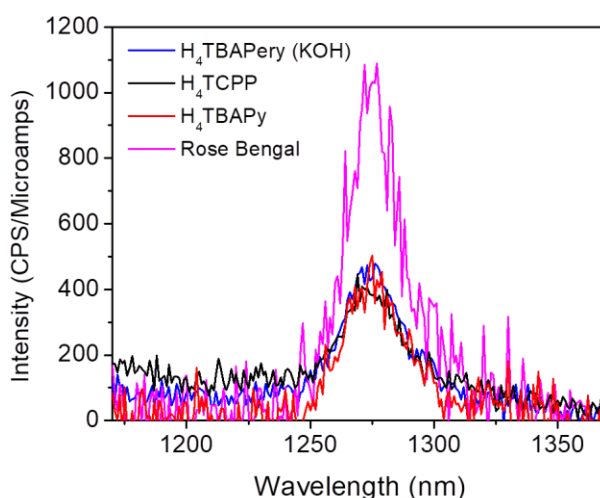


**Figure 3-6** Singlet oxygen emission observed on linker excitation in methanol corrected for optical density (0.3). Extracted data shown in **Table 3-1**. H<sub>4</sub>TBAPery required the addition of KOH to solubilize.

**Table 3-1** Singlet oxygen quantum yields of the MOF linkers in methanol

Linker	$\Phi (^1\text{O}_2)^*$
Rose Bengal	0.76
H <sub>4</sub> TBAPery	0.45
H <sub>4</sub> TBAPy	0.40
H <sub>4</sub> TCPP	0.38

Importantly, across all three MOFs, the  $^1\text{H}$  NMR spectra showed no detectable amount  $\text{CEESO}_2$ , indicating the reaction is selective for the partially oxidized product, CEESO. Note that methanol is thought to be essential for promoting the formation of the singly oxidized product.<sup>190,191</sup> Additionally, the MOFs retain their crystallinity during the reaction<sup>24,162</sup>, and thus have the ability to be reused.

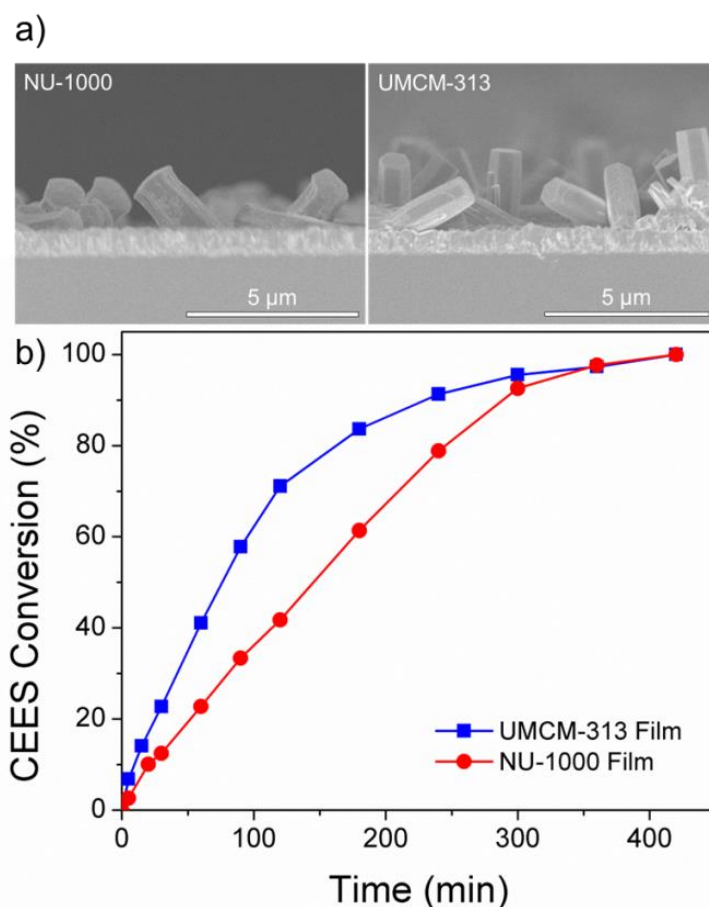


**Figure 3-7** a) Side views of the thin films and b) their reaction profiles for the oxidation of CEES. UMCM-313 thin film was irradiated with blue LEDs and NU-1000 was irradiated with UV LEDs of equivalent power density.

The thin films of PCN-222/MOF-545 were omitted in this study because a phase-pure synthetic procedure for solvothermally grown thin films of this MOF could not be realized. We note that the substrate FTO is transparent to the output wavelengths of the LEDs used in this

study. Consequently, there is no conversion in the presence of FTO without MOF (confirmed by GC-FID of methanolic CEES solution after 5 h of LED irradiation in the presence of FTO). Because the loading of NU-1000 and UMCM-313 varied slightly depending on the size of the FTO, CEES amounts were adjusted in an effort to keep the mole percent of catalyst constant. As shown in **Figure 3-7**, the UMCM-313 thin film gave a CEES half-life of 75 min while the NU-1000 thin film has a CEES half-life of 145 min. This observed trend is consistent with the bulk powders and with the quantum yields of the respective chromophoric linkers. Initial TOFs for the thin film reactions are on the order of  $100 \text{ mol}_{\text{CEES}} \cdot \text{mol}_{\text{chromophore}}^{-1} \cdot \text{min}^{-1}$ , compared to 8–14  $\text{mol}_{\text{CEES}} \cdot \text{mol}_{\text{chromophore}}^{-1} \cdot \text{min}^{-1}$  for the bulk MOFs. The increase in activity is attributed to a lower MOF loading, and therefore greater local concentration of CEES, but also to greater exposure of the catalyst to the incident light and the minimized light scattering (and subsequent increased photon penetration) by the MOF particles when fixed to the FTO substrate.

### 3.4 Conclusions

Three  $\text{Zr}_6$ -based MOFs, PCN-222/MOF-545, NU-1000, and UMCM-313, whose linkers are porphyrin-, pyrene-, and perylene-based, were used as catalysts to generate singlet oxygen under LED irradiation. Using 0.5 mol% of MOF, the singlet oxygen selectively oxidized the mustard gas simulant, CEES, to the non-toxic product, CEESO, with simulant half-lives of 11, 6, and 4 minutes, respectively. The rate of the reaction correlated with the singlet oxygen generation quantum yield of the MOF linkers in solution. To minimize scattering by MOF particles and increase exposure of the catalyst to the incident light, thin films of NU-1000 and UMCM-313 were solvothermally grown on glass substrates and irradiated with LEDs to generate singlet oxygen. With only 0.0032 mol% of MOF, the thin films were still active for the selective

oxidation of CEES, with simulant half-lives of 145 and 75 min, respectively, and much higher TOFs than those determined for the bulk MOFs. These results encourage further optimization of photosensitizers in MOFs as bulk materials and coatings for CWA remediation.

**Chapter 4 . Adsorption of a catalytically accessible polyoxometalate in a mesoporous channel-type metal–organic framework**

Portions of this chapter appear in the following manuscript:

Buru, C. T.; Li, P.; Mehdi, B. L.; Dohnalkova, A.; Platero-Prats, A. E.; Browning, N. D.; Chapman, K. W.; Hupp, J. T.; Farha, O.K. Adsorption of a catalytically accessible polyoxometalate in a mesoporous channel-type metal–organic framework. *Chem. Mater.* **2017**, *29*, 5174-5181.

## 4.1 Introduction

Polyoxometalates (POMs) are anionic metal oxide clusters, mainly composed of high valent early-transition-metal ions bridged by oxygen atoms.<sup>28,30,32</sup> Their modular composition and size give rise to many examples of POMs.<sup>29,192</sup> Owing to their acid-base and redox properties, POMs have found many applications in chemical catalysis<sup>193</sup>, such as water oxidation,<sup>44,45,194</sup> alkene epoxidation,<sup>42,195</sup> and phosphoester hydrolysis.<sup>196,197</sup> The recovery and reusability of POMs in these catalytic systems is hindered by their high solubility, low specific area, and poor stability under catalytic conditions.<sup>48,198</sup> To overcome these drawbacks, supports such as mesoporous silica,<sup>49,199</sup> polymers,<sup>200,201</sup> covalent organic frameworks (COFs),<sup>202</sup> and metal–organic frameworks (MOFs)<sup>9,203</sup> have been used to anchor POMs to create hybrid heterogeneous materials.

MOFs are a class of materials consisting of metal nodes connected by multi-topic organic linkers.<sup>10,138</sup> The tunability and porosity of MOFs makes them promising heterogeneous catalysts<sup>204</sup> or excellent supports for anchored homogeneous catalysts.<sup>205</sup> Two techniques have been reportedly used to incorporate POMs in MOFs (also POM@MOF): impregnation and encapsulation.<sup>170</sup> The first instance of a POM@MOF was synthesized by Ferey and coworkers using the impregnation method with MIL-101, due to the large apertures and mesopores in its structure.<sup>9</sup> The impregnation method involves directly adding preformed POM to a MOF. This method necessitates large apertures in the MOF for POM diffusion. Though straightforward, the impregnation method has a number of limitations when used to obtain a potential catalytic material: low maximum loading (~0.2 POM/node), low homogeneity, occupation of large cavities limiting diffusion, and leaching.<sup>83,97,170,206</sup> The encapsulation method, also known as the ‘bottle around ship method’, involves building the MOF in the presence of POM. Such a

technique has been useful for HKUST-1 and other Cu-BTC frameworks (BTC = 1,3,5-benzene-tricarboxylate, these POM@MOFs are also known as the NENU series),<sup>207</sup> MIL-100/101 (Fe, Cr, Al),<sup>97,98,113,208,209</sup> and UiO-67.<sup>210</sup> The cavities inside these MOFs are large enough to contain the desired POM, while the apertures are small enough to keep the POM from leaching out of the pores. This usually leads to reduced activity of the POM because the pores are blocked, such that the substrate cannot easily diffuse through the framework.<sup>97,211</sup> Gascon and coworkers have demonstrated that one approach to avoid these problems is to use MIL-101 to encapsulate 2 POMs per medium cavity, leaving the larger cavities open.<sup>83</sup> This material relies on metal exchange of tungsten with the chromium framework, potentially limiting the scope of the POMs which can be encapsulated into this MOF.

To overcome some of these problems of POM and substrate diffusion, we propose to use a zirconium MOF with micro- and mesoporous channels, NU-1000, as a support for POMs. NU-1000, an eight-connected MOF, composed of  $Zr_6(\mu_3-O)_4(\mu_3-OH)_4(H_2O)_4(OH)_4$  nodes connected by 1,3,6,8-tetrakis(p-benzoate)pyrene linkers (TBAPy),<sup>119,212</sup> fulfills these requirements because it has small triangular channels (12 Å) which will permit the incorporation of large POMs, while the larger (31 Å) hexagonal channels provide an auxiliary path for substrate diffusion (**Figure 4-1**). The use of this hierarchical MOF should ultimately circumvent the previously stated limitations imposed by other MOFs. Additionally, NU-1000 has been shown to be an excellent host material, supporting guests from the size of a single atom<sup>59,213,214</sup> or small molecule<sup>163,215</sup> to an enzyme.<sup>216</sup> Intermediate-sized charged guests, like POMs, have yet to be studied in NU-1000. Previous studies have shown that NU-1000 readily adsorbs small oxyanions (selenites/selenates,<sup>118</sup> sulfates<sup>169</sup>) via displacement of hydroxide ions on the  $Zr_6$  node for charge

balancing. We hypothesized that guest molecules could be extended to larger oxyanions, namely POMs.

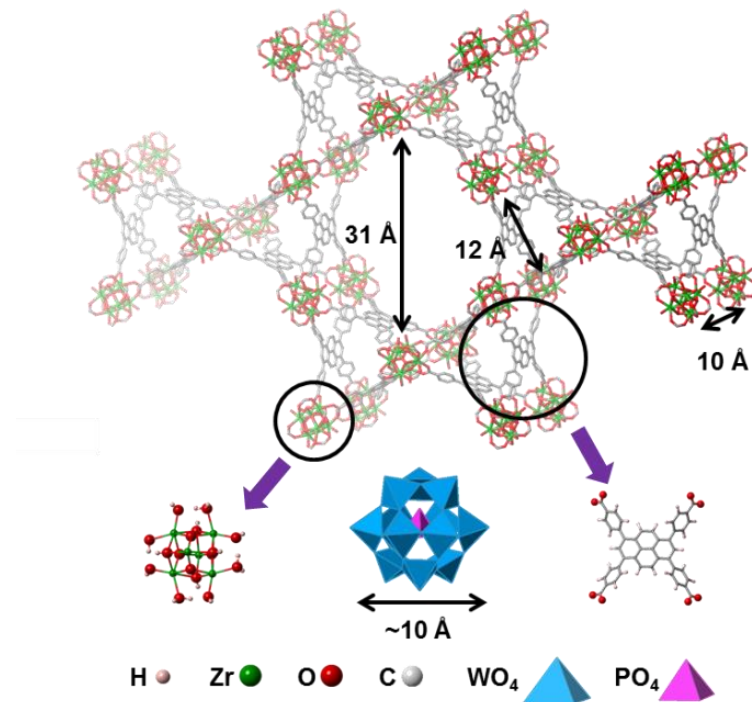


**Figure 4-1** The crystal structure of NU-1000, showing the 31 and 12 Å channels. Each layer is separated by 10 Å windows. The structure for the nodes and linkers are given. The structure and size of the POM, [PW<sub>12</sub>O<sub>40</sub>]<sup>3-</sup>, are shown.

H<sub>3</sub>PW<sub>12</sub>O<sub>40</sub> was selected as an archetypal POM based on size and demonstrated catalytic activity for the oxidation of organosulfides in the presence of peroxide.<sup>106,217,218</sup> On the other hand, the nodes on NU-1000 have a structure analogous to zirconia, which can act as a counterion for [PW<sub>12</sub>O<sub>40</sub>]<sup>3-</sup> to prevent the Keggin unit from leaching once the nodes are protonated.<sup>219</sup> Zirconia can also catalyze the oxidation of sulfides.<sup>220,221</sup> Therefore, if the POMs and MOF nodes are accessible, then the proposed composite material should be active in the oxidation of 2-chloroethyl ethyl sulfide (CEES), a mustard gas simulant (**Figure 4-2**). Two oxidation products are possible, a singly oxidized sulfoxide (CEESO) and a doubly oxidized sulfone (CEESO<sub>2</sub>).<sup>144</sup> In the case of mustard gas (a lethal chemical warfare agent), the sulfoxide

product is considered non-toxic, while the sulfone has vesicant properties similar to the parent agent.<sup>20</sup> Thus, selectivity is important when designing a catalyst for mustard gas detoxification.

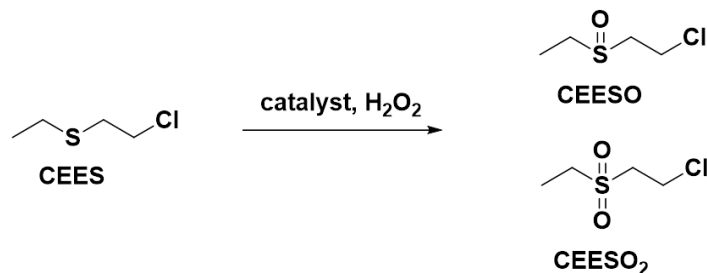


**Figure 4-2** General catalytic conditions and reaction pathways for 2-chloroethyl ethyl sulfide oxidation with hydrogen peroxide

Here we demonstrate the adsorption of a representative POM,  $[\text{PW}_{12}\text{O}_{40}]^{3-}$ , within the pores of NU-1000. To our knowledge, this is the first channel POM@MOF composite and achieves the highest POM/node loading attainable via impregnation as of yet.<sup>9,48,206</sup> Furthermore, we demonstrate the POMs and MOF nodes in the composite material to be catalytically accessible. For the catalytic sulfide oxidation,  $\text{PW}_{12}$ @NU-1000 has higher activity than either component alone.

## 4.2 Experimental Methods

### 4.2.1 Material Syntheses

**General.** NU-1000 was synthesized according to literature procedure.<sup>120</sup> Phosphotungstic acid was purchased from Sigma Aldrich. TGA analysis showed that an average of 24 water molecules were associated with each POM. For NMR comparisons, 2-chloroethyl ethyl sulfoxide (CEESO) was synthesized from 2-chloroethyl ethyl sulfide (CEES) under 1 atm O<sub>2</sub> in the presence of NU-1000 under UV-LED irradiation.<sup>162</sup> The identity and purity were confirmed by GC-MS, <sup>1</sup>H NMR, and <sup>13</sup>C NMR spectroscopy. All other chemicals were used as received from

Fisher Scientific or Sigma Aldrich. All gasses for activation and quantification were Ultra High Purity Grade 5.

**Synthesis of  $PW_{12}@NU-1000$ .** In a centrifuge tube,  $H_3PW_{12}O_{40}$  (303 mg, 0.09 mol) was dissolved in 20 mL deionized water. The solution (pH about 2.5) was divided into two 10 mL quantities. To one solution, NU-1000 (50 mg, 0.023 mmol) was added and suspended by sonicating for about 1 minute. The suspension was shaken periodically. To monitor uptake of POM, the solutions with and without NU-1000 were analyzed by ICP-OES and compared to each other. After 3 days, the solid was washed with water three times. Then, the solid was washed with acetone.  $PW_{12}@NU-1000$  was allowed to sit in acetone overnight before washing two more times with acetone to ensure adequate removal of water. Samples were dried at 80 °C for 4 hours under vacuum prior to activation on the Smart VacPrep. The solid material was subject to ICP-OES to determine the final POM loading.

#### **4.2.2 Physical Methods**

Inductively coupled plasma optical emission spectroscopy (ICP-OES) samples of solids were prepared in a 2-5 mL Biotage microwave vial by dissolving 1-2 mg of NU-1000 or  $PW_{12}@NU-1000$  in 750  $\mu$ L  $H_2SO_4$  and slowly adding 25  $\mu$ L of  $H_2O_2$  (30 wt% in water). The vial was cringe-capped and heated to 150 °C for 5 min in a SPX microwave re-actor (software version 2.3, build 6250). The resulting clear solutions were diluted to 10 mL with deionized water and analyzed with Thermo iCap7600 ICP-OES spectrometer, equipped with a CCD detector and Ar plasma covering 175-785 nm range. For liquid samples, a known amount of solution was taken, filtered, and diluted to 10 mL with 5 %  $HNO_3$  in water. All samples were compared to standard solutions at W (339.198, 343.823, 327.305, 349.621 nm) and Zr radial emissions (224.875, 207.911, 209.475, 239.709 nm). Diffuse reflectance infrared Fourier

transform (DRIFT) spectra were collected using a Nicolet S4 7600 FT-IR spectrometer equipped with an MCT detector under Ar purge at room temperature. Solid KBr was used as the background, which was subtracted from sample spectra. All spectra have a  $1\text{ cm}^{-1}$  resolution over 64 scans. Powder X-ray diffraction (PXRD) patterns were collected on a Rigaku Smartlab instrument. Samples were scanned at 45 kV and 160 mA, a step size of  $2\theta = 0.05^\circ$  over a  $2\theta$  range of 2 to  $20^\circ$ . High resolution powder X-ray diffraction (PXRD) data were collected at beamline 17-BM at the Advanced Photon Source (APS) at Argonne National Laboratory (ANL). The incident X-ray wavelength was  $0.45336\text{ \AA}$ . Data were collected using a Perkin Elmer flat panel area detector (XRD 1621 CN3/EHS) over the angular range  $0.5\text{-}9^\circ\ 2\theta$ . Samples were carefully ground and loaded into 1 mm diameter kapton capillaries. All measurements were performed at room temperature and ambient pressure. Lattice parameters and peak intensities were extracted from diffraction patterns via Le Bail whole pattern fitting<sup>222</sup> using Jana2006,<sup>223</sup> based on the reported structural model for NU-1000 (P6/mmm,  $a \sim 40\text{ \AA}$ ,  $c \sim 17\text{ \AA}$ ).<sup>119</sup> Lattice and pseudo-Voigt profile parameters were refined over a  $0.5\text{-}9^\circ\ 2\theta$  range. Structure envelopes were generated using the intensities of low index reflections.<sup>224</sup> Difference envelope densities (DEDs) were then obtained via subtraction of the envelope for pristine NU-1000 from the envelope for POM@NU-1000. Solution NMR spectra were collected on a 500 MHz Bruker Avance III system equipped with DCH CryoProbe or on a 400 MHz Agilent DD MR-400 system at IMSERC (Integrated Molecular Structure Education and Research Center) at Northwestern University. Solid-state NMR spectra were collected on a Varian 400 MHz VNMRS system. Scanning electron microscopy (SEM) images and energy dispersive spectroscopy (EDS) line scans were collected using a Hitachi SU8030 FE-SEM microscope at Northwestern University's EPIC/NUANCE facility. All samples were coated with  $\sim 15\text{ nm}$  of  $\text{OsO}_4$  or Au/Pd immediately

prior to imaging. The (scanning) transmission electron microscope (STEM) experiments were performed on a FEI 80-300kV Cs corrected Titan microscope equipped with Schottky field-emission electron source, a monochromator and a CEOS hexapole spherical probe aberration corrector. For these experiments the microscope was operated at 300 keV in the high angle annular dark field (HAADF) or Z-contrast imaging mode. Gas chromatography mass spectrometry (GC-MS) analyses were performed on a time-of-flight GC mass spectrometer from Agilent 6890 GC. Starting temperature: 40 °C, Ramp: 20 °C/min, End temperature: 250 °C. GC-FID measurements were carried out on an Agilent Technologies 7820A GC system equipped with an Agilent J&W GC HP-5 capillary column (30 m × 320 μm × 0.25 μm film thickness). All samples were filtered and diluted with di-chloromethane prior to injection. Starting temperature: 70 °C, Hold: 0.5 min, Ramp: 30 °C/min, Time: 1 min, Ramp: 75 °C/min, End temperature: 250 °C. The disappearance of the reactant was calculated relative to a 0-minute time point. Thermogravimetric analyses (TGA) were performed on a Mettler Toledo STAR<sup>e</sup> TGA/DSC 1 under a N<sub>2</sub> flow at a 10 °C/min ramp rate from 25 to 700 °C. For TGA-MS measurements, a Netzsch Simultaneous Thermal Analysis (STA 449F3) instrument coupled to a GC-MS was used. All MOF samples were activated by heating 20 to 100 mg of material at 120 °C for 12 hours under high vacuum on a Micromeritics Smart VacPrep instrument. N<sub>2</sub> adsorption and desorption isotherm measurements were performed on a Micromeritics Tristar II at 77 K. To calculate volumetric plots, the density of NU-1000 was reported to be 0.486 cm<sup>3</sup>/g<sup>119</sup> and PW12@NU-1000 was calculated to be 1.00 g/cm<sup>3</sup>. Cyclovoltammograms were recorded with a Solartron Analytical Modulab using a 1 MS/s potentiostat module. The working electrode was made of glassy carbon, the counter electrode was a platinum wire, and the reference electrode was a saturated calomel electrode (SCE). All electrolyte solutions were prepared with de-ionized

water. A pH 2.5 H<sub>2</sub>SO<sub>4</sub>/Na<sub>2</sub>SO<sub>4</sub> buffer solution was prepared by mixing 0.5 M Na<sub>2</sub>SO<sub>4</sub> solution with H<sub>2</sub>SO<sub>4</sub>. The solution was deoxygenated with N<sub>2</sub> for 20 minutes prior to electrochemical measurements. To measure solid PW<sub>12</sub>@NU-1000, the powder was suspended in acetone and drop-casted onto the glassy carbon surface.

### 4.2.3 Catalytic Measurements

For 2-chloroethyl ethyl sulfide (CEES) oxidation experiments, the catalyst (1.7 μmol of active site) was dispersed in 1 mL of acetonitrile in a 2 dram vial. For the POM and POM@MOF, the water weight was considered, so 1.7 μmol active sites was equivalent to 3.7 mg NU-1000, 5.7 mg H<sub>3</sub>PW<sub>12</sub>O<sub>40</sub>, and 4.7 mg PW<sub>12</sub>@NU-1000. CEES (10 μL, 85 μmol) and an internal standard (1-bromo-3,5-difluorobenzene, 5 μL) was added to the reaction vial. Then, hydrogen peroxide (30 wt% in water, 13 μL, 1.5 eq) was added. The vial was placed in a sand bath, which was pre-heated to 45 °C. Variations to this procedure are summarized in **Table 4-2**. Aliquots, approximately 50 μL, were withdrawn from the vials with a glass pipette at different time points, filtered, and diluted with dichloromethane for GC-FID or deuterated acetonitrile for NMR spectroscopy. GC-FID was used to monitor conversion and NMR spectroscopy was used to determine selectivity. **Figure 4-16** is a representative NMR spectrum of CEES, CEESO, and CEESO<sub>2</sub>. Conversion was calculated by subtracting the peak at 3.71 ppm from the peaks at 3.93 ppm, and selectivity was calculated by subtracting the peak at 3.47 ppm from 3.93 ppm. In the event that the peak at 3.93 ppm was convoluted, the peak at 3.05 ppm was used instead. GC-MS at the final time point was used to confirm the identity of the products. For leaching studies, PW<sub>12</sub>@NU-1000 was filtered out at 2 minutes and any remaining reaction was monitored. To recycle the catalyst, the reaction mixture was centrifuged and the solvent extracted. The solid material was washed three times with acetone and dried under vacuum at 70 °C before reuse.

Turnover frequencies were calculated using the first time point for each run and  $TOF =$

$$\frac{\text{moles of product}}{\text{moles of clusters} \times \text{amount of time}}$$

**Equation 4-1:**

$$TOF = \frac{\text{moles of product}}{\text{moles of clusters} \times \text{amount of time}}$$

**Equation 4-1**

Where moles of product are equal to the sum of CEESO and CEESO<sub>2</sub>. The moles of catalytic clusters (POM or MOF node) were constant 1.7 μmol.

### 4.3 Results and Discussion

Due to the large channels in NU-1000, the direct impregnation method of installing [PW<sub>12</sub>O<sub>40</sub>]<sup>3-</sup> was considered. Since NU-1000 has anionic character at neutral pH<sup>225</sup> and the POM is also anionic in water, the incorporation of the POM should rely upon the acidic nature of the POM precursor (H<sub>3</sub>PW<sub>12</sub>O<sub>40</sub>). When the hydroxyl ligands on the MOF nodes are protonated at a highly acidic pH, then the MOF will no longer be anionic and POM uptake should be favorable. To synthesize PW<sub>12</sub>@NU-1000, NU-1000 was added and suspended in an aqueous H<sub>3</sub>PW<sub>12</sub>O<sub>40</sub> solution (pH 2.5). After 3 days at room temperature, the solid was washed and rigorously solvent exchanged with acetone, resulting in PW<sub>12</sub>@NU-1000. Detailed synthesis and activation of PW<sub>12</sub>@NU-1000 are discussed in the Experimental section.

#### 4.3.1 Material Characterization

Inductively coupled plasma-optical emission spectroscopy (ICP-OES) data suggest that approximately 0.8 [PW<sub>12</sub>O<sub>40</sub>]<sup>3-</sup> per Zr<sub>6</sub> node is the maximum POM loading in NU-1000 after thorough washing. This loading can be obtained from soaking the MOF in 2 or more equivalents of POM per node and is equivalent to 52 wt%. The loading of [PW<sub>12</sub>O<sub>40</sub>]<sup>3-</sup>, however, can be

modulated by soaking the MOF in lower concentrations of POM. Further characterization of  $\text{PW}_{12}@NU-1000$  refers to the maximum 0.8  $\text{PW}_{12}/\text{Zr}_6$  loading.

Scanning electron microscopy (SEM) images show that the size and morphology of NU-1000 crystallites are maintained during POM installation (**Figure 4-3**). Energy dispersive X-ray spectroscopy (EDS) mapping suggests these POMs are located uniformly within, not just on the surface of, the MOF, except in the center where the crystal is known to have blocked pores<sup>119</sup> (**Figure 4-3**).

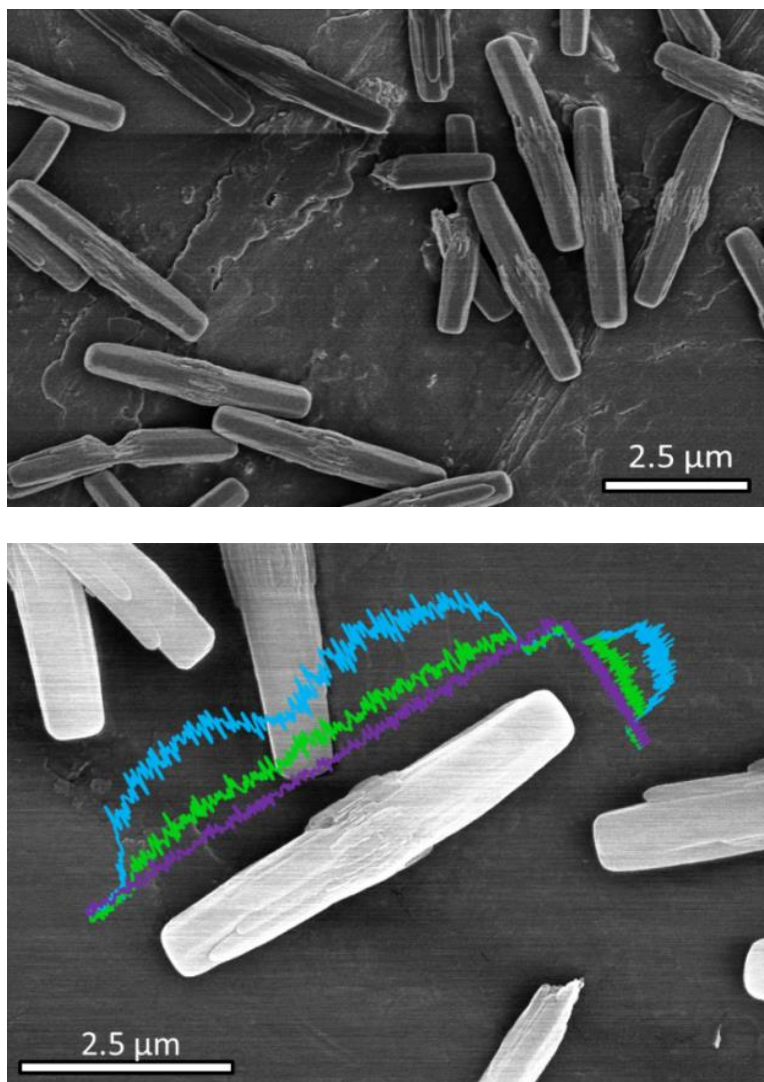


**Figure 4-3** SEM images of NU-1000 before (above) and after (below)  $[\text{PW}_{12}\text{O}_{40}]^{3-}$  incorporation. EDS line scan of NU-1000 after  $[\text{PW}_{12}\text{O}_{40}]^{3-}$  incorporation. EDS legend: Light Blue=W, Green=Zr, Purple=Zn (baseline)

The unit cell of  $\text{PW}_{12}@$ NU-1000, as seen by the Bragg peak positions on powder X-ray diffraction (PXRD, **Figure 4-4**), resembles that of NU-1000. However, locating the POM is not straightforward. Though the large mesopores in NU-1000 are large enough to accommodate the POM (Figure 3b), this possibility can be excluded by comparing the simulated and experimental PXRD of  $\text{PW}_{12}@$ NU-1000 (**Figure 4-6**). The diffraction pattern matches well with a predicted

pattern where the POM is located between two nodes in the windows (**Figure 4-5**), but does not definitively prove the location of these POMs.

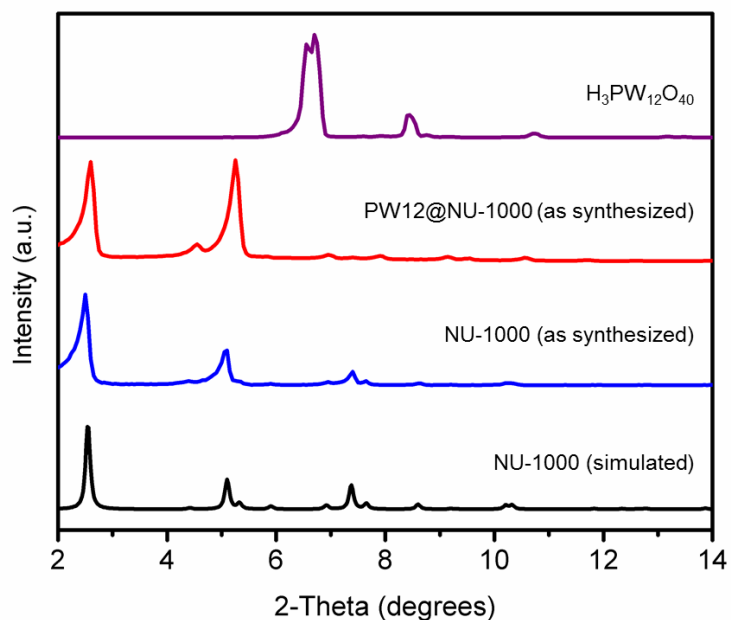


**Figure 4-4** Powder patterns for  $\text{H}_3\text{PW}_{12}\text{O}_{40}$ , NU-1000, and  $\text{PW}_{12}@$ NU-1000 compared to the simulated NU-1000.

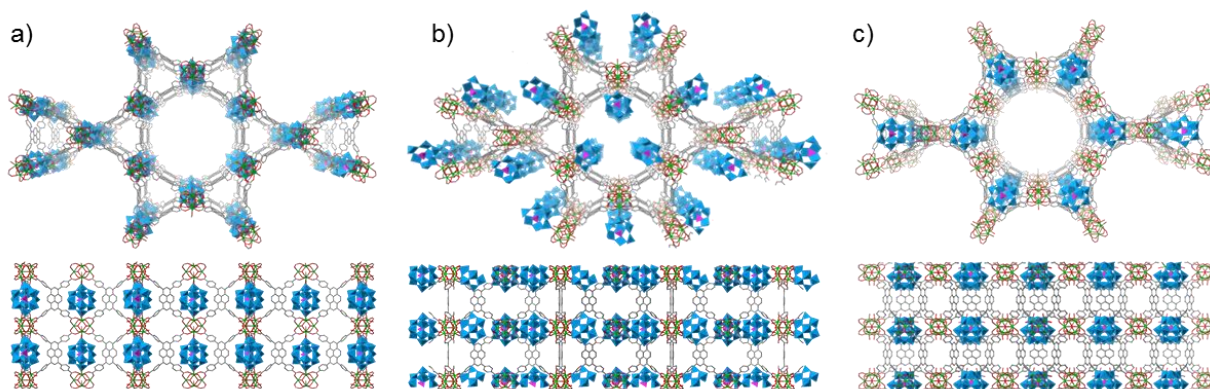


**Figure 4-5** Visual representations (top and side view) of the proposed structures for  $\text{PW}_{12}@$ NU-1000, where the POM is located inside the windows between the channels (a), in the hexagonal channels (b), or in the small triangular channels (c). DED mapping of  $\text{PW}_{12}@$ NU-1000 has led to the conclusion that (c) is most representative of the material.

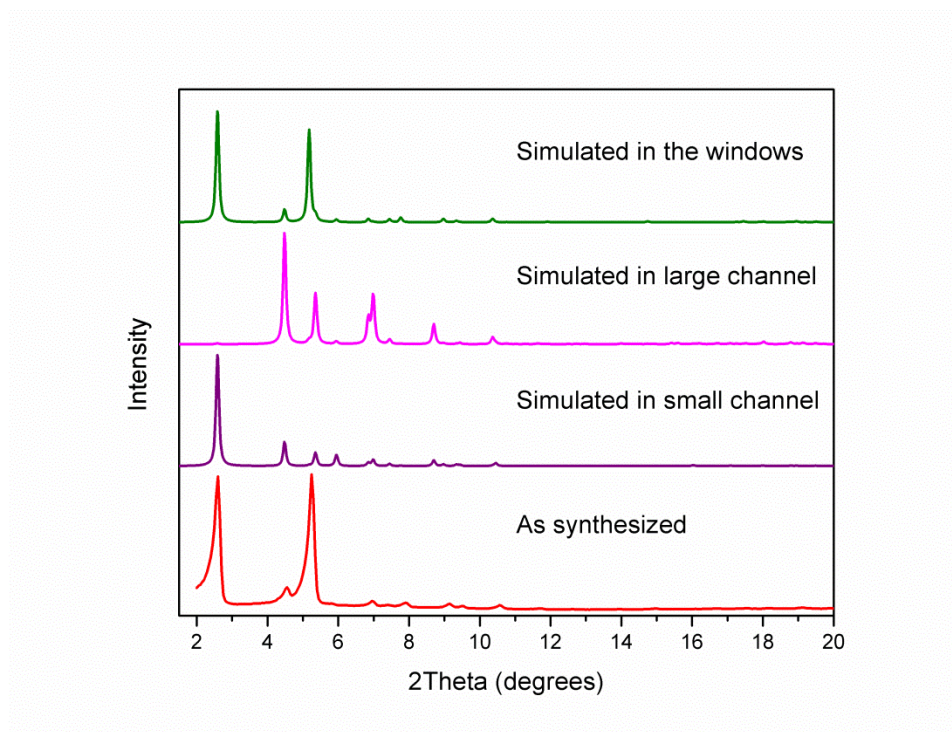


**Figure 4-6** PXR D patterns for the as synthesized  $PW_{12}@NU-1000$  compared to simulated patterns where the POM is in the mesopores or between the nodes (representations in Figures S2 and 4, respectively)

Scanning transmission electron microscopy (STEM) images were taken of  $PW_{12}@NU-1000$  in the attempt to locate the POMs. STEM images have previously been used to determine dispersion of POMs in carbon nanotubes.<sup>226</sup> **Figure 4-7** shows two Z-contrast images obtained from orthogonal directions where the node distribution in a representative area of the MOF is observed. The standard hexagonal distribution of nodes is clearly observed in the top half of **Figure 4-7**. The orientation of the sample changes slightly across the image (bending) and the hexagonal pattern becomes distorted in the lower half of the image. This distortion could have been caused by sample preparation or the nature of the flexible organic linkers. The orthogonal direction shows a clear cubic arrangement of the nodes (**Figure 4-7**). Importantly, no electron density within the hexagonal channels is consistent with a distribution like **Figure 4-5a**.

However, further analysis is needed to pinpoint the exact location of the POM directly from the images.

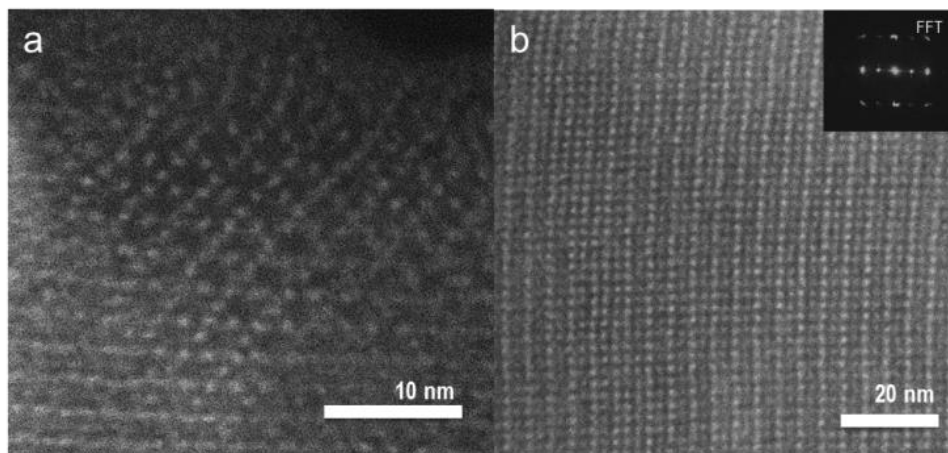


**Figure 4-7** STEM Z-contrast images of  $\text{PW}_{12}@NU-1000$  showing (a) a clear hexagonal arrangement of nodes for the c-axis projection and (b) a cubic arrangement of nodes in the a/b projection. These images are consistent with the structures observed in undoped NU-1000 and imply that the POM exists in regular locations relative to the nodes.

To further elucidate the location of the POM, difference envelope density (DED) analysis was employed. This technique generates a surface envelope between regions of high and low electron density which can be extracted from low order, intense, independent reflections in a high resolution PXRD pattern. Using differential analysis with a parent framework can yield a coarse map of electron density attributed to the incorporation of guest molecules.<sup>227,228</sup> DED analysis (**Figure 4-8**) of  $\text{PW}_{12}@NU-1000$  localizes the electron density in the small channels in the plane of the nodes, akin to **Figure 4-5c**. This orientation maximizes the hydrogen bonding interaction between the oxo groups on the POM and the hydroxyl groups on the nodes.

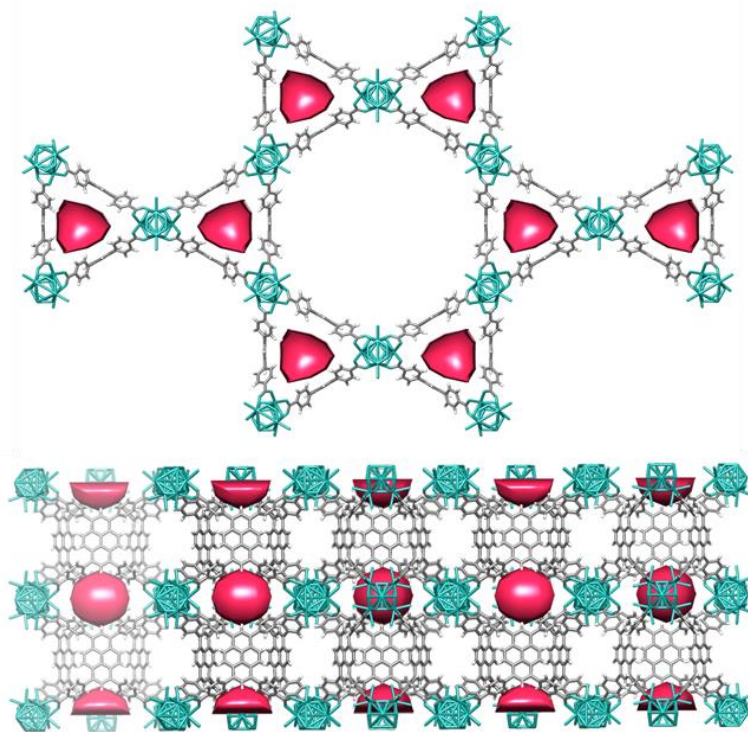


**Figure 4-8** Experimental ex-situ XRD data collected at 17-BM beamline, APS Room temperature, air atmosphere. Pink spheres represent electron density.

The Brunauer-Emmett-Teller (BET) surface area calculated from the  $N_2$  isotherm of  $PW_{12}@NU-1000$  significantly decreases from 2100 to 850  $m^2/g$  relative to bare NU-1000, which is consistent with POM incorporation in NU-1000. Volumetrically, however, they achieve similar BET surface areas (1020 to 850  $m^2/cm^3$  for NU-1000 and  $PW_{12}@NU-1000$  respectively) (**Figure 4-9**). The  $N_2$  isotherm of  $PW_{12}@NU-1000$  shows a type IV feature, similar to that of NU-1000 which is associated with the mesoporous channel, and is also present in the pore size distribution (**Figure 4-9**). The calculated average pore width indicates a decrease in the length of the large hexagonal pores from 31 Å to 25 Å compared to NU-1000, but not as significant decrease as if the POMs were located inside the hexagonal channels. This effect was also observed when smaller metal ions were deposited solvothermally in the windows between the channels of NU-1000.<sup>59,213,214</sup> More strikingly, the large decrease in the differential pore volume

of the micropores ( $3.8$  to  $1.0 \text{ cm}^3/\text{cm}^3$ ) further indicates that the POMs are located in the small channels.

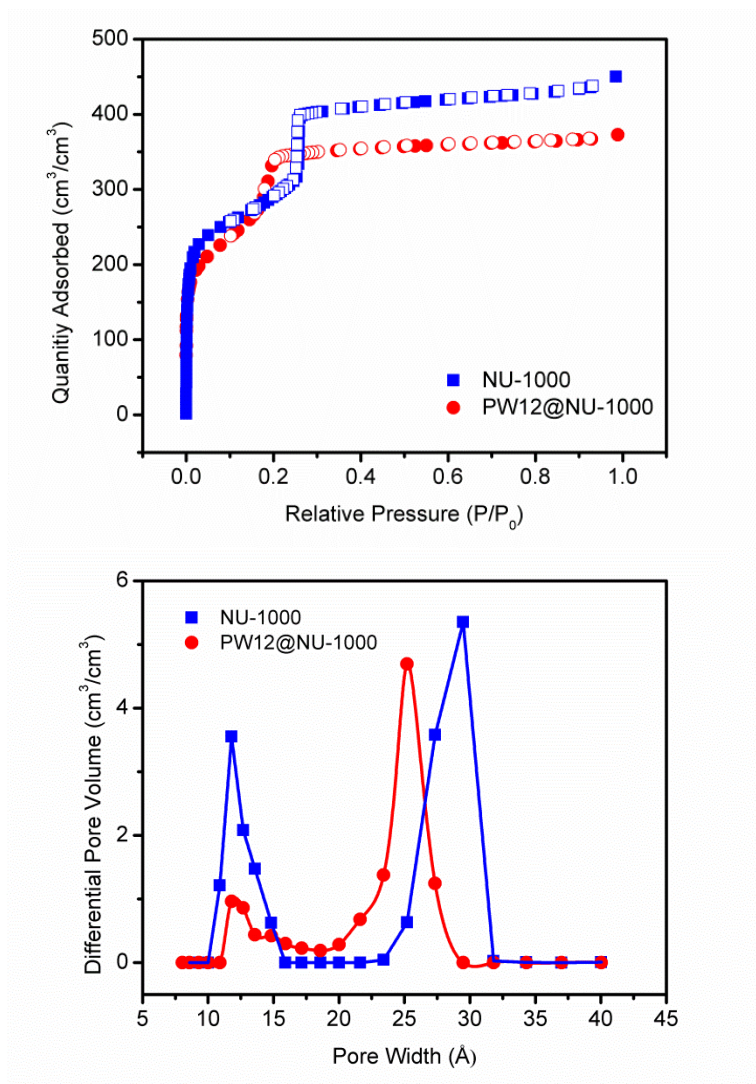


**Figure 4-9** Volumetric  $N_2$  isotherm (above) and pore size distribution (below) of NU-1000 and  $PW_{12}@NU-1000$

Thermal gravimetric analysis (TGA) shows a mass loss of 50 % for bare NU-1000 between 25 and 700  $^{\circ}\text{C}$  (**Figure 4-10**). The majority of this mass loss is due to the carbon decomposition at 500  $^{\circ}\text{C}$ . The TGA trace of the POM,  $H_3PW_{12}O_{40}$ , matches well with those reported in the literature,<sup>229</sup> losing 13 % of its initial mass due to water. The corresponding

PW<sub>12</sub>@NU-1000 loses 20 % of its initial mass, consistent with a greater percentage of inorganic composition compared to NU-1000 which is not lost below 700 °C. The two features seen in the TGA profile indicate physisorbed water loss from the POM below 100 °C and carbon decomposition from NU-1000 around 500 °C (**Figure 4-10**). The composite material is highly hygroscopic, corroborated by TGA-mass spectrometry (MS). Water makes up approximately 10 wt% of the as-synthesized PW<sub>12</sub>@NU-1000 mass prior to any catalytic studies.

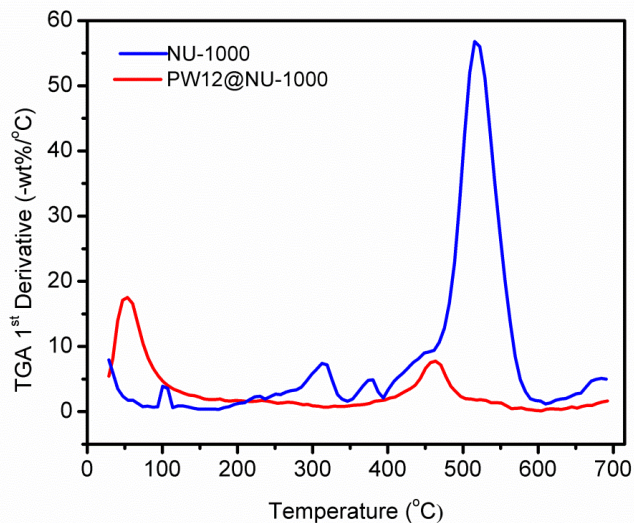
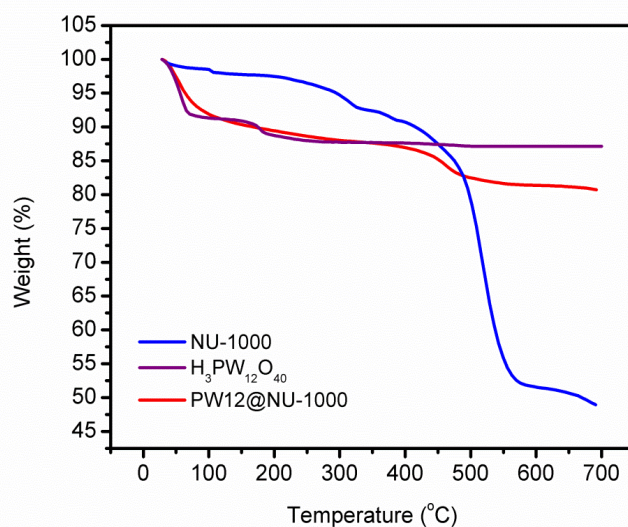
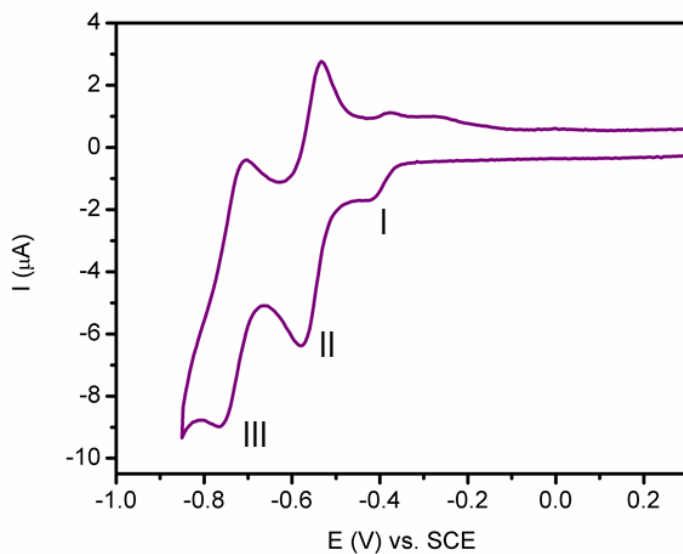


**Figure 4-10** TGA (above) showing weight loss of NU-1000,  $\text{H}_3\text{PW}_{12}\text{O}_{40}$  and  $\text{PW}_{12}@NU-1000$  from 25 °C to 700 °C and first derivative curve (below) for NU-1000 and  $\text{PW}_{12}@NU-1000$  over the same range

Cyclic voltammetry (CV) shows that the redox activity of the POM in the MOF is retained (**Figure 4-11** and **Figure 4-12**). The slight positive shift in formal reduction potentials could indicate that the POM interacts with the support.<sup>210,230</sup> Additionally, the solid state  $^{31}\text{P}$  magic angle spinning (MAS) NMR spectrum of  $\text{H}_3\text{PW}_{12}\text{O}_{40}$  has two resonances (**Figure 4-13**), ascribed to a well-crystallized anhydrous phase (-13.9 ppm) and an amorphous phase (-15.3 ppm).<sup>231</sup> A phosphoric acid impurity can be seen above 0 ppm. The  $^{31}\text{P}$  MAS NMR spectrum of the composite  $\text{PW}_{12}@NU-1000$  shows a slight downfield chemical shift and much broader signal compared to the POM alone. Based on the shape, the observed signal is likely the sum of three overlapping resonances (-13.3, -14.2, -15.9 ppm), which has been reported and caused by either different amounts of protons associated with each POM<sup>232,233</sup> or distortion of the POM when interacting with the support.<sup>234</sup> Diffuse reflectance infrared Fourier transform spectroscopy (DRIFTS) shows that both POM and MOF components are present in the composite material, as highlighted in the boxes in **Figure 4-14**. The features in the 750 to 1100  $\text{cm}^{-1}$  range correspond to W-O and P-O of the POM (893, 984, 1080  $\text{cm}^{-1}$ ), and the bands between 1300 and 1700  $\text{cm}^{-1}$  correspond to carboxylate stretches in NU-1000 (1420, 1520, 1610  $\text{cm}^{-1}$ ). The sharp O-H stretch at 3670  $\text{cm}^{-1}$  from the non-H bonded -OH and  $\text{H}_2\text{O}$  on the NU-1000 node is noticeably absent in the composite. The H-bonded  $\text{H}_2\text{O}$  and -OH peak<sup>212</sup> at 2551 and 2745  $\text{cm}^{-1}$  are also absent. Based on these observations, it is tempting to conclude that the non-hydrogen-bonded aqua and hydroxyl ligands are quantitatively displaced by the POM. Caution is called for, however, as the spectrum is complicated by the presence of physisorbed water; its broad resonance (from ~2500

to  $\sim 3700\text{ cm}^{-1}$ ) might obscure, or partially obscure, residual features at 3670, 2551 and 2745  $\text{cm}^{-1}$



1.

**Figure 4-11** Cyclic voltammogram of  $\text{H}_3\text{PW}_{12}\text{O}_{40}$  under  $\text{N}_2$  in pH 2.5  $\text{H}_2\text{SO}_4/\text{Na}_2\text{SO}_4$  0.5 M buffer solution at  $0.025\text{ Vs}^{-1}$  scan rate. Reductive events labeled.  $\text{W}^{\text{V/VI}}$  reduction events labeled. Formal reduction potentials are -335, -555 and -735 mV vs SCE. The fourth redox event was obscured by hydrogen evolution.

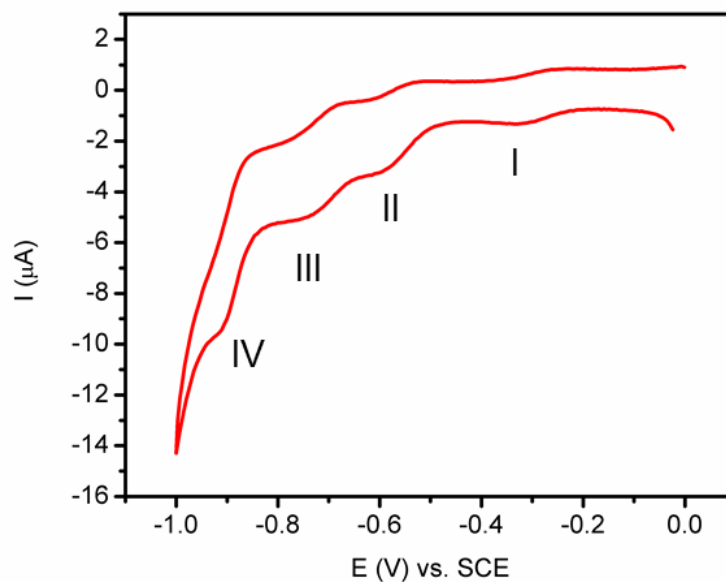


**Figure 4-12** Cyclic voltammogram of  $\text{PW}_{12}@NU-1000$  under  $\text{N}_2$  immobilized at a glassy carbon electrode in pH 2.5  $\text{H}_2\text{SO}_4/\text{Na}_2\text{SO}_4$  0.5 M buffer solution at  $0.025 \text{ V s}^{-1}$  scan rate. W-reduction events labeled. Formal reduction potentials are -300, -560, -715, and -890 mV vs SCE. Bare NU-1000 shows no reductive activity in this window.

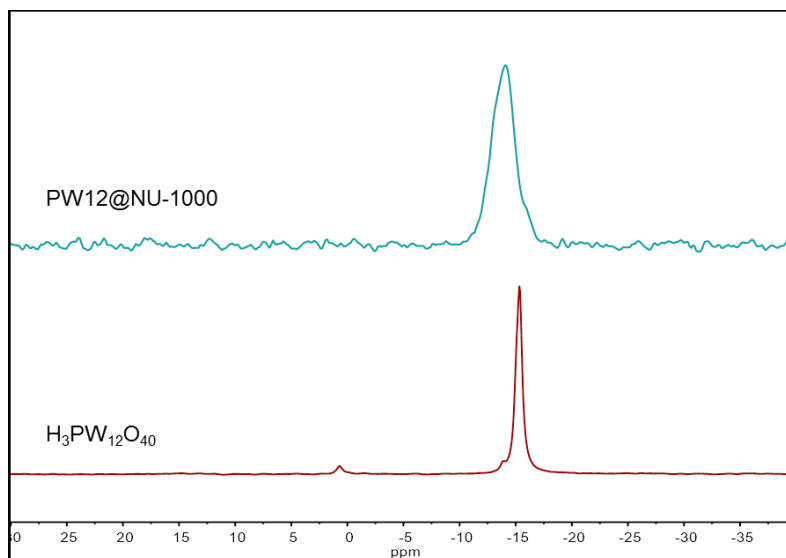


**Figure 4-13**  $^{31}\text{P}$  MAS NMR spectra of  $\text{H}_3\text{PW}_{12}\text{O}_{40}$  and  $\text{PW}_{12}@NU-1000$ . External reference: 0.8ppm  $\text{NH}_4\text{H}_2\text{PO}_4$

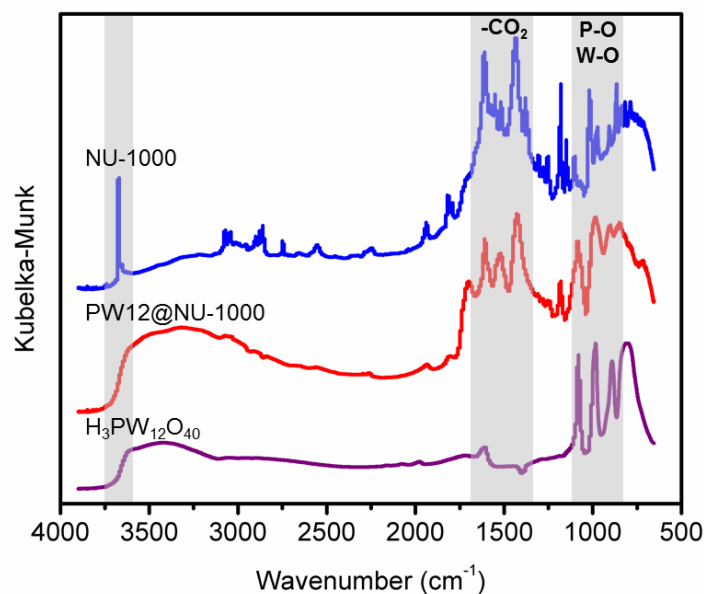


**Figure 4-14** DRIFTS spectra of the  $\text{H}_3\text{PW}_{12}\text{O}_{40}$ , NU-1000, and the  $\text{PW}_{12}@$ NU-1000. The non-hydrogen bonded O-H stretches, carboxylate stretches, and P-O/W-O stretches are highlighted.

To test the stability towards leaching,  $\text{PW}_{12}@$ NU-1000 was exposed to aqueous solutions of HCl at pH ranging from 2-7 (**Table 4-1**). Zr-based MOFs are known for their chemical stability (pH 1-11).<sup>235</sup> However, stability at higher pH was not investigated because of known decomposition of the POM in basic solutions.<sup>236</sup> After one week under near neutral conditions (pH 6), the material lost only 13 % of POMs by ICP-OES. At lower pH values less POM was lost, demonstrating that the POMs are not easily displaced by competing chloride ions.

**Table 4-1** Amount of leached POM in aqueous solutions at different pHs. Amount determined by ICP-OES, ppm was converted to percent of total POM

pH	3hrs		24hrs		7days	
2	0.212	1.2%	0.485	2.7%	0.948	5.3%
3	0.332	1.9%	0.921	5.1%	0.961	5.4%
4	0.495	2.8%	1.365	7.6%	1.73	9.7%
5	0.595	3.3%	1.49	8.3%	1.845	10.3%
6	0.648	3.6%	1.653	9.2%	2.363	13.2%
7	0.595	3.3%	1.287	7.2%	2.077	11.6%

### 4.3.2 Catalytic Measurements

POM@MOFs typically have reduced catalytic activity due to the blocking of pores and subsequent inhibition of substrate diffusion.<sup>97,211</sup> In order to determine if  $\text{PW}_{12}\text{@NU-1000}$  can overcome these limitations, the composite was tested for CEES oxidation (**Figure 2-1**). Activity of  $\text{H}_3\text{PW}_{12}\text{O}_{40}$  for the oxidation of sulfides in the presence of peroxide has been well documented.<sup>106,217,218</sup> Zirconia, with composition analogous to the  $\text{Zr}_6$  MOF nodes, also has the ability to oxidize sulfides in the presence of peroxides.<sup>220,221</sup> To compare the catalysts, the loadings were normalized to the amount of active clusters, including both the POM and the  $\text{Zr}_6$  nodes. In a typical run, the catalyst was suspended in 1 mL of acetonitrile (MeCN). CEES and hydrogen peroxide were added stepwise to the reaction vial, and the reaction was kept at 45 °C in a sand bath. Since NU-1000 has been reported to oxidize CEES in the presence of UV LED irradiation and  $\text{O}_2$ ,<sup>162</sup> the sand bath was necessary to block light and suppress any background reaction. Aliquots were taken at different time intervals, and analyzed via gas chromatography-flame ionization detector (GC-FID) or solution NMR. The average reaction profile is shown in **Figure 4-15**. The initial turnover frequencies (TOF) from the graph are  $3.1 \text{ min}^{-1}$  for NU-1000,  $9.3 \text{ min}^{-1}$  for  $\text{H}_3\text{PW}_{12}\text{O}_{40}$ , and  $10.4 \text{ min}^{-1}$  for  $\text{PW}_{12}\text{@NU-1000}$  (**Table 4-2** entries 4, 6, and 8).  $\text{H}_3\text{PW}_{12}\text{O}_{40}$  goes to full conversion after 90 minutes, while  $\text{PW}_{12}\text{@NU-1000}$  takes only 20 minutes under the same conditions. The experimental section has the TOF formula and a detailed procedure on calculating yield and conversion from NMR (**Figure 4-16**).

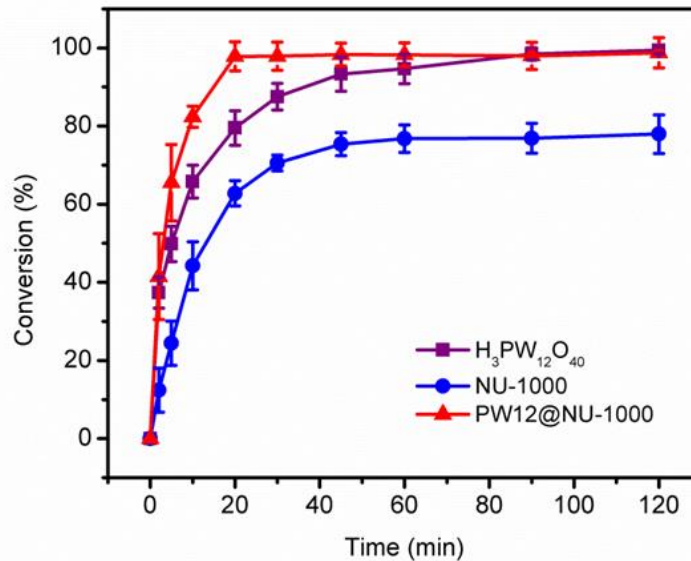


**Figure 4-15** Reaction profile of CEES oxidation for the H<sub>3</sub>PW<sub>12</sub>O<sub>40</sub>, NU-1000, and PW<sub>12</sub>@NU-1000 with standard deviation over three trials

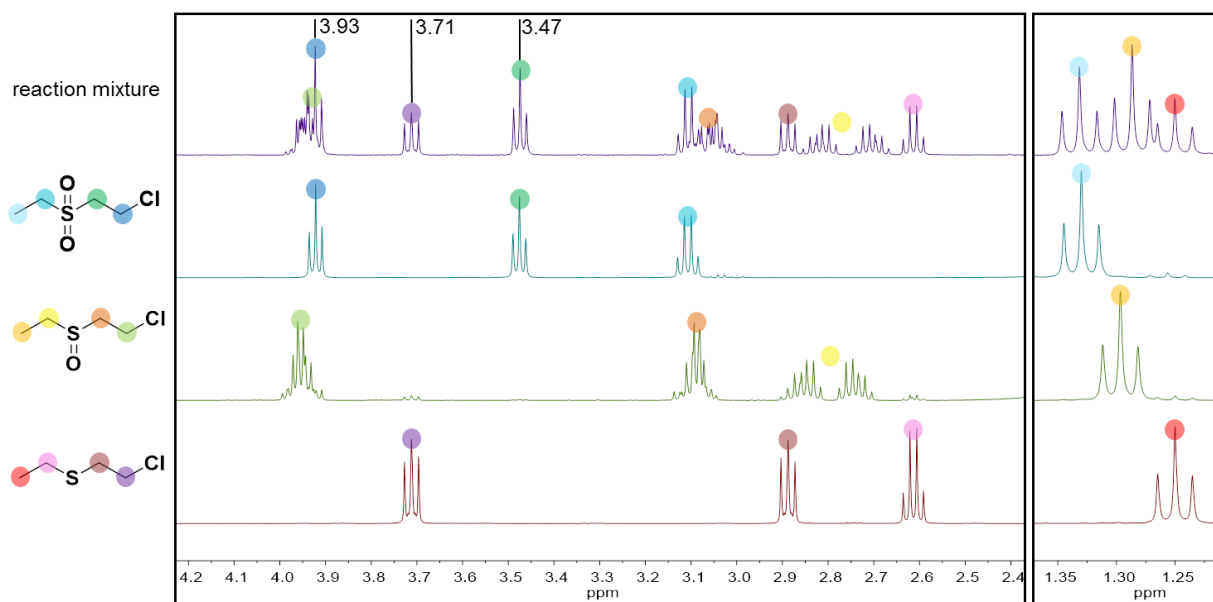


**Figure 4-16** Selected regions of the <sup>1</sup>H NMR spectra of CEES, CEESO, CEESO<sub>2</sub>, and a reaction mixture with all three compounds in CD<sub>3</sub>CN. The peaks used for calculation are labeled with chemical shift

**Table 4-2** shows yield and selectivity under different catalytic conditions. All trials with reported error were performed in at least triplicate. Background reactions without catalyst or peroxide, entries 1-3, showed minimal activity. The homogeneous  $\text{H}_3\text{PW}_{12}\text{O}_{40}$  showed selective partial oxidation of the sulfide to CEESO (entry 4). Even in the presence of excess peroxide (entry 5), CEESO is the only observed product. Bare NU-1000 showed preference to the doubly oxidized  $\text{CEESO}_2$  (entry 6). The MOF reaction was limited by the amount of peroxide, and in the presence of excess peroxide the reaction goes to completion with  $\text{CEESO}_2$  as the only product (entry 7).  $\text{PW}_{12}@$ NU-1000 showed faster initial rate and higher conversion than the POM or the MOF alone (entry 8). Since the amount of catalyst was normalized to the sum of the POM and  $\text{Zr}_6$  nodes, the enhanced activity can be attributed to the cooperative effect of the POM and the MOF node. The sulfoxide selectivity suggests that both POM and MOF are active in the catalysis because CEESO and  $\text{CEESO}_2$  are present in roughly equal amounts (entry 8).

**Table 4-2** Summary of catalytic data.

	Catalyst	Loading (mol%)	Temp. (°C)	Time (min)	Oxidant (eq)	Initial TOF ( $\text{min}^{-1}$ ) <sup>a</sup>	Yield (%)	Sulfoxide Selectivity (%)
1	none	--	45	180	1.5	--	5	--
2	$\text{H}_3\text{PW}_{12}\text{O}_{40}$	2	45	180	0	0.02 <sup>b</sup>	7	--
3	NU-1000	2	45	180	0	0.01 <sup>b</sup>	5	--
4	$\text{H}_3\text{PW}_{12}\text{O}_{40}$	2	45	90	1.5	9.3 <sup>d</sup>	98 (2)	100 (0)
5	$\text{H}_3\text{PW}_{12}\text{O}_{40}$	2	45	60	5	1.6 <sup>c</sup>	100 (0)	98 (2)
6	NU-1000	2	45	90	1.5	3.1 <sup>d</sup>	77 (4)	23 (1)
7	NU-1000	2	45	60	5	1.3 <sup>c</sup>	99 (1)	0 (0)
8	$\text{PW}_{12}@$ NU-1000	1.1	45	20	1.5	10.4 <sup>d</sup>	98 (2)	57 (1)

General: 1 mL MeCN, 10  $\mu\text{L}$  CEES, 5  $\mu\text{L}$  internal standard (1-bromo-3,5-difluorobenzene),  $\text{H}_2\text{O}_2$  as the oxidant. <sup>a</sup>TOF=moles product/(moles of total catalytic clusters  $\times$  amount of time) <sup>b</sup> time=180 min <sup>c</sup> time=30 min <sup>d</sup> time=2 min

To determine if the POMs are leaching out of the MOF during catalysis, the  $\text{PW}_{12}@$ NU-1000 reaction mixture was filtered at 2 min and the reaction progress was further monitored

(**Figure 4-17**). The conversion was approximately 10 % after 1 hour, which is only 5 % above the background reaction. This indicates that minimal POMs are leaching under these conditions, if at all. Solution phase NMR spectroscopy of the filtered reactions shows no phosphorous signal, reaffirming that the material does not leach. Upon recycling,  $\text{PW}_{12}@NU-1000$  was shown to be reusable. The retention of selectivity and reactivity upon recycling reaffirm that the material is stable under these catalytic conditions (**Figure 4-18**). Additionally, the PXRD, DRIFTS, and  $^{31}\text{P}$  MAS NMR spectroscopy results show that the integrity of the composite material remain unchanged (**Figure 4-19**, **Figure 4-20**, and **Figure 4-21**).<sup>48</sup><sup>48</sup><sup>21</sup><sup>103</sup><sup>103</sup><sup>103</sup><sup>103</sup> Interestingly, the three broad overlapping peaks observed in  $^{31}\text{P}$  MAS NMR spectrum prior to any catalysis become more distinct post-catalysis.

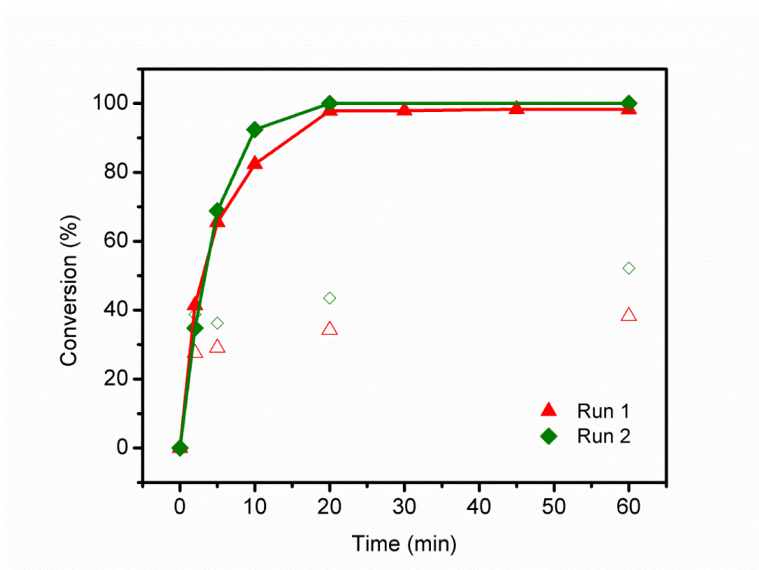


**Figure 4-17** Reaction profiles for  $\text{PW}_{12}@NU-1000$  for the first run and recycle. Open symbols indicate the reaction was filtered at 2 minutes.

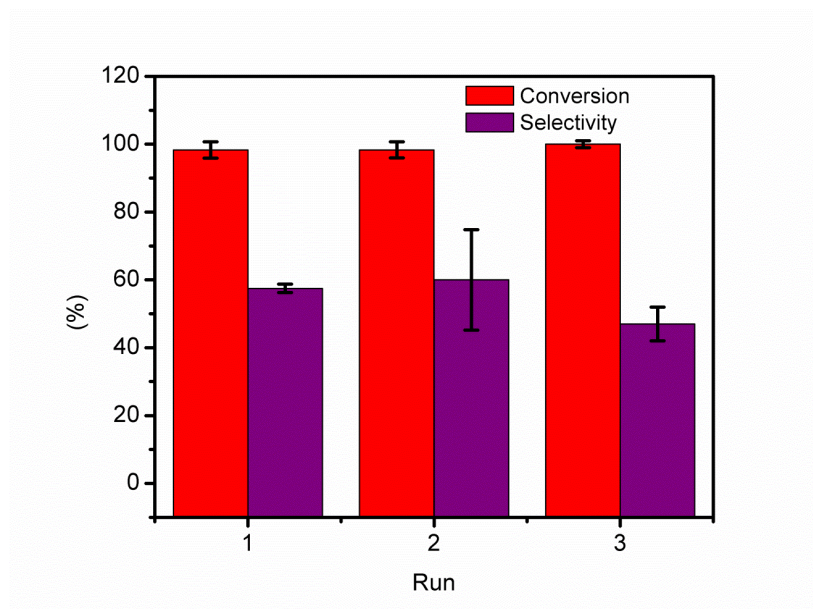


**Figure 4-18** Conversion and selectivity of  $PW_{12}@NU-1000$  at 60 min over the first run and 2 recycles. Error bars are standard deviation over at least 2 trials. Selectivity was determined by sulfoxide amount / total product.

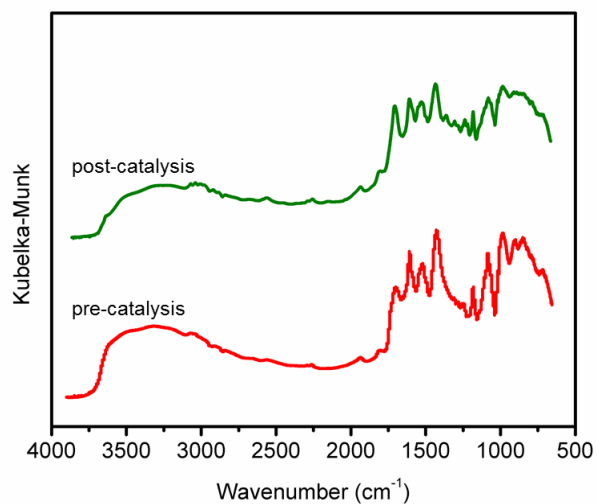


**Figure 4-19** DRIFTS of  $PW_{12}@NU-1000$  before and after catalysis

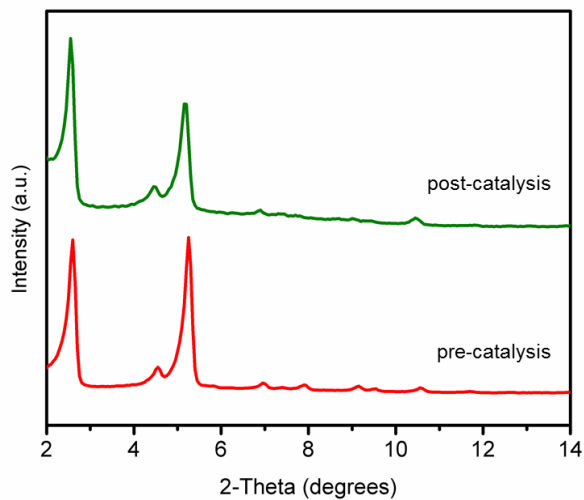


**Figure 4-20** PXRD patterns of  $\text{PW}_{12}@NU-1000$  before and after catalysis

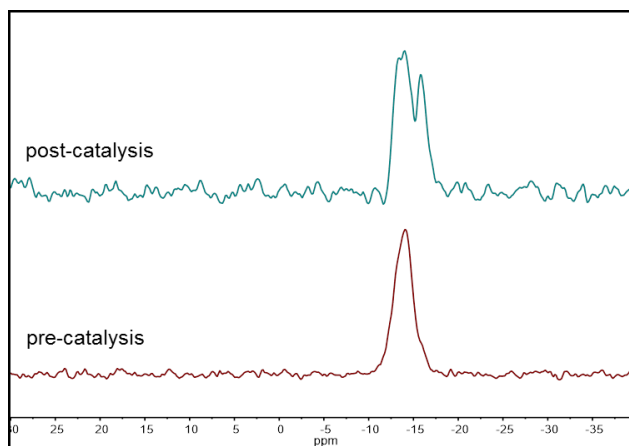


**Figure 4-21**  $^{31}\text{P}$  MAS NMR spectra of solid  $\text{PW}_{12}@NU-1000$  before and after catalysis

These catalytic studies indicate that active sites in the MOF are accessible after the installation of  $[\text{PW}_{12}\text{O}_{40}]^{3-}$ . Importantly, the selectivity of the composite material suggests that the MOF nodes are also active, meaning that they are not completely blocked by the POM. Having access to all potential catalytic sites is important in the development of a robust catalyst. This study has demonstrated that with careful selection of MOF, we can incorporate POMs while

maintaining accessibility and high surface area of the parent MOF. Future directions are aimed at improving composite selectivity by passivating the exposed Zr-node in NU-1000.

#### **4.4 Conclusions**

We have synthesized and fully characterized a POM@MOF material,  $\text{PW}_{12}$ @NU-1000. This composite achieves the highest POM/node loading for a POM@MOF synthesized via impregnation, while still maintaining high porosity.  $\text{PW}_{12}$ @NU-1000 has been shown to have enhanced catalytic activity for the oxidation of sulfide by hydrogen peroxide than either the POM or MOF under the same conditions. Future studies will explore other catalytically interesting POMs to be incorporated in NU-1000 and its family.

## **Chapter 5 . Thermally induced migration of a polyoxometalate within a metal–organic framework and its catalytic effects**

Portions of this chapter appear in the following manuscript:

Buru, C. T.; Platero-Prats, A.E; Chica, D. G.; Kanatzidis, M. G.; Chapman, K. W.; Farha, O.K. Thermally induced migration of a polyoxometalate within a metal–organic framework and its catalytic effects. *J. Mat. Chem.A* **2018**, *6*, 7389-7394.

## 5.1 Introduction

Active catalysts, ranging from single atoms<sup>237</sup> to molecular complexes<sup>238</sup> to large nanoparticles,<sup>239</sup> are often immobilized on heterogeneous supports in order to improve their reactivity by preventing aggregation and subsequent deactivation, while concurrently facilitating their separation from substrate and product allowing for reuse of the catalyst material.<sup>240–242</sup> Deposition on these supports is most commonly accomplished using electrostatic interactions, encapsulation, adsorption, precipitation, or covalent tethering.<sup>243–245</sup> Dependent on the nature of the support and catalyst, deposited species can adopt several positions and orientations. Precise knowledge and control over the three dimensional location of these active species on/in a support is essential for understanding the role of the support, as location can control reactivity and selectivity in some systems.<sup>246–248</sup>

Often sensitive to its environment and plagued with low surface area, polyoxometalates (POMs) are one such class of catalyst species that greatly benefit from being dispersion on solid supports.<sup>48,198,249</sup> POMs are highly soluble anionic metal oxide clusters composed of group V or VI transition metals, which can be partially substituted with virtually any element from the periodic table.<sup>29,30,32,192</sup> Their ability to undergo multielectron redox transformations allows for applications in redox catalysis.<sup>193</sup> Solid supports, including activated carbon,<sup>250,251</sup> mesoporous silica,<sup>49,199</sup> metal/metal oxide surfaces,<sup>252,253</sup> covalent-organic frameworks,<sup>55</sup> zeolites,<sup>52</sup> and metal-organic frameworks (MOFs),<sup>210,254</sup> have been used to stabilize POMs under catalytic conditions. The latter four benefit from crystalline structures, thereby permitting rapid structure determination of the POM/support composite. MOFs, composed of metal ion or metal oxide nodes connected by organic linkers,<sup>10,138</sup> are exceptional support materials as their tunability

gives rise to several desirable properties, such as crystallinity, permanent porosity, high surface area, large apertures, and high chemical and thermal stability.<sup>131</sup>

Targeted assembling strategies toward POM/MOF composites often use a “bottle around ship” approach<sup>13,203,255</sup> or ion exchange<sup>206,256</sup> to direct a catalyst to a desired location; however, these systems lack the ability to further modify the POM’s location postsynthetically. For example, MIL-101 has a hierarchical pore structure containing 29 Å and 34 Å pores connected via 12 Å or 16 × 15 Å apertures.<sup>9</sup> When Keggin-type POMs are incorporated into MIL-101 via impregnation, POMs are located in the larger mesopore only. On the other hand, when POM@MIL-101 is synthesized via encapsulation, the POMs are directed not only to the larger pores, but also to the smaller pores, which have apertures small enough to prevent the POM from leaching. The location of the POMs was found to have slight effects on the rates of reactions like acetaldehyde-phenol condensation and the acetalization of benzaldehyde.<sup>111,112</sup>

In hopes of synthesizing a more dynamic system, we recently reported the incorporation of the Keggin-type POM,  $[PW_{12}O_{40}]^{3-}$ , into the microporous channels of the **csq**-net MOF, NU-1000 (PW<sub>12</sub>@NU-1000, **Figure 5-1**).<sup>122</sup> In the report, the material was activated at 120 °C under vacuum prior to characterization, and the resulting material’s crystallinity resembled that of the parent NU-1000.<sup>119</sup> Slight differences between the MOF and POM@MOF powder X-ray diffraction (PXRD) patterns were analyzed using difference envelope density (DED) analyses, which concluded that the electron density corresponding to the POM guest lied within the 12 Å microporous channels of NU-1000 and not the 31 Å mesoporous channels. The hierarchical framework allowed substrate diffusion and enhanced sulfide oxidation relative to the POM or MOF alone, while the interactions between the framework and POM were stable to leaching.

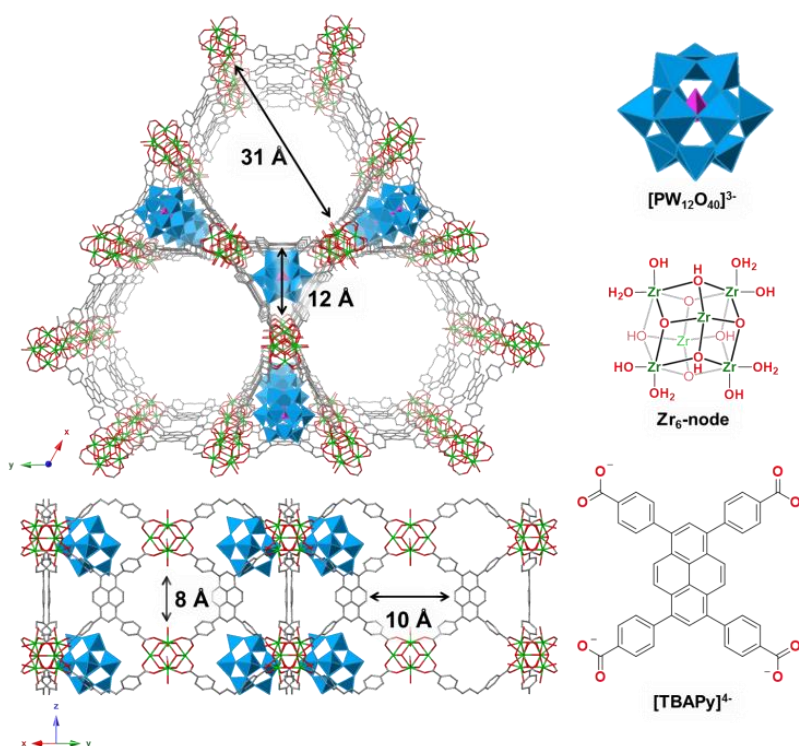


**Figure 5-1** Structural representations (left) of the  $\text{PW}_{12}@NU-1000$  previously published, also referred to as  $\text{PW}_{12}@NU-1000-120^\circ\text{C}$ . Structures of the corresponding POM  $[(\text{PW}_{12}\text{O}_{40})^{3-}]$ , MOF node  $[(\text{Zr}_6(\mu_3\text{-O})_4(\mu_3\text{-OH})_4(\text{H}_2\text{O})_4(\text{OH})_4)^{8+}]$ , and MOF linker  $[1,3,6,8\text{-tetrakis}(p\text{-benzoate})\text{pyrene}, (\text{TBAPy})^{4+}]$  given (right). Light blue prisms= $\text{WO}_5$ , pink prisms= $\text{PO}_4$ , green= $\text{Zr}$ , red= $\text{O}$ , gray= $\text{C}$ , hydrogen atoms omitted for clarity.

In the present work, we report the mild activation of  $\text{PW}_{12}@NU-1000$  and the movement of the incorporated POM during heat exposure. The influence of the POM location on catalytic rate and selectivity of the composite are also investigated. To our knowledge, this is the first system where the location of POMs within a MOF can be monitored and controlled postsynthetically.

## 5.2 Experimental Methods

### 5.2.1 Material Syntheses

**General** NU-1000 and  $PW_{12}@NU-1000-120^{\circ}C$  were synthesized according to previously published procedure.<sup>120,122</sup> Phosphotungstic acid hydrate was purchased from Sigma Aldrich, and TGA analysis indicated an average of 24 water molecules were associated with each POM. For NMR comparisons, 2-chloroethyl ethyl sulfoxide (CEESO) was synthesized from 2-chloroethyl ethyl sulfide (CEES) under using NU-1000 catalyst under UV-LED irradiation and 1 atm  $O_2$ .<sup>162</sup> The identity and purity were confirmed by GC-MS,  $^1H$  NMR, and  $^{13}C$  NMR spectroscopy. All other chemicals were used as received from Fisher Scientific or Sigma Aldrich. All gasses for activation and quantification were Ultra High Purity Grade 5.

**$PW_{12}@NU-1000-scCO_2$**  In a centrifuge tube,  $H_3PW_{12}O_{40}$  (130 mg, 0.04 mmol) was dissolved in 10 mL deionized water. To the solution, NU-1000 (50 mg, 0.023 mmol) was added and suspended by sonicating for about 1 minute. The suspension was shaken periodically. After 3 days, the solid was washed with water three times.

Then, the solid was washed with absolute ethanol, allowed to sit overnight in ethanol, and washed two more times with ethanol. The solid from the final wash was suspended in a minimum amount of ethanol and transferred to a glass dish fitted for the supercritical drier. The supercritical drying process used a Tousimis™ Samdri PVT-3D critical point drier in which liquid  $CO_2$  was used to exchange ethanol 4 times over 8 h. The material was then heated above  $31^{\circ}C$  ( $P = 73$  atm), the critical point of  $CO_2$  before the instrument was evacuated at a rate of 0.1 sccm.<sup>257–259</sup>

### 5.2.2 Physical Methods

$N_2$  adsorption and desorption isotherm measurements were performed on a Micromeritics Tristar II at 77 K. To calculate volumetric plots, the density of NU-1000 was reported to be  $0.486\text{ cm}^3/\text{g}$ <sup>119</sup> and  $PW_{12}@NU-1000-x$  were calculated to be  $1.00\text{ g}/\text{cm}^3$ . Inductively coupled

plasma optical emission spectroscopy (ICP-OES) samples of solids were analyzed with Thermo iCap7600 ICP-OES spectrometer, equipped with a CCD detector and Ar plasma covering 175-785 nm range. Powder X-ray diffraction (PXRD) patterns were collected on a Stoe STADI-MP instrument using  $K\alpha_1$  Cu radiation. Samples were scanned at 40 kV and 40 mA, a step size of  $2\theta = 0.015^\circ$ . For variable temperature measurements, the instrument was equipped with a furnace. The sample was loaded into a capillary, heated at a rate of  $20^\circ\text{C}/\text{min}$  to  $120^\circ\text{C}$ , and held at  $120^\circ\text{C}$  for 12 h, then cooled to room temperature. High resolution powder X-ray diffraction data were collected at beamline 17-BM at the Advanced Photon Source (APS) at Argonne National Laboratory (ANL). The incident X-ray wavelength was  $0.45336 \text{ \AA}$ . Data were collected using a Perkin Elmer flat panel area detector (XRD 1621 CN3/EHS) over the angular range  $0.5\text{-}9^\circ 2\theta$ . Samples were carefully ground and loaded into 1 mm diameter kapton capillaries. All measurements were performed at room temperature and ambient pressure. Lattice parameters and peak intensities were extracted from diffraction patterns via Le Bail whole pattern fitting<sup>222</sup> using Jana2006,<sup>223</sup> based on the reported structural model for NU-1000 (P6/mmm,  $a \sim 40 \text{ \AA}$ ,  $c \sim 17 \text{ \AA}$ ).<sup>119</sup> Lattice and pseudo-Voigt profile parameters were refined over a  $0.5\text{-}9^\circ 2\theta$  range. Structure envelopes were generated using the intensities of low index reflections.<sup>224</sup> Difference envelope densities (DEDs) were then obtained via subtraction of the envelope for pristine NU-1000 from the envelope for POM@NU-1000. Solution NMR spectra were collected on a 500 MHz Bruker Avance III system equipped with DCH CryoProbe or on a 400 MHz Agilent DD MR-400 system at IMSERC (Integrated Molecular Structure Education and Research Center) at Northwestern University. Solid-state NMR spectra were collected on a Varian 400 MHz VNMRS system. Scanning electron microscopy (SEM) images and energy dispersive spectroscopy (EDS) line scans were collected using a Hitachi SU8030 FE-SEM microscope at

Northwestern University's EPIC/NUANCE facility. All samples were coated with ~15 nm of OsO<sub>4</sub> or Au/Pd immediately prior to imaging. GC-FID measurements were carried out on an Agilent Technologies 7820A GC system equipped with an Agilent J&W GC HP-5 capillary column (30 m × 320 μm × 0.25 μm film thickness). All samples were filtered and diluted with dichloromethane prior to injection. Starting temperature: 70 °C, Hold: 0.5 min, Ramp: 30 °C/min, Time: 1 min, Ramp: 75 °C/min, End temperature: 250 °C. The disappearance of the reactant was calculated relative to a 0-minute time point. Thermogravimetric analyses (TGA) were performed on a Mettler Toledo STAR<sup>e</sup> TGA/DSC 1 under a N<sub>2</sub> flow at a 10 °C/min ramp rate from 25 to 700 °C. Cyclovoltammograms were recorded with a Solartron Analytical Modulab using a 1 MS/s potentiostat module. The working electrode was made of glassy carbon, the counter electrode was a platinum wire, and the reference electrode was a saturated calomel electrode (SCE). All electrolyte solutions were prepared with de-ionized water. A pH 2.5 H<sub>2</sub>SO<sub>4</sub>/Na<sub>2</sub>SO<sub>4</sub> buffer solution was prepared by mixing 0.5 M Na<sub>2</sub>SO<sub>4</sub> solution with H<sub>2</sub>SO<sub>4</sub>. The solution was deoxygenated with N<sub>2</sub> for 20 min prior to electrochemical measurements. To measure solid PW<sub>12</sub>@NU-1000-x, the powder was suspended in acetone and drop-casted onto the working electrode. The steady state emission spectra were measured on a Photon Technology International (PTI) QuantaMaster 400 fluorometer. The samples were excited at 380 nm and emission spectra were monitored between 400 nm to 700 nm. Diffuse reflectance spectra were collected on a Shimadzu UV-3600 PC double-beam, double-monochromator spectrophotometer in the range of 900 to 250 nm. BaSO<sub>4</sub> was taken as the 100% R baseline in the range measured. The powdered sample was firmly pressed on a bed of BaSO<sub>4</sub>. The reflectance data was converted to absorbance data using the Kubelka - Munk equation  $\alpha/S = (1 - R)^2 / 2R$

**Equation 5-1).**

$$\alpha/S = (1 - R)^2 / 2R$$

**Equation 5-1**

where R is reflectance,  $\alpha$  is the absorption coefficient, and S is the scattering coefficient.

### **5.2.3 Catalytic Measurements**

For 2-chloroethyl ethyl sulfide (CEES) oxidation experiments, the catalyst (1.7  $\mu\text{mol}$  of active site) was dispersed in 1 mL of acetonitrile in a 2-dram vial. For the POM and POM@MOF, the water weight was considered, so 1.7  $\mu\text{mol}$  active sites was equivalent to 3.7 mg NU-1000, 5.7 mg  $\text{H}_3\text{PW}_{12}\text{O}_{40}$ , and 4.7 mg  $\text{PW}_{12}@NU-1000\text{-scCO}_2$ . To ensure the same amount of material was used for  $\text{PW}_{12}@NU-1000-120^\circ\text{C}$ , 4.7 mg  $\text{PW}_{12}@NU-1000\text{-scCO}_2$  was heated in a 120  $^\circ\text{C}$  oven for 2 h prior to catalysis.

CEES (10  $\mu\text{L}$ , 85  $\mu\text{mol}$ ) and an internal standard (1-bromo-3,5-difluorobenzene, 5  $\mu\text{L}$ ) was added to the reaction vial. Then, hydrogen peroxide (30 wt% in water, 13  $\mu\text{L}$ , 1.5 eq) was added. The vial was placed in a sand bath, which was pre-heated to 45  $^\circ\text{C}$ . Aliquots, approximately 10  $\mu\text{L}$ , were withdrawn from the vials with a glass pipette, filtered, and diluted with dichloromethane for GC-FID or deuterated acetonitrile for NMR spectroscopy. GC-FID was used to monitor conversion and NMR spectroscopy was used to determine selectivity.

For leaching studies,  $\text{PW}_{12}@NU-1000\text{-scCO}_2$  was filtered out around 30 s (approximately 5 min in solvent total) and any remaining reaction was monitored.

## **5.3 Results and Discussion**

Both  $\text{PW}_{12}@NU-1000\text{-scCO}_2$  and  $\text{PW}_{12}@NU-1000-120^\circ\text{C}$  have a maximum loading of 0.8 POMs per  $\text{Zr}_6$  node by inductively coupled plasma optical emission spectroscopy (ICP-OES) measurements of the acidic piranha-digested materials. Scanning electron microscopy (SEM)

images indicate that the integrity and morphology of the crystallites are maintained during POM incorporation, and energy dispersive spectroscopy (EDS) line scans show a near uniform distribution of POM throughout the framework, except in the center of the crystal, where known defects occur (**Figure 5-2**).<sup>119,260</sup>

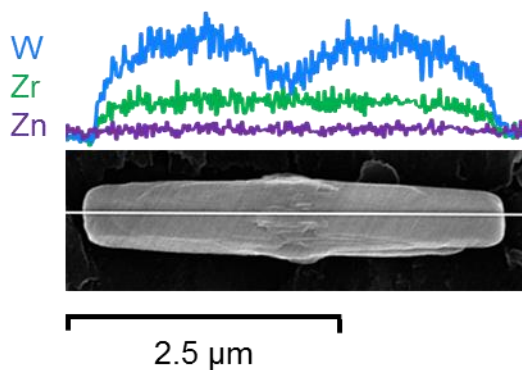


**Figure 5-2** SEM-EDS image and W, Zr, Zn line scans of  $\text{PW}_{12}@ \text{NU-1000-scCO}_2$ . Elemental distributions are identical to those found in  $\text{PW}_{12}@ \text{NU-1000-120}^\circ\text{C}$ .<sup>122</sup> Zn is shown as a baseline.

The powder X-ray diffraction (PXRD) pattern of  $\text{PW}_{12}@ \text{NU-1000-120}^\circ\text{C}$  resembles that of the parent NU-1000 (**Figure 5-3**). However, the PXRD pattern of  $\text{PW}_{12}@ \text{NU-1000-scCO}_2$  has peaks at similar d-spacing to  $\text{PW}_{12}@ \text{NU-1000-120}^\circ\text{C}$ , but very different intensities. Assuming no preferred orientation of MOF crystallites and retention of MOF structure, the peak intensities indicate major differences in guest location within the same unit cell. To understand the structural changes, in-situ variable temperature PXRD patterns were measured (**Figure 5-4**). The  $\text{PW}_{12}@ \text{NU-1000-scCO}_2$  sample was loaded into a rotating capillary and heated to and held at  $120^\circ\text{C}$ . The evolution of the  $\text{PW}_{12}@ \text{NU-1000-scCO}_2$  sample pattern to the  $\text{PW}_{12}@ \text{NU-1000-120}^\circ\text{C}$  pattern was observed. This change was not reversible; the material retained the  $\text{PW}_{12}@ \text{NU-1000-120}^\circ\text{C}$  PXRD pattern upon cooling to room temperature.

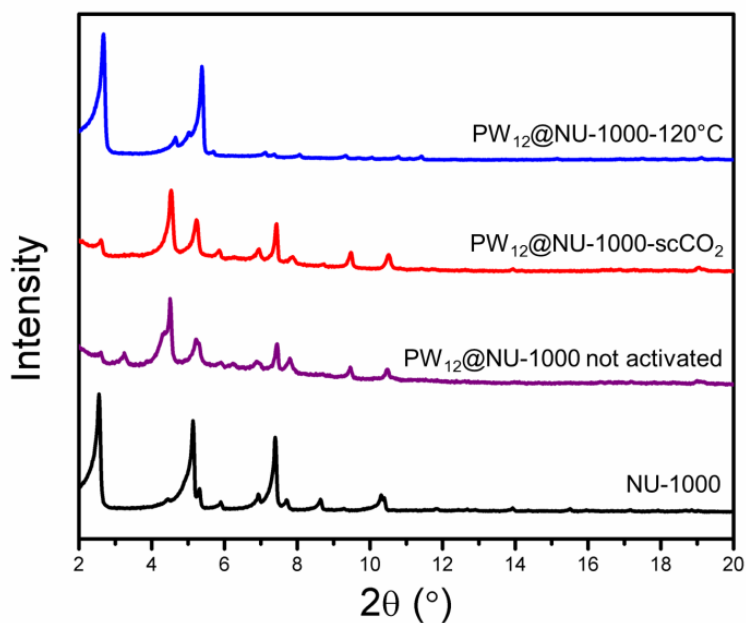


**Figure 5-3** PXR D patterns for NU-1000 and PW<sub>12</sub>@NU-1000 as-synthesized without solvent removal, activated by supercritical CO<sub>2</sub>, and activated at 120 °C.

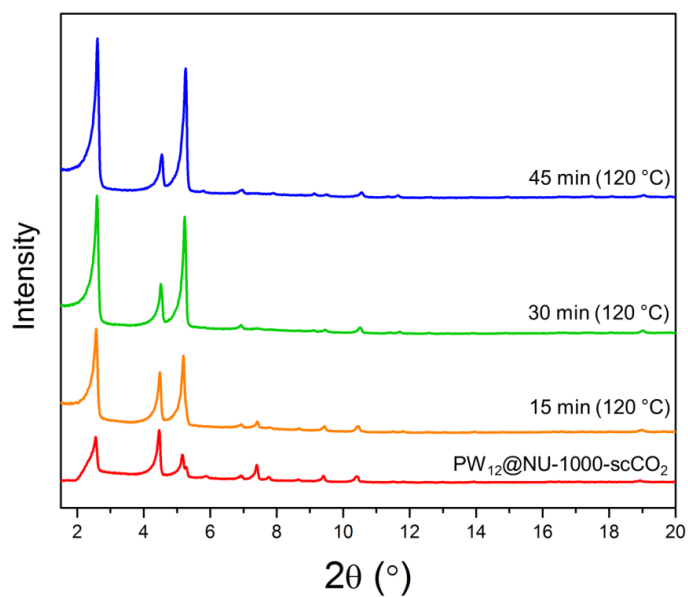


**Figure 5-4** Variable-temperature powder X-ray diffraction patterns for PW<sub>12</sub>@NU-1000-scCO<sub>2</sub> showing dynamic changes in peak intensities as the material is held at 120 °C

Inspired by the observed transformation in PXRD patterns, differential envelope density (DED) analyses were performed. DED analysis uses high intensity, low angle diffraction peaks generated by a synchrotron X-ray source to create an electron envelope. If the envelope of the parent material is known, its subtraction from the composite material results in a map of electron density corresponding to the guest molecules within a known structure.<sup>227,228</sup> By applying this technique to  $\text{PW}_{12}@NU-1000$  composites, the electron density corresponding to the POMs were located close to the c-pore, the  $8 \times 10 \text{ \AA}$  windows in Figure 1 which connect the large and small channels, and in the hexagonal mesoporous channels of  $\text{PW}_{12}@NU-1000\text{-scCO}_2$  (**Figure 5-5** and **Figure 5-6**), instead of residing in triangular microporous channels like in  $\text{PW}_{12}@NU-1000-120^\circ\text{C}$ .<sup>122</sup> In both cases, the POMs resided on the same plane as the MOF nodes. Of note, the electron density in Figure S3 has six equally spaced areas around the mesopore corresponding to the POM guests' locations. The POMs likely are disordered over different orientations centered at these six sites. Additionally, if each of these sites were 100% occupied, then the expected POM loading would be 2 POMs/node. Because ICP-OES measurements calculated only a 0.8 POM/node loading, the electron clouds represent approximately 40% POM occupancy (idealized in **Figure 5-5**).

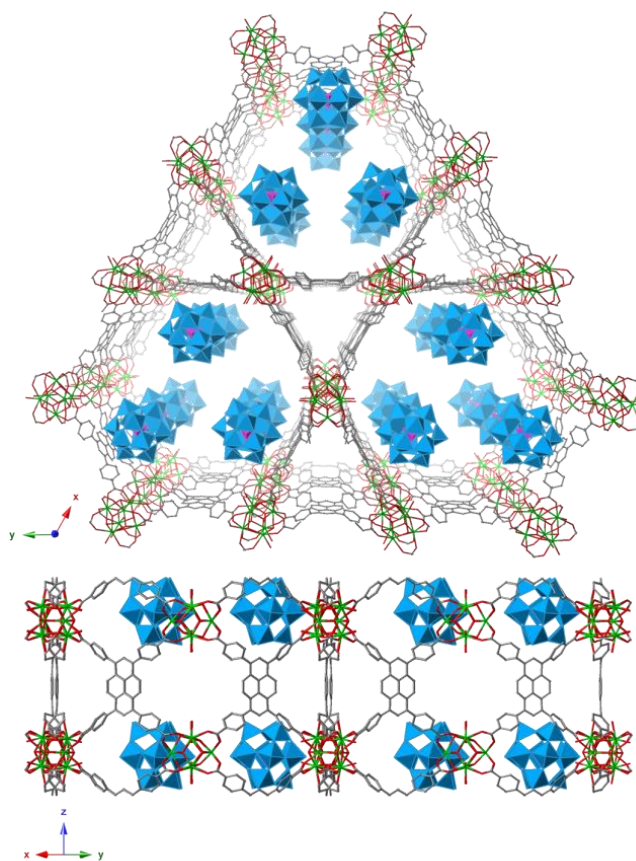


**Figure 5-5** Structural representation of one possible POM conformation in  $PW_{12}@NU-1000-scCO_2$  inferred by DED analysis. Light blue prism= $WO_5$ , pink prism= $PO_4$ , green= $Zr$ , red= $O$ , gray= $C$ , hydrogen atoms omitted for clarity.

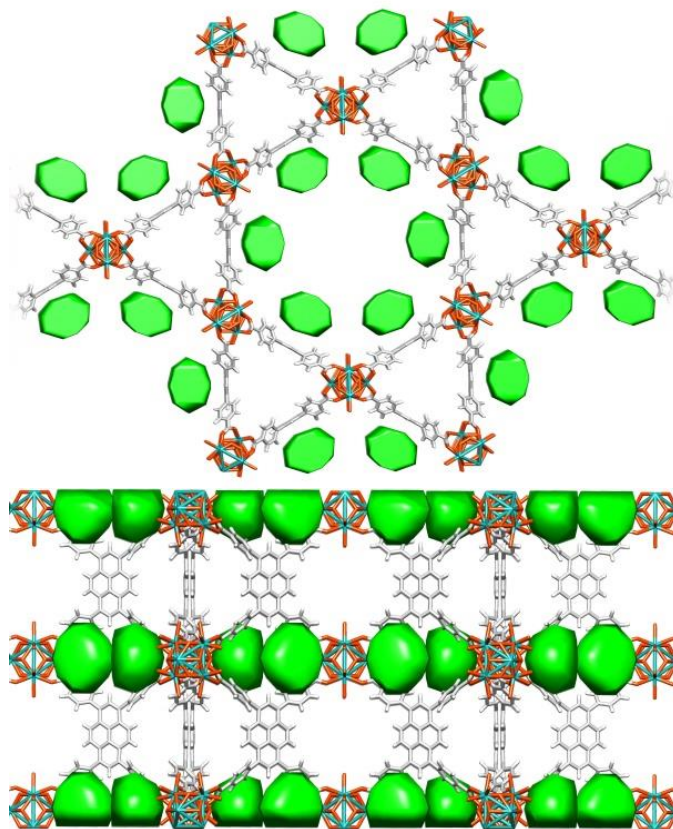


**Figure 5-6** Difference envelope density maps of  $\text{PW}_{12}@NU-1000\text{-scCO}_2$  derived from experimental ex-situ XRD data collected at 17-BM beamline, APS Room temperature, air atmosphere. Two views are shown: down the c-axis (left) and an orthogonal view (right). Green spheres represent electron density for  $[\text{PW}_{12}\text{O}_{40}]^{3-}$ . Teal=Zr, red=O, light gray=C, white=H, hydrogens on the nodes are not shown.

This location change manifests in other characterization techniques as well. Volumetric  $\text{N}_2$  sorption isotherms and density functional theory (DFT) pore size distributions (**Figure 5-7**) reveal that  $\text{PW}_{12}@NU-1000\text{-scCO}_2$  has a reduced mesopore volume, while  $\text{PW}_{12}@NU-1000-120^\circ\text{C}$  has reduced micropore volume. These observations are in agreement with partial occupation of the mesopores or micropores in the respective samples. The Brunauer-Emmett-Teller (BET) areas of these materials are 1020, 850, and 700  $\text{m}^2/\text{g}$  for NU-1000,  $\text{PW}_{12}@NU-1000-120^\circ\text{C}$ , and  $\text{PW}_{12}@NU-1000\text{-scCO}_2$ . The differences in surface area between the two POM@MOF samples are attributed to the additional 5 wt% water present in the supercritical

CO<sub>2</sub> activated sample, determined by TGA (**Figure 5-8**). In the PW<sub>12</sub>@NU-1000-scCO<sub>2</sub> sample, a small mass loss occurs around 170 °C, which has been observed with free H<sub>3</sub>PW<sub>12</sub>O<sub>40</sub>, could be assigned to the loss of water that is hydrogen bonded to the acidic protons of the POM.<sup>261</sup> Around the same temperature in the TGA-DSC, a slight exothermic change in the heat flow rate of PW<sub>12</sub>@NU-1000-scCO<sub>2</sub> could correlate to the POM movement from the mesopore to the micropore (Figure S4b). This exothermicity is consistent with POM positioned at an intrinsically favored binding site, possibly due to increased van der Waals interactions, as the POM is surrounded by only one pyrene linker in the mesopore and three pyrene linkers in the micropore. Interestingly, these interactions appear to be strong enough to immobilize the POM in the MOF, while also weak enough to allow POM movement.

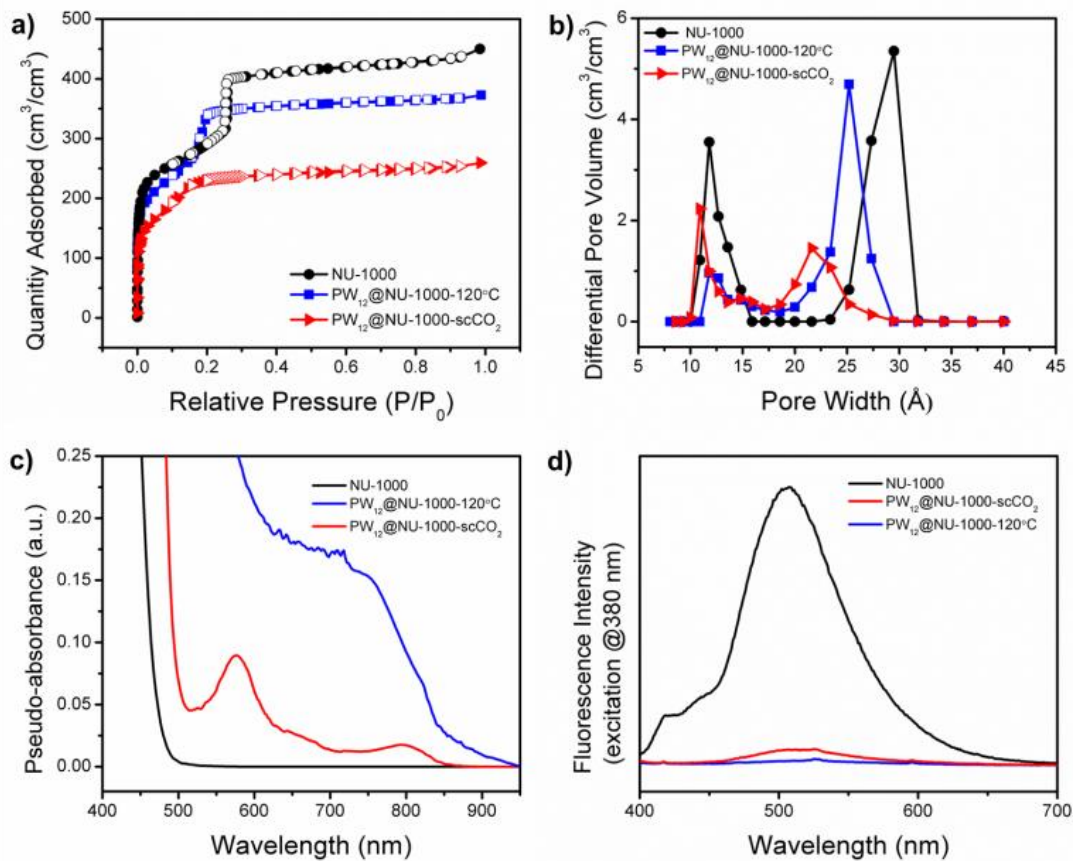


**Figure 5-7** a) Volumetric  $N_2$  isotherms collected at 77 K, b) DFT-calculated pore size distribution. c) Diffuse reflectance UV-vis spectra, and d) emission spectra at 380 nm excitation of NU-1000,  $PW_{12}@NU-1000-scCO_2$ , and  $PW_{12}@NU-1000-120^\circ C$ .

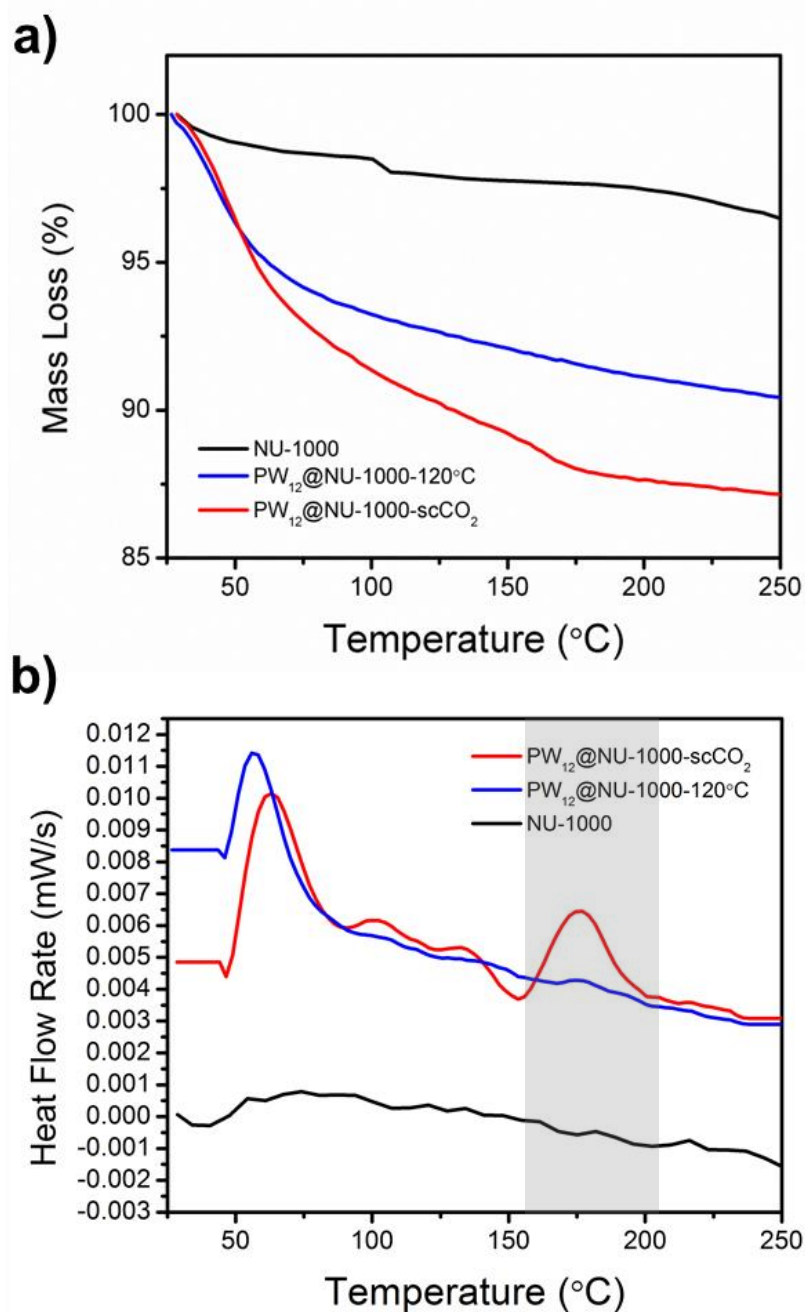


**Figure 5-8** a) Thermogravimetric analysis curve (20  $^{\circ}\text{C}$  /min) showing weight loss of NU-1000,  $\text{H}_3\text{PW}_{12}\text{O}_{40}$  and  $\text{PW}_{12}@NU-1000$  from 25  $^{\circ}\text{C}$  to 250  $^{\circ}\text{C}$  where water loss occurs and b) differential scanning calorimetry curves which were taken simultaneously. Difference in rate around 175  $^{\circ}\text{C}$  attributed to the movement of the POM from mesopores to micropores. The discrepancy in this transition temperature and the temperature in the in situ PXRD is attributed to the ramp temperature (120 to 175  $^{\circ}\text{C}$  takes less than 3 min).

Based on these observations, we believe the POMs sit in the mesopores close to the c-pore, when synthesized and remain there if no heat is applied (up to 80 °C). POM movement to the micropores is facilitated by elevated temperature coupled with partial removal of the POM's waters of hydration. Because of the consistent distribution of POM in the crystallite and its ability to change location in the absence of solvent, we propose that the POM migrates through the c-pore of NU-1000 to the more thermodynamically favorable micropore upon application of heat.

The different interactions of the POM and MOF as a function of location were also investigated spectroscopically. The  $^{31}\text{P}$  MAS NMR spectrum of  $\text{PW}_{12}@NU-1000\text{-scCO}_2$  is identical to free  $\text{H}_3\text{PW}_{12}\text{O}_{40}$  (**Figure 5-9**). The  $^{31}\text{P}$  signal shifts and become broader in  $\text{PW}_{12}@NU-1000-120^\circ\text{C}$ , indicating loss of symmetry around the phosphorous and suggesting a strong interaction between the POM and the support.<sup>262-264</sup> In the cyclic voltammograms, the reduction events shift to more positive potentials from  $\text{H}_3\text{PW}_{12}\text{O}_{40}$  to  $\text{PW}_{12}@NU-1000-120^\circ\text{C}$  to  $\text{PW}_{12}@NU-1000\text{-scCO}_2$  (**Figure 5-10** and **Table 5-1**), again indicating stronger interaction of the POM with the pyrene in  $\text{PW}_{12}@NU-1000\text{-scCO}_2$  since the composite is easier to reduce;<sup>210,230</sup> bare NU-1000 has no redox activity in the window scanned. Contrasting to the spectrum of bare NU-1000, a charge transfer band emerges in the diffuse reflectance UV-vis (DRUV-vis) spectra of both  $\text{PW}_{12}@NU-1000$  samples (**Figure 5-7c**). In confirming the charge transfer mechanism, by fluorescence emission spectroscopy,  $\text{PW}_{12}@NU-1000-120^\circ\text{C}$  and  $\text{PW}_{12}@NU-1000\text{-scCO}_2$  quenched the pyrene's fluorescence 95% and 99%, respectively, after excitation at 380 nm (**Figure 5-7d**). These data suggest an efficient electron transfer from the excited pyrene-based linkers to the POM similar to what was observed when nickel bis(dicarbollide) was installed in

NU-1000.<sup>265</sup> Of note, the evidence of interactions with the linker and the POM's position does not rule out potential interactions with the zirconia-like MOF nodes.<sup>252,266</sup>

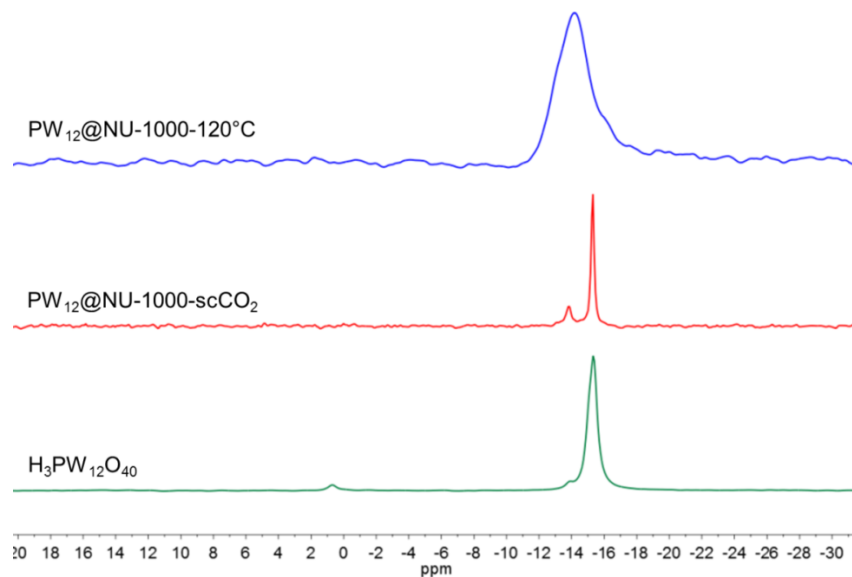


**Figure 5-9**  $^{31}\text{P}$  MAS NMR spectra of  $\text{H}_3\text{PW}_{12}\text{O}_{40}$  and  $\text{PW}_{12}@NU-1000-x$ . External reference: 0.8ppm  $\text{NH}_4\text{H}_2\text{PO}_4$

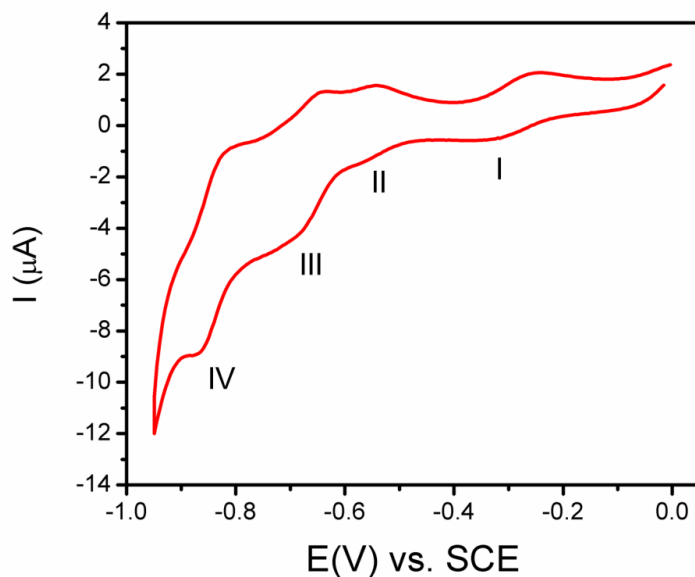


**Figure 5-10** Cyclic voltammogram of  $\text{PW}_{12}@NU-1000\text{-scCO}_2$  under  $\text{N}_2$  in pH 2.5  $\text{H}_2\text{SO}_4/\text{Na}_2\text{SO}_4$  0.5 M buffer solution at  $0.025 \text{ V s}^{-1}$  scan rate. Reductive events labeled.  $\text{W}^{\text{V/VI}}$  reduction events labeled.

**Table 5-1** Formal reduction potentials expressed in mV. The fourth redox event of the POM was obscured by hydrogen evolution.

$\text{H}_3\text{PW}_{12}\text{O}_{40}$		-735	-555	-335
$\text{PW}_{12}@NU-1000-120^\circ\text{C}$	-890	-715	-560	-300
$\text{PW}_{12}@NU-1000\text{-scCO}_2$	-840	-670	-555	-285

With the knowledge that different activation procedures site the POM in either the mesopores or micropores and affect the electronic structure, we attempted to determine if the location impacted a substrate's accessibility to the catalytic sites. As a model reaction, we chose to study the oxidation of 2-chloroethyl ethyl sulfide (CEES) to 2-chloroethyl ethyl sulfoxide (CEESO) and 2-chloroethyl ethyl sulfone (CEESO<sub>2</sub>) (**Figure 5-11a**). CEES is a simulant of the chemical warfare agent (CWA) mustard gas (HD or sulfur mustard), and one possible pathway

for detoxification of HD involves oxidation of the central thioether to a sulfoxide.<sup>267</sup> However, over-oxidation to the sulfone yields another toxic compound.<sup>20</sup> Therefore, selectivity is paramount when designing materials for HD detoxification via oxidation.

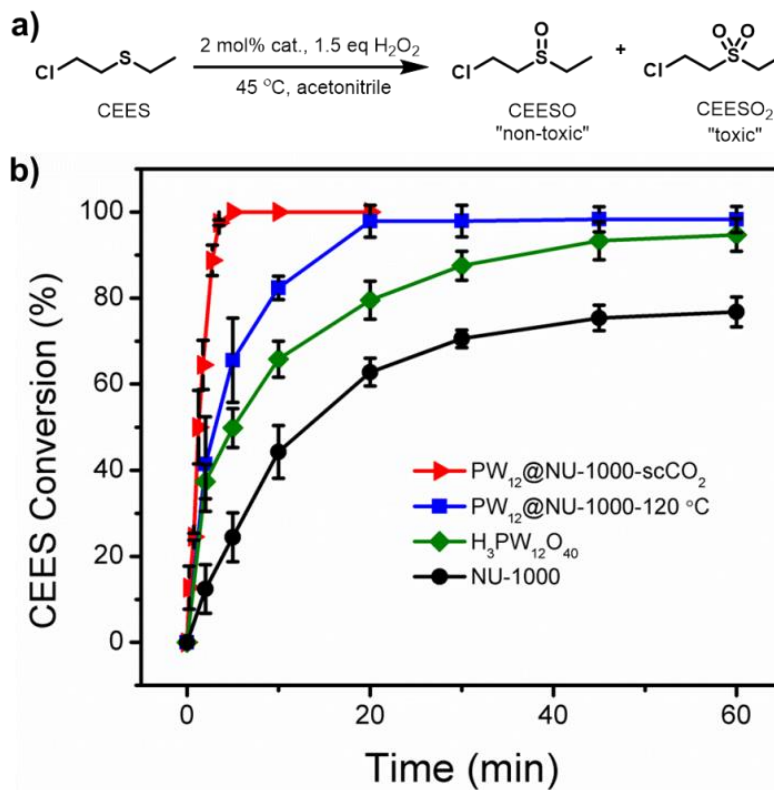


**Figure 5-11** a) Scheme of the reaction pathway for the oxidation of CEES to CEESO and CEESO<sub>2</sub> under the conditions presented in this work. b) Reaction profiles for the reaction in a) using the catalysts: NU-1000, H<sub>3</sub>PW<sub>12</sub>O<sub>40</sub>, PW<sub>12</sub>@NU-1000-120°C, and PW<sub>12</sub>@NU-1000-scCO<sub>2</sub>.

Our previous findings<sup>122</sup> showed that in a 45 °C acetonitrile solution using H<sub>2</sub>O<sub>2</sub> as an oxidant, NU-1000 nodes, with a structure similar to zirconia,<sup>220,221</sup> catalyzed the oxidation of CEES with a half-life (time to 50% conversion) of 13 min (**Figure 5-11b**) and preferred selectivity toward the doubly-oxidized product (**Figure 5-12**). Meanwhile under identical

conditions,  $\text{H}_3\text{PW}_{12}\text{O}_{40}$  was likewise active<sup>106,217,218</sup> with a half-life of 5 min and preferred selectivity for the singly-oxidized product. The composite  $\text{PW}_{12}@NU-1000-120^\circ\text{C}$ , normalized to the total number of active clusters (POMs and MOF nodes), decreased the half-life of the reaction to 3 min with an intermediate selectivity of  $59 \pm 7\%$ .  $\text{PW}_{12}@NU-1000-\text{scCO}_2$  further reduces the half-life of CEES conversion to 1 min with a greater selectivity ( $90 \pm 5\%$ ) for the preferred singly oxidized product. Because the initial rate of reaction using 2 mol% catalyst was too fast for time points with low conversion to be collected reliably, initial turnover frequencies (TOFs) were therefore determined using 1 mol% catalyst (**Figure 5-13**). The TOF of  $\text{PW}_{12}@NU-1000-\text{scCO}_2$  was found to be about 3 times higher than that of  $\text{PW}_{12}@NU-1000-120^\circ\text{C}$ .

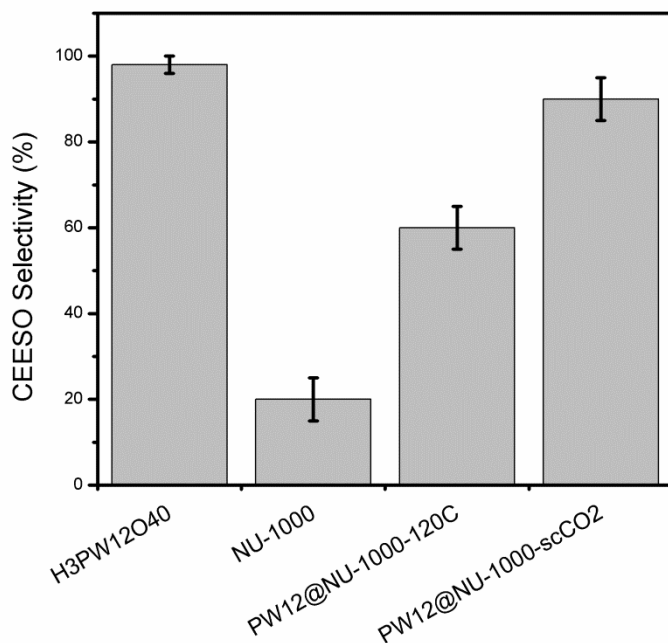


**Figure 5-12** Selectivities for CEESO of the catalysts for the reaction in **Figure 5-11a** measured at completion. \*When NU-1000 is exposed to enough (5 equivalents)  $\text{H}_2\text{O}_2$ , the reaction is 100% selective for  $\text{CEESO}_2$ .

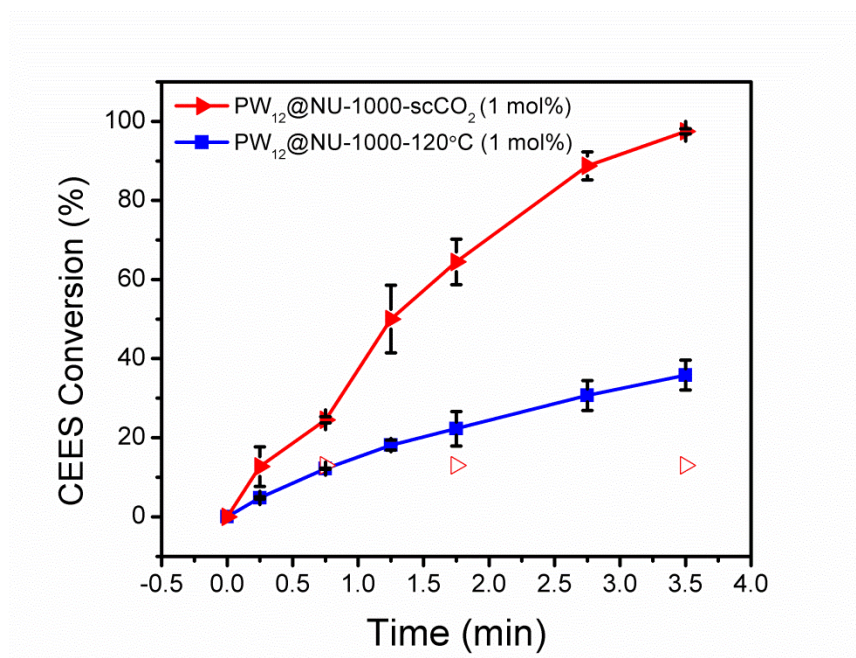


**Figure 5-13** Reaction profiles for the reaction in **Figure 5-11a** using only 1 mol% of active clusters with the catalysts PW<sub>12</sub>@NU-1000-120°C and PW<sub>12</sub>@NU-1000-scCO<sub>2</sub>. Open symbols indicate the reaction was filtered at approximately 30 s.

The difference in selectivity has been attributed to the different mechanisms which occur on the MOF node or the POM.<sup>200,220,268</sup> The intermediate selectivity when using PW<sub>12</sub>@NU-1000-120°C could indicate that both the POM and MOF are accessible. The micropores are blocked so access to the POM requires diffusion through the windows connecting the channels, which has been observed and calculated in other NU-1000-based systems.<sup>216,269</sup> When the POMs are situated in the mesopores, diffusion of the substrate to POM is no longer hindered; and therefore, the sulfide readily reacts with the POM to produce the singly-oxidized product almost exclusively. Since these reactions are normalized to the number of active clusters, the increased activities of the composites compared to the individual components alone are attributed to the stabilization of in the POM on the MOF. Leach tests confirm these reactions occur

heterogeneously (**Figure 5-13**) and post-catalysis PXRD patterns indicate the POMs do not move during catalysis (**Figure 5-14**).

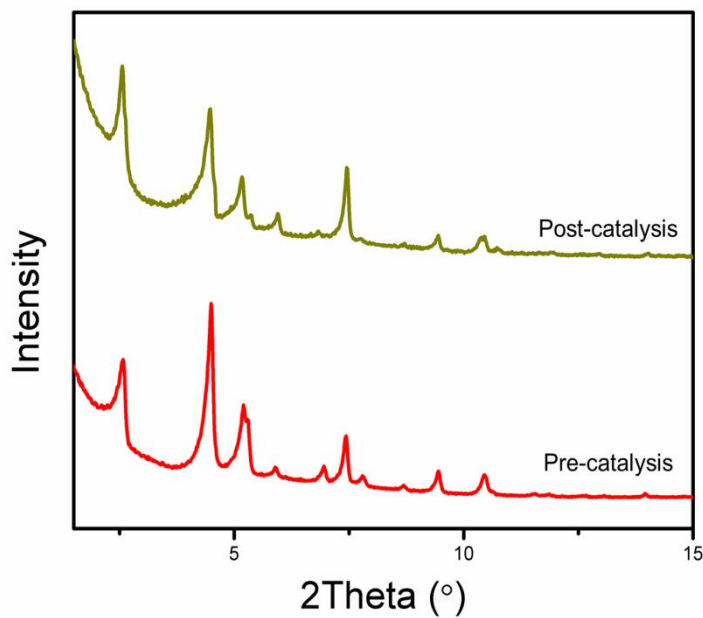


**Figure 5-14** PXRD patterns of  $\text{PW}_{12}@NU-1000\text{-scCO}_2$  before and after catalysis.

## 5.4 Conclusions

$\text{PW}_{12}@NU-1000$  has been synthesized by postsynthetic incorporation of  $[\text{PW}_{12}\text{O}_{40}]^{3-}$  in NU-1000. The composite material was activated by using supercritical  $\text{CO}_2$  and by 120 °C under vacuum. Differences in the diffraction patterns of these materials suggested that the POMs are located in the mesopores when supercritical  $\text{CO}_2$  is used to evacuate the pores of solvent molecules and migrate to the micropores when heated to 120 °C; these structural changes were corroborated by sorption and spectroscopic properties.  $\text{PW}_{12}@NU-1000\text{-scCO}_2$  displayed a faster rate of reaction and higher product selectivity in the partial oxidation of CEES, a mustard

gas simulant. To our knowledge, this is the first system where a POM catalyst can be monitored and controlled postsynthetically within a MOF. These findings highlight the importance of knowing and controlling catalyst location to engender favorable synergistic effects between a catalyst and support. Current efforts aim to identify other systems with similar control over catalyst location.

**Chapter 6 . Restricting polyoxometalate movement within metal–organic frameworks to assess the role of residual water in catalytic thioether oxidation using these dynamic composites**

Portions of this chapter appear in the following manuscript:

Buru, C. T.; Lyu, J.; Liu, J.; Farha, O.K. Restricting polyoxometalate movement within metal–organic frameworks to assess the role of residual water in catalytic thioether oxidation using these dynamic composites. *Front. Mater.* **2019**, *6*, 152.

## 6.1 Introduction

The active sites in catalysts are often sensitive to their surrounding environments. Consequently, active site engineering has been developed to allow the modulation of a catalyst environment to exploit or inhibit activity;<sup>270–274</sup> however, tuning of the solid support, as in single-site heterogeneous catalyst systems, is often difficult to achieve. For this reason, metal–organic frameworks (MOFs) with a high degree of tunability are attractive support materials.<sup>272,275–277</sup> Constructed from metal or metal cluster nodes linked via multitopic organic ligands, MOFs are an increasing popular class of designer materials due to the ability to obtain highly crystalline, porous, and stable structures.<sup>8,133,140,278–280</sup>

One ubiquitous class of materials which has benefitted from heterogenization and immobilization on solid supports is polyoxometalates (POMs).<sup>29,200,281</sup> POMs are isolated metal oxide clusters, whose tunable size, charge density, and acid strength allow for a wide range of applications, primarily in catalysis.<sup>32,43,282–284</sup> However, POMs suffer from low surface areas, high solubility in polar solvents, and limited stability in aqueous environments, making POMs difficult to exploit as reusable catalysts.<sup>285</sup> To increase surface area and impart some stability, POMs can be supported on porous heterogeneous materials, among which are metal–organic frameworks (MOFs).<sup>71,72,91</sup>

As support materials<sup>11</sup>, MOFs can interact with POMs and other guest molecules via chemical bonds, steric encapsulation within pores, or electrostatic interactions. With chemical bonding as found in polyoxometalate open frameworks, POMs serve as the nodes of the framework,<sup>201,286</sup> and consequently the active sites are blocked by the structural linkers. Steric trapping relies on a MOF whose pores can accommodate a POM, but whose apertures are much smaller than the POM thus preventing POM diffusion out of the MOF.<sup>210,211,287</sup> This aperture

dependence was investigated in a recent report.<sup>288</sup> Lastly, functionalities in MOFs can impart favorable electrostatic interactions.<sup>9</sup> For example, in Zr-based MOFs, the nodes have an affinity for oxyanions.<sup>118</sup> Without these weak interactions, the POM guests are able to freely diffuse in and out of the MOF, making a composite structure difficult to isolate and recycle.

NU-1000 is a Zr-based **csq**-net MOF comprised of mesoporous 31 Å hexagonal channels and microporous 12 Å triangular channels (**Figure 6-1**). We have recently reported the impregnation of NU-1000 with phosphotungstic acid ( $\text{H}_3\text{PW}_{12}\text{O}_{40}$ ) resulting in the composite material,  $\text{PW}_{12}@$ NU-1000, which was stable to leaching<sup>122,289,290</sup> due to favorable electrostatic interactions. When the material activated (removing the solvent guest molecules) using supercritical  $\text{CO}_2$  ( $\text{scCO}_2$ ) drying, the  $[\text{PW}_{12}\text{O}_{40}]^{3-}$  clusters were found in the easily accessible mesopore. Evidence of this location was observed in the pore-size distribution calculated using the  $\text{N}_2$  isotherm and confirmed via difference envelope density analysis, where the high intensity, low angle peaks of a powder X-ray diffraction (PXRD) pattern generated from a synchrotron X-ray source were used to create an electron envelope from with the known parent MOF was subtracted and the residual electron density mapped onto the parent MOF indicated the location of the guest molecules.<sup>227,228</sup> Upon heating the  $\text{scCO}_2$ -dried material, the  $[\text{PW}_{12}\text{O}_{40}]^{3-}$  clusters migrate from the mesoporous channel to the microporous channel, likely owing to the enhanced electrostatic and van der Waals interactions when cited in the micropore. The movement was also accompanied by the loss of water weight from thermogravimetric analysis (TGA). We proposed that this movement occurs because the POM can fit in the c-pores, the  $8 \times 10$  Å windows between the channels, since this transformation readily occurs in the absence of solvent. Different activations of these materials yielded different rates and selectivities in the oxidation of 2-chloroethyl ethyl sulfide (CEES), a mustard gas (bis(2-chloroethyl)sulfide)

simulant (**Figure 6-2**). Interestingly, due to mechanistic differences,<sup>220,291</sup> the homogeneous  $\text{H}_3\text{PW}_{12}\text{O}_{40}$  promoted the selective oxidation of CEES, while the MOF alone catalyzed the over-oxidation. This allowed for insight into which clusters were more accessible in the composite material through analysis of reaction selectivity.

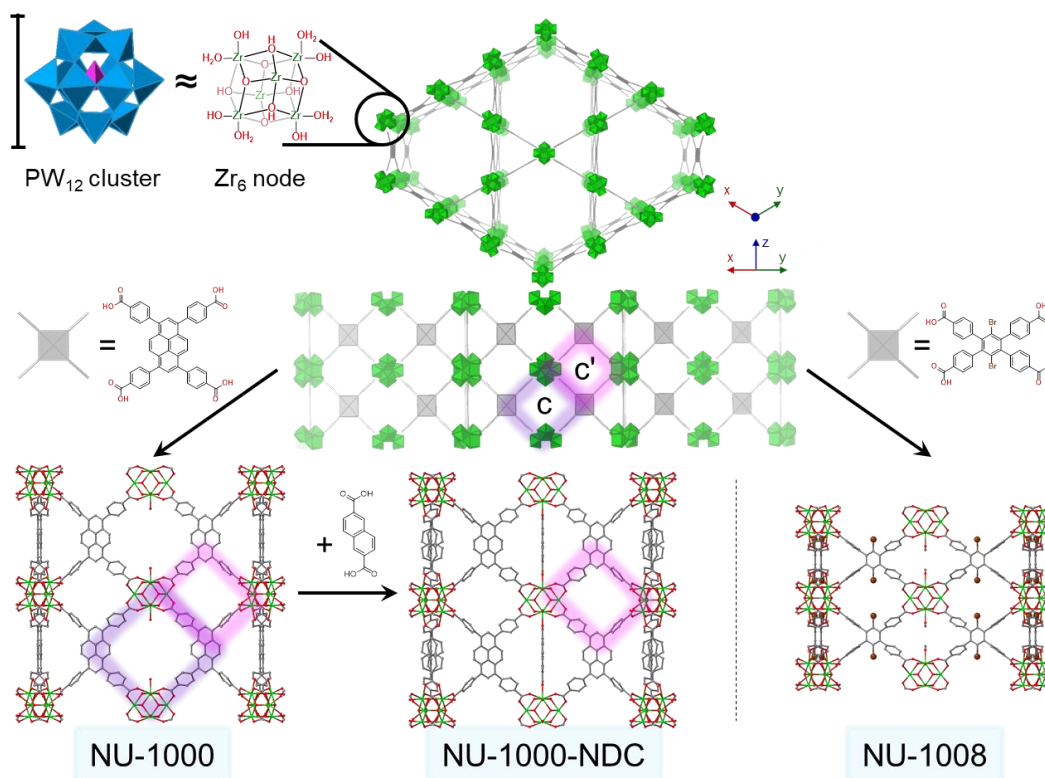


**Figure 6-1** Generic *csq* structure (top) viewed down the *c*-axis and an orthogonal view. Structures for zirconium node and size comparison to  $\text{PW}_{12}$  cluster (top left). Crystal structures and structural linkers of NU-1000 (lower left), NU-1000-NDC (lower center), and NU-1008 (lower right) viewed from the *ab* direction. The *c*- and *c'*- pores are highlighted in purple and pink, respectively. For clarity, hydrogens are omitted, and one possible conformation of NDC has been extracted. Green polyhedron =  $\text{Zr}_6$  node, blue polyhedron =  $\text{WO}_5$ , pink polyhedron =  $\text{PO}_4$ , green sphere = Zr, red = O, gray = C, brown = Br.



solution and sonicated for 1 min. The mixture was allowed to sit for 3 days, with occasional agitation. Then, the tube was centrifuged, and the solid material was washed with water ( $3 \times 10$  mL) and allowed to sit in dry ethanol overnight. The powder was rinsed with dry ethanol ( $3 \times 10$  mL) and suspended in a minimum amount of ethanol and kept in a minimal amount of ethanol.

***PW<sub>12</sub>@NU-1008.*** H<sub>3</sub>PW<sub>12</sub>O<sub>40</sub> (130 mg, 0.04 mmol) was dissolved in 10 mL deionized water in a centrifuge tube. NU-1008 (50 mg, 0.02 mmol) was added to the solution and sonicated for 1 min. The mixture was allowed to sit for 3 days, with occasional agitation. Then, the tube was centrifuged, and the solid material was washed with water ( $3 \times 10$  mL) and allowed to sit in dry ethanol overnight. The powder was rinsed with dry ethanol ( $3 \times 10$  mL) and kept in a minimal amount of ethanol.

***ScCO<sub>2</sub> Drying.*** PW<sub>12</sub>@MOF suspended in a minimal amount of absolute ethanol was placed in a glass dish and loaded into the critical point drier. Liquid CO<sub>2</sub> was used to exchange ethanol 4 times over 8 h. The material was then heated above 31 °C (P = 73 atm), the critical point of CO<sub>2</sub> before the instrument was evacuated at a rate of 0.1 sccm<sup>257–259</sup>. The powder was transferred to a sorption tube, where the material was kept at room temperature under dynamic vacuum for at least 1 hour prior to subsequent characterization.

***120 °C Heating.*** PW<sub>12</sub>@MOF-scCO<sub>2</sub> (approximately ½ of the batch) was heated in a 120 °C oven for 2-12 hours. The supercritically dried materials can also be heated under dynamic vacuum to afford the same result.

### ***6.2.2 Physical Methods***

Supercritical CO<sub>2</sub> drying was done on a Tousimis™ Samdri PVT-3D critical point drier. Inductively coupled plasma optical emission spectroscopy (ICP-OES) samples of solids were prepared in a 2-5 mL Biotage microwave vial by dissolving 1-2 mg of composite in 1 mL HNO<sub>3</sub>.

The vial was cringe-capped and heated to 150 °C for 15 min in a microwave reactor. H<sub>2</sub>O<sub>2</sub> (0.1 mL, 30 wt%) was added and the solution was heated in a sand bath at 110 °C for 1 hours. If the solution was still colored, 0.1 mL increments of H<sub>2</sub>O<sub>2</sub> were added until the solution became colorless. The resulting solutions were diluted to 10 mL with deionized water and analyzed with Thermo iCap7600 ICP-OES spectrometer, equipped with a CCD detector and Ar plasma covering 175-785 nm range. Powder X-ray diffraction (PXRD) patterns were collected on a STOE STADI P instrument using a CuK $\alpha$ 1 source. Variable temperature PXRD patterns were taken on a STOE STADI MP instrument using a MoK $\alpha$ 1 source. The VT samples were loaded into a capillary and flame sealed. Solution NMR spectra were collected on a 500 MHz Bruker Avance III system equipped with DCH CryoProbe or on a 400 MHz Bruker Avance III HD Nanobay system at IMSERC (Integrated Molecular Structure Education and Research Center) at Northwestern University. Scanning electron microscopy (SEM) images and energy dispersive spectroscopy (EDS) line scans were collected using a Hitachi SU8030 FE-SEM microscope at Northwestern University's EPIC/NUANCE facility. All samples were coated with ~15 nm of OsO<sub>4</sub> or Au/Pd immediately prior to imaging. GC-FID measurements were carried out on an Agilent Technologies 7820A GC system equipped with an Agilent J&W GC HP-5 capillary column (30 m  $\times$  320  $\mu$ m  $\times$  0.25  $\mu$ m film thickness). All samples were filtered and diluted with dichloromethane prior to injection. Starting temperature: 70 °C, Hold: 0.5 min, Ramp: 30 °C/min, Time: 1 min, Ramp: 75 °C/min, End temperature: 250 °C. The disappearance of the reactant was calculated relative to a 0-minute time point. Thermogravimetric analyses (TGA) were performed on a Mettler Toledo STAR<sup>e</sup> TGA/DSC 1 under a N<sub>2</sub> or air flow at a 10 °C/min ramp rate from 25 to 700 to 25 °C. All MOF samples were evacuated under high vacuum on a Micromeritics Smart VacPrep instrument. N<sub>2</sub> adsorption and desorption isotherm measurements

were performed on a Micromeritics Tristar II at 77 K. To calculate volumetric plots, the density of NU-1000-NDC was reported to be 0.533 g/cm<sup>3</sup> and PW<sub>12</sub>@NU-1000-NDC was calculated to be 1.01 g/cm<sup>3</sup>; the density of NU-1008 was reported to be 0.675 g/cm<sup>3</sup> and PW<sub>12</sub>@NU-1008 was calculated to be 1.36 g/cm<sup>3</sup>.

### 6.2.3 Catalytic Measurements

Since both the MOF node and the POM are active for catalysis, the catalyst loadings were 1 mol% by active clusters (0.86 μmol). This normalized the loadings so that the number of clusters (node or POM) remained constant for comparison.

The catalyst was weighed out in a 2 dram vial, and 1 mL acetonitrile was added. The mixture was sonicated for 1 min. Then, CEES (10 μL, 85 μmol) and an internal standard (1-bromo-3,5-difluorobenzene, 5 μL) was added to the reaction vial. For GC quantification, the zero time point was taken. Then, hydrogen peroxide (30 wt% in water, 13 μL, 1.5 eq) was added. The vial was placed in a sand bath, which was pre-heated to 45 °C. Aliquots, approximately 10 μL, were taken, filtered, and diluted with dichloromethane for GC-FID.

## 6.3 Results and Discussion

NU-1000-NDC and NU-1008 were selected for this study to investigate whether the [PW<sub>12</sub>O<sub>40</sub>]<sup>3-</sup> moves through the c- and c'-pores (**Figure 6-1**) as previously proposed. In NU-1000-NDC, 2,6-naphthalene dicarboxylate (NDC) bridges two nodes in the c-pore, effectively reducing the size of that aperture.<sup>292</sup> Both the c- and c'-pore diameters in NU-1008 are reduced in size compared to those in NU-1000-NDC.<sup>293,294</sup> If the mechanism involved complete

desorption from the mesopore and re-adsorption into the microporous channel of the POM, the size and accessibility to the  $c/c'$ -pores would have negligible effect on POM movement.

$PW_{12}@NU-1000-NDC$  and  $PW_{12}@NU-1008$  were prepared in a similar manner to  $PW_{12}@NU-1000$ .<sup>122</sup> Briefly, the MOFs were soaked in an aqueous  $H_3PW_{12}O_{40}$  solution for 3 days, followed by rigorous washing with water and ethanol. After soaking in ethanol overnight, the composites were subjected to supercritical  $CO_2$  drying. Half the material was then heated to  $120\text{ }^\circ\text{C}$  for at least 2 hours and designated  $PW_{12}@NU-1008-120\text{ }^\circ\text{C}$  and  $PW_{12}@NU-1000-NDC-120\text{ }^\circ\text{C}$ , while the other half was used “as-is” for subsequent characterization and designated  $PW_{12}@NU-1008-scCO_2$  and  $PW_{12}@NU-1000-NDC-scCO_2$ .

Inductively coupled plasma optical emission spectroscopy (ICP-OES) analyses of the digested MOFs show that  $[PW_{12}O_{40}]^{3-}$  does not leach during heating. The loadings were found to be 0.7  $PW_{12}/Zr_6$  node for NU-1000-NDC and 0.8  $PW_{12}/Zr_6$  node in NU-1008. Scanning electron microscopy (SEM) images reveal that the size and shape of the MOF crystallites remains the same before and after POM loading (**Figure 6-3** and **Figure 6-4**). Energy dispersive X-ray spectroscopy (EDS) line scans display that the POM distribution in the MOF is homogeneous throughout the crystallites.

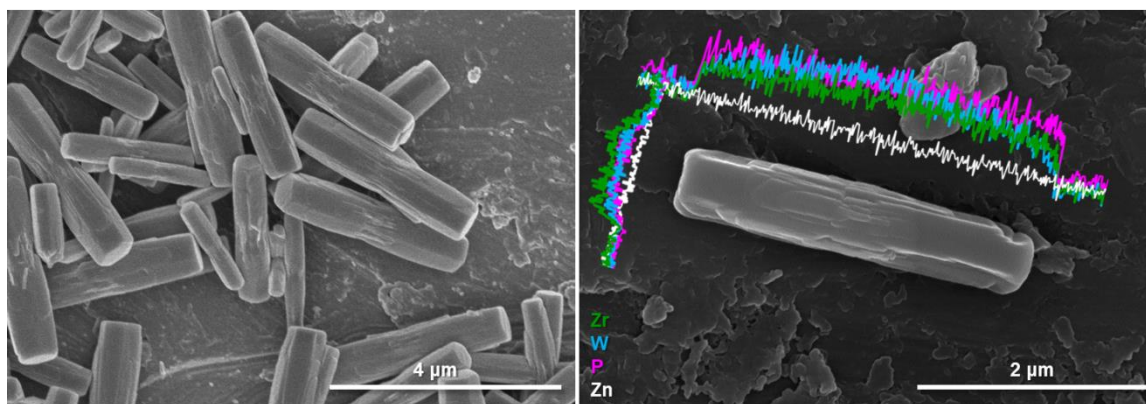


**Figure 6-3** SEM-EDX images of NU-1000-NDC before (left) and after (right) PTA loading.

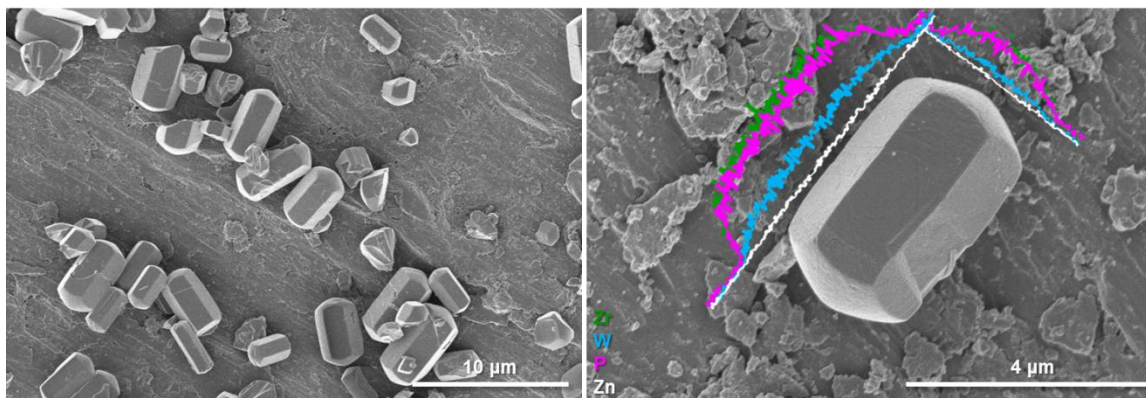


**Figure 6-4** SEM-EDX images of NU-1008 before (left) and after (right) PTA loading.

From the TGA traces (**Figure 6-5**) of the materials under nitrogen, both  $\text{scCO}_2$ -activated MOFs lost approximately 5 wt% more than the 120 °C-activated counterparts at 250 °C. This initial loss has been attributed to residual water physisorbed to the POM species, which remain after removal of solvent. Once heated to 120 °C, the elevated temperature activation step removes the physisorbed water which was difficult to remove from the POM after  $\text{scCO}_2$ -drying alone. These residual waters were factored into catalyst loading calculations.

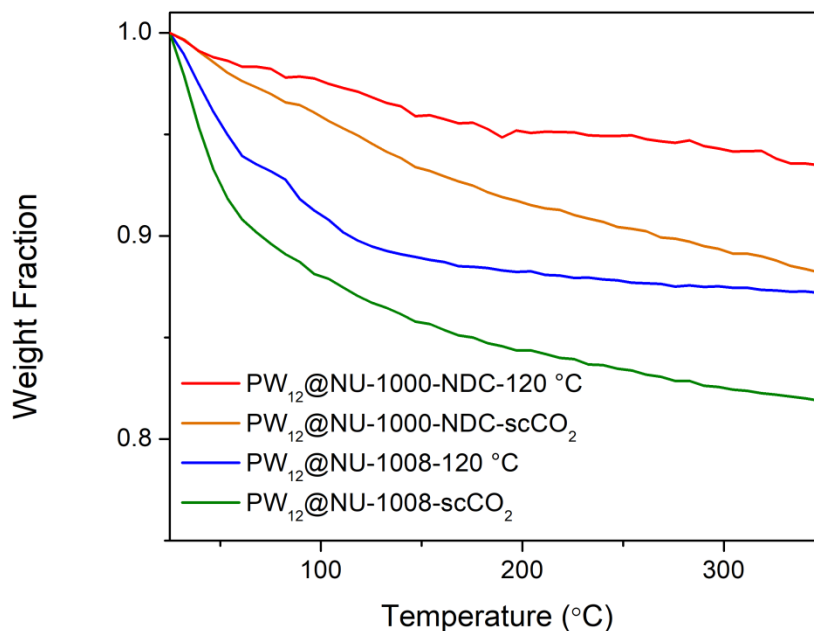


**Figure 6-5** TGA traces of PW<sub>12</sub>@NU-1000-NDC and PW<sub>12</sub>@NU-1008 under N<sub>2</sub>.

In the N<sub>2</sub> sorption isotherms, the maximum uptakes of the composites are significantly lower gravimetrically than the parent MOFs. Since the POMs constitute >50 wt% according to ICP analyses, volumetric equivalents were obtained after estimating densities to determine whether the decreased uptake was a result of mass gain or the degradation of the MOF (**Figure 6-6**). For NU-1000-NDC, the MOF has a Brunauer-Emmett-Teller (BET) area of 1150 m<sup>2</sup>/cm<sup>3</sup> which slightly decreases to 990 m<sup>2</sup>/cm<sup>3</sup> in PW<sub>12</sub>@NU-1000-NDC-scCO<sub>2</sub> and 1100 m<sup>2</sup>/cm<sup>3</sup> for PW<sub>12</sub>@NU-1000-NDC-120 °C. Similarly, in NU-1008 the MOF has a BET area of 910 m<sup>2</sup>/cm<sup>3</sup>, and the scCO<sub>2</sub> and 120 °C activated composites have areas of 820 and 880 m<sup>2</sup>/cm<sup>3</sup>, respectively. With these marginal decreases in BET areas, the decreased gravimetric uptake can be attributed primarily to the additional mass of the POMs and not the degradation of the MOF. In the density functional theory (DFT)-calculated pore size distribution (PSD) for NU-1000-NDC, the mesopore around 30 Å decreases after POM loading and scCO<sub>2</sub>-drying (**Figure 6-6C**). Once

heated to 120 °C, some of the mesopore volume is regained. This hints that the POM occupies the mesopore after scCO<sub>2</sub> drying and some POM leaves after heating. The PSD for NU-1008 shows a similar behavior from the MOF to the scCO<sub>2</sub>-dried sample (**Figure 6-6D**); however, after heating the mesopore volume is retained, suggesting that the POMs are unable to move from the mesopore.

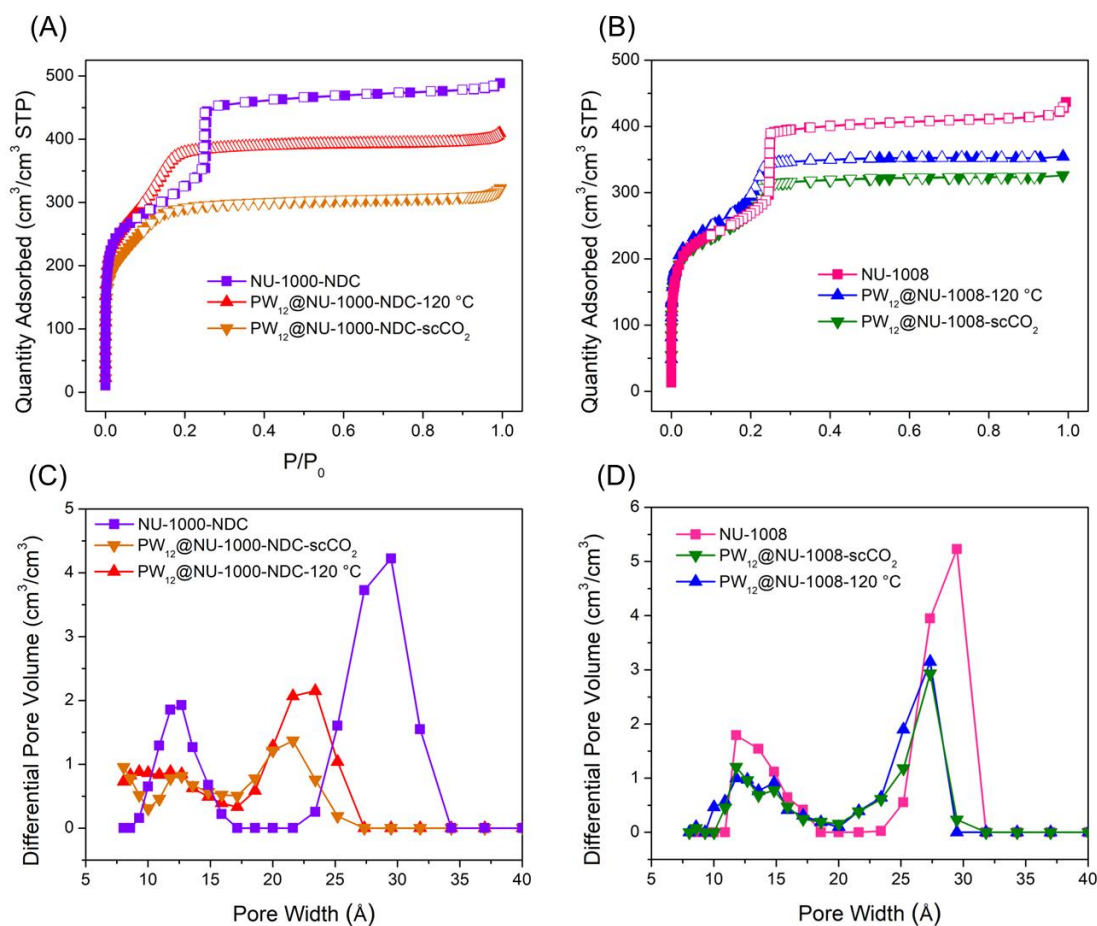


**Figure 6-6** N<sub>2</sub> sorption isotherms of (A) NU-1000-NDC with and without POM and (B) NU-1008 with and without POM. Corresponding DFT-calculated PSD of (C) NU-1000-NDC and its composites and (D) NU-1008 and its composites.

The PXRD patterns for the parent NU-1000-NDC and NU-1008 are similar (**Figure 6-7**); the most prominent peaks arise from the (100) plane around  $2\theta = 2.5^\circ$  and (200) peak around  $5^\circ$ . Once the POM is installed, the highest intensity is the (2-10) Bragg peak appearing around  $2\theta =$

4°, indicating the extra electron density from the POMs resides in the mesopore.<sup>289</sup> ScCO<sub>2</sub> drying has minimal effect on the composites PXRD pattern (**Figure 6-8**), suggesting little to no POM movement during activation. After heating to 120 °C for 2 h, neither composite appears to have changed. However, after 12 h of heating at 120 °C, the PW<sub>12</sub>@NU-1000-NDC closely resembles the parent MOF, indicating that the POMs now occupy the micropores (**Figure 6-9**). This change is indicative of the c'-pores being flexible enough to allow POM movement. In PW<sub>12</sub>@NU-1000, complete movement of the POM from the meso- to micropores occurs, suggesting that PW<sub>12</sub>@NU-1000-NDC requires more energy to undergo the same transformation, so while blocking the c-pore does not prevent the POM from moving, it does force the POM through a higher energy barrier intermediate. Interestingly, PW<sub>12</sub>@NU-1008 appears to have retained its PXRD pattern under the same heating conditions, indicating the POMs remain in the mesopore (**Figure 6-9**) and supporting the previously proposed mechanism where the POMs move through the c- or c'-pores. *In situ* variable temperature PXRD patterns (**Figure 6-10**) show this transformation occurs gradually over time.

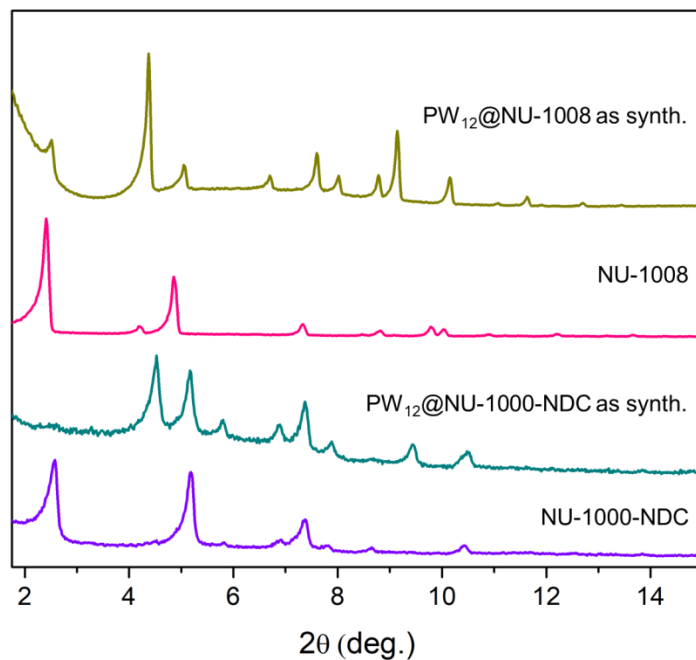


**Figure 6-7** PXR D patterns of the MOFs before and after POM encapsulation.

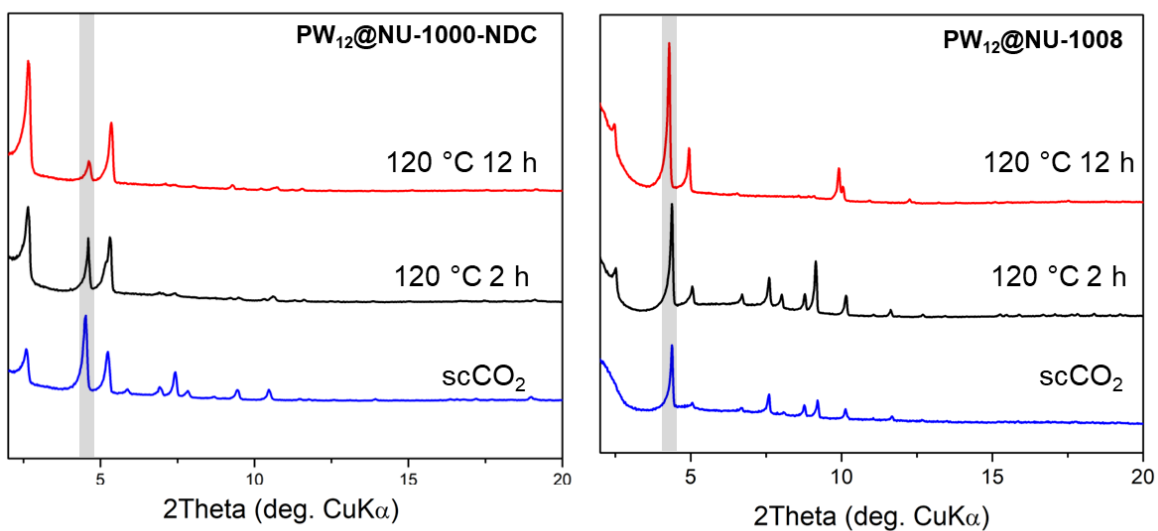


**Figure 6-8.** *Ex situ* PXR D patterns of  $\text{PW}_{12}@NU-1000-NDC$  (left) and  $NU-1008$  (right). Gray boxes the (2-10) reflection.

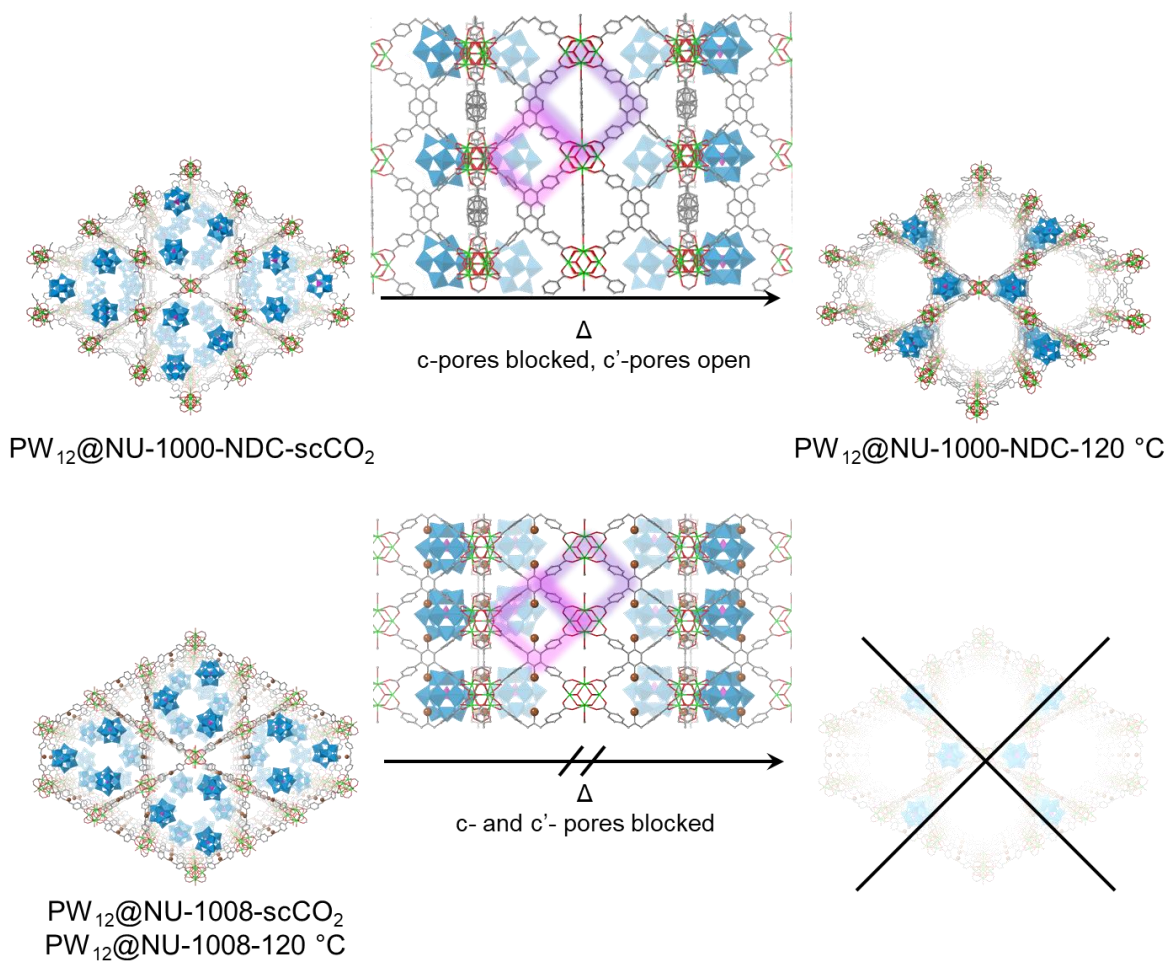


**Figure 6-9** Proposed structures and transitions for  $PW_{12}@NU-1000-NDC$  (top) and  $PW_{12}@NU-1008$  (bottom) under heating conditions. The *c*- and *c'*- pores are highlighted in purple and pink, respectively. For clarity, hydrogens are omitted. Green polyhedron =  $Zr_6$  node, blue polyhedron =  $WO_5$ , pink polyhedron =  $PO_4$ , green sphere = Zr, red = O, gray = C, brown = Br.

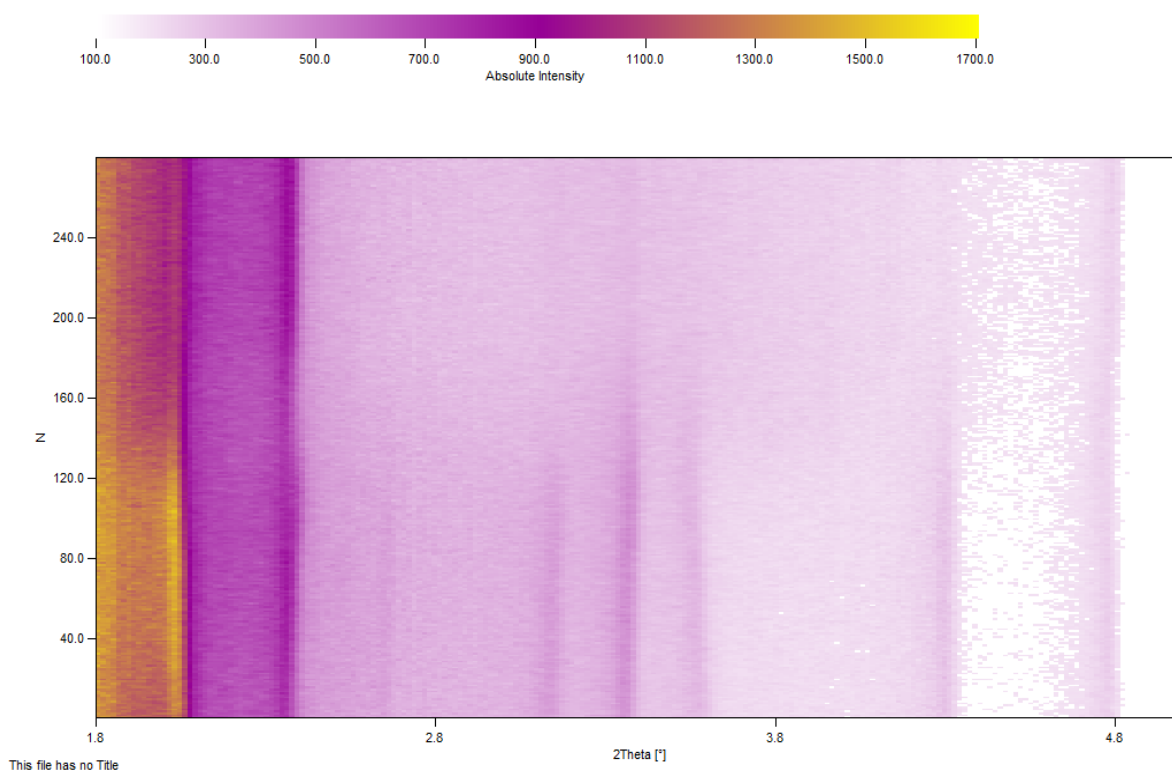


**Figure 6-10** *In-situ* PXRD pattern for  $PW_{12}@NU-1000-NDC$  taken with  $MoK\alpha$  radiation source.  $N=0$  is the  $scCO_2$ -dried sample which was heated to  $120\text{ }^\circ\text{C}$  and held for 12 h.

The oxidation of CEES was selected as a model reaction (**Figure 6-2**). The catalytic setup consists of 1 mol% catalyst ( $0.86\ \mu\text{mol}$  active clusters, i.e. a node or POM) in a vial suspended in acetonitrile and heated to  $45\text{ }^\circ\text{C}$ . CEES and internal standard were then added once the vial reached the set temperature. Then to start the reaction, 1.5 eq of 30% aqueous  $H_2O_2$  was added. The disappearance of CEES was monitored by GC-FID. From the kinetic traces (**Figure 6-11**), the  $H_3PW_{12}O_{40}$ , NU-1008, and NU-1000-NDC alone exhibit similar rates, achieving approximately 50% conversion after 30 min. With the same number of active clusters,  $PW_{12}@NU-1000-NDC$  and  $PW_{12}@NU-1008$  convert CEES at faster rates than the individual components alone. For  $PW_{12}@NU-1000-NDC$  (**Figure 6-11** left), the reactivity trend is consistent with  $PW_{12}@NU-1000$ , where the  $scCO_2$ -activated sample goes to full conversion at the highest rate, and the  $120\text{ }^\circ\text{C}$ -activated sample has slightly lower activity. The marginal

difference in initial turnover frequencies (TOF; 25 and 29  $\text{min}^{-1}$  for  $\text{scCO}_2$ - and 120  $^\circ\text{C}$ -activated, respectively) suggests that the POMs exist in both meso- and microporous channels; this can be compared to the three-fold difference in initial rates in NU-1000 when the POM is located exclusively in one or the other channel. Interestingly,  $\text{PW}_{12}@NU-1008-\text{scCO}_2$  is slower for CEES oxidation than  $\text{PW}_{12}@NU-1008-120^\circ\text{C}$ , exhibiting TOFs of 14 and 21  $\text{min}^{-1}$  respectively. In this case, the POMs are located only in the mesopore, unable to migrate to the micropores. This finding suggests that the removal of water when not accompanied by POM movement leads to rate enhancement, and that limiting POM migration to a more thermodynamically favorable site allows for better accessibility of the active sites. Note, the apparent enhanced rate of the NU-1000-NDC over NU-1008 can be attributed to particle size differences and the poor catalyst accessibility of the substrate from the micropore, both hindering substrate diffusion.

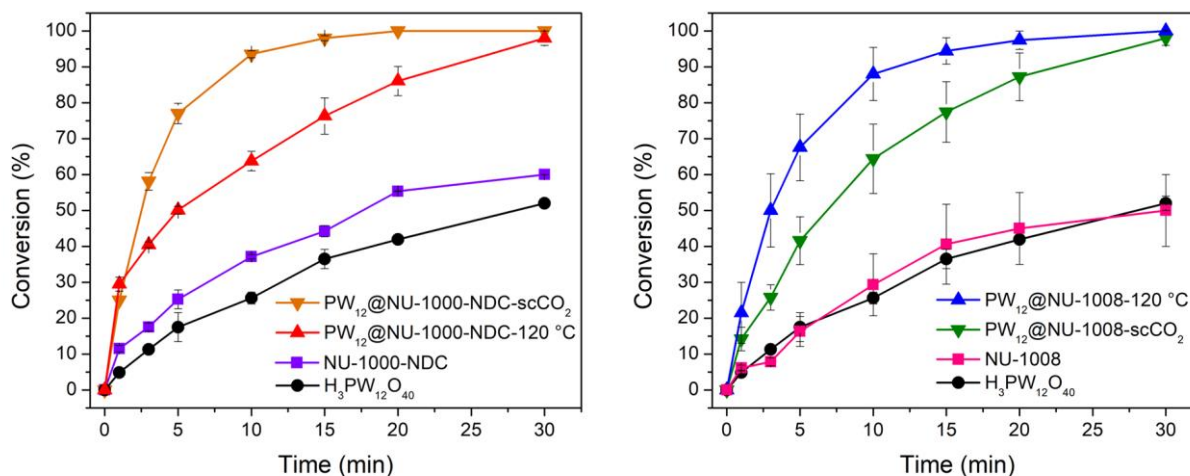


**Figure 6-11** CEES conversion over time with (left) NU-1000-NDC and its POM composites and (right) NU-1008 and its POM composites. Error bars represent standard deviation of at least 2 trials.

## 6.4 Conclusions

Two MOFs, NU-1000-NDC and NU-1008 were used to immobilize  $\text{H}_3\text{PW}_{12}\text{O}_{40}$ . The composite materials were activated via supercritical drying and/or heating to 120 °C, resulting in  $\text{PW}_{12}@NU-1008\text{-scCO}_2$ ,  $\text{PW}_{12}@NU-1008-120$  °C,  $\text{PW}_{12}@NU-1000\text{-NDC-scCO}_2$  and  $\text{PW}_{12}@NU-1000\text{-NDC-120}$  °C. POM location in each was confirmed via PXRD pattern analysis. For NU-1000-NDC, the POM required longer heating for POM movement to occur than in previously reported NU-1000. In NU-1008, POM movement is completely inhibited and the POM remains in the mesopore after heating. The composite materials were more active than the individual components alone. Among the composites, the location of POM and water content in composite was found to affect the oxidation rate of a mustard gas simulant, CEES. In NU-1000-NDC, the  $[\text{PW}_{12}\text{O}_{40}]^{3-}$  cluster in the mesopore is more active than when the material is heated and the cluster resides in the micropore. In contrast, when comparing the NU-1008 composites where both materials have the  $[\text{PW}_{12}\text{O}_{40}]^{3-}$  cluster in the mesopore, heating the sample to remove water yields the more reactive catalyst. These findings highlight the importance of active site location on a heterogeneous support, and future studies aim to exploit the effect of POM location on catalysis.

**Chapter 7 . Aerobic oxidation of a mustard gas simulant using the  
 $H_5PV_2Mo_{10}O_{40}$  polyoxometalate encapsulated in NU-1000 metal–organic  
framework**

Portions of this chapter appear in the following manuscript:

Buru, C. T.; Wasson, M. C.; Farha, O.K.  $H_5PV_2Mo_{10}O_{40}$  Polyoxometalate Encapsulated in NU-1000 Metal–Organic Framework for Aerobic Oxidation of a Mustard Gas Simulant. *ACS Appl. Nano Mater.* **2020**, *3*, 658-664.

## 7.1 Introduction

The catalytic activation of dioxygen in the atmosphere to accomplish practical and sustainable oxidation processes has garnished substantial interest. In practice, processes such as methanol oxidation, olefin (ep)oxidation, and desulfurization typically utilize ill-defined, low surface area metal oxide catalysts to activate O<sub>2</sub> on an industrial scale.<sup>295</sup> As an alternative approach to these traditional metal oxide catalyst, polyoxometalates (POMs), discrete anionic metal oxide clusters,<sup>28,43</sup> provide more active sites at the surface of the cluster.<sup>296</sup> Owing to their rich redox properties, POMs have been reported as acid<sup>283</sup> and oxidation catalysts,<sup>35</sup> among other applications. However, their tendency to aggregate and instability in solution prevent wide implementation.<sup>285</sup> To prevent aggregation and engender stability, POMs have been previously immobilized on a variety of supports.<sup>297</sup> Among the possible supports, metal–organic frameworks (MOFs) offer a robust, versatile, functionalizable platform on which to install POMs.<sup>83,211,298</sup> MOFs are a class of highly porous materials composed of inorganic nodes connected via organic linkers forming 2D or 3D extended networks.<sup>8,138,140,204</sup> Due to their high crystallinity, MOF structures have been investigated and understood through techniques such as single crystal X-ray diffraction. As support materials, MOFs have been used to immobilize a range of active guests,<sup>82,299</sup> from single atoms<sup>59,277</sup> to relatively large nanoparticles<sup>242,300</sup> and biomolecules.<sup>117,301,302</sup>

In recent work, we reported the immobilization of the POM phosphotungstic acid (H<sub>3</sub>PW<sub>12</sub>O<sub>40</sub>) in the **csq**-net MOF, NU-1000,<sup>116,122,290</sup> which is comprised of 1,3,6,8-tetrakis(*p*-benzoate)pyrene (TBAPy) linkers and eight-connected Zr<sub>6</sub>(μ<sub>3</sub>-OH)<sub>4</sub>(μ<sub>3</sub>-O)<sub>4</sub>(OH)<sub>4</sub>(OH<sub>2</sub>)<sub>4</sub> nodes (**Figure 1** middle). The composite material, PW<sub>12</sub>@NU-1000 was found to be active for oxidation of 2-chloroethyl ethyl sulfide (CEES), a mustard gas simulant, using hydrogen

peroxide as the oxidant. Mustard gas (bis(2-chloroethyl) sulfide; also known as HD or sulfur mustard) is a commonly used chemical warfare agent (CWA) which was first introduced in World War I.<sup>123</sup> Continued use, demand for stockpile destruction, and recent surfacing of buried munitions necessitate the development of materials to safely handle mustard gas and other CWAs.<sup>4,303</sup> A possible route for the detoxification of mustard gas is selective oxidation to the sulfoxide.<sup>5</sup> Over-oxidation in this process generates the toxic sulfone derivative,<sup>267</sup> so the selection of catalyst material is crucial. Using  $\text{H}_3\text{PW}_{12}\text{O}_{40}$  as a catalyst slowly, but selectively, produced the singly oxidized product, 2-chloroethyl ethyl sulfoxide (CEESO).<sup>122,200,268</sup> On the other hand, hydrogen peroxide can also decompose on the zirconia-like nodes of NU-1000,<sup>220,221</sup> yielding the over-oxidized product, 1-chloro-2-(ethylsulfonyl)ethane (CEESO<sub>2</sub>). Unsurprisingly, the composite  $\text{PW}_{12}@\text{NU-1000}$  was not selective for CEES oxidation because the nodes in the MOF framework remained accessible and contributed to the activity. Modifying the material to promote POM accessibility in the MOF greatly improved selectivity using the composite, but the reaction was never completely selective. To improve upon this system, we sought to incorporate an aerobically active POM to render the nodes inert in the oxidation reaction.

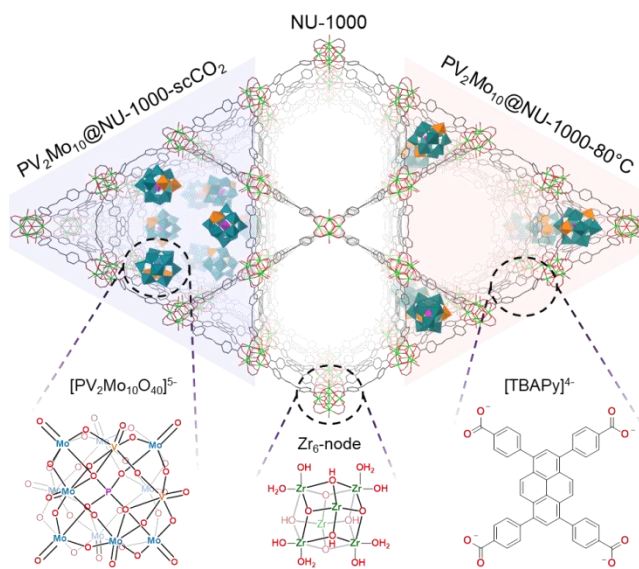


**Figure 7-1** Visual representations of [PV<sub>2</sub>Mo<sub>10</sub>O<sub>40</sub>] clusters in NU-1000. Blue shaded area (left) depicts one possible configuration of PV<sub>2</sub>Mo<sub>10</sub>@NU-1000-scCO<sub>2</sub>. Red shaded area (right) depicts one possible structure of PV<sub>2</sub>Mo<sub>10</sub>@NU-1000-80°C. Unshaded area (middle) is unmodified NU-1000 crystal structure. Arrangements of the two vanadium atoms were random selected. Teal polyhedra=MoO<sub>5</sub>, Orange polyhedra=VO<sub>5</sub>, Pink polyhedra=PO<sub>4</sub>, Red=O, Green=Zr, Gray=C. Hydrogens omitted for clarity.

Here, we employ the POM, decamolybdodivanadophosphoric acid (H<sub>5</sub>PV<sub>2</sub>Mo<sub>10</sub>O<sub>40</sub>), immobilized in NU-1000 for the catalytic oxidation of CEES. H<sub>5</sub>PV<sub>2</sub>Mo<sub>10</sub>O<sub>40</sub>, which exists as five inseparable isomers, has been used as a catalyst in peroxide-based and O<sub>2</sub>-based oxidation reactions<sup>304</sup> both homogeneously in solution<sup>305,306</sup> and heterogeneously on a variety of support materials.<sup>307–309</sup> Notably, this POM has been widely reported for its utility in desulfurization of diesel,<sup>310,311</sup> the mechanism of which relies upon an initial electron transfer step from the  $\alpha$ -aryl group to reduce the POM.<sup>312</sup> Few reports attempt to immobilize these POMs on crystalline supports to, not only improve stability, but also investigate the structure in detail to tune reactivity.

In MOF-based systems, H<sub>5</sub>PV<sub>2</sub>Mo<sub>10</sub>O<sub>40</sub> has been previously introduced into HKUST-1 and *rho*-ZIF for oxidative transformations using H<sub>2</sub>O<sub>2</sub><sup>94,309,313</sup> and O<sub>2</sub>.<sup>92</sup> When the POM was

installed in MIL-101, the composite materials exhibited slightly higher CEES decontamination (uptake plus catalysis) than the MOF alone. The increase was probed by mass spectrometry and attributed to evidence of aerobic oxidation reaction of the CEES with the POM.<sup>108</sup> We believe that immobilization in the hierarchical NU-1000 MOF will allow for enhanced substrate diffusion since pores will not be blocked with POM and favorable interaction between the POM and MOF to prevent POM leaching; issues which arise with the HKUST-1 and MIL-101 MOF systems, respectively.<sup>97,170,206,211</sup> The crystallinity of the NU-1000 will allow for insights into the structure of the composite material. Selection of reaction conditions to promote aerobic oxidation of the alkyl sulfide will also be discussed.

## 7.2 Experimental Methods

### 7.2.1 Materials Syntheses

**General** NU-1000 and was synthesized according to literature procedure.<sup>120</sup>  $H_5V_2Mo_{10}O_{40}$  was synthesized by a scaled down version of literature procedure.<sup>314</sup> For NMR comparisons, 2-chloroethyl ethyl sulfoxide (CEESO) was synthesized from the reported partial oxidation of CEES.<sup>162</sup> All other chemicals were used as received from Fisher Scientific or Sigma Aldrich. All gasses for activation and quantification were Ultra High Purity Grade 5.

**$PV_2Mo_{10}@NU-1000-scCO_2$ .** In a centrifuge tube, 200 mg  $H_5V_2Mo_{10}O_{40}$  was added and dissolved in 10 mL of deionized water. NU-1000 (50 mg) was added and the suspension sonicated for 1 min to ensure dispersion. After 3 days of periodic agitation, the solid was collected via centrifugation. The solid was washed with water 2x and absolute ethanol before sitting overnight in absolute ethanol. If the solution was colored, more washes were performed to

eliminate all free POM. After one more washing with ethanol, the solid was suspended in a minimum amount of ethanol and transfer to a glass dish compatible with the supercritical CO<sub>2</sub> drier.

***PV<sub>2</sub>Mo<sub>10</sub>@NU-1000-80°C***. The PV<sub>2</sub>Mo<sub>10</sub>@NU-1000-scCO<sub>2</sub> was heated at 80°C for at least 1 h.

***PMo<sub>12</sub>@NU-1000***. In a centrifuge tube, 200 mg H<sub>3</sub>Mo<sub>12</sub>O<sub>40</sub> was added and dissolved in 10 mL of deionized water. NU-1000 (50 mg) was added and the suspension sonicated for 1 min to ensure dispersion. After 3 days of periodic agitation, the solid was collected via centrifugation. The solid was washed with water 2x and absolute ethanol before sitting overnight in absolute ethanol. After one more washing with ethanol, the solid was suspended in a minimum amount of ethanol and transfer to a glass dish compatible with the supercritical CO<sub>2</sub>

### ***7.2.2 Physical Methods***

The supercritical drying process used a Tousimis™ Samdri PVT-3D critical point drier in which liquid CO<sub>2</sub> was used to exchange ethanol 4 times over 8 h. The material was then heated above 31 °C (P = 73 atm), the critical point of CO<sub>2</sub> before the instrument was evacuated at a rate of 0.1 sccm.<sup>257–259</sup> All MOF samples were activated by exposure of 20 to 100 mg of material for 12 hours under high vacuum on a Micromeritics Smart VacPrep instrument. N<sub>2</sub> adsorption and desorption isotherm measurements were performed on a Micromeritics Tristar II at 77 K. Inductively coupled plasma optical emission spectroscopy (ICP-OES) samples of solids were prepared in a 2-5 mL Biotage microwave vial by dissolving 1-2 mg of sample in 5 drops of H<sub>2</sub>SO<sub>4</sub> and slowly adding 2 mL of HNO<sub>3</sub>. The vial was cringe-capped and heated to 150 °C for 15 min in a SPX microwave reactor. The resulting orange-yellow solution was made colorless by adding 0.5 mL H<sub>2</sub>O<sub>2</sub> (30 wt% in water) and heating in a sand bath for 10 min. To the colorless or

pale solution, 10 mL of deionized water was added, and the resulting dilution analyzed with Thermo iCap7600 ICP-OES spectrometer, equipped with a CCD detector and Ar plasma covering 175-785 nm range. Powder X-ray diffraction (PXRD) patterns were collected on a Stoe STADI-P instrument. Samples were using  $K\alpha_1$  Cu radiation, a step size of  $2\theta = 0.015^\circ$  over a  $2\theta$  range of 1 to  $25^\circ$ . Variable temperature powder X-ray diffraction (PXRD) patterns were collected on a Stoe STADI-MP instrument equipped with a furnace using  $K\alpha_1$  Mo radiation. Solution NMR spectra were collected on a 400 MHz Agilent DD MR-400 system at IMSERC (Integrated Molecular Structure Education and Research Center) at Northwestern University. Solid-state NMR spectra were collected on a Bruker 400 MHz NMR system spinning at 10,000 Hz. Scanning electron microscopy (SEM) images and energy dispersive spectroscopy (EDS) line scans were collected using a Hitachi SU8030 FE-SEM microscope at Northwestern University's EPIC/NUANCE facility. All samples were coated with ~15 nm of  $OsO_4$  immediately prior to imaging. GC-FID measurements were carried out on an Agilent Technologies 7820A GC system equipped with an Agilent J&W GC HP-5 capillary column (30 m  $\times$  320  $\mu$ m  $\times$  0.25  $\mu$ m film thickness). All samples were filtered and diluted with dichloromethane prior to injection. Starting temperature: 70  $^\circ$ C, Hold: 0.5 min, Ramp: 30  $^\circ$ C/min, Time: 1 min, Ramp: 75  $^\circ$ C/min, End temperature: 250  $^\circ$ C. Thermogravimetric analyses (TGA) were performed on a Mettler Toledo STAR<sup>c</sup> TGA/DSC 1 under a  $N_2$  flow at a 10  $^\circ$ C/min ramp rate from 25 to 700  $^\circ$ C. For TGA-MS measurements, a Netzsch Simultaneous Thermal Analysis (STA 449F3) instrument coupled to a GC-MS was used.

### ***7.2.3 Catalytic Measurements***

In a typical set up, the catalyst was added to a microwave vial. To the vial, 1 mL of solvent was dispensed. The vial was cringe-capped and purged with  $O_2$  for 15 min. The

suspensions were then placed in a 70 °C sand bath to raise the temperature, to which 0.2 mmol of CEES was added. Then, to take an initial time point, a 20  $\mu\text{L}$  aliquot was taken, diluted with 750  $\mu\text{L}$  of dichloromethane, filtered, and analyzed by GC-FID. The reaction was monitored by taking aliquots in a similar manner after the addition of isobutyraldehyde and quantified by comparison to a calibration curve. Internal standards were not used due to lack of sufficiently unreactive commonly used standards.

### 7.3 Results and Discussion

The composite material  $\text{PV}_2\text{Mo}_{10}\text{@NU-1000}$  was synthesized in a similar manner to  $\text{PW}_{12}\text{@NU-1000}$ .<sup>115,116,122</sup> Briefly,  $\text{NU-1000}$ <sup>119–121</sup> was added to an aqueous solution of  $\text{H}_5\text{PV}_2\text{Mo}_{10}\text{O}_{40}$ <sup>314</sup> and allowed to sit for 3 days. After, the solid was washed rigorously with water and ethanol before activation via supercritical  $\text{CO}_2$  drying, yielding  $\text{PV}_2\text{Mo}_{10}\text{@NU-1000-scCO}_2$  (**Figure 1** left; see Supporting Information). Gentle heating of the composite in an 80 °C vacuum oven for 1 h yielded  $\text{PV}_2\text{Mo}_{10}\text{@NU-1000-80}^\circ\text{C}$  (**Figure 1** right). Note, that the material denoted with 80 °C can be obtained with longer heating at lower temperatures. Differences in these two materials will be explored *vide infra*.

To quantify the amount of  $[\text{PV}_2\text{Mo}_{10}\text{O}_{40}]$ , inductively couple plasma optical emission spectroscopy (ICP-OES) was used. The ratio of  $\text{PV}_2\text{Mo}_{10}$  per  $\text{Zr}_6$  node was found to be 1.3. Scanning electron microscopy (SEM) images (Figure S1) show that the NU-1000 crystallite was unaffected by POM incorporation, and energy dispersive X-ray spectroscopy (EDS) line scans indicate homogeneous distribution of POM through the crystallite.

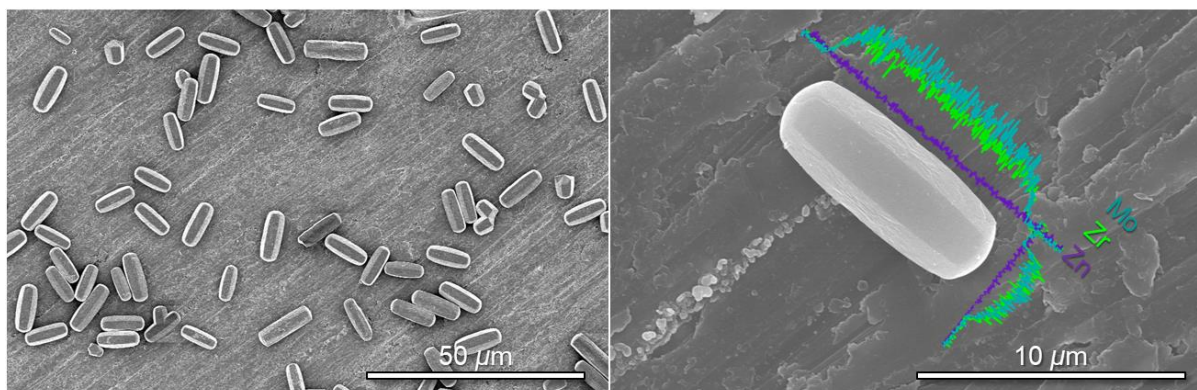


**Figure 7-2** SEM images of NU-1000 before (left) and after (right)  $[\text{PV}_2\text{Mo}_{10}\text{O}_{40}]^{5-}$  incorporation. EDS line scans of Mo and Zr compared to baseline Zn.

The volumetric  $\text{N}_2$  isotherms (**Figure 2A**) indicate that minimal surface area is lost during POM installation. The significant decrease in adsorbed quantity from the MOF to composite in the corresponding gravimetric isotherms (Figure S2) can be attributed to the increase in density. The Brunauer-Emmett-Teller areas calculated from these isotherms are 1020, 1160, 1190  $\text{m}^2/\text{cm}^3$  for NU-1000,  $\text{PV}_2\text{Mo}_{10}@$ NU-1000- $\text{scCO}_2$ , and  $\text{PV}_2\text{Mo}_{10}@$ NU-1000- $80^\circ\text{C}$  respectively, signifying that the POM is possibly acting as  $\text{N}_2$  adsorption sites within the framework. The density functional theory (DFT) calculated pore size distribution (PSD; Figure S3) show the reduction of the mesoporous peak and retention the microporous peak from NU-1000 to  $\text{PV}_2\text{Mo}_{10}@$ NU-1000- $\text{scCO}_2$ . After heating the sample to obtain  $\text{PV}_2\text{Mo}_{10}@$ NU-1000- $80^\circ\text{C}$ , the mesoporous peak in the PSD regained volume while the microporous peak reduced in volume. This suggests that the POMs occupy the mesoporous peak in the  $\text{scCO}_2$ -activated sample, and the POMs are located in the microporous peak after exposure to  $80^\circ\text{C}$ . In the thermogravimetric analysis (TGA) curves, the composite materials were found to contain approximately 11(2) wt% physisorbed water which was accounted for in the density calculations used for volumetric corrections.

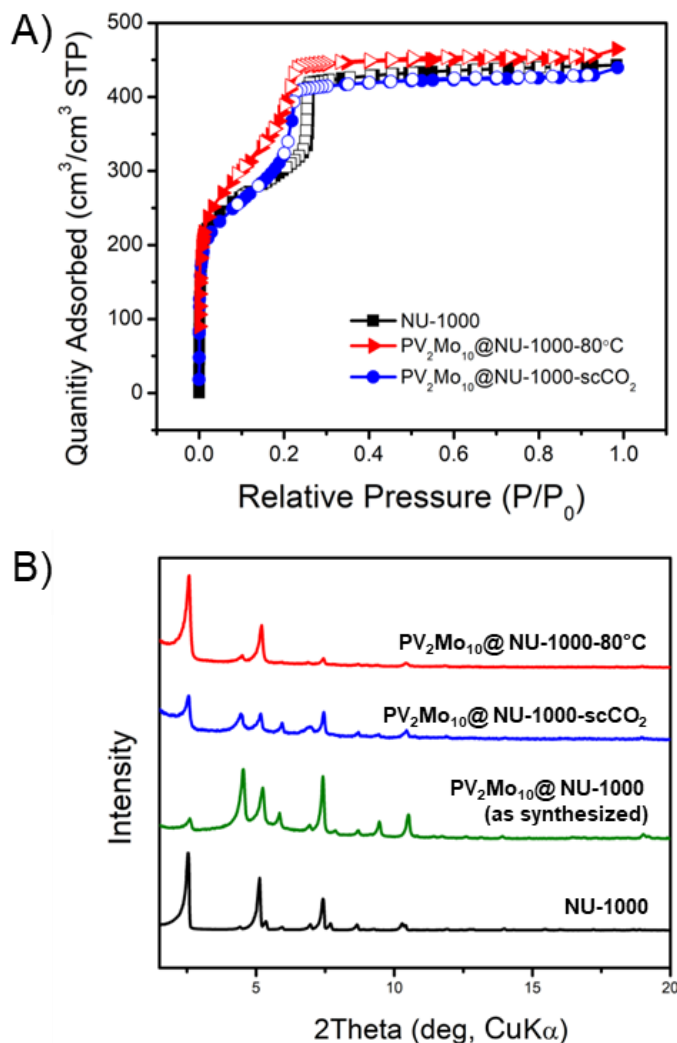


**Figure 7-3** The (A) N<sub>2</sub> adsorption-desorption isotherms and (B) PXRD patterns of NU-1000, PV<sub>2</sub>Mo<sub>10</sub>@NU-1000-scCO<sub>2</sub>, and PV<sub>2</sub>Mo<sub>10</sub>@NU-1000-80°C. Closed symbols in the isotherm represent points collected during adsorption, and open symbols represent points collected during desorption.

The powder X-ray diffraction (PXRD) patterns (**Figure 2B**) further corroborate the location of the POMs as suggested by the DFT-calculated PSD. The NU-1000 PXRD pattern has the characteristic peaks at 2.5°, 5°, and 7.5°, corresponding to the (100), (200), and (300) planes. The as-synthesized composite and the PV<sub>2</sub>Mo<sub>10</sub>@NU-1000-scCO<sub>2</sub> have similar PXRD patterns, where the (2-10) peak around 4° has high intensity. This pattern was previously assigned to a

structure where the POMs resided in the mesopores of NU-1000.<sup>116</sup> On the other hand, the  $\text{PV}_2\text{Mo}_{10}\text{@NU-1000-80}^\circ\text{C}$  has a similar PXRD pattern to the parent NU-1000, which has been assigned to the POMs being located in the micropore.<sup>122</sup> The transformation of these PXRD patterns was probed using *in situ* heating (Figure S4), where the  $\text{scCO}_2$  material was placed in a capillary and heated in a furnace. Unlike  $\text{PW}_{12}\text{@NU-1000}$ , the change in pattern occurred much earlier in the heating process, likely due to the slightly smaller kinetic diameter and the  $[\text{PV}_2\text{Mo}_{10}\text{O}_{40}]^{5-}$  compared to  $[\text{PW}_{12}\text{O}_{40}]^{3-}$ .<sup>315</sup>

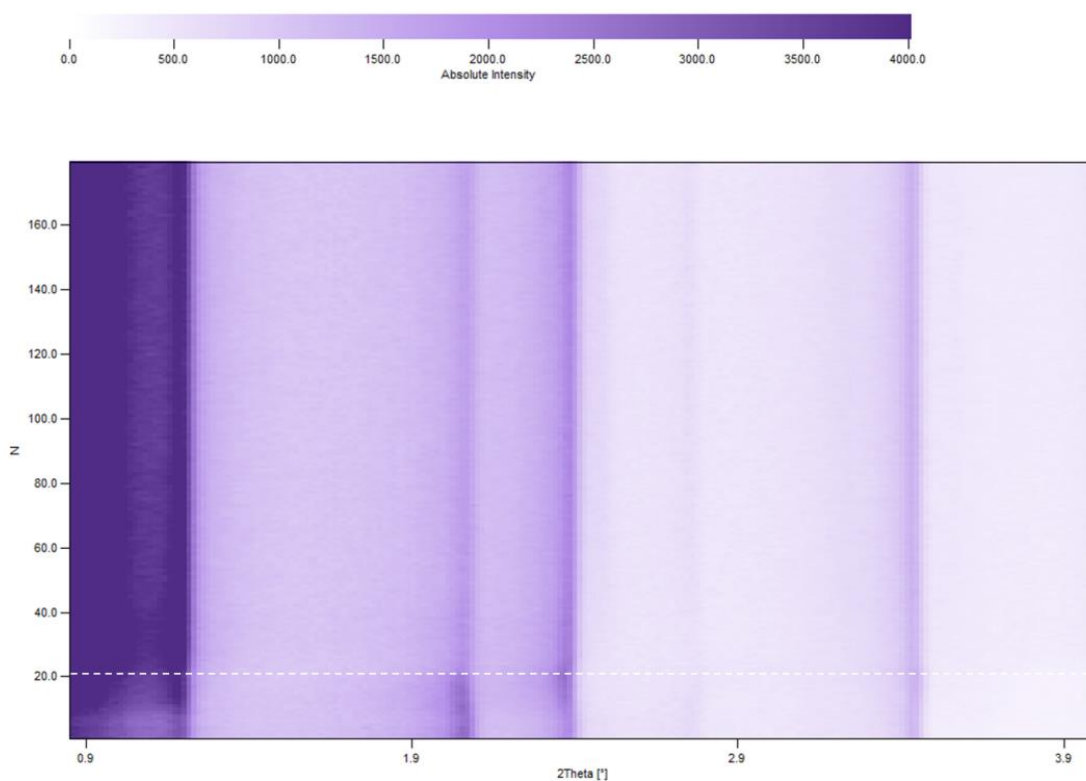


**Figure 7-4** *In situ* variable temperature PXRD patterns for  $\text{PV}_2\text{Mo}_{10}\text{@NU-1000-scCO}_2$ . N (y-axis) indicates the number of scans taken at  $80^\circ\text{C}$ . Each scan is 1 min apart. The horizontal dotted white line highlights where the structural change occurs.

To verify the integrity of the POM structure within the MOF, the solid state  $^{31}\text{P}$  cross polarization magic angle spinning (CP MAS) NMR spectra were collected (Figure S5). The  $\text{H}_5\text{PV}_2\text{Mo}_{10}\text{O}_{40}$  has a broad signal and shoulder centered around -2.9 ppm. Note, that the different isomers are typically well-resolved in the solution phase  $^{31}\text{P}$  NMR spectrum, but are indistinguishable in the solid state spectrum. In the composite materials, the peak becomes broader as slightly shifts to -3.5 ppm and -4.6 ppm for  $\text{PV}_2\text{Mo}_{10}@ \text{NU-1000-scCO}_2$  and  $\text{PV}_2\text{Mo}_{10}@ \text{NU-1000-80}^\circ\text{C}$ , respectively. This broadening and shift is attributed to slight distortion and interaction of the MOF framework with the POM, rather than decomposition of the cluster.

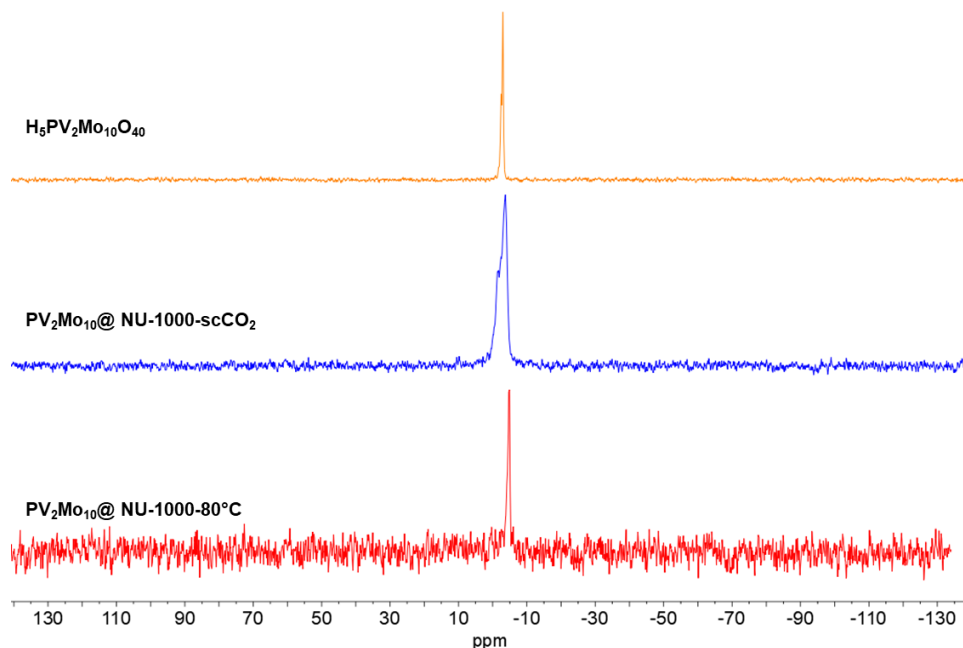


**Figure 7-5**  $^{31}\text{P}$  CPMAS NMR spectra of  $\text{H}_5\text{PV}_2\text{Mo}_{10}\text{O}_{40}$  and  $\text{PV}_2\text{Mo}_{10}@ \text{NU-1000}$ .

The aerobic oxidation of an alkyl sulfide, specifically CEES, was used as a model reaction (Figure 3A). The reaction of  $\text{PV}_2\text{Mo}_{10}\text{O}_{40}$  with  $\text{O}_2$  occurs at the V centers and requires reduction of the POM to  $\text{PV}^{\text{IV}}\text{V}^{\text{V}}\text{Mo}_{10}\text{O}_{40}$ . With substrates possessing aromatic functionality, this reduction typically occurs via electron transfer from the aromatic ring to the POM.<sup>312</sup> With alkyl

substrates, electrochemical reduction<sup>316</sup> or sacrificial reductant<sup>149,306,317</sup> can be used to prime the POM for reaction with molecular oxygen. Here, we selected isobutyraldehyde as a sacrificial reductant.

Since  $\text{H}_5\text{PV}_2\text{Mo}_{10}\text{O}_{40}$  is not soluble in cyclohexane, each reaction proceeds heterogeneously. Accompanying the reduction of the POM, a color change is observed from red to dark green with  $\text{H}_5\text{PV}_2\text{Mo}_{10}\text{O}_{40}$  or yellow to darker yellow in NU-1000 composites. From the kinetic traces (Figure 3B and S9), the composites react at higher initial rates than the  $\text{H}_5\text{PV}_2\text{Mo}_{10}\text{O}_{40}$  alone. The  $\text{scCO}_2$ -activated material exhibits a two-fold enhancement of the initial turnover frequency over the 80 °C-activated material. However, this initial rate enhancement is not as sustained and not as significant as in the previously reported  $\text{PW}_{12}$ @NU-1000 case. The POM and composites were compared to  $\text{PMo}_{12}$ @NU-1000 (Figures S6-S8), which converted <5% of CEES. This confirmed that the vanadium atoms were responsible for the aerobic activity in agreement with previous reports. To verify the source of oxygen, the reaction was also performed under  $\text{N}_2$  atmosphere, where the reaction vial was purged with  $\text{N}_2$  instead of  $\text{O}_2$ , and no reaction was observed.

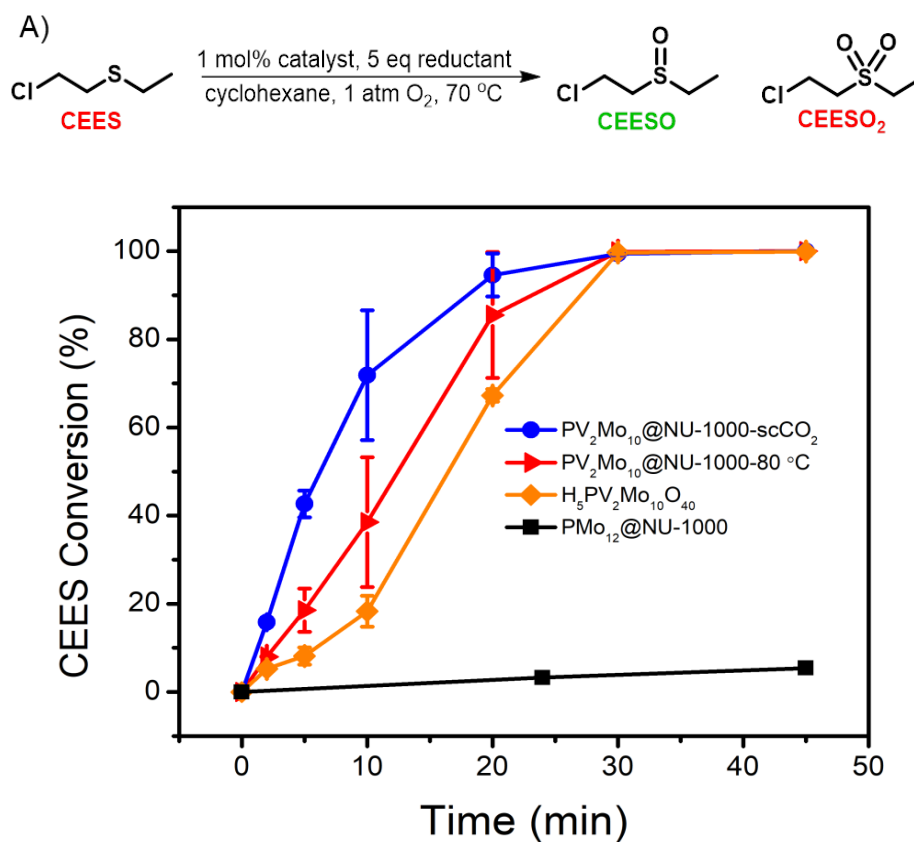


**Figure 7-6** The (A) reaction of CEES under the condition reported here. (B) The kinetic traces of each material used for reaction (A). Catalyst is normalized to the number of POM clusters, the reductant is isobutyraldehyde, 1 mL cyclohexane was used as solvent. Traces are averages of at least 3 trials.

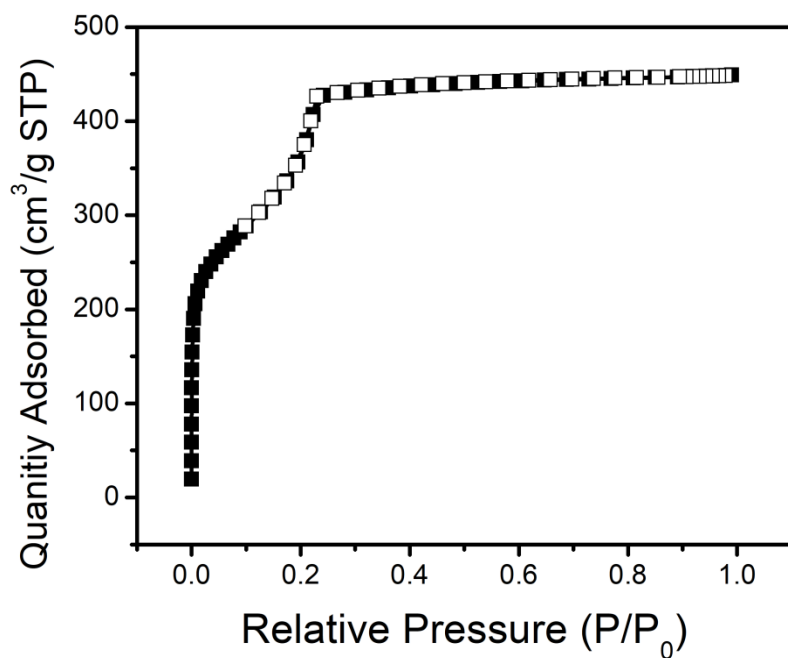


**Figure 7-7** Gravimetric N<sub>2</sub> adsorption (filled) and desorption (unfilled) isotherms for PMo<sub>12</sub>@NU-1000 after scCO<sub>2</sub> activation (BET: 1450 m<sup>2</sup>/g).

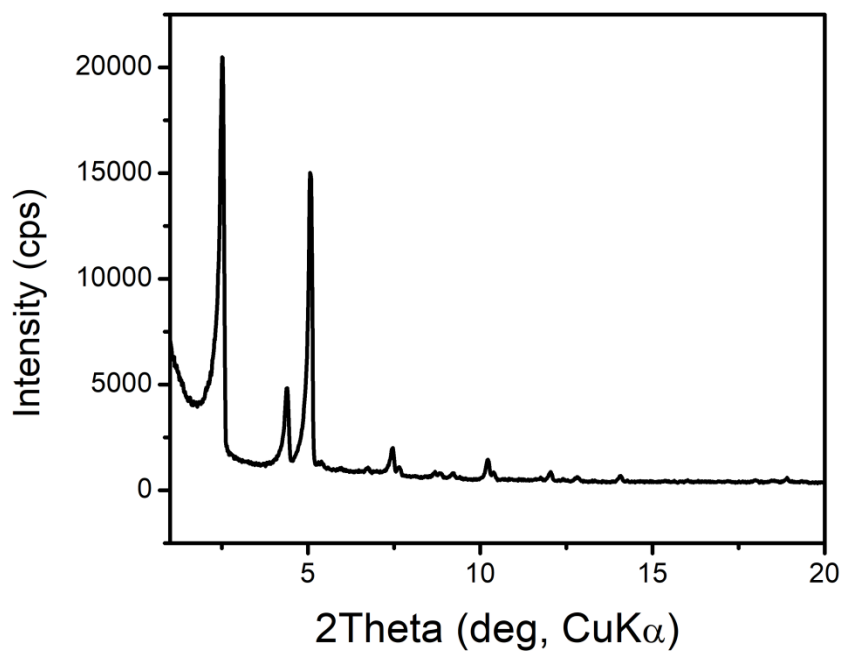


**Figure 7-8** PXRD patterns for PMo<sub>12</sub>@NU-1000 after scCO<sub>2</sub> activation showing POMs primarily located in micropores.

Unfortunately, the reaction conditions led almost exclusively to the over-oxidized CEESO<sub>2</sub>. Even after CEES consumption, CEESO<sub>2</sub> was still being generated from CEESO. The one-electron pathway enabled by the reduction of the POM leads to this unselective radical mechanism.<sup>317</sup> In attempts to mitigate the over-oxidation product, several parameters were tuned: reductant amount, temperature, solvent, O<sub>2</sub> partial pressure. These modified reaction conditions and yield are summarized in Table S1. In all cases, however, the reaction rate severely decreased, and the over-oxidized product always formed anyways.

**Table 7-1** Reaction conditions tuning amount of reductant, temperature, atmosphere, and solvent collected at 45 min.

Catalyst	Reductant	Temperature (°C)	Atmosphere	Solvent	Conversion (%)
H <sub>5</sub> PV <sub>2</sub> Mo <sub>10</sub> O <sub>40</sub>	5 eq	70	O <sub>2</sub>	Cyclohexane	100
H <sub>5</sub> PV <sub>2</sub> Mo <sub>10</sub> O <sub>40</sub>	5 eq	70	<b>Air</b>	Cyclohexane	23
H <sub>5</sub> PV <sub>2</sub> Mo <sub>10</sub> O <sub>40</sub>	5 eq	70	<b>N<sub>2</sub></b>	Cyclohexane	<1
H <sub>5</sub> PV <sub>2</sub> Mo <sub>10</sub> O <sub>40</sub>	<b>2 eq</b>	70	O <sub>2</sub>	Cyclohexane	27
H <sub>5</sub> PV <sub>2</sub> Mo <sub>10</sub> O <sub>40</sub>	<b>1 eq</b>	70	O <sub>2</sub>	Cyclohexane	3
H <sub>5</sub> PV <sub>2</sub> Mo <sub>10</sub> O <sub>40</sub>	<b>0 eq</b>	70	O <sub>2</sub>	Cyclohexane	1
H <sub>5</sub> PV <sub>2</sub> Mo <sub>10</sub> O <sub>40</sub>	5 eq	<b>22</b>	O <sub>2</sub>	Cyclohexane	14
H <sub>5</sub> PV <sub>2</sub> Mo <sub>10</sub> O <sub>40</sub>	5 eq	70	O <sub>2</sub>	<b>Acetonitrile</b>	9
H <sub>3</sub> Mo <sub>12</sub> O <sub>40</sub>	5 eq	70	O <sub>2</sub>	Cyclohexane	4
PMo <sub>12</sub> @NU-1000	5 eq	70	O <sub>2</sub>	Cyclohexane	5
PV <sub>2</sub> Mo <sub>10</sub> @NU-1000-scCO <sub>2</sub>	5 eq	70	O <sub>2</sub>	Cyclohexane	100
PV <sub>2</sub> Mo <sub>10</sub> @NU-1000-80°C	5 eq	70	O <sub>2</sub>	Cyclohexane	100
Recycled PV <sub>2</sub> Mo <sub>10</sub> @NU-1000	5 eq	70	O <sub>2</sub>	Cyclohexane	100
Recycled H <sub>5</sub> PV <sub>2</sub> Mo <sub>10</sub> O <sub>40</sub>	5 eq	70	O <sub>2</sub>	Cyclohexane	5

After the reaction in Figure 3A, the composite materials were recovered, washed rigorously with cyclohexane and acetone, dried, and analyzed by ICP-OES. Approximately 80% of the POM was retained in both PV<sub>2</sub>Mo<sub>10</sub>@NU-1000-scCO<sub>2</sub> and PV<sub>2</sub>Mo<sub>10</sub>@NU-1000-80°C. Because of this retention of the catalytically active species within the MOFs, the materials were recycled for a second catalytic trial. After 45 min, the reaction with PV<sub>2</sub>Mo<sub>10</sub>@NU-1000 went to 100% CEES conversion. Surprisingly, the recycled H<sub>5</sub>PV<sub>2</sub>Mo<sub>10</sub>O<sub>40</sub> only gave 5% conversion. The <sup>31</sup>P NMR spectrum of the recycled POM showed no signal, suggesting that the cluster

decomposed and subsequently the soluble phosphorous component washed away. This highlights the enhanced stability that can be provided by a MOF support.

Interestingly, the PXRD pattern of  $PV_2Mo_{10}@NU-1000-scCO_2$  post-catalysis exhibited minimal change, despite the composite being exposed to temperatures promoting POM movement if they had been applied during activation. To understand this lack of transformation, *in situ* PXRD patterns were collected of the composite both as a dry powder and as a suspension in cyclohexane. In agreement with the post-catalysis pattern, the composite suspended in cyclohexane had no change where the dry powder started changing structure (Figure 4). This suggests that solvent molecules are able to hinder POM migration from the mesopores to the micropores.

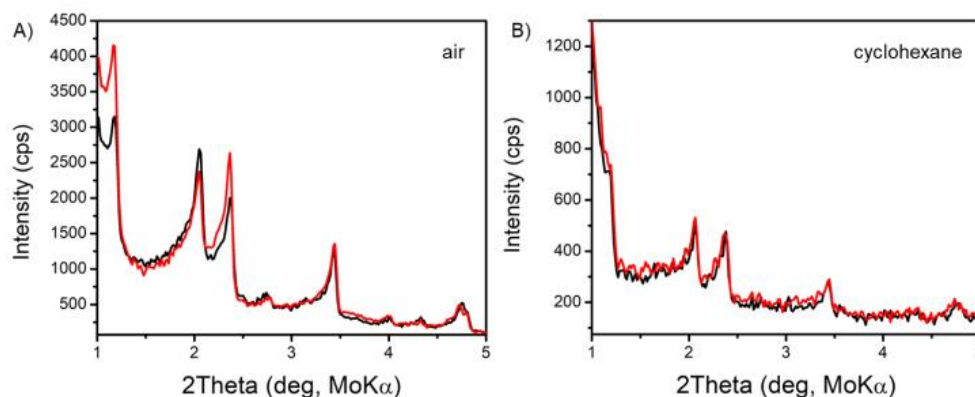


**Figure 7-9** PXRD patterns of  $PV_2Mo_{10}@NU-1000$  collected *in situ* in (A) air and (B) cyclohexane. Black traces were collected at 30 °C and red traces were collected after ramping

## 7.4 Conclusions

To conclude, the composite material  $PV_2Mo_{10}@NU-1000$  was synthesized via post-synthetic impregnation. The material was activated under  $scCO_2$  condition to yield  $PV_2Mo_{10}@NU-1000-scCO_2$  where the introduced POM was found in the mesopore. Heating of

the material at 80 °C moved the POM from the mesopore to the micropore. The two composites were used for aerobic oxidation of CEES in cyclohexane using a sacrificial reductant and were found to enhance the rate compared to using the POM alone. Upon recycling, the  $PV_2Mo_{10}@NU-1000$  materials were able to achieve 100% CEES conversion, while the POM had decomposed, yielding minimal product. These results highlight the utility of crystalline MOFs in supporting guest molecules to understand the structure and the stabilization that MOFs provide to improve reaction rates and stability. Future studies will aim to finely tune control over selectivity using this class of materials for other oxidation reactions of interest.

## References

- (1) Robinson, M. L. J. P. The Rise in CB Weapons. In *The Problem of Chemical and Biological Warfare*; Almquist & Wiksells: Stockholm, 1971.
- (2) Watson, A.; Opresko, D.; Young, R.; Hauschild, V.; King, J.; Bakshi, K. *Handbook of Toxicology of Chemical Warfare Agents*; Gupta, R. C., Ed.; Academic Press: San Diego, 2009.
- (3) Wessely, S., and Krasnov, V.N., eds. *Psychological Responses to the New Terrorism: A NATO-Russia Dialogue*. Amsterdam, NLD: IOS Press, 2005. ProQuest ebrary. Web. 4 April 2016. Copyright © 2005. IOS Press. All rights reserved. **2016**, No. April.
- (4) Geraci, M. J. Mustard gas: Imminent danger or eminent threat? *Ann. Pharmacother.* **2008**, *42* (2), 237–246.
- (5) Smith, B. M. Catalytic methods for the destruction of chemical warfare agents under ambient conditions. *Chem. Soc. Rev.* **2008**, *37* (3), 470–478.
- (6) Karasik, T. W. *Toxic Warfare*; RAND: Santa Monica, 2002.
- (7) Hoskin, B. F.; Robson, R. Design and construction of a new class of scaffolding-like materials comprising infinite polymeric frameworks of 3D-linked molecular rods. A reappraisal of the Zn(CN)<sub>2</sub> and Cd(CN)<sub>2</sub> Structures and the Synthesis and Structure of the Diamond-Related Frameworks. *J. Am. Chem. Soc.* **1990**, *112*, 1546–1554.
- (8) Kitagawa, S.; Kitaura, R.; Noro, S. Functional porous coordination polymers. *Angew. Chemie - Int. Ed.* **2004**, *43*, 2334–2375.
- (9) Férey, G.; Mellot-Draznieks, C.; Serre, C.; Millange, F.; Dutour, J.; Surblé, S.; Margiolaki, I. A chromium terephthalate-based solid with unusually large pore volumes and surface area. *Science* **2005**, *309* (5743), 2040–2042.
- (10) Howarth, A. J.; Peters, A. W.; Vermeulen, N. A.; Wang, T. C.; Hupp, J. T.; Farha, O. K. Best Practices for the Synthesis, Activation, and Characterization of Metal–Organic Frameworks. *Chem. Mater.* **2016**, 26–39.
- (11) Sosa, J. D.; Bennett, T. F.; Nelms, K. J.; Tovar, R. C.; Liu, Y. Metal–Organic Framework Hybrid Materials and Their Applications. *Crystals* **2018**, No. 8, 325.
- (12) Tu, W.; Xu, Y.; Yin, S.; Xu, R. Rational Design of Catalytic Centers in Crystalline Frameworks. *Adv. Mater.* **2018**, *30*, 1707582.
- (13) Juan-Alcañiz, J.; Gascon, J.; Kapteijn, F. Metal–organic frameworks as scaffolds for the encapsulation of active species : state of the art and future perspectives. *J. Mater. Chem.* **2012**, *22*, 10102–10118.
- (14) Bigley, A. N.; Rauschel, F. M. Catalytic Mechanisms for Phosphotriesterases. *Biochim Biophys Acta* **2013**, *1834* (1), 443–453.
- (15) Peterson, G. W.; Moon, S. Y.; Wagner, G. W.; Hall, M. G.; Decoste, J. B.; Hupp, J. T.; Farha, O. K. Tailoring the Pore Size and Functionality of UiO-Type Metal-Organic Frameworks for Optimal Nerve Agent Destruction. *Inorg. Chem.* **2015**, *54* (20), 9684–9686.
- (16) Moon, S. Y.; Wagner, G. W.; Mondloch, J. E.; Peterson, G. W.; DeCoste, J. B.; Hupp, J. T.; Farha, O. K. Effective, Facile, and Selective Hydrolysis of the Chemical Warfare Agent VX Using Zr<sub>6</sub>-Based Metal-Organic Frameworks. *Inorg. Chem.* **2015**, *54* (22), 10829–10833.
- (17) Kehe, K.; Szinicz, L. Medical aspects of sulphur mustard poisoning. *Toxicology* **2005**, 214

- (3), 198–209.
- (18) Davis, K. G.; Aspera, G. Exposure to liquid sulfur mustard. *Ann. Emerg. Med.* **2001**, *37* (6), 653–656.
- (19) Herriott, R. M. Solubility of mustard gas [bis(2-chloroethyl)sulfide] in water, molar sodium chloride and in solutions of detergents. *J. Gen. Physiol.* **1947**, *30* (6), 449–456.
- (20) Hirade, J.; Ninomiya, A. The mechanism of the toxic action of organic halogen compounds. *J. Biochem.* **1950**, *37*, 19–34.
- (21) Ringenbach, C. R.; Livingston, S. R.; Kumar, D.; Landry, C. C. Vanadium-doped acid-prepared mesoporous silica: Synthesis, characterization, and catalytic studies on the oxidation of a mustard gas analogue. *Chem. Mater.* **2005**, *17* (22), 5580–5586.
- (22) Boring, E.; Geletii, Y. V.; Hill, C. L. A Homogeneous Catalyst for Selective O<sub>2</sub> Oxidation at Ambient Temperature. Diversity-Based Discovery and Mechanistic Investigation of Thioether Oxidation by the Au(III)Cl<sub>2</sub>NO<sub>3</sub> (thioether)/O<sub>2</sub> System. *J. Am. Chem. Soc.* **2001**, *123* (8), 1625–1635.
- (23) Marques, A.; Marin, M.; Ruasse, M. F. Hydrogen peroxide oxidation of mustard-model sulfides catalyzed by iron and manganese tetraarylporphyrines. Oxygen transfer to sulfides versus H<sub>2</sub>O<sub>2</sub> dismutation and catalyst breakdown. *J. Org. Chem.* **2001**, *66* (23), 7588–7595.
- (24) Liu, Y.; Howarth, A. J.; Hupp, J. T.; Farha, O. K. Selective Photooxidation of a Mustard-Gas Simulant Catalyzed by a Porphyrinic Metal-Organic Framework. *Angew. Chemie - Int. Ed.* **2015**, *54* (31), 9001–9005.
- (25) Liu, Y.; Moon, S. Y.; Hupp, J. T.; Farha, O. K. Dual-Function Metal-Organic Framework as a Versatile Catalyst for Detoxifying Chemical Warfare Agent Simulants. *ACS Nano* **2015**, *9* (12), 12358–12364.
- (26) Hansen, R. E.; Das, S. Biomimetic di-manganese catalyst cage-isolated in a MOF: robust catalyst for water oxidation with Ce(IV), a non-O-donating oxidant. *Energy Environmental Sci.* **2014**, No. 7, 317–322.
- (27) Xue, Y.; Zheng, S.; Xue, H.; Pang, H. Metal – organic framework composites and their electrochemical applications. *J. Mater. Chem. A* **2019**.
- (28) Long, D. L.; Tsunashima, R.; Cronin, L. Polyoxometalates: Building blocks for functional nanoscale systems. *Angew. Chemie - Int. Ed.* **2010**, *49* (10), 1736–1758.
- (29) Long, D.-L.; Burkholder, E.; Cronin, L. Polyoxometalate clusters, nanostructures and materials: from self assembly to designer materials and devices. *Chem. Soc. Rev.* **2007**, *36* (1), 105–121.
- (30) Hill, C. L. Polyoxometalates: Reactivity. *Compr. Coord. Chem. II* **2004**, *4*, 679–759.
- (31) Pope, M. T. Introduction to Polyoxometalate Chemistry. In *Polyoxometalate Molecular Science*. **2003**, 3–31.
- (32) Pope, M. *Heteropoly and Isopoly Oxometalates*; Springer-Verlag: New York, 1983.
- (33) Nyman, M.; Alam, T. M.; Rodriguez, M. a; Cherry, B. R.; Krumhansl, J. L.; Nenoff, T. M.; Sattler, A. M. A General Synthetic Procedure for Heteropolyniobates. *Science* (80-. ). **2002**, *297* (August), 996–998.
- (34) Nyman, M.; Burns, P. C. A comprehensive comparison of transition-metal and actinyl polyoxometalates. *Chem. Soc. Rev.* **2012**, *41* (22), 7354–7367.
- (35) Weinstock, I. A.; Schreiber, R. E.; Neumann, R. Dioxygen in Polyoxometalate Mediated Reactions. *Chem. Rev.* **2018**, *118* (5), 2680–2717.

- (36) Katsoulis, D. E. A survey of applications of polyoxometalates. *Chem. Rev.* **1998**, *98* (1), 359–387.
- (37) Misra, A.; Franco Castillo, I.; Müller, D. P.; González, C.; Eyssautier-Chuine, S.; Ziegler, A.; de la Fuente, J. M.; Mitchell, S. G.; Streb, C. Polyoxometalate-Ionic Liquids (POM-ILs) as Anticorrosion and Antibacterial Coatings for Natural Stones. *Angew. Chemie - Int. Ed.* **2018**, *57* (45), 14926–14931.
- (38) Chen, J. J.; Ye, J. C.; Zhang, X. G.; Symes, M. D.; Fan, S. C.; Long, D. L.; Zheng, M. Sen; Wu, D. Y.; Cronin, L.; Dong, Q. F. Design and Performance of Rechargeable Sodium Ion Batteries, and Symmetrical Li-Ion Batteries with Supercapacitor-Like Power Density Based upon Polyoxovanadates. *Adv. Energy Mater.* **2018**, *8* (6), 1–6.
- (39) Chen, J. J.; Symes, M. D.; Fan, S. C.; Zheng, M. Sen; Miras, H. N.; Dong, Q. F.; Cronin, L. High-Performance Polyoxometalate-Based Cathode Materials for Rechargeable Lithium-Ion Batteries. *Adv. Mater.* **2015**, *27* (31), 4649–4654.
- (40) Yang, X.; Feng, X.; Tan, H.; Zang, H.; Wang, X.; Wang, Y.; Wang, E.; Li, Y. N-Doped graphene-coated molybdenum carbide nanoparticles as highly efficient electrocatalysts for the hydrogen evolution reaction. *J. Mater. Chem. A* **2016**, *4* (10), 3947–3954.
- (41) Blasco-Ahicart, M.; Soriano-López, J.; Galán-Mascarós, J. R. Conducting Organic Polymer Electrodes with Embedded Polyoxometalate Catalysts for Water Splitting. *ChemElectroChem* **2017**, *4* (12), 3296–3301.
- (42) Lv, H.; Geletii, Y. V.; Zhao, C.; Vickers, J. W.; Zhu, G.; Luo, Z.; Song, J.; Lian, T.; Musaev, D. G.; Hill, C. L. Polyoxometalate water oxidation catalysts and the production of green fuel. *Chem. Soc. Rev.* **2012**, *41* (22), 7572–7589.
- (43) Sullivan, K. P.; Yin, Q.; Collins-Wildman, D. L.; Tao, M.; Geletii, Y. V.; Musaev, D. G.; Lian, T.; Hill, C. L. Multi-tasking POM systems. *Front. Chem.* **2018**, *6*, 365.
- (44) Stracke, J. J.; Finke, R. G. Distinguishing homogeneous from heterogeneous water oxidation catalysis when beginning with polyoxometalates. *ACS Catal.* **2014**, *4* (3), 909–933.
- (45) Bloor, L. G.; Solaraska, R.; Bienkowski, K.; Kulesza, P. J.; Augustynski, J.; Symes, M. D.; Cronin, L. Solar-driven water oxidation and decoupled hydrogen production mediated by an electron-coupled-proton buffer. *J. Am. Chem. Soc.* **2016**, *138* (21), 6707–6710.
- (46) Alharbi, W.; Kozhevnikova, E. F.; Kozhevnikov, I. V. Dehydration of Methanol to Dimethyl Ether over Heteropoly Acid Catalysts: The Relationship between Reaction Rate and Catalyst Acid Strength. *ACS Catal.* **2015**, *5* (12), 7186–7193.
- (47) Macht, J.; Janik, M. J.; Neurock, M.; Iglesia, E. Mechanistic consequences of composition in acid catalysis by polyoxometalate keggins clusters. *J. Am. Chem. Soc.* **2008**, *130* (31), 10369–10379.
- (48) Hill, C. L.; Kholdeeva, O. A. Selective Liquid Phase Oxidations in the Presence of Supported Polyoxometalates. In *Liquid Phase Oxidation via Heterogeneous Catalysis: Organic Synthesis and Industrial Applications*; Clerici, M. G., Kholdeeva, O. A., Eds.; John Wiley & Sons, Inc.: Hoboken, NJ, 2013; pp 263–319.
- (49) Thompson, D. J.; Zhang, Y.; Ren, T. Polyoxometalate [ $\gamma$ -SiW<sub>10</sub>O<sub>34</sub>(H<sub>2</sub>O)<sub>2</sub>]<sup>4-</sup> on MCM-41 as catalysts for sulfide oxygenation with hydrogen peroxide. *J. Mol. Catal. A Chem.* **2014**, *392*, 188–193.
- (50) Liu, R.; Li, S.; Yu, X.; Zhang, G.; Zhang, S.; Yao, J.; Keita, B.; Nadjo, L.; Zhi, L. Facile synthesis of Au-nanoparticle/polyoxometalate/graphene tricomponent nanohybrids: An

- enzyme-free electrochemical biosensor for hydrogen peroxide. *Small* **2012**, 8 (9), 1398–1406.
- (51) Ma, Z.; Qiu, Y.; Yang, H.; Huang, Y.; Liu, J.; Lu, Y.; Zhang, C.; Hu, P. Effective Synergistic Effect of Dipeptide-Polyoxometalate-Graphene Oxide Ternary Hybrid Materials on Peroxidase-like Mimics with Enhanced Performance. *ACS Appl. Mater. Interfaces* **2015**, 7 (39), 22036–22045.
- (52) Lefebvre, F. Synthesis, Characterization and Applications in Catalysis of Polyoxometalate / Zeolite Composites. *Inorganics* **2016**, 4 (2), 13.
- (53) Qi, W.; Wu, L. Polyoxometalate/polymer hybrid materials: Fabrication and properties. *Polym. Int.* **2009**, 58 (11), 1217–1225.
- (54) Duan, Y.; Wei, W.; Xiao, F.; Xi, Y.; Chen, S.-L.; Wang, J.-L.; Xu, Y.; Hu, C. High-valent cationic metal-organic macrocycles as novel supports for immobilization and enhancement of activity of polyoxometalate catalysts. *Catal. Sci. Technol.* **2016**, 6 (24), 8540–8547.
- (55) Gao, W.; Sun, X.; Niu, H.; Song, X.; Li, K.; Gao, H.; Zhang, W.; Yu, J.; Jia, M. Phosphomolybdic acid functionalized covalent organic frameworks: Structure characterization and catalytic properties in olefin epoxidation. *Microporous Mesoporous Mater.* **2015**, 213, 59–67.
- (56) Chen, G.; Zhou, Y.; Wang, X.; Li, J.; Xue, S.; Liu, Y.; Wang, Q.; Wang, J. Construction of porous cationic frameworks by crosslinking polyhedral oligomeric silsesquioxane units with N-heterocyclic linkers. *Sci. Rep.* **2015**, 5, 11236.
- (57) Lian, X.; Fang, Y.; Joseph, E.; Wang, Q.; Li, J.; Banerjee, S.; Lollar, C.; Wang, X.; Zhou, H.-C. Enzyme-MOF (metal-organic framework) composites. *Chem. Soc. Rev.* **2017**, 46, 3386–3401.
- (58) Majewski, M. B.; Peters, A. W.; Wasielewski, M. R.; Hupp, J. T.; Farha, O. K. Metal-Organic Frameworks as Platform Materials for Solar Fuels Catalysis. *ACS Energy Lett.* **2018**, 3, 598–611.
- (59) Li, Z.; Peters, A. W.; Bernales, V.; Ortuño, M. a.; Schweitzer, N. M.; DeStefano, M. R.; Gallington, L. C.; Platero-Prats, A. E.; Chapman, K. W.; Cramer, C. J.; et al. Metal-Organic Framework Supported Cobalt Catalysts for the Oxidative Dehydrogenation of Propane at Low Temperature. *ACS Cent. Sci.* **2017**, 3 (1), 31–38.
- (60) Thompson, A. B.; Pahls, D. R.; Bernales, V.; Gallington, L. C.; Malonzo, C. D.; Webber, T.; Tereniak, S. J.; Wang, T. C.; Desai, S. P.; Li, Z.; et al. Installing Heterobimetallic Cobalt-Aluminum Single Sites on a Metal Organic Framework Support. *Chem. Mater.* **2016**, 28 (18), 6753–6762.
- (61) Feng, X.; Ji, P.; Li, Z.; Drake, T.; Oliveres, P.; Chen, E. Y.; Song, Y.; Wang, C.; Lin, W. Aluminum Hydroxide Secondary Building Units in a Metal-Organic Framework Support Earth-Abundant Metal Catalysts for Broad-Scope Organic Transformations. *ACS Catal.* **2019**, 9 (4), 3327–3337.
- (62) Hagrman, D.; Sangregorio, C.; O'Connor, C. J.; Zubieta, J. Solid state coordination chemistry: two-dimensional oxides constructed from polyoxomolybdate clusters and copper-organoamine subunits. *J. Chem. Soc. Trans.* **1998**, 2 (22), 3707–3709.
- (63) Hagrman, D.; Hagrman, P. J.; Zubieta, J. Solid-State Coordination Chemistry: The Self-Assembly of Microporous Organic - Inorganic Hybrid Frameworks Constructed from Tetrapyridylporphyrin and Bimetallic Oxide Chains or Oxide Clusters. *Angew. Chem. Int.*

- Ed.* **1999**, 38, 3165–3168.
- (64) Ghahramaninezhad, M.; Soleimani, B.; Niknam Shahrak, M. A simple and novel protocol for Li-trapping with a POM/MOF nano-composite as a new adsorbent for CO<sub>2</sub> uptake. *New J. Chem.* **2018**, 42, 4639–4645.
- (65) Pires, J.; Pinto, M. L.; Granadeiro, C. M.; Barbosa, A. D. S.; Cunha-Silva, L.; Balula, S. S.; Saini, V. K. Effect on selective adsorption of ethane and ethylene of the polyoxometalates impregnation in the metal-organic framework MIL-101. *Adsorption* **2014**, 20, 533–543.
- (66) Ma, F.; Liu, S.; Liang, D.; Ren, G.; Zhang, C.; Wei, F.; Su, Z. Hydrogen Adsorption in Polyoxometalate Hybrid Compounds Based on Porous Metal-Organic Frameworks. *Eur. J. Inorg. Chem.* **2010**, 24, 3756–3761.
- (67) Huang, Y.; Wang, R. Highly selective separation of H<sub>2</sub>S and CO<sub>2</sub> using a H<sub>2</sub>S-imprinted polymers loaded on a polyoxometalate@Zr-based metal-organic framework with a core-shell structure at ambient temperature. *J. Mater. Chem. A* **2019**, 7 (19), 12105–12114.
- (68) Chen, Q.; Wang, M. M.; Hu, X.; Chen, X. W.; Wang, J. H. An octamolybdate-metal organic framework hybrid for the efficient adsorption of histidine-rich proteins. *J. Mater. Chem. B* **2016**, 4 (42), 6812–6819.
- (69) Li, R.; Ren, X.; Zhao, J.; Feng, X.; Jiang, X.; Fan, X.; Lin, Z.; Li, X.; Hu, C.; Wang, B. Polyoxometallates trapped in a zeolitic imidazolate framework leading to high uptake and selectivity of bioactive molecules. *J. Mater. Chem. A* **2014**, 2 (7), 2168–2173.
- (70) Zou, F.; Yu, R.; Li, R.; Li, W. Microwave-assisted synthesis of HKUST-1 and functionalized HKUST-1-@H3PW12O<sub>40</sub>: Selective adsorption of heavy metal ions in water analyzed with synchrotron radiation. *ChemPhysChem* **2013**, 14 (12), 2825–2832.
- (71) Salomon, W.; Dolbecq, A.; Roch-marchal, C.; Paille, G.; Dessapt, R.; Mialane, P.; Serierbrault, H.; Parker, D. A Multifunctional Dual-Luminescent Polyoxometalate @ Metal-Organic Framework EuW10@UiO-67 Composite as Chemical Probe and Temperature Sensor. *Front. Chem.* **2018**, 6, 425.
- (72) Wang, C.; Zhou, M.; Ma, Y.; Tan, H.; Wang, Y.; Li, Y. Hybridized Polyoxometalate-Based Metal–Organic Framework with Ketjenblack for the Nonenzymatic Detection of H<sub>2</sub>O<sub>2</sub>. *Chem. - An Asian J.* **2018**, 13 (16), 2054–2059.
- (73) Liu, Y.; Yang, X.; Miao, J.; Tang, Q.; Liu, S.; Shi, Z.; Liu, S. Polyoxometalate-functionalized metal–organic frameworks with improved water retention and uniform proton-conducting pathways in three orthogonal directions. *Chem. Commun.* **2014**, 50 (70), 10023–10026.
- (74) Zhou, E. L.; Qin, C.; Wang, X. L.; Shao, K. Z.; Su, Z. M. Steam-Assisted Synthesis of an Extra-Stable Polyoxometalate-Encapsulating Metal Azolate Framework: Applications in Reagent Purification and Proton Conduction. *Chem. - A Eur. J.* **2015**, 21 (37), 13058–13064.
- (75) Zhang, Y.; Lin, B.; Sun, Y.; Han, P.; Wang, J.; Ding, X.; Zhang, X.; Yang, H. MoO<sub>2</sub>@Cu@C Composites Prepared by Using Polyoxometalates@Metal-Organic Frameworks as Template for All-Solid-State Flexible Supercapacitor. *Electrochim. Acta* **2016**, 188, 490–498.
- (76) Wang, H. N.; Zhang, M.; Zhang, A. M.; Shen, F. C.; Wang, X. K.; Sun, S. N.; Chen, Y. J.; Lan, Y. Q. Polyoxometalate-Based Metal-Organic Frameworks with Conductive

- Polypyrrole for Supercapacitors. *ACS Appl. Mater. Interfaces* **2018**, *10* (38), 32265–32270.
- (77) Salomon, W.; Lan, Y.; Rivière, E.; Yang, S.; Roch-Marchal, C.; Dolbecq, A.; Simonnet-Jégat, C.; Steunou, N.; Leclerc-Laronze, N.; Ruhlmann, L.; et al. Single-Molecule Magnet Behavior of Individual Polyoxometalate Molecules Incorporated within Biopolymer or Metal-Organic Framework Matrices. *Chem. - A Eur. J.* **2016**, *22* (19), 6564–6574.
- (78) Roch-Marchal, C.; Hidalgo, T.; Banh, H.; Fischer, R. A.; Horcajada, P. A Promising Catalytic and Theranostic Agent Obtained through the In-Situ Synthesis of Au Nanoparticles with a Reduced Polyoxometalate Incorporated within Mesoporous MIL-101. *Eur. J. Inorg. Chem.* **2016**, *2016* (27), 4387–4394.
- (79) Li, J.-S.; Sang, X.-J.; Chen, W.-L.; Zhang, L.-C.; Zhu, Z.-M.; Li, Y.-G.; Su, Z.-M.; Wang, E.-B. A strategy for breaking the MOF template to obtain small-sized and highly dispersive polyoxometalate clusters loaded on solid films. *J. Mater. Chem. A* **2015**, *3* (28), 14573–14577.
- (80) Rafiee, E.; Nobakht, N.; Behbood, L. Influence of pH, temperature, and alternating magnetic field on drug release from Keggin-type heteropoly acid encapsulated in iron-carboxylate nanoscale metal-organic framework. *Res. Chem. Intermed.* **2017**, *43* (2), 951–969.
- (81) Xu, W.; Pei, X.; Diercks, C. S.; Lyu, H.; Ji, Z.; Yaghi, O. M. A Metal – Organic Framework of Organic Vertices and Polyoxometalate Linkers as a Solid-State Electrolyte. *J. Am. Chem. Soc.* **2019**.
- (82) Wasson, M. C.; Buru, C. T.; Chen, Z.; Islamoglu, T.; Farha, O. K. Metal-Organic Frameworks: A Tunable Platform to Access Single-Site Heterogeneous Catalysts. *Appl. Catal. A Gen.* **2019**, *586* (May), 117214.
- (83) Juan-Alcañiz, J.; Ramos-Fernandez, E. V.; Lafont, U.; Gascon, J.; Kapteijn, F. Building MOF bottles around phosphotungstic acid ships: One-pot synthesis of bi-functional polyoxometalate-MIL-101 catalysts. *J. Catal.* **2010**, *269*, 229–241.
- (84) James, S. L.; Adams, C. J.; Bolm, C.; Braga, D.; Collier, P.; Friščić, T.; Grepioni, F.; Harris, K. D. M.; Hyett, G.; Jones, W.; et al. Playing with organic radicals as building blocks for functional molecular materials. *Chem. Soc. Rev.* **2012**, *41* (1), 413–447.
- (85) Friščić, T. Supramolecular concepts and new techniques in mechanochemistry: Cocrystals, cages, rotaxanes, open metal-organic frameworks. *Chem. Soc. Rev.* **2012**, *41* (9), 3493–3510.
- (86) Klimakow, M.; Klobes, P.; Thünemann, A. F.; Rademann, K.; Emmerling, F. Mechanochemical synthesis of metal-organic frameworks: A fast and facile approach toward quantitative yields and high specific surface areas. *Chem. Mater.* **2010**, *22* (18), 5216–5221.
- (87) Garay, A. L.; Pichon, A.; James, S. L. Solvent-free synthesis of metal complexes. *Chem. Soc. Rev.* **2007**, *36* (6), 846–855.
- (88) Karadeniz, B.; Howarth, A. J.; Stolar, T.; Islamoglu, T.; Dejanović, I.; Tireli, M.; Wasson, M. C.; Moon, S. Y.; Farha, O. K.; Friščić, T.; et al. Benign by Design: Green and Scalable Synthesis of Zirconium UiO-Metal-Organic Frameworks by Water-Assisted Mechanochemistry. *ACS Sustain. Chem. Eng.* **2018**, *6* (11), 15841–15849.
- (89) Užarević, K.; Wang, T. C.; Moon, S. Y.; Fidelli, A. M.; Hupp, J. T.; Farha, O. K.; Friščić, T. Mechanochemical and solvent-free assembly of zirconium-based metal-organic

- frameworks. *Chem. Commun.* **2016**, 52 (10), 2133–2136.
- (90) Fidelli, A. M.; Karadeniz, B.; Howarth, A. J.; Huskić, I.; Germann, L. S.; Halasz, I.; Etter, M.; Moon, S. Y.; Dinnebier, R. E.; Stilinović, V.; et al. Green and rapid mechanochemical synthesis of high-porosity NU- and UiO-type metal-organic frameworks. *Chem. Commun.* **2018**, 54 (51), 6999–7002.
- (91) Zhong, X.; Lu, Y.; Luo, F.; Liu, Y.; Li, X.; Liu, S. A Nanocrystalline POM@MOFs Catalyst for the Degradation of Phenol: Effective Cooperative Catalysis by Metal Nodes and POM Guests. *Chem. - A Eur. J.* **2018**, 24, 3045–3051.
- (92) Liu, Y.; Liu, S.; Liu, S.; Liang, D.; Li, S.; Tang, Q.; Wang, X.; Miao, J.; Shi, Z.; Zheng, Z. Facile synthesis of a nanocrystalline metal-organic framework impregnated with a phosphovanadomolybdate and its remarkable catalytic performance in ultradeep oxidative desulfurization. *ChemCatChem* **2013**, 5 (10), 3086–3091.
- (93) Li, G.; Zhang, K.; Li, C.; Gao, R.; Cheng, Y.; Hou, L.; Wang, Y. Solvent-free method to encapsulate polyoxometalate into metal-organic frameworks as efficient and recyclable photocatalyst for harmful sulfamethazine degrading in water. *Appl. Catal. B Environ.* **2019**, 245, 753–759.
- (94) Zhao, X.; Duan, Y.; Yang, F.; Wei, W.; Xu, Y.; Hu, C. Efficient Mechanochemical Synthesis of Polyoxometalate@ZIF Complexes as Reusable Catalysts for Highly Selective Oxidation. *Inorg. Chem.* **2017**, 56 (23), 14506–14512.
- (95) Wilke, M.; Klimakow, M.; Rademann, K.; Emmerling, F. Fast and efficient synthesis of a host guest system: A mechanochemical approach. *CrystEngComm* **2016**, 18 (7), 1096–1100.
- (96) Wang, S.; Liu, Y.; Zhang, Z.; Li, X.; Tian, H.; Yan, T.; Zhang, X.; Liu, S.; Sun, X.; Xu, L.; et al. One-Step Template-Free Fabrication of Ultrathin Mixed-Valence Polyoxovanadate-Incorporated Metal-Organic Framework Nanosheets for Highly Efficient Selective Oxidation Catalysis in Air. *ACS Appl. Mater. Interfaces* **2019**, 11 (13), 12786–12796.
- (97) Maksimchuk, N. V.; Kholdeeva, O. A.; Kovalenko, K. A.; Fedin, V. P. MIL-101 supported polyoxometalates: Synthesis, characterization, and catalytic applications in selective liquid-phase oxidation. *Isr. J. Chem.* **2011**, 51 (2), 281–289.
- (98) Maksimchuk, N. V.; Timofeeva, M. N.; Melgunov, M. S.; Shmakov, A. N.; Chesalov, Y. A.; Dybtsev, D. N.; Fedin, V. P.; Kholdeeva, O. A. Heterogeneous selective oxidation catalysts based on coordination polymer MIL-101 and transition metal-substituted polyoxometalates. *J. Catal.* **2008**, 257, 315–323.
- (99) Granadeiro, C. M.; Barbosa, A. D. S.; Silva, P.; Paz, F. A. A.; Saini, V. K.; Pires, J.; De Castro, B.; Balula, S. S.; Cunha-Silva, L. Monovacant polyoxometalates incorporated into MIL-101(Cr): Novel heterogeneous catalysts for liquid phase oxidation. *Appl. Catal. A Gen.* **2013**, 453, 316–326.
- (100) Balula, S. S.; Granadeiro, C. M.; Barbosa, A. D. S.; Santos, I. C. M. S.; Cunha-Silva, L. Multifunctional catalyst based on sandwich-type polyoxotungstate and MIL-101 for liquid phase oxidations. *Catal. Today* **2013**, 210, 142–148.
- (101) Granadeiro, C. M.; Barbosa, A. D. S.; Ribeiro, S.; Santos, I. C. M. S.; de Castro, B.; Cunha-Silva, L.; Balula, S. S. Oxidative catalytic versatility of a trivacant polyoxotungstate incorporated into MIL-101(Cr). *Catal. Sci. Technol.* **2014**, 4 (5), 1416–1425.

- (102) Saedi, Z.; Tangestaninejad, S.; Moghadam, M.; Mirkhani, V.; Mohammadpoor-Baltork, I. The effect of encapsulated Zn-POM on the catalytic activity of MIL-101 in the oxidation of alkenes with hydrogen peroxide. *J. Coord. Chem.* **2012**, *65* (3), 463–473.
- (103) Granadeiro, C. M.; Silva, P.; Saini, V. K.; Paz, F. A. A.; Pires, J.; Cunha-Silva, L.; Balula, S. S. Novel heterogeneous catalysts based on lanthanopolyoxometalates supported on MIL-101(Cr). *Catal. Today* **2013**, *218–219*, 35–42.
- (104) Abednatanzi, S.; Leus, K.; Derakhshandeh, P. G.; Nahra, F.; De Keukeleere, K.; Van Hecke, K.; Van Driessche, I.; Abbasi, A.; Nolan, S. P.; Van Der Voort, P. POM@IL-MOFs – inclusion of POMs in ionic liquid modified MOFs to produce recyclable oxidation catalysts. *Catal. Sci. Technol.* **2017**, *7* (7), 1478–1487.
- (105) Ribeiro, S.; Barbosa, A. D. S.; Gomes, A. C.; Pillinger, M.; Gonçalves, I. S.; Cunha-Silva, L.; Balula, S. S. Catalytic oxidative desulfurization systems based on Keggin phosphotungstate and metal-organic framework MIL-101. *Fuel Process. Technol.* **2013**, *116*, 350–357.
- (106) Fazaeli, R.; Aliyan, H.; Masoudinia, M.; Heidari, Z. Building MOF Bottles (MIL-101 Family as Heterogeneous Single-Site Catalysts) Around H3PW12O40 Ships: An Efficient Catalyst for Selective Oxidation of Sulfides to Sulfoxides and Sulfones. *J. Mater. Chem. Eng.* **2014**, *2* (2), 46–55.
- (107) Julião, D.; Gomes, A. C.; Pillinger, M.; Cunha-Silva, L.; De Castro, B.; Gonçalves, I. S.; Balula, S. S. Desulfurization of model diesel by extraction/oxidation using a zinc-substituted polyoxometalate as catalyst under homogeneous and heterogeneous (MIL-101(Cr) encapsulated) conditions. *Fuel Process. Technol.* **2015**, *131*, 78–86.
- (108) Li, Y.; Gao, Q.; Zhang, L.; Zhou, Y.; Zhong, Y.; Ying, Y.; Zhang, M.; Huang, C. C.; Wang, Y. H5PV2Mo10O40 encapsulated in MIL-101(Cr): Facile synthesis and characterization of rationally designed composite materials for efficient decontamination of sulfur mustard. *Dalt. Trans.* **2018**, *47* (18), 6394–6403.
- (109) Saikia, M.; Bhuyan, D.; Saikia, L. Keggin type phosphotungstic acid encapsulated chromium (III) terephthalate metal organic framework as active catalyst for Biginelli condensation. *Appl. Catal. A Gen.* **2015**, *505*, 501–506.
- (110) Khder, A. E. R. S.; Hassan, H. M. A.; El-Shall, M. S. Metal-organic frameworks with high tungstophosphoric acid loading as heterogeneous acid catalysts. *Appl. Catal. A Gen.* **2014**, *487*, 110–118.
- (111) Bromberg, L.; Hatton, T. A. Aldehyde-Alcohol Reactions Catalyzed under Mild Conditions by Chromium(III) Terephthalate Metal Organic Framework (MIL-101) and Phosphotungstic Acid Composites. *ACS Appl. Mater. Interfaces* **2011**, *3*, 4756–4764.
- (112) Bromberg, L.; Diao, Y.; Wu, H.; Speakman, S. A.; Hatton, T. A. Chromium(III) terephthalate metal organic framework (MIL-101): HF-free synthesis, structure, polyoxometalate composites, and catalytic properties. *Chem. Mater.* **2012**, *24* (9), 1664–1675.
- (113) Juan-Alcañiz, J.; Goesten, M. G.; Ramos-Fernandez, E. V.; Gascon, J.; Kapteijn, F. Towards efficient polyoxometalate encapsulation in MIL-100(Cr): influence of synthesis conditions. *New J. Chem.* **2012**, *36* (4), 977–987.
- (114) Wee, L. H.; Bonino, F.; Lamberti, C.; Bordiga, S.; Martens, J. A. Cr-MIL-101 encapsulated Keggin phosphotungstic acid as active nanomaterial for catalysing the alcoholysis of styrene oxide. *Green Chem.* **2014**, *16* (3), 1351–1357.

- (115) Buru, C. T.; Lyu, J.; Liu, J.; Farha, O. K. Restricting polyoxometalate movement within metal-organic frameworks to assess the role of residual water in catalytic thioether oxidation using these dynamic composites. *Front. Mater.* **2019**, *6*, 152.
- (116) Buru, C. T.; Platero-Prats, A. E.; Chica, D. G.; Kanatzidis, M. G.; Chapman, K. W.; Farha, O. K. Thermally induced migration of a polyoxometalate within a metal-organic framework and its catalytic effects. *J. Mater. Chem. A* **2018**, *6* (17), 7389–7394.
- (117) Chen, Y.; Li, P.; Noh, H.; Kung, C. W.; Buru, C. T.; Wang, X.; Zhang, X.; Farha, O. K. Stabilization of Formate Dehydrogenase in a Metal–Organic Framework for Bioelectrocatalytic Reduction of CO<sub>2</sub>. *Angew. Chemie - Int. Ed.* **2019**, *58* (23), 7682–7686.
- (118) Howarth, A. J.; Katz, M. J.; Wang, T. C.; Platero-Prats, A. E.; Chapman, K. W.; Hupp, J. T.; Farha, O. K. High Efficiency Adsorption and Removal of Selenate and Selenite from Water Using Metal-Organic Frameworks. *J. Am. Chem. Soc.* **2015**, *137* (23), 7488–7494.
- (119) Mondloch, J. E.; Bury, W.; Fairen-Jimenez, D.; Kwon, S.; Demarco, E. J.; Weston, M. H.; Sarjeant, A. A.; Nguyen, S. T.; Stair, P. C.; Snurr, R. Q.; et al. Vapor-phase metalation by atomic layer deposition in a metal-organic framework. *J. Am. Chem. Soc.* **2013**, *135* (28), 10294–10297.
- (120) Wang, T. C.; Vermeulen, N. A.; Kim, I. S.; Martinson, A. B. F.; Stoddart, J. F.; Hupp, J. T.; Farha, O. K. Scalable synthesis and post-modification of a mesoporous metal-organic framework called NU-1000. *Nat. Protoc.* **2015**, *11* (1), 149–162.
- (121) Islamoglu, T.; Otake, K.; Li, P.; Buru, C. T.; Peters, A. W.; Akpınar, I.; Garibay, S. J.; Farha, O. K. Revisiting the structural homogeneity of NU-1000, a Zr-based metal–organic framework. *CrystEngComm* **2018**, *20*, 5913–5918.
- (122) Buru, C. T.; Li, P.; Mehdi, B. L.; Dohnalkova, A.; Platero-Prats, A. E.; Browning, N. D.; Chapman, K. W.; Hupp, J. T.; Farha, O. K. Adsorption of a catalytically accessible polyoxometalate in a channel-type metal-organic framework. *Chem. Mater.* **2017**, *29* (12), 5174–5181.
- (123) Szinicz, L. History of chemical and biological warfare agents. *Toxicology* **2005**, *214* (3), 167–181.
- (124) Katz, M. J.; Mondloch, J. E.; Totten, R. K.; Park, J. K.; Nguyen, S. T.; Farha, O. K.; Hupp, J. T. Simple and Compelling Biomimetic Metal–Organic Framework Catalyst for the Degradation of Nerve Agent Simulants. *Angew. Chemie Int. Ed.* **2013**, *53* (2), 497–501.
- (125) DeCoste, J. B.; Peterson, G. W. Metal–Organic Frameworks for Air Purification of Toxic Chemicals. *Chem. Rev.* **2014**, *114* (11), 5695–5727.
- (126) Katz, M. J.; Moon, S.-Y.; Mondloch, J. E.; Beyzavi, M. H.; Stephenson, C. J.; Hupp, J. T.; Farha, O. K. Exploiting parameter space in MOFs: a 20-fold enhancement of phosphate-ester hydrolysis with UiO-66-NH<sub>2</sub>. *Chem. Sci.* **2015**, *6* (4), 2286–2291.
- (127) Li, P.; Klet, R. C.; Moon, S.-Y. Y.; Wang, T. C.; Deria, P.; Peters, A. W.; Klahr, B. M.; Park, H.-J. J.; Al-Juaid, S. S.; Hupp, J. T.; et al. Synthesis of nanocrystals of Zr-based metal–organic frameworks with csq-net: significant enhancement in the degradation of a nerve agent simulant. *Chem. Commun.* **2015**, *51* (54), 10925–10928.
- (128) López-maya, E.; Montoro, C.; Rodríguez-albelo, L. M.; Cervantes, S. D. A.; Lozano-pérez, A. A.; Cenís, J. L.; Barea, E.; Navarro, J. A. R. Textile/Metal–Organic-Framework Composites as Self-Detoxifying Filters for Chemical-Warfare Agents. *Angew. Chem. Int.*

- Ed.* **2015**, *54*, 6790–6794.
- (129) Moon, S. Y.; Liu, Y.; Hupp, J. T.; Farha, O. K. Instantaneous Hydrolysis of Nerve-Agent Simulants with a Six-Connected Zirconium-Based Metal-Organic Framework. *Angew. Chemie - Int. Ed.* **2015**, *66* (23), 6795–6799.
- (130) Mondloch, J. E.; Katz, M. J.; Isley III, W. C.; Ghosh, P.; Liao, P.; Bury, W.; Wagner, G. W.; Hall, M. G.; Decoste, J. B.; Peterson, G. W.; et al. Destruction of chemical warfare agents using metal–organic frameworks. *Nat. Mater.* **2015**, *14*, 512–516.
- (131) Howarth, A. J.; Liu, Y.; Li, P.; Li, Z.; Wang, T. C.; Hupp, J. T.; Farha, O. K. Chemical, thermal and mechanical stabilities of metal–organic frameworks. *Nat. Rev. Mater.* **2016**, *1*, No. 15018.
- (132) Mondal, S. S.; Holdt, H. J. Breaking Down Chemical Weapons by Metal-Organic Frameworks. *Angew. Chemie - Int. Ed.* **2015**, 42–44.
- (133) Yaghi, O. M.; O’Keeffe, M.; Ockwig, N. W.; Chae, H. K.; Eddaoudi, M.; Kim, J. Reticular synthesis and the design of new materials. *Nature* **2003**, *423* (6941), 705–714.
- (134) Férey, G. Hybrid porous solids: past, present, future. *Chem. Soc. Rev.* **2008**, *37* (1), 191–214.
- (135) Horike, S.; Shimomura, S.; Kitagawa, S. Soft porous crystals. *Nat. Chem.* **2009**, *1* (9), 695–704.
- (136) Farha, O. K.; Hupp, J. T. Rational design, synthesis, purification, and activation of metal-organic framework materials. *Acc. Chem. Res.* **2010**, *43* (8), 1166–1175.
- (137) Li, H.; Moler, D. B.; O’Keeffe, M.; Yaghi, O. M.; Chen, B.; Reineke, T. M.; Eddaoudi, M. Modular Chemistry: Secondary Building Units as a Basis for the Design of Highly Porous and Robust Metal–Organic Carboxylate Frameworks. *Acc. Chem. Res.* **2002**, *34* (4), 319–330.
- (138) Zhou, H. C.; Long, J. R.; Yaghi, O. M. Introduction to metal-organic frameworks. *Chem. Rev.* **2012**, *112* (2), 673–674.
- (139) Kreno, L. E.; Leong, K.; Farha, O. K.; Allendorf, M.; Van Richard P., D.; Hupp, J. T. Metal-Organic Framework Materials as Chemical Sensors. *Chem. Rev.* **2012**, *112*, 1105–1125.
- (140) Furukawa, H.; Cordova, K. E.; O’Keeffe, M.; Yaghi, O. M. The chemistry and applications of metal-organic frameworks. *Science (80- )*. **2013**, *341* (6149), 1230444.
- (141) Liu, J.; Chen, L.; Cui, H.; Zhang, J.; Zhang, L.; Su, C.-Y. Applications of metal-organic frameworks in heterogeneous supramolecular catalysis. *Chem. Soc. Rev.* **2014**, *43* (16), 6011–6061.
- (142) Munro, N. B.; Talmage, S. S.; Griffin, G. D.; Waters, L. C.; Watson, A. P.; King, J. F.; Hauschild, V. The sources, fate, and toxicity of chemical warfare agent degradation products. *Environ. Health Perspect.* **1999**, *107* (12), 933–974.
- (143) Horcajada, P.; Surblé, S.; Serre, C.; Hong, D.-Y.; Seo, Y.-K.; Chang, J.-S.; Grenèche, J.-M.; Margiolaki, I.; Férey, G. Synthesis and catalytic properties of MIL-100(Fe), an iron(iii) carboxylate with large pores. *Chem. Commun.* **2007**, No. 27, 2820–2822.
- (144) Gall, R. D.; Faraj, M.; Hill, C. L. Role of Water in Polyoxometalate-Catalyzed Oxidations in Nonaqueous Media - Scope, Kinetics, and Mechanism of Oxidation of Thioether Mustard (Hd) Analogs By Tert-Butyl Hydroperoxide Catalyzed By H5Pv2Mo10O40. *Inorg. Chem.* **1994**, *33* (22), 5015–5021.
- (145) Richardson, D. E.; Yao, H.; Frank, K. M.; Bennett, D. A. Equilibria, kinetics, and

- mechanism in the bicarbonate activation of hydrogen peroxide: Oxidation of sulfides by peroxydicarbonate. *J. Am. Chem. Soc.* **2000**, *122* (8), 1729–1739.
- (146) Wagner, G. W.; Yang, Y.-C. Rapid nucleophilic/oxidative decontamination of chemical warfare agents. *Ind. Eng. Chem. Res.* **2002**, *41* (8), 1925–1928.
- (147) Yao, H.; Richardson, D. E. Bicarbonate surfactants: Micellar oxidations of aryl sulfides with bicarbonate-activated hydrogen peroxide. *J. Am. Chem. Soc.* **2003**, *125* (20), 6211–6221.
- (148) Okun, N. M.; Tarr, J. C.; Hilleshiem, D. A.; Zhang, L.; Hardcastle, K. I.; Hill, C. L. Highly reactive catalysts for aerobic thioether oxidation: The Fe-substituted polyoxometalate/hydrogen dinitrate system. *J. Mol. Catal. A* **2006**, *246*, 11–17.
- (149) Livingston, S. R.; Landry, C. C. Oxidation of a Mustard Gas Analogue Using an Aldehyde/O<sub>2</sub> System Catalyzed by V-Doped Mesoporous Silica. *J. Am. Chem. Soc.* **2008**, *130*, 13214–13215.
- (150) Derosa, M. C.; Crutchley, R. J. Photosensitized Singlet Oxygen and its Applications. *Coord. Chem. Rev.* **2002**, *233–234*, 351–371.
- (151) Schweitzer, C.; Schmidt, R. Physical mechanisms of generation and deactivation of singlet oxygen. *Chem. Rev.* **2003**, *103* (5), 1685–1757.
- (152) Lu, K.; He, C.; Lin, W. Nanoscale metal-organic framework for highly effective photodynamic therapy of resistant head and neck cancer. *J. Am. Chem. Soc.* **2014**, *136* (48), 16712–16715.
- (153) Park, J.; Jiang, Q.; Feng, D.; Zhou, H. C. Controlled Generation of Singlet Oxygen in Living Cells with Tunable Ratios of the Photochromic Switch in Metal–Organic Frameworks. *Angew. Chemie - Int. Ed.* **2016**, *55* (25), 7188–7193.
- (154) Howarth, A. J.; Majewski, M. B.; Wolf, M. O. Photophysical properties and applications of coordination complexes incorporating pyrene. *Coord. Chem. Rev.* **2015**, *282–283*, 139–149.
- (155) Abdel-Shafi, A. A.; Worrall, D. R.; Wilkinson, F. Singlet oxygen formation efficiencies following quenching of excited singlet and triplet states of aromatic hydrocarbons by molecular oxygen. *J. Photochem. Photobiol. A Chem.* **2001**, *142* (2–3), 133–143.
- (156) Stylianou, K. C.; Heck, R.; Chong, S. Y.; Bacsá, J.; Jones, J. T. A.; Khimiyak, Y. Z.; Bradshaw, D.; Rosseinsky, M. J. A guest-responsive fluorescent 3D microporous metal-organic framework derived from a long-lifetime pyrene core. *J. Am. Chem. Soc.* **2010**, *132* (12), 4119–4130.
- (157) Romanias, M. N.; Andrade-Eiroa, A.; Shahla, R.; Bedjanian, Y.; Zogka, A. G.; Philippidis, A.; Dagaut, P. Photodegradation of pyrene on Al<sub>2</sub>O<sub>3</sub> surfaces: A detailed kinetic and product study. *J. Phys. Chem. A* **2014**, *118* (34), 7007–7016.
- (158) Hod, I.; Bury, W.; Karlin, D. M.; Deria, P.; Kung, C. W.; Katz, M. J.; So, M.; Klahr, B.; Jin, D.; Chung, Y. W.; et al. Directed growth of electroactive metal-organic framework thin films using electrophoretic deposition. *Adv. Mater.* **2014**, *26* (36), 6295–6300.
- (159) Watanabe, Y.; Kuriki, N.; Ishiguro, K.; Sawaki, Y. Persulfoxide and Thiadioxirane Intermediates in the Reaction of Sulfides and Singlet Oxygen. *J. Am. Chem. Soc.* **1991**, *113* (7), 2677–2682.
- (160) Clennan, E. L. Persulfoxide: Key intermediate in reactions of singlet oxygen with sulfides. *Acc. Chem. Res.* **2001**, *34* (11), 875–884.
- (161) Ghabili, K.; Agutter, P. S.; Ghanei, M.; Ansarin, K.; Panahi, Y.; Shoja, M. M. Sulfur

- mustard toxicity: history, chemistry, pharmacokinetics, and pharmacodynamics. *Crit. Rev. Toxicol.* **2011**, *41* (5), 384–403.
- (162) Liu, Y.; Buru, C. T.; Howarth, A. J.; Mahle, J. J.; Buchanan, J. H.; DeCoste, J. B.; Hupp, J. T.; Farha, O. K. Efficient and selective oxidation of sulfur mustard using singlet oxygen generated by a pyrene-based metal–organic framework. *J. Mater. Chem. A* **2016**, *4* (36), 13809–13813.
- (163) Howarth, A. J.; Buru, C. T.; Liu, Y.; Ploskonka, A. M.; Hartlieb, K. J.; McEntee, M.; Mahle, J. J.; Buchanan, J. H.; Durke, E. M.; Al-Juaid, S. S.; et al. Postsynthetic Incorporation of a Singlet Oxygen Photosensitizer in a Metal-Organic Framework for Fast and Selective Oxidative Detoxification of Sulfur Mustard. *Chem. - A Eur. J.* **2016**, *22*, 214–218.
- (164) Goswami, S.; Miller, C. E.; Logsdon, J. L.; Buru, C. T.; Wu, Y.; Bowman, D. N.; Islamoglu, T.; Asiri, A. M.; Cramer, C. J.; Wasielewski, M. R.; et al. Atomistic Approach toward Selective Photocatalytic Oxidation of a Mustard-Gas Simulant: A Case Study with Heavy-Chalcogen-Containing PCN-57 Analogues. *ACS Appl. Mater. Interfaces* **2017**, *9*, 19535–19540.
- (165) Atilgan, A.; Islamoglu, T.; Howarth, A. J.; Hupp, J. T.; Farha, O. K. Detoxification of a Sulfur Mustard Simulant Using a BODIPY- Functionalized Zirconium-Based Metal – Organic Framework. *ACS Appl. Mater. Interfaces* **2017**, *9* (29), 24555–24560.
- (166) Zhang, W.; Cheng, K.; Zhang, H.; Li, Q.; Wang, Z.; Sheng, J.; Li, Y.; Zhao, X.; Wang, X. Highly Efficient and Selective Photooxidation of Sulfur Mustard Simulant by a Triazolobenzothiadiazole-Moiety-Functionalized Metal – Organic Framework in Air. *Inorg. Chem.* **2018**, *57*, 4230–4233.
- (167) Bartelt-Hunt, S. L.; Knappe, D. R. U.; Barlaz, M. A. A review of chemical warfare agent simulants for the study of environmental behavior. *Crit. Rev. Environ. Sci. Technol.* **2008**, *38* (2), 112–136.
- (168) Li, J.-R.; Kuppler, R. J.; Zhou, H.-C. Selective gas adsorption and separation in metal–organic frameworks. *Chem. Soc. Rev.* **2009**, *38* (5), 1477.
- (169) Howarth, A. J.; Wang, T. C.; Al-Juaid, S. S.; Aziz, S. G.; Hupp, J. T.; Farha, O. K. Efficient extraction of sulfate from water using a Zr-metal-organic framework. *Dalt. Trans.* **2015**, *45* (1), 93–97.
- (170) Juan-Alcañiz, J.; Ramos-Fernandez, E. V; Kapteijn, F.; Gascon, J. MOFs as nano-reactors. In *RSC Catalysis Series: Metal Organic Frameworks as Heterogeneous Catalysts*; Xamena, F. L. i, Gascon, J., Eds.; The Royal Society of Chemistry, 2013; Vol. 12, pp 310–343.
- (171) Roman, E. S. Heterogeneous Singlet Oxygen Sensitizers. In *Singlet Oxygen: Applications in Biosciences and Nanosciences*; Nonell, S., Flors, C., Eds.; The Royal Society of Chemistry, 2016; pp 183–208.
- (172) Tanielian, C.; Wolff, C.; Esch, M. Singlet Oxygen Production in Water : Aggregation and Charge-Transfer Effects. *J. Phys. Chem* **1996**, *2* (100), 6555–6560.
- (173) Xie, M.; Yang, X.; Zou, C.; Wu, C. A SnIV Porphyrin-Based Metal- Organic Framework for the Selective Photo-Oxygenation of Phenol and Sulfides. *Inorg. Chem.* **2011**, *50*, 5318–5320.
- (174) Chen, Y. Z.; Wang, Z. U.; Wang, H.; Lu, J.; Yu, S. H.; Jiang, H. L. Singlet oxygen-engaged selective photo-oxidation over pt nanocrystals/porphyrinic MOF: The roles of

- photothermal effect and Pt electronic state. *J. Am. Chem. Soc.* **2017**, *139* (5), 2035–2044.
- (175) Xu, C.; Liu, H.; Li, D.; Su, J.-H.; Jiang, H.-L. Direct evidence of charge separation in a metal–organic framework: efficient and selective photocatalytic oxidative coupling of amines via charge and energy transfer. *Chem. Sci.* **2018**, *9*, 3152–3158.
- (176) Figueiredo, T. L. C.; Johnstone, R. A. W.; Snrrensenl, A. M. P. S.; Burget, D.; Jacques, P. Determination of Fluorescence Yields, Singlet Lifetimes and Singlet Oxygen Yields of Water-Insoluble Porphyrins and Metalloporphyrins in Organic Solvents and in Aqueous Media. *Photochem. Photobiol.* **1999**, *69* (5), 517–528.
- (177) Wilkinson, F.; Helman, W. P.; Ross, A. B. Quantum Yields for the Photosensitized Formation of the Lowest Electronically Excited Singlet State of Molecular Oxygen in Solution. *J. Phys. Chem. Ref. Data* **1993**, *22* (1), 113–262.
- (178) Robinson, A. L.; Stavila, V.; Zeitler, T. R.; White, M. I.; Thornberg, S. M.; Greathouse, A.; Allendorf, M. D. Ultrasensitive Humidity Detection Using Metal–Organic Framework-Coated Microsensors. *Anal. Chem.* **2012**, *84*, 7043–7051.
- (179) Salama, K. N.; Yassine, O.; Shekhah, O.; Eddaoudi, M.; Salama, K. N. MOFs for the Sensitive Detection of Ammonia: Deployment of fcu-MOF Thin Films as Effective Chemical Capacitive Sensors. *ACS Sensors* **2017**, *2*, 1294–1301.
- (180) Shekhah, O.; Liu, J.; Fischer, R. A.; Woll, C. MOF thin films: existing and future applications. *Chem. Soc. Rev.* **2011**, *40*, 1081–1106.
- (181) Zacher, D.; Shekhah, O.; Woll, C.; Fischer, R. A. Thin Films of Metal–Organic Frameworks. *Chem. Soc. Rev.* **2009**, *38*, 1418–1429.
- (182) Kung, C.; Wang, T. C.; Mondloch, J. E.; Fairen-jimenez, D.; Gardner, D. M.; Bury, W.; Klingsporn, J. M.; Barnes, J. C.; Duyne, R. Van; Stoddart, J. F.; et al. Metal–Organic Framework Thin Films Composed of Free-Standing Acicular Nanorods Exhibiting Reversible Electrochromism. *Chem. Mater.* **2013**, *25*, 5012–5017.
- (183) Kung, C.; Mondloch, J. E.; Wang, T. C.; Bury, W.; Ho, W.; Klahr, B. M.; Klet, R. C.; Pellin, M. J.; Farha, O. K.; Hupp, J. T. Metal–Organic Framework Thin Films as Platforms for Atomic Layer Deposition of Cobalt Ions To Enable Electrocatalytic Water Oxidation. *ACS Appl. Mater. Interfaces* **2015**, *7*, 28223–28230.
- (184) Feng, D.; Gu, Z.; Li, J.; Jiang, H.; Wei, Z.; Zhou, H. Zirconium-Metalloporphyrin PCN-222: Mesoporous Metal–Organic Frameworks with Ultrahigh Stability as Biomimetic Catalysts. *Angew. Chemie - Int. Ed.* **2012**, *51*, 10307–10310.
- (185) Tran, L. D.; Ma, J.; Wong-foy, A. G.; Matzger, A. J. A Perylene-Based Microporous Coordination Polymer Interacts Selectively with Electron-Poor Aromatics. *Chem. - A Eur. J.* **2016**, *22*, 5509–5513.
- (186) Li, P.; Moon, S.-Y.; Guelta, M. A.; Lin, L.; Gomez-Gualdrón, D. A.; Snurr, R. Q.; Harvey, S. P.; Hupp, J. T.; Farha, O. K. Nanosizing a Metal – Organic Framework Enzyme Carrier for Accelerating Nerve Agent Hydrolysis. *ACS Nano* **2016**, *10*, 9174–9182.
- (187) Deibert, B. J.; Li, J. A distinct reversible colorimetric and fluorescent low pH response on a water-stable zirconium-porphyrin metal-organic framework. *Chem. Commun.* **2014**, *50* (68), 9636–9639.
- (188) Thornburg, N. E.; Liu, Y.; Li, P.; Hupp, J. T.; Farha, O. K.; Notestein, J. M. MOFs and their grafted analogues: regioselective epoxide ring-opening with Zr<sub>6</sub> nodes. *Catal. Sci. Technol.* **2016**, *6*, 6480–6484.

- (189) Lakowicz, J. R. *Principles of Fluorescence Spectroscopy Principles of Fluorescence Spectroscopy*, 3rd ed.; Springer: New York, 2006.
- (190) Clennan, E. L.; Yang, K. The Remarkable Effect of Methanol on Sulfide Photooxidation. Evidence for its Dual Reactivity. *Tetrahedron Lett.* **1993**, *34* (11), 1697–1700.
- (191) Jensen, F.; Greer, A.; Clennan, E. L. Reaction of organic sulfides with singlet oxygen. A revised mechanism. *J. Am. Chem. Soc.* **1998**, *120* (18), 4439–4449.
- (192) Gouzerh, P.; Proust, A. Main-group element, organic, and organometallic derivatives of polyoxometalates. *Chem. Rev.* **1998**, *98* (1), 77–112.
- (193) Kozhevnikov, I. V. Catalysis by heteropoly acids and multicomponent polyoxometalates in liquid-phase reactions. *Chem. Rev.* **1998**, *98* (1), 171–198.
- (194) Vasylyev, M. V.; Neumann, R. New Heterogeneous Polyoxometalate Based Mesoporous Catalysts for Hydrogen Peroxide Mediated Oxidation Reactions. *J. Am. Chem. Soc.* **2004**, *126* (3), 884–890.
- (195) Mizuno, N.; Yamaguchi, K.; Kamata, K. Epoxidation of olefins with hydrogen peroxide catalyzed by polyoxometalates. *Coord. Chem. Rev.* **2005**, *249*, 1944–1956.
- (196) Cartuyvels, E.; Absillis, G.; Parac-Vogt, T. N. Questioning the paradigm of metal complex promoted phosphodiester hydrolysis: [Mo7O24](6-) polyoxometalate cluster as an unlikely catalyst for the hydrolysis of a DNA model substrate. *Chem. Commun.* **2008**, 85–87.
- (197) Guo, W.; Lv, H.; Sullivan, K. P.; Gordon, W. O.; Balboa, A.; Wagner, G. W.; Musaev, D. G.; Bacsa, J.; Hill, C. L. Broad-Spectrum Liquid- and Gas-Phase Decontamination of Chemical Warfare Agents by One-Dimensional Heteropoly-niobates. *Angew. Chemie - Int. Ed.* **2016**, *55* (26), 7403–7407.
- (198) Bligaard, T.; Nørskov, J. K. Heterogeneous catalysis. *Chem. Bond. Surfaces Interfaces* **2008**, *98* (96), 255–321.
- (199) Fazaeli, R.; Aliyan, H.; Ahmadi, M. A.; Hashemian, S. Host (aluminum incorporated mesocellulose silica foam (Al-MCF))-guest (tungsten polyoxometalate) nanocomposite material: An efficient and reusable catalyst for selective oxidation of sulfides to sulfoxides and sulfones. *Catal. Commun.* **2012**, *29*, 48–52.
- (200) Frenzel, R.; Morales, D.; Romanelli, G.; Sathicq, G.; Blanco, M.; Pizzio, L. Synthesis, characterization and catalytic evaluation of H3PW12O40 included in acrylic acid/acrylamide polymer for the selective oxidation of sulfides. *J. Mol. Catal. A Chem.* **2016**, *420*, 124–133.
- (201) Miras, H. N.; Vilà-Nadal, L.; Cronin, L. Polyoxometalate based open-frameworks (POM-OFs). *Chem. Soc. Rev.* **2014**, *43* (16), 5679–5699.
- (202) Ma, H.; Liu, B.; Li, B.; Zhang, L.; Li, Y. G.; Tan, H. Q.; Zang, H. Y.; Zhu, G. Cationic Covalent Organic Frameworks: A Simple Platform of Anionic Exchange for Porosity Tuning and Proton Conduction. *J. Am. Chem. Soc.* **2016**, *138* (18), 5897–5903.
- (203) Du, D.-Y.; Qin, J.-S.; Li, S.-L.; Su, Z.-M.; Lan, Y.-Q. Recent advances in porous polyoxometalate-based metal-organic framework materials. *Chem. Soc. Rev.* **2014**, *43* (13), 4615–4632.
- (204) Lee, J.; Farha, O. K.; Roberts, J.; Scheidt, K. A.; Nguyen, S. T.; Hupp, J. T. Metal-organic framework materials as catalysts. *Chem. Soc. Rev.* **2009**, *38* (5), 1450–1459.
- (205) Wang, Z.; Cohen, S. M. Postsynthetic modification of metal-organic frameworks. *Chem. Soc. Rev.* **2009**, *38* (5), 1315–1329.

- (206) Salomon, W.; Yazigi, F.-J.; Roch-Marchal, C.; Mialane, P.; Horcajada, P.; Serre, C.; Haouas, M.; Taulelle, F.; Dolbecq, A. Immobilization of Co-containing polyoxometalates in MIL-101(Cr): structural integrity versus chemical transformation. *Dalt. Trans.* **2014**, *43* (33), 12698–12705.
- (207) Sun, C. Y.; Liu, S. X.; Liang, D. D.; Shao, K. Z.; Ren, Y. H.; Su, Z. M. Highly stable crystalline catalysts based on a microporous metal-organic framework and polyoxometalates. *J. Am. Chem. Soc.* **2009**, *131* (5), 1883–1888.
- (208) Canioni, R.; Roch-Marchal, C.; Secheresse, F.; Horcajada, P.; Serre, C.; Hardi-Dan, M.; Ferey, G.; Greneche, J.-M.; Lefebvre, F. F.; Chang, J.-S.; et al. Stable polyoxometalate insertion within the mesoporous metal organic framework MIL-100(Fe). *J. Mater. Chem.* **2011**, *21* (4), 1226–1233.
- (209) Juan-Alcañiz, J.; Goesten, M.; Martinez-Joaristi, A.; Stavitski, E.; Petukhov, A. V.; Gascon, J.; Kapteijn, F. Live encapsulation of a Keggin polyanion in NH<sub>2</sub>-MIL-101(Al) observed by in situ time resolved X-ray scattering. *Chem. Commun.* **2011**, *47* (30), 8578.
- (210) Salomon, W.; Roch-Marchal, C.; Mialane, P.; Rouschmeyer, P.; Serre, C.; Haouas, M.; Taulelle, F.; Yang, S.; Ruhlmann, L.; Dolbecq, A. Immobilization of polyoxometalates in the Zr-based metal organic framework UiO-67. *Chem. Commun.* **2015**, *51* (14), 2972–2975.
- (211) Song, J.; Luo, Z.; Britt, D. K.; Furukawa, H.; Yaghi, O. M.; Hardcastle, K. I.; Hill, C. L. A Multiunit Catalyst with Synergistic Stability and Reactivity: A Polyoxometalate-Metal Organic Framework for Aerobic Decontamination. *J. Am. Chem. Soc.* **2011**, *133* (42), 16839–16846.
- (212) Planas, N.; Mondloch, J. E.; Tussupbayev, S.; Borycz, J.; Gagliardi, L.; Hupp, J. T.; Farha, O. K.; Cramer, C. J. Defining the Proton Topology of the Zr 6 -Based Metal-Organic Framework NU-1000. *J. Phys. Chem. Lett.* **2014**, *6*, 3716–3723.
- (213) Noh, H.; Cui, Y.; Peters, A. W.; Pahls, D. R.; Ortuno, M. A.; Vermeulen, N. A.; Cramer, C. J.; Gagliardi, L.; Hupp, J. T.; Farha, O. K. An Exceptionally Stable Metal-Organic Framework Supported Molybdenum(VI) Oxide Catalyst for Cyclohexene Epoxidation. *J. Am. Chem. Soc.* **2016**, *138* (44), 14720–14726.
- (214) Ahn, S.; Thornburg, N. E.; Li, Z.; Wang, T. C.; Gallington, L. C.; Chapman, K. W.; Notestein, J. M.; Hupp, J. T.; Farha, O. K. Stable metal-organic framework-supported niobium catalysts. *Inorg. Chem.* **2016**, *55* (22), 11954–11961.
- (215) Deria, P.; Bury, W.; Hupp, J. T.; Farha, O. K. Versatile functionalization of the NU-1000 platform by solvent-assisted ligand incorporation. *Chem. Commun.* **2014**, *50* (16), 1965–1968.
- (216) Li, P.; Modica, J. A.; Howarth, A. J.; Vargas L., E.; Moghadam, P. Z.; Snurr, R. Q.; Mrksich, M.; Hupp, J. T.; Farha, O. K. Toward Design Rules for Enzyme Immobilization in Hierarchical Mesoporous Metal-Organic Frameworks. *Chem* **2016**, *1* (1), 154–169.
- (217) Ebrahimi, N.; Fazaeli, R.; Aliyan, H. One-pot hydrothermal synthesis of H<sub>3</sub>PW<sub>12</sub>O<sub>40</sub> supported on zeolite imidazolate frameworks (ZIF-8): a highly efficient heterogeneous catalyst for oxidation of sulfides to sulfoxides and sulfones. *Zeitschrift fuer Naturforsch. B* **2016**, *71* (3), 211–217.
- (218) Frenzel, R.; Pizzio, L.; Blanco, M.; Sathicq, G.; Romanelli, G. Evaluation of the Catalytic Activity of H<sub>3</sub>PW<sub>12</sub>O<sub>40</sub> in the Selective Oxidation of Sulfides to the Corresponding Sulfoxides or Sulfones. *Curr. Catal.* **2016**, *5* (3), 124–130.

- (219) Salavati, H.; Tavakkoli, N.; Hosseinpour, M. Preparation and characterization of polyphosphotungstate/ZrO<sub>2</sub> nanocomposite and their sonocatalytic and photocatalytic activity under UV light illumination. *Ultrason. Sonochem.* **2012**, *19* (3), 546–553.
- (220) Lousada, C. M.; Johansson, A. J.; Brinck, T.; Jonsson, M. Mechanism of H<sub>2</sub>O<sub>2</sub> Decomposition on Transition Metal Oxide Surfaces. *J. Phys. Chem. C* **2012**, *116* (17), 9533–9543.
- (221) Faccioli, F.; Bauer, M.; Pedron, D.; Sorarù, A.; Carraro, M.; Gross, S. Hydrolytic Stability and Hydrogen Peroxide Activation of Zirconium-Based Oxoclusters. *Eur. J. Inorg. Chem.* **2015**, *2015* (2), 210–225.
- (222) Le Bail, A.; Duroy, H.; Fourquet, J. L. Ab-initio structure determination of LiSbWO<sub>6</sub> by X-ray powder diffraction. *Mater. Res. Bull.* **1988**, *23* (3), 447–452.
- (223) Petříček, V.; Dušek, M.; Palatinus, L. Crystallographic Computing System JANA2006: General features. *Zeitschrift für Krist. - Cryst. Mater.* **2014**, *229*, 345.
- (224) Yakovenko, A. A.; Reibenspies, J. H.; Bhuvanesh, N.; Zhou, H.-C. Generation and applications of structure envelopes for porous metal-organic frameworks. *J. Appl. Crystallogr.* **2013**, *46* (2), 346–353.
- (225) Klet, R. C.; Liu, Y.; Wang, T. C.; Hupp, J. T.; Farha, O. K. Evaluation of Bronsted acidity and proton topology in Zr- and Hf-based metal-organic frameworks using potentiometric acid-base titration. *J. Mater. Chem. A* **2016**, *4* (4), 1479–1485.
- (226) Prabhakaran, V.; Mehdi, B. L.; Ditto, J. J.; Engelhard, M. H.; Wang, B.; Gunaratne, K. D. D.; Johnson, D. C.; Browning, N. D.; Johnson, G. E.; Laskin, J. Rational design of efficient electrode-electrolyte interfaces for solid-state energy storage using ion soft landing. *Nat. Commun.* **2016**, *7*, 11399.
- (227) Gallington, L. C.; Kim, I. S.; Liu, W. G.; Yakovenko, A. A.; Platero-Prats, A. E.; Li, Z.; Wang, T. C.; Hupp, J. T.; Farha, O. K.; Truhlar, D. G.; et al. Regioselective Atomic Layer Deposition in Metal-Organic Frameworks Directed by Dispersion Interactions. *J. Am. Chem. Soc.* **2016**, *138* (41), 13513–13516.
- (228) Yakovenko, A. A.; Wei, Z.; Wriedt, M.; Li, J.-R.; Halder, G. J.; Zhou, H. Study of Guest Molecules in Metal – Organic Frameworks by Powder X-ray Diffraction: Analysis of Difference Envelope Density. *Cryst. Growth Des.* **2014**, *14*, 5397–5407.
- (229) Armatas, G. S.; Katsoulidis, A. P.; Petrakis, D. E.; Pomonis, P. J. Synthesis and acidic catalytic properties of ordered mesoporous alumina–tungstophosphoric acid composites. *J. Mater. Chem.* **2010**, *20* (39), 8631.
- (230) De Sousa, P. M. P.; Grazina, R.; Barbosa, A. D. S.; De Castro, B.; Moura, J. J. G.; Cunha-Silva, L.; Balula, S. S. Insights into the electrochemical behaviour of composite materials: Monovacant polyoxometalates @ porous metal-organic framework. *Electrochim. Acta* **2013**, *87*, 853–859.
- (231) Ganapathy, S.; Fournier, M.; Paul, J. F.; Delevoye, L.; Guelton, M.; Amoureux, J. P. Location of protons in anhydrous kegglin heteropolyacids H<sub>3</sub>PMo<sub>12</sub>O<sub>40</sub> and H<sub>3</sub>PW<sub>12</sub>O<sub>40</sub> by <sup>1</sup>H{<sup>31</sup>P}/<sup>31</sup>P{<sup>1</sup>H} REDOR NMR and DFT quantum chemical calculations. *J. Am. Chem. Soc.* **2002**, *124* (26), 7821–7828.
- (232) Chidichimo, G.; Golemme, A.; Imbardelli, D.; Iannibello, A. <sup>31</sup>P Nuclear Magnetic Resonance Investigation of Solid Dodecatungstophosphoric Acid H<sub>3</sub>PW<sub>12</sub>O<sub>40</sub> xH<sub>2</sub>O at Different Hydration Levels. *J. Chem. Soc. Faraday Transactions* **1992**, *88* (3), 483–487.
- (233) Maksimchuk, N. V.; Kovalenko, K. A.; Arzumanov, S. S.; Chesalov, Y. A.; Melgunov,

- M. S.; Stepanov, A. G.; Fedin, V. P.; Kholdeeva, O. A. Hybrid polyoxotungstate/MIL-101 materials: Synthesis, characterization, and catalysis of H<sub>2</sub>O<sub>2</sub>-based alkene epoxidation. *Inorg. Chem.* **2010**, *49* (6), 2920–2930.
- (234) Mastikhin, V. M.; Terskikh, V. V.; Timofeeva, M. N.; Krivoruchko, O. P. <sup>1</sup>H, <sup>31</sup>P NMR MAS, infrared and catalytic studies of heteropolyacid H<sub>3</sub>PW<sub>12</sub>O<sub>40</sub> supported on MgF<sub>2</sub>. *J. Mol. Catal. A Chem.* **1995**, *95* (2), 135–140.
- (235) Cavka, J. H.; Jakobsen, S.; Olsbye, U.; Guillou, N.; Lamberti, C.; Bordiga, S.; Lillerud, K. P. A new zirconium inorganic building brick forming metal organic frameworks with exceptional stability. *J. Am. Chem. Soc.* **2008**, *130* (42), 13850–13851.
- (236) Zhu, Z.; Tain, R.; Rhodes, C. A study of the decomposition behaviour of 12-tungstophosphate heteropolyacid in solution. *Can. J. Chem.* **2003**, *81* (10), 1044–1050.
- (237) Yang, X.-F.; Wang, A.; Qiao, B.; Li, J.; Liu, J.; Zhang, T. Single-Atom Catalysts: A New Frontier in Heterogeneous Catalysis. *Acc. Chem. Res.* **2013**, *46* (8), 1740–1748.
- (238) Yang, D.; Odoh, S. O.; Wang, T. C.; Farha, O. K.; Hupp, J. T.; Cramer, C. J.; Gagliardi, L.; Gates, B. C. Metal – Organic Framework Nodes as Nearly Ideal Supports for Molecular Catalysts: NU-1000- and UiO-66-Supported Iridium Complexes. *J. Am. Chem. Soc.* **2015**, *137*, 7391–7396.
- (239) Byun, J.; Patel, H. A.; Kim, D. J.; Jung, C. H.; Park, J. Y.; Choi, J. W.; Yavuz, C. T. Nanoporous networks as caging supports for uniform, surfactant-free Co<sub>3</sub>O<sub>4</sub> nanocrystals and their applications in energy storage and conversion. *J. Mater. Chem. A* **2015**, *3*, 15489–15497.
- (240) Collman, J. P.; Hegedus, L. S.; Cooke, M. P.; Norton, J. R.; Dolcetti, G.; Marquardt, D. N. Resin-Bound Transition Metal Complexes. *J. Am. Chem. Soc.* **1972**, *94* (5), 1789–1790.
- (241) Michalska, B. Z. M.; Webster, D. E. Supported Homogeneous Catalysts: Transition Metal Complexes with Polymeric Ligands. *Platin. Met. Rev.* **1974**, *18* (2), 65–73.
- (242) Mines, P. D.; Byun, J.; Hwang, Y.; Patel, H. A.; Andersen, H. R.; Yavuz, C. T. Nanoporous networks as effective stabilisation matrices for nanoscale zero-valent iron and groundwater pollutant removal. *J. Mater. Chem. A* **2015**, *4*, 632–639.
- (243) McMorn, P.; Hutchings, G. J. Heterogeneous enantioselective catalysts: strategies for the immobilisation of homogeneous catalysts. *Chem. Soc. Rev.* **2004**, *33*, 108–122.
- (244) Wegener, S. L.; Marks, T. J.; Stair, P. C. Design Strategies for the Molecular Level Synthesis of Supported Catalysts. *Acc. Chem. Res.* **2012**, *45* (2), 206–214.
- (245) Munnik, P.; de Jongh, P. E.; de Jong, K. P. Recent Developments in the Synthesis of Supported Catalysts. *Chem. Rev.* **2015**, *115*, 6687–6718.
- (246) Védrine, J. C. Revisiting active sites in heterogeneous catalysis: Their structure and their dynamic behaviour. *Appl. Catal. A, Gen.* **2014**, *474*, 40–50.
- (247) Zhang, D.; Li, X.; Liu, S.; Zhu, X.; Chen, F.; Xu, L. Metathesis of 1-Butene to Propene over Mo/Al<sub>2</sub>O<sub>3</sub>@SBA-15: Influence of Alumina Introduction Methods on Catalytic Performance. *Chem. - An Asian J.* **2015**, *10* (8), 1647–1659.
- (248) Mejía, C. H.; Otter, J. H. Den; Weber, J. L.; Jong, K. P. De. Applied Catalysis A, General Crystalline niobia with tailored porosity as support for cobalt catalysts for the Fischer – Tropsch synthesis. *Appl. Catal. A, Gen.* **2017**, *548*, 143–149.
- (249) Ye, J.-J.; Wu, C. Immobilization of polyoxometalates in crystalline solids for highly efficient heterogeneous catalysis. *Dalt. Trans.* **2016**, *45* (25), 10101–10112.
- (250) Izumi, Y.; Urabe, K. Catalysis of Heteropoly Acids Entrapped in Activated Carbon.

- Chem. Lett.* **1981**, *10* (5), 663–666.
- (251) Genovese, M.; Lian, K. Polyoxometalate modified pine cone biochar carbon for supercapacitor electrodes. *J. Mater. Chem. A* **2017**, *5*, 3939–3947.
- (252) Herna, J. G.; Corte, M. A.; Lo, E.; Armenda, H.; Lo, T. Skeletal isomerization of 1-butene on 12-tungstophosphoric acid supported on zirconia. *Appl. Catal. A, Gen.* **1998**, *175*, 43–53.
- (253) Lauinger, S. M.; Sumliner, J. M.; Yin, Q.; Xu, Z.; Liang, G.; Glass, E. N.; Lian, T.; Hill, C. L. High Stability of Immobilized Polyoxometalates on TiO<sub>2</sub> Nanoparticles and Nanoporous Films for Robust, Light-Induced Water Oxidation. **2015**.
- (254) Gomez-Mingot, M.; Roch-Marchal, C.; Lassalle-Kaiser, B.; Mialane, P.; Fontecave, M.; Mellot-Draznieks, C.; Dolbecq, A. A Fully Noble Metal-Free Photosystem Based on Cobalt- Polyoxometalates Immobilized in a Porphyrinic Metal–Organic Framework for Water Oxidation. *J. Am. Chem. Soc.* **2018**, *140* (10), 3613–3618.
- (255) Chen, L.; Luque, R.; Li, Y. Controllable design of tunable nanostructures inside metal – organic frameworks. *Chem. Soc. Rev.* **2017**, *46*, 4614–4630.
- (256) Bromberg, L.; Su, X.; Hatton, T. A. Heteropolyacid-functionalized aluminum 2-aminoterephthalate metal-organic frameworks as reactive aldehyde sorbents and catalysts. *ACS Appl. Mater. Interfaces* **2013**, *5* (12), 5468–5477.
- (257) Nelson, A. P.; Farha, O. K.; Mulfort, K. L.; Hupp, J. T. Supercritical Processing as a Route to High Internal Surface Areas and Permanent Microporosity in Metal - Organic Framework Materials. *J. Am. Chem. Soc.* **2009**, *131*, 458–460.
- (258) Farha, O. K.; Shultz, A. M.; Sarjeant, A. A.; Nguyen, S. T.; Hupp, J. T. Active-Site-Accessible, Porphyrinic Metal À Organic Framework Materials. *J. Am. Chem. Soc.* **2011**, *133*, 5652–5655.
- (259) Shultz, A. M.; Farha, O. K.; Adhikari, D.; Sarjeant, A. A.; Hupp, J. T.; Nguyen, S. T. Selective Surface and Near-Surface Modification of a Noncatenated, Catalytically Active Metal-Organic Framework Material Based on Mn(salen) Struts. *Inorg. Chem.* **2011**, *50*, 3174–3176.
- (260) Webber, T. E.; Liu, W.; Desai, S. P.; Lu, C. C.; Truhlar, D. G.; Penn, R. L. Role of a Modulator in the Synthesis of Phase-Pure NU-1000. *ACS Appl. Mater. Interfaces* **2017**, *9*, 39342–39346.
- (261) Fournier, M.; Feumi-Jantou, C.; Rabia, C.; Herve, G.; Launay, S. Polyoxometalates Catalyst Materials: X-Ray Thermal Stability Study of Phosphorus-containing Heteropolyacids H<sub>3</sub>+xPM<sub>12</sub>-xV<sub>x</sub>O<sub>40</sub> 13-14H<sub>2</sub>O (M=Mo, W; x=0-1). *J. Mater. Chem.* **1992**, *2* (9), 971–978.
- (262) Lefebvre, F. 31P MAS NMR Study of H<sub>3</sub>PW<sub>12</sub>O<sub>40</sub> Supported on Silica. *J. Chem. Soc., Chem. Commun.* **1992**, *0*, 756–757.
- (263) Damyanova, S.; Fierro, J. L. G.; Sobrados, I.; Sanz, J. Surface Behavior of Supported 12-Heteropoly Acid As Revealed by Nuclear Magnetic Resonance , X-ray Photoelectron Spectroscopy , and Fourier Transform. *Langmuir* **1999**, *15* (2), 469–476.
- (264) Sofia, L. T. A.; Krishnan, A.; Sankar, M.; Raj, N. K. K.; Manikandan, P.; Rajamohanam, P. R.; Ajithkumar, T. G. Immobilization of Phosphotungstic Acid ( PTA ) on Imidazole Functionalized Silica : Evidence for the Nature of PTA Binding by Solid State NMR and Reaction Studies. *J. Phys. Chem. C* **2009**, *113*, 21114–21122.
- (265) Kung, C.; Otake, K.; Buru, C. T.; Goswami, S.; Cui, Y.; Hupp, J. T.; Spokoyny, A. M.;

- Farha, O. K. Increased Electrical Conductivity in a Mesoporous Metal – Organic Framework Featuring Metallacarboranes Guests. *J. Am. Chem. Soc.* **2018**, DOI: 10.1021/jacs.8b00605.
- (266) López-salinas, E.; Hernández-cortéz, J. G.; Schifter, I.; Torres-Garcia, E.; Navarrete, J.; Gutierrez-Carrillo, A.; Lopez, T.; Lottici, P. P.; Bersani, D. Thermal stability of 12-tungstophosphoric acid supported on zirconia. *Appl. Catal. A, Gen.* **2000**, *193*, 215–225.
- (267) Riches, J.; Read, R. W.; Black, R. M. Analysis of the sulphur mustard metabolites thiodiglycol and thiodiglycol sulphoxide in urine using isotope-dilution gas chromatography-ion trap tandem mass spectrometry. *J. Chromatogr. B Anal. Technol. Biomed. Life Sci.* **2007**, *845* (1), 114–120.
- (268) Doherty, S.; Knight, J. G.; Carroll, M. A.; Clemmet, A. R.; Ellison, J. R.; Backhouse, T.; Holmes, N.; Thompson, L. A.; Bourne, R. A. Efficient and selective oxidation of sulfides in batch and continuous flow using styrene-based polymer immobilised ionic liquid phase supported peroxotungstates. *RSC Adv.* **2016**, *6*, 73118–73131.
- (269) Vargas L., E.; Snurr, R. Q. Heterogeneous Diffusion of Alkanes in the Hierarchical Metal–Organic Framework NU-1000. *Langmuir* **2015**, *31*, 10056–10065.
- (270) Reiner, B. R.; Kassie, A. A.; Wade, C. R. Unveiling Reactive Metal Sites in a Pd Pincer MOF : Insights into Lewis Acid catalysis. *Dalt. Trans.* **2019**.
- (271) Garce, J. M.; Meima, G. R.; Jacobs, Æ. P. A.; Martens, Æ. J. A.; Lee, G. J. Shape Selective Chemistries with Modified Mordenite Zeolites. *Top Catal.* **2009**, *52*, 1175–1181.
- (272) Liu, J.; Ye, J.; Li, Z.; Otake, K.; Liao, Y.; Peters, A. W.; Noh, H.; Truhlar, D. G.; Gagliardi, L.; Cramer, C. J.; et al. Beyond the Active Site: Tuning the Activity and Selectivity of a Metal–Organic Framework-Supported Ni Catalyst for Ethylene Dimerization. *J. Am. Chem. Soc.* **2018**, *140*, 11174–11178.
- (273) Nasalevich, M. A.; Veen, M. Van Der; Kapteijn, F.; Gascon, J. Metal–organic frameworks as heterogeneous photocatalysts: advantages and challenges. *CrystEngComm* **2014**, *16*, 4919–4926.
- (274) Pikus, J. D.; Studts, J. M.; Mcclay, K.; Steffan, R. J.; Fox, B. G. Changes in the Regiospecificity of Aromatic Hydroxylation Produced by Active Site Engineering in the Diiron Enzyme Toluene 4-Monooxygenase. *Biochemistry* **1997**, *36*, 9283–9289.
- (275) Vermoortele, F.; Ameloot, R.; Alaerts, L.; Matthesen, R.; Carlier, B.; Fernandez, E. V. R.; Gascon, J.; Vos, D. E. De. Tuning the catalytic performance of metal–organic frameworks in fine chemistry by active site engineering. *J. Mater. Chem.* **2012**, *22*, 10313–10321.
- (276) Vandichel, M.; Hajek, J.; Vermoortele, F.; Waroquier, M.; Vos, D. E. De; Speybroeck, V. Van. Active site engineering in UiO-66 type metal–organic frameworks by intentional creation of defects: a theoretical rationalization. *CrystEngComm* **2015**, *17*, 395–406.
- (277) Palmer, R. H.; Kung, C.; Liu, J.; Farha, O. K.; Hupp, J. T. Nickel – Carbon – Zirconium Material Derived from Nickel-Oxide Clusters Installed in a Metal – Organic Framework Scaffolded by Atomic Layer Deposition. *Langmuir* **2018**, *34*, 14143–14150.
- (278) Yang, D.; Gates, B. C. Catalysis by Metal Organic Frameworks : Perspective and Suggestions for Future Research. *ACS Catal.* **2019**, *9*, 1779–1798.
- (279) Jiao, L.; Yen, J.; Seow, R.; Skinner, W. S.; Wang, Z. U.; Jiang, H. Metal–Organic frameworks : Structures and functional applications. *Mater. Today* **2018**.

- (280) Chen, Z.; Hanna, S. L.; Redfern, L. R.; Alezi, D.; Islamoglu, T.; Farha, O. K. Reticular chemistry in the rational synthesis of functional zirconium cluster-based MOFs. *Coord. Chem. Rev.* **2019**, *386*, 32–49.
- (281) Hou, Y.; An, H.; Zhang, Y.; Hu, T.; Yang, W.; Chang, S. Rapid Destruction of Two Types of Chemical Warfare Agent Simulants by Hybrid Polyoxomolybdates Modified by Carboxylic Acid Ligands. *ACS Catal.* **2018**, *8*, 6062–6069.
- (282) Anyushin, A. V.; Sap, A.; Quanten, T.; Proost, P.; Parac-Vogt, T. N. Selective hydrolysis of ovalbumin promoted by Hf(IV)-substituted Wells-Dawson-type polyoxometalate. *Front. Chem.* **2018**, *6*, 614.
- (283) Wang, S.; Yang, G. Recent Advances in Polyoxometalate-Catalyzed Reactions. *Chem. Rev.* **2015**, *115*, 4893–4962.
- (284) Gumerova, N. I.; Rompel, A. Synthesis, structures and applications of electron-rich polyoxometalates. *Nat. Rev. Chem.* **2018**, *2*, 0112.
- (285) Kholdeeva, O. A.; Maksimchuk, N. V.; Maksimov, G. M. Polyoxometalate-based heterogeneous catalysts for liquid phase selective oxidations: Comparison of different strategies. *Catal. Today* **2010**, *157*, 107–113.
- (286) Nohra, B.; Moll, H. El; Albelo, L. M. R.; Mialane, P.; Mellot-draznieks, C.; Kee, M. O.; Biboum, R. N.; Keita, B.; Nadjjo, L.; Dolbecq, A.; et al. Polyoxometalate-based metal organic frameworks (POMOFs): Structural trends, energetics, and high electrocatalytic efficiency for hydrogen evolution reaction. *J. Am. Chem. Soc.* **2011**, *133* (34), 13363–13374.
- (287) Cai, X.; Xu, Q.; Tu, G.; Fu, Y.; Zhang, F.; Zhu, W. Synergistic catalysis of ruthenium nanoparticles and polyoxometalate integrated within single UiO-66 microcrystals for boosting the efficiency of methyl levulinate to  $\gamma$ -valerolactone. *Front. Chem.* **2019**, *7*, 42.
- (288) Lin, Z. J.; Zheng, H. Q.; Chen, J.; Zhuang, W. E.; Lin, Y. X.; Su, J. W.; Huang, Y. B.; Cao, R. Encapsulation of Phosphotungstic Acid into Metal-Organic Frameworks with Tunable Window Sizes: Screening of PTA@MOF Catalysts for Efficient Oxidative Desulfurization. *Inorg. Chem.* **2018**, *57* (20), 13009–13019.
- (289) Buru, C. T.; Platero-Prats, A. E.; Chica, D. G.; Kanatzidis, M. G.; Chapman, W.; Farha, O. K. Thermally induced migration of a polyoxometalate within a metal-organic framework and its catalytic. *J. Mater. Chem. A* **2018**, *6*, 7389–7394.
- (290) Ahn, S.; Nauert, S. L.; Buru, C. T.; Rimoldi, M.; Choi, H.; Schweitzer, N. M.; Hupp, J. T.; Farha, O. K.; Notestein, J. M. Pushing the Limits on Metal-Organic Frameworks as a Catalyst Support: NU-1000 Supported Tungsten Catalysts for o-Xylene Isomerization and Disproportionation. *J. Am. Chem. Soc.* **2018**, *140* (27), 8535–8543.
- (291) Al-Ajlouni, A. M.; Daiafla, T. M.; El-Khateeb, M. New nitrophenyl-substituted polyperoxotungstate catalyst: A more active and selective for the oxidation of sulfides by hydrogen peroxide. *J. Mol. Catal. A* **2007**, *275*, 139–147.
- (292) Peters, A. W.; Otake, K.; Platero-Prats, A. E.; Li, Z.; Destefano, M. R.; Chapman, K. W.; Farha, O. K.; Hupp, J. T. Site-directed synthesis of cobalt oxide clusters in a metal-organic framework. *ACS Appl. Mater. Interfaces* **2018**, *10*, 15073–15078.
- (293) Lyu, J.; Zhang, X.; Otake, K.; Wang, X.; Li, P.; Li, Z.; Chen, Z.; Zhang, Y.; Wasson, M. C.; Ying, Y.; et al. Topology and porosity control of metal-organic frameworks through linker functionalization. *Chem. Sci.* **2018**.
- (294) Wasson, M. C.; Lyu, J.; Islamoglu, T.; Farha, O. K. Linker Competition within a Metal-

- Organic Framework for Topological Insights. *Inorg. Chem.* **2018**, *58*, 1513–1517.
- (295) Védrine, J. C. Heterogeneous catalysis on metal oxides. *Catalysts* **2017**, *7* (11), 341.
- (296) Okun, N. M.; Anderson, T. M.; Hill, C. L. [(FeIII(OH2)2)3(A-r-PW9O34)2]9- on Cationic Silica Nanoparticles, a New Type of Material and Efficient Heterogeneous Catalyst for Aerobic Oxidations. *J. Am. Chem. Soc.* **2003**, *3*, 3194–3195.
- (297) Zhou, Y.; Chen, G.; Long, Z.; Wang, J. Recent advances in polyoxometalate-based heterogeneous catalytic materials for liquid-phase organic transformations. *RSC Adv.* **2014**, *4* (79), 42092–42113.
- (298) Song, X.; Hu, D.; Yang, X.; Zhang, H.; Zhang, W.; Li, J.; Jia, M.; Yu, J. Polyoxomolybdic Cobalt Encapsulated within Zr-Based Metal-Organic Frameworks as Efficient Heterogeneous Catalysts for Olefins Epoxidation. *ACS Sustain. Chem. Eng.* **2019**, *7* (3), 3624–3631.
- (299) Rogge, S. M. J.; Bavykina, A.; Hajek, J.; Garcia, H.; Olivos-Suarez, A. I.; Sepúlveda-Escribano, A.; Vimont, A.; Clet, G.; Bazin, P.; Kapteijn, F.; et al. Metal–organic and covalent organic frameworks as single-site catalysts. *Chem. Soc. Rev.* **2017**, *46* (11), 3134–3184.
- (300) Moon, H. R.; Lim, D.-W.; Suh, M. P. Fabrication of metal nanoparticles in metal–organic frameworks. *Chem. Soc. Rev.* **2013**, *42* (4), 1807–1824.
- (301) Chen, Y.; Li, P.; Modica, J. A.; Drout, R. J.; Farha, O. K. Acid-Resistant Mesoporous Metal-Organic Framework toward Oral Insulin Delivery: Protein Encapsulation, Protection, and Release. *J. Am. Chem. Soc.* **2018**, *140* (17), 5678–5681.
- (302) Majewski, M. B.; Howarth, A. J.; Li, P.; Wasielewski, M. R.; Hupp, J. T.; Farha, O. K. Enzyme encapsulation in metal-organic frameworks for applications in catalysis. *CrystEngComm* **2017**, *19* (29), 4082–4091.
- (303) Giannakoudakis, D. A.; Barczak, M.; Florent, M.; Bandosz, T. J. Analysis of interactions of mustard gas surrogate vapors with porous carbon textiles. *Chem. Eng. J.* **2019**, *362* (December 2018), 758–766.
- (304) Neumann, R.; Khenkin, A. M. Molecular oxygen and oxidation catalysis by phosphovanadomolybdates. *Chem. Commun.* **2006**, No. 24, 2529–2538.
- (305) Liu, J.; Du, Z.; Yang, Y.; Lu, T.; Lu, F.; Xu, J. Catalytic Oxidative Decarboxylation of Malic Acid into Dimethyl Malonate in Methanol with Dioxygen. *ChemSusChem* **2012**, *5*, 2151–2154.
- (306) Shinachi, S.; Matsushita, M.; Yamaguchi, K.; Mizuno, N. Oxidation of adamantane with 1 atm molecular oxygen by vanadium-substituted polyoxometalates. *J. Catal.* **2005**, *233*, 81–89.
- (307) Khenkin, A. M.; Rosenberger, A.; Vigdergauz, I.; Neumann, R. Aerobic Oxidations Catalyzed by Polyoxometalates. In *Polyoxometalate Chemistry*; Pope, M. T., Muller, A., Eds.; Kluwer Academic Publishers, 2001; pp 347–362.
- (308) Khenkin, A. M.; Neumann, R.; Sorokin, A. B.; Tuel, A. Aerobic hydrocarbon oxidation catalyzed by the vanadomolybdophosphate polyoxometalate, H5PV2Mo10O40, supported on mesoporous MCM-41. *Catal. Letters* **1999**, *63*, 189–192.
- (309) Zhu, J.; Shen, M.; Zhao, X.; Wang, P.; Lu, M. Polyoxometalate-based metal-organic frameworks as catalysts for the selective oxidation of alcohols in micellar systems. *Chempluschem* **2014**, *79* (6), 872–878.
- (310) Lu, H.; Gao, J.; Jiang, Z.; Yang, Y.; Song, B.; Li, C. Oxidative desulfurization of

- dibenzothiophene with molecular oxygen using emulsion catalysis. *Chem. Commun.* **2007**, 150–152.
- (311) Trakarnpruk, W.; Rujiraworawut, K. Oxidative desulfurization of Gas oil by polyoxometalates catalysts. *Fuel Process. Technol.* **2009**, *90* (3), 411–414.
- (312) Khenkin, A. M.; Leitus, G.; Neumann, R. Electron Transfer - Oxygen Transfer Oxygenation of Sulfides Catalyzed by the H5PV2Mo10O40 Polyoxometalate. *J. Am. Chem. Soc.* **2010**, *132*, 11446–11448.
- (313) Zhu, J.; Wang, P. C.; Lu, M. Study on the one-pot oxidative esterification of glycerol with MOF supported polyoxometalates as catalyst. *Catal. Sci. Technol.* **2015**, *5* (6), 3383–3393.
- (314) Tsigdinos, G. A.; Hallada, C. J. Molybdovanadophosphoric Acids and Their Salts. I. Investigation of Methods of Preparation and Characterization. *Inorg. Chem.* **1968**, *7* (3), 5–9.
- (315) Barats-Damatov, D.; Shimon, L. J. W.; Feldman, Y.; Bendikov, T.; Neumann, R. Solid-state crystal-to-crystal phase transitions and reversible structure-temperature behavior of phosphovanadomolybdic acid, H5PV2Mo10O40. *Inorg. Chem.* **2015**, *54* (2), 628–634.
- (316) Kim, M.; Chamack, M.; Geletii, Y. V.; Hill, C. L. Synergetic Catalysis of Copper and Iron in Oxidation of Reduced Keggin Heteropolytungstates by Dioxygen. *Inorg. Chem.* **2018**, *57* (1), 311–318.
- (317) Khenkin, A. M.; Rosenberger, A.; Neumann, R. Reaction of Aldehydes with the H5PV2Mo10O40 Polyoxometalate and Cooxidation of Alkanes with Molecular Oxygen. *J. Catal.* **1999**, *182*, 82–91.